Université de Montréal

Exploitation du potentiel sismique des étoiles naines blanches

par

Noemi Giammichele

Département de physique

Faculté des arts et des sciences

Thèse présentée à la Faculté des études supérieures

en vue de l'obtention du grade de

Philosophiae Doctor (Ph.D.)

en physique

Décembre, 2015

Université de Montréal

Faculté des études supérieures

Cette thèse intitulée:

Exploitation du potentiel sismique des étoiles naines blanches

présentée par:

Noemi Giammichele

a été évaluée par un jury composé des personnes suivantes:

Patrick Dufour,	Président-rapporteur
Gilles Fontaine,	Directeur de recherche
Pierre Brassard,	Directeur de recherche
Pierre Bergeron,	Membre du jury
John Landstreet,	Examinateur externe
Richard Martel,	Représentant du Doyen de la FES

Thèse acceptée le: _____

Sommaire

Le but de cette thèse est d'explorer le potentiel sismique des étoiles naines blanches pulsantes, et en particulier celles à atmosphères riches en hydrogène, les étoiles ZZ Ceti. La technique d'astérosismologie exploite l'information contenue dans les modes normaux de vibration qui peuvent être excités lors de phases particulières de l'évolution d'une étoile. Ces modes modulent le flux émergent de l'étoile pulsante et se manifestent principalement en termes de variations lumineuses multi-périodiques. L'astérosismologie consiste donc à examiner la luminosité d'étoiles pulsantes en fonction du temps, afin d'en extraire les périodes, les amplitudes apparentes, ainsi que les phases relatives des modes de pulsation détectés, en utilisant des méthodes standards de traitement de signal, telles que des techniques de Fourier. L'étape suivante consiste à comparer les périodes de pulsation observées avec des périodes générées par un modèle stellaire en cherchant l'accord optimal avec un modèle physique reconstituant le plus fidèlement possible l'étoile pulsante. Afin d'assurer une recherche optimale dans l'espace des paramètres, il est nécessaire d'avoir de bons modèles physiques, un algorithme d'optimisation de comparaison de périodes efficace, et une puissance de calcul considérable. Les périodes des modes de pulsation de modèles stellaires de naines blanches peuvent être généralement calculées de manière précise et fiable sur la base de la théorie linéaire des pulsations stellaires dans sa version adiabatique. Afin de définir dans son ensemble un modèle statique de naine blanche propre à l'analyse astérosismologique, il est nécessaire de spécifier la gravité de surface, la température effective, ainsi que différents paramètres décrivant la disposition en couche de l'enveloppe. En utilisant parallèlement les informations obtenues de manière indépendante (température effective et gravité de surface) par la méthode spectroscopique, il devient possible de vérifier la validité de la solution obtenue et de restreindre de manière

remarquable l'espace des paramètres. L'exercice astérosismologique, s'il est réussi, mène donc à la détermination précise des paramètres de la structure globale de l'étoile pulsante et fournit de l'information unique sur sa structure interne et l'état de sa phase évolutive.

On présente dans cette thèse l'analyse complète réussie, de l'extraction des fréquences à la solution sismique, de quatre étoiles naines blanches pulsantes. Il a été possible de déterminer les paramètres structuraux de ces étoiles et de les comparer remarquablement à toutes les contraintes indépendantes disponibles dans la littérature, mais aussi d'inférer sur la dynamique interne et de reconstruire le profil de rotation interne. Dans un premier temps, on analyse le duo d'étoiles ZZ Ceti, GD 165 et Ross 548, afin de comprendre les différences entre leurs propriétés de pulsation, malgré le fait qu'elles soient des étoiles similaires en tout point, spectroscopiquement parlant. L'analyse sismique révèle des structures internes différentes, et dévoile la sensibilité de certains modes de pulsation à la composition interne du noyau de l'étoile. Afin de palier à cette sensibilité, nouvellement découverte, et de rivaliser avec les données de qualité exceptionnelle que nous fournissent les missions spatiales *Kepler* et *Kepler*2, on développe une nouvelle paramétrisation des profils chimiques dans le cœur, et on valide la robustesse de notre technique et de nos modèles par de nombreux tests. Avec en main la nouvelle paramétrisation du noyau, on décroche enfin le "Saint Graal" de l'astérosismologie, en étant capable de reproduire pour la première fois les périodes observées à la précision des observations, dans le cas de l'étude sismique des étoiles KIC 08626021 et de GD 1212.

Mots clés : étoiles : naines blanches - astérosismologie - paramètres fondamentaux - composition du coeur - rotation interne - étoiles : individuelles : GD 165 - Ross 548 - GD 1212 - KIC 08626021 -

Abstract

The goal of this thesis is to explore the seismic potential of pulsating white dwarf stars, and in particular those having an hydrogen-rich atmosphere, the ZZ Ceti stars. The technique of asteroseismology relies on the information contained in the normal modes of vibration that can be excited during specific phases of the evolution of a star. These modes modulate the emerging flux of the pulsating star and mainly present themselves as multi-periodic luminosity variations. Asteroseismology is the science that examines the luminosity of pulsating stars as a function of time, to better extract the periods, apparent amplitudes and relative phases of the detected pulsation modes, using standard methods of signal processing such as Fourier techniques. We then compare the observed pulsation periods to periods generated from a stellar model by searching the optimal match with a physically sound model that best describes the pulsating star. To better search in parameter space, it is primordial to have good physically sound models, an efficient algorithm comparing the periods, and significant computing power. The periods of the pulsation modes of white dwarf stellar models can be generally calculated very precisely on the basis of the linear theory of stellar pulsations in its adiabatic version. To define a static white dwarf model suitable for a seismic analysis, it is necessary to specify the surface gravity, the effective temperature, and the various parameters describing the onion-like structure of the star. By using a posteriori the informations obtained independently (effective temperature and surface gravity) with the spectroscopic technique, it is then possible to confirm the validity of the solution obtained. The asteroseismic exercise, when successful, precisely determines the various parameters of the global structure of the pulsating star, and gives unique information on the internal structure of the star and the current state of its evolutionary phase.

We present in this thesis the complete and successful analyses, from frequency extraction to the finding of the seismic solution, of four pulsating white dwarf stars. It was possible to determine the structural parameters of these stars and to compare them to every possible independent constraints found in the literature, but to also infer on the internal dynamic and to reconstruct the internal rotation profile. At first, we analyse the pair of ZZ Ceti stars, GD 165 and Ross 548, to better understand the differences in their pulsation spectra, notwithstanding their identical spectroscopic properties. The seismic analysis reveals different internal structures, and unravels the sensitivity of some pulsation modes to the internal composition of the core of the star. To compensate for this newly discovered sensitivity, and to rival the exceptional quality of the data coming from the spatial missions *Kepler* and *Kepler*2, we develop a new parameterization of the core chemical profiles, and we validate the robustness of our technique and our models by various tests. Having in hand the new parameterization of the core, we reach the "Holy Grail" of asteroseismology, by being capable of reproducing for the first time the observed periods to the precision of the observations, in the study case of the stars KIC 08626021 and GD 1212.

Subject headings : stars : white dwarfs - asteroseismology - fundamental parameters - core composition - internal rotation - stars : individual : GD 165 - Ross 548 - GD 1212 - KIC 08626021 -

Table des matières

Liste des figures

Liste des tableaux

Remerciements

Je tiens en premier lieu à remercier mon directeur de thèse Gilles Fontaine pour son immense soutien, son enthousiasme, les longues discussions scientifiques et celles un peu moins, mais tout aussi intéressantes! Gilles m'a permis de mener à bien mon doctorat et a été un véritable père scientifique pour moi. Sans lui, je n'y serais pas arrivée. Pour tout son soutien technique, à n'importe quel petit problème j'ai pu rencontrer, je dois remercier mon co-directeur de thèse: Pierre Brassard. Je dois également remercier Stéphane Charpinet pour m'avoir épaulé tout au long de ma thèse et d'avoir toujours accepté sans sourciller de répondre à toutes mes questions. Il faut également que je mentionne l'aide inestimable de Luc Turbide pour avoir répondu patiemment, oui oui patiemment, à toutes mes questions naïves de problèmes informatiques en tout genre.

Je tiens également à remercier ma famille et Antoine pour toujours avoir été là, même à distance, surtout dans les moments plus difficiles.

Je tiens finalement à dire un grand merci à tous mes amis et collègues, en particulier Marie-Michèle, Amélie, Pier-Emmanuel, Alex, Marilyn, Marie-Ève, Cassandra et Patrick, avec qui j'ai partagé beaucoup de beaux moments tant en missions d'observation, qu'en conférences, mais surtout dans la vie de tous les jours. Ce ne serait pas complet si je ne mentionnais pas mes amis du hockey, qui m'ont permis plusieurs fois par semaine de me défouler, et de mes amis de toujours Léo, Thierry, Ksenia, Ben, Véro, Louis-Étienne, pour leur immense soutien moral.

Chapitre 1

Introduction

1.1 L'astérosismologie d'étoiles pulsantes naines blanches

L'astérosismologie, ou la sismologie stellaire, est la science qui étudie la structure interne d'étoiles pulsantes par l'interprétation du spectre des périodes de vibration de l'étoile. Différents modes d'oscillation pénètrent à différentes profondeurs à l'intérieur de l'étoile, fournissant l'information autrement inobservable du coeur même des étoiles. La méthode est similaire à celle qu'utilise les sismologistes pour étudier l'intérieur de la Terre à l'aide des oscillations des tremblements de terre. L'astérosismologie est donc un outil puissant permettant de déchiffrer la structure interne des étoiles pulsantes en comparant les propriétés des pulsations observées à celles prédites par des modèles théoriques et la théorie des pulsations.

Les naines blanches représentent le dernier stage évolutif de près de 97 % des étoiles de la séquence principale, incluant notre Soleil. En effet, une naine blanche résulte de l'effondrement gravitationnel du coeur d'une étoile géante rouge qui a épuisé son carburant stellaire, et se refroidit inexorablement. La phase de refroidissement des naines blanches, une période exempte d'évènements marquants d'un point de vue évolutif, est par contre, une des phases les plus actives en ce qui concerne l'évolution chimique de l'enveloppe. La variété d'abondances d'éléments chimiques que l'on peut parfois observer à la surface des naines blanches est un indicateur direct des différents processus physiques en compétition, que ce soit la sédimentation gravitationnelle (mécanisme principal) ou le mélange convectif, la diffusion, les forces

radiatives, les vents et l'accrétion du milieu interstellaire ou des débris de sytèmes planétaires. Les naines blanches, en se refroidissant, vont transiter par des bandes d'instabilités dans le diagramme luminosité-température défini par Hertzsprung-Russell (HR) (voir figure 1.1) et se mettre à vibrer, donnant ainsi de l'information supplémentaire via la courbe de lumière reçue.

Trois principales familles de naines blanches pulsantes sont détectées à ce jour, toutes à des stades évolutifs différents. On peut observer des portions de leur courbe de lumière à la figure 1.2. Les pulsateurs GW Vir, dont la Teff avoisine les 120,000 K, ont une atmosphère composée d'He/C/O, alors que les étoiles V777 Her (DBV), dont l'atmosphère est dominée par de l'hélium, ont une Teff $\sim$ 25,000 K. La dernière catégorie, les étoiles d'intérêt principal ici, les étoiles ZZ Ceti (DAV), des naines blanches dont la Teff $\sim$ 12,000 K ont une atmosphère dominée par l'hydrogène.

La cause des instabilités de pulsation observées dans 3 distinctes catégories de naines blanches pulsantes est la même: l'ionisation partielle du constituant principal de l'enveloppe. En effet, les ions de la couche K du carbone et de l'oxygène s'ionisent et se recombinent durant la phase des GW Vir, l'hélium se recombine en ce qui a trait aux naines blanches riches en He dans le régime V777 Her, ainsi que l'hydrogène dans la phase encore plus froide pour les étoiles riches en hydrogène correspondant au régime des ZZ Ceti. Dans chaque cas, l'ionisation partielle engendre une importante augmentation de l'opacité de l'enveloppe, et cela tend à étouffer le flux d'énergie sortant, comme on peut le voir à la figure 1.3. Dans le cas des modèles de V777 Her, et encore plus dans le cas des modèles de ZZ Ceti, la bosse d'opacité devient si large qu'une zone de convection superficielle se développe causée par la croissance d'un gradient de température superadiabatique. Cela affecte significativement la mécanique du processus responsable de l'excitation des modes de pulsations. Le transport d'énergie par convection doit être pris en compte en plus du classique transport radiatif.

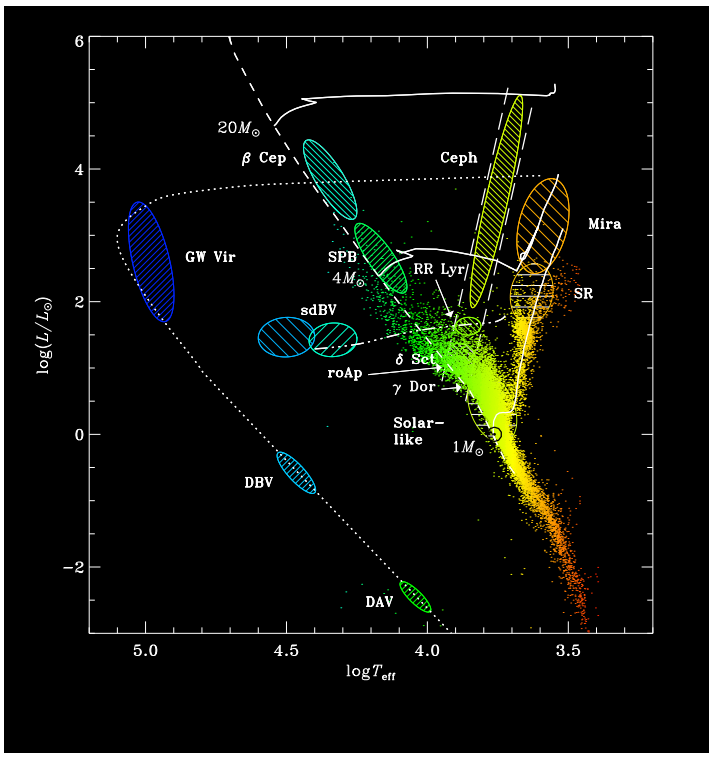

FIGURE 1.1 – Diagramme de Hertzsprung-Russell montrant les différentes familles d'étoiles pulsantes (Christensen-Dalsgaard (2007)). On retrouve la famille de naines blanches d'intérêt ici, les ZZ Ceti (DAV), dans le bas du diagramme H-R.

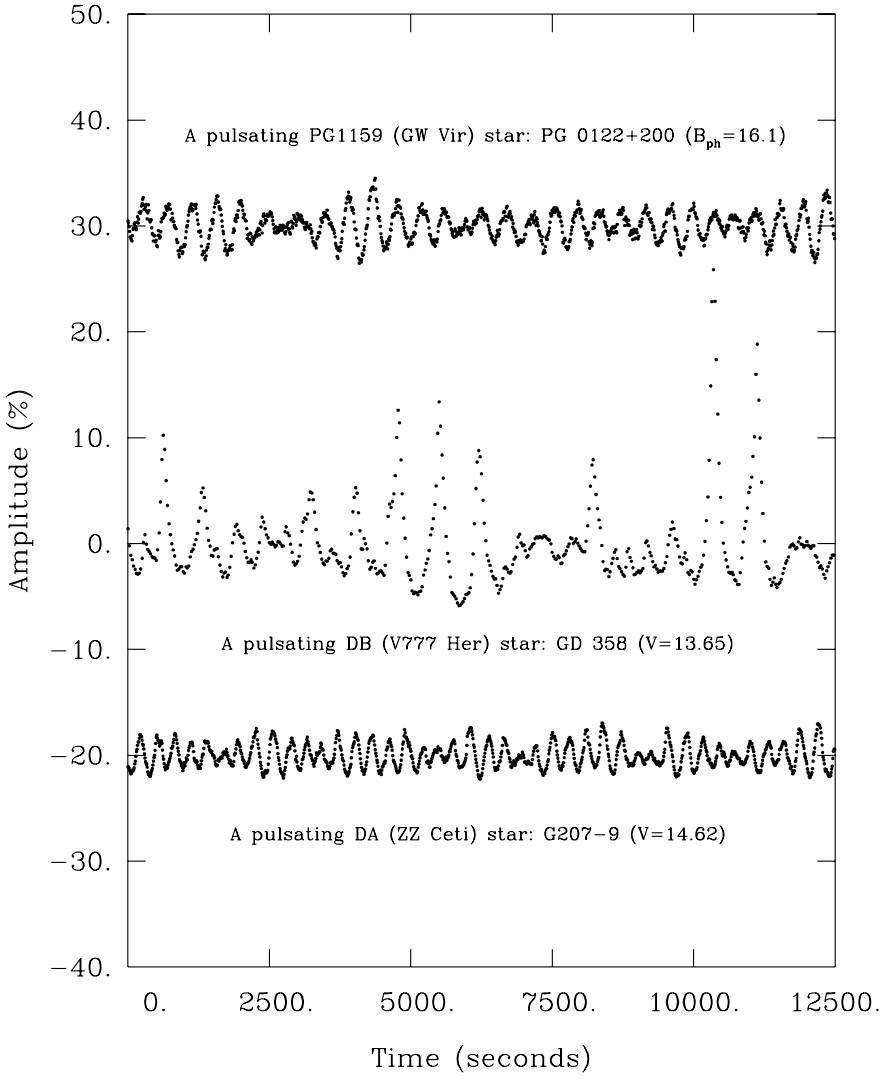

FIGURE 1.2 – Portions de courbes de lumière pour chacune des trois familles connues de naines blanches pulsantes isolées.

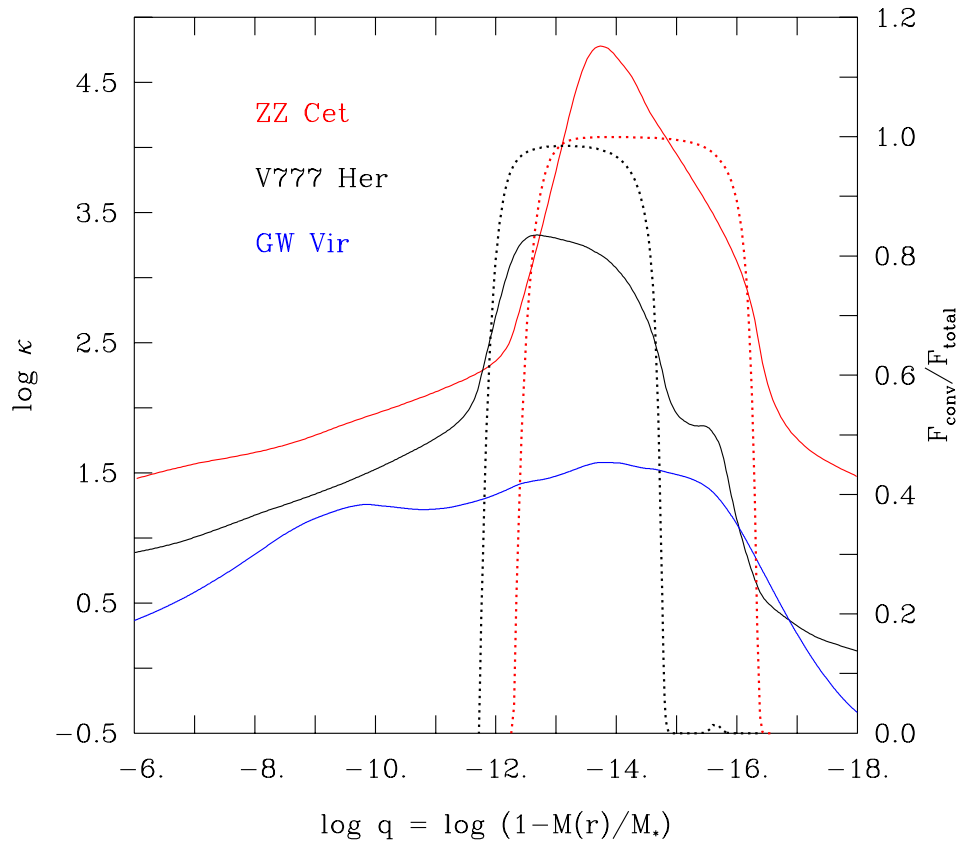

FIGURE 1.3 – Profils d'opacité (en trait plein) dans les enveloppes de modèles représentatifs d'étoiles GW Vir, V777 Her, et ZZ Ceti. L'abscisse est exprimée en termes du logarithme de la fraction de masse. Le centre du modèle se situe à une valeur de log $q = 0$ sur cette échelle, mais l'emphase à été mise sur les couches les plus externes où l'action est concentrée en termes d'excitation/atténuation des pulsations dans les naines blanches. Le rapport du flux convectif sur le flux total est également présenté (en trait pointillé) pour les modèles de V777 Her et de ZZ Ceti. Il n'y a pas de convection dans le modèle d'étoile GW Vir. Fontaine & Brassard (2008b)

1.2 Pulsations: théorie et propriétés

1.2.1 Principes de base

L'un des piliers de l'astérosismologie se base sur la théorie des pulsations stellaires. Un excellent résumé est fait dans la première section de Fontaine et al. (en préparation), dont est inspirée cette section. La théorie des pulsations stellaires énonce qu'une étoile, comme tout système mécanique, a la possibilité de vibrer dans certains modes particuliers possédant chacun une fréquence propre. On parle ici d'un système qui peut osciller en trois dimensions autour d'une structure d'équilibre possédant une symétrie sphérique (par simplicité et en très bonne approximation, on suppose que la rotation et les champs magnétiques ne brisent pas la sphéricité de l'étoile). Le système contient des solutions stables en équilibre non-statique, c'est-à-dire dépendantes du temps. Par contre en raison de la non-linéarité des équations hydrodynamiques, la détermination de ces solutions générales est un processus particulièrement complexe. Toutefois, dans la nature, les étoiles pulsantes subissent rarement des déformations de grandes amplitudes. On peut donc simplifier le problème en linéarisant les équations.

Si l'on considère l'hypothèse spécifique que les déplacements de matière ont de faibles amplitudes comparés aux dimensions du système, base de l'approche linéaire, le comportement de perturbations spatiales et temporelles dans un milieu homogène élastique est décrit par l'équation d'onde,

$$\frac{\partial^2 \overrightarrow{\psi}(\overrightarrow{r},t)}{\partial t^2} = \frac{\sigma(k)^2}{k^2}\nabla^2 \overrightarrow{\psi}(\overrightarrow{r},t) \tag{1.1}$$

où $\overrightarrow{\psi}(\overrightarrow{r},t)$ est dans notre cas le déplacement d'un élément par rapport à sa position d'équilibre. Dans cette équation, $\sigma(k)$ est la fréquence angulaire et k le nombre d'onde.

La solution générale de cette équation correspond à une onde acoustique qui se propage à une vitesse $c = \sigma/k$. Pour un problème aux dimensions finies tel celui qui nous occupe présentement, les conditions frontières aux bornes du domaine font en sorte que seules les longeurs d'onde "correctes" vont résonner, les autres disparaissants à cause d'interférences destructives après plusieurs reflexions sur les parois. Les modes normaux de vibration sont les solutions de l'équation d'onde classique en présence de conditions frontières. Seules certaines

solutions sont permises (les modes normaux ou fonctions propres) correspondant au spectre discret des valeurs possibles de fréquences angulaires d'oscillations (les valeurs propres $\sigma_0 < \sigma_1 < \sigma_2, ...$).

Les étoiles ne sont pas des systèmes homogènes, et peuvent être généralement considérées, en première approximation, comme des sphères auto-gravitantes gaseuses avec une composition chimique dépendante de la profondeur. La vitesse du son définie précédemment n'est plus uniforme, et les éléments de fluide dans l'étoile sont assujettis à une accélération gravitationnelle variable. Les ondes qui se propagent dans l'étoile ne sont plus typiquement acoustiques, mais sont de type gravito-acoustiques. La théorie linéaire des oscillations stellaires non-radiales commence avec les équations d'hydrodynamique qui gouvernent un fluide en présence d'un champ gravitationnel, l'équation de mouvement (équation de Navier-Stokes):

$$\rho(\frac{\partial}{\partial t} + \overrightarrow{v} \cdot \overrightarrow{\nabla})\overrightarrow{v} = -\overrightarrow{\nabla} P - \rho\overrightarrow{\nabla}\Phi, \tag{1.2}$$

l'équation de continuité

$$\frac{\partial \rho}{\partial t} + \overrightarrow{\nabla} \cdot (\rho \overrightarrow{v}) = 0, \tag{1.3}$$

ainsi que l'équation de Poisson qui relie le potentiel gravitationnel à la distribution de matière.

$$\nabla^2\Phi = 4\pi G\rho, \tag{1.4}$$

L'échange d'énergie entre le bain thermique (l'énergie interne du fluide) et les oscillations (l'énergie cinétique des mouvements macroscopiques du fluide) est négligé dans le cas présent. C'est l'approximation adiabatique, qui adresse seulement le comportement mécanique des oscillations mais ne permet pas de traiter la question de la stabilité des modes. On ne peut pas avoir d'information sur l'excitation ou non d'un mode. Cependant, les effets non-adiabatiques n'influencent que marginalement la valeur de la fréquence d'oscillation d'un mode de pulsation dans un modèle stellaire. On peut donc utiliser la version adiabatique pour calculer les périodes à une précision suffisante pour notre exercice astérosismologique. La prochaine étape est de considérer uniquement des petites pertubations à la position d'équilibre, qui est celle

d'un modèle stellaire sphérique, afin de pouvoir linéariser les équations hydrodynamiques. En accord avec les propriétés fondamentales d'un mode normal de vibration, toutes les quantités perturbées oscillent en phase et passent par les positions d'équilibre en même temps. Les variables dépendantes qui apparaissent dans les équations linéarisées ont une dépendance temporelle donnée par $e^{i\sigma t}$, où σ est la fréquence et t, le temps. La technique de séparation des variables est ici utilisée afin de caractériser le comportement spatial en terme d'une partie radiale et d'une partie angulaire. Pour un modèle sphérique non perturbé, le comportement angulaire d'un mode est donné par une fonction harmonique sphérique Y_l^m. On arrive donc à un système de 4 équations différentielles linéaires avec des variables réelles, qui à cause des conditions frontières au centre et à la surface de l'étoile, permet seulement certaines solutions (les modes) correspondant aux valeurs spécifiques de fréquence d'oscillation σ (les fréquences propres). Un mode de pulsation stellaire est défini en terme de 3 nombres, k, l, et m. k, l'ordre radial, donne le nombre de noeuds dans la direction radiale de la fonction propre, et peut avoir comme valeur tout entier positif, $k = 0, 1, 2, ...$ Les autres nombres, l et m, sont les indices de la fonction harmonique sphérique qui spécifie la géométrie angulaire du mode. L'indice l, appelé degré du mode, donne le nombre de plans nodaux qui divise la sphère stellaire et prend aussi comme valeur les entiers positifs, $l = 0, 1, 2, ...$ Le nombre m, l'ordre azimuthal, donne par sa valeur absolue le nombre de plans qui divise la sphère stellaire perpendiculairement à l'équateur et qui passe par les pôles. Il existe $2l + 1$ valeurs pour m pour chaque valeur de l, $m = -l, -l + 1, ..., 0, ..., l - 1, l$. Une étoile qui ne tourne pas (modèle sphérique) a des fréquences propres dégénérées en m, dû à la symétrie du problème.

1.2.2 Fréquences fondamentales et relations asymptotiques

Il existe deux comportements distincts mais complémentaires d'ondes gravito-acoustique dans une étoile sphérique, un fondamentalement d'origine acoustique, et l'autre relié à l'action de la gravité. En terme de modes normaux de vibration, ces comportements sont respectivement appelés "modes de pression" (modes p) et "modes de gravité" (mode g). Ces deux comportements différents sont reliés aux deux quantités fondamentales qui apparaîssent dans

les équations de pulsations linéarisées: la fréquence de Brunt-Väisälä, N, définie par:

$$N^2 \equiv g(\frac{1}{\Gamma_1}\frac{dlnP}{dr} - \frac{dln\rho}{dr}), \tag{1.5}$$

et la fréquence de Lamb, L_l, définie par:

$$L^2 \equiv \frac{l(l+1)c^2}{r^2}, c^2 = \frac{\Gamma_1 P}{\rho} \tag{1.6}$$

où c est la vitesse du son adiabatique locale.

On considère un élément de fluide en équilibre avec le milieu à une profondeur arbitraire dans l'étoile. Si une perturbation est appliquée à cet élément de telle sorte qu'il est comprimé sans en changer la position dans l'étoile, une force de rappel proportionnelle au contraste en densité va s'instaurer entre l'élément perturbé et le milieu. Libéré de sa contrainte initiale, l'élément va osciller en volume (densité, pression) autour de sa position d'équilibre en réaction à la force de rappel. Ces oscillations vont correspondre à une fréquence caractéristique, la fréquence de Lamb, qui est étroitement reliée à la vitesse locale du son au point d'équilibre dans l'étoile. Ces oscillations sont essentiellement acoustiques et on parle d'ondes acoustiques, ou de manière équivalente d'*ondes de pression*, vu que la force de rappel est un gradient de pression.

On considère maintenant un élément de fluide en équilibre avec son environnement dans l'étoile et on le déplace au dessus de sa position d'équilibre. L'élément va maintenant être plus lourd que le milieu dans lequel il interagit (sa densité est plus grande que son nouvel environnement), et libéré de sa contrainte initiale, va osciller de haut en bas autour de sa position d'équilibre. Ces oscillations vont également correspondre à une fréquence caractéristique qui dépend des conditions physiques locales au point d'équilibre, la fréquence de Brunt-Väisälä. Dans ce cas précis, vu que la force de rappel est la force d'Archimède, et que celle-ci est directement reliée à la magnitude de l'accélération locale, on parle alors d'*ondes de gravité*.

On ne peut, à toute fin pratique, séparer complètement l'effet de la pression de celui de la gravité. Et même s'il est commun de diviser les ondes gravito-acoustiques en deux branches distinctes, les modes de pression (mode p) et les modes de gravité (mode g), les fréquences

propres des modes de pulsation de l'étoile dépendent à la fois de la variation de la fréquence de Lamb avec la profondeur ainsi que celle de la fréquence de Brunt-Väisälä.

Il est possible de dériver une relation de dispersion pour les ondes gravito-acoustiques en faisant 2 approximations. La première, l'approximation dite de Cowling, consiste à négliger la perturbation du potentiel gravitationnel. Dans cette approximation, les équations de pulsation adiabatique se réduisent en un système de 2 équations différentielles linéaires. Cette approximation n'est pas très bonne pour les modes ayant des faibles valeurs de k et l, et plus généralement pour les modes p, mais suffit dans le contexte présent. La deuxième approximation, l'approximation locale, précise que dans une couche arbitraire du modèle stellaire la plupart des quantités apparaissant dans les 2 équations de pulsation restantes (vitesse du son, fréquence de Lamb, fréquence de Brunt-Väisälä, accélération gravitationnelle locale) peuvent être considérée comme ne variant quasiment pas dans la direction radiale dans la région de la couche du modèle, qui dans le même temps couvre un grand nombre de longueurs d'onde radiales. Ceci est possible uniquement pour des modes ayant de grandes valeurs d'ordre radial k. Si l'on néglige complètement les variations radiales, on trouve que les fonctions propres ont un comportement du type $\exp(\mathrm{i}k_r r)$, où k_r est le nombre d'onde radial qui obéit à la relation de dispersion suivante,

$$k_r^2 = \frac{1}{c^2\sigma^2}(\sigma^2 - L_l^2)(\sigma^2 - N^2). \tag{1.7}$$

Ceci indique que les oscillations se propagent radialement (comportement oscillatoire) si k_r est une quantité réelle, ou sont évanescentes (comportement exponentiel) si k_r est une quantité imaginaire.

Selon l'équation de dispersion, il existe deux zones de propagation dans un modèle stellaire correspondant à deux types de modes de pulsation. Si k_r^2 est positif (et k_r est donc réel) lorsque $\sigma^2 > L_l^2, N^2$, on a des modes p. Lorsque $\sigma^2 < L_l^2, N^2$, on a des modes g. Dans les régions de l'étoile où $L_l^2 < \sigma^2 < N^2$, k_r^2 est négatif (k_r est imaginaire), les ondes gravito-acoustiques sont évanescentes.

On peut obtenir de l'information supplémentaire quant au comportement des fréquences propres (périodes) des modes p et de modes g en considérant les cas limites extrêmes. Dans

la limite où $\sigma^2 \gg L_l^2, N^2$, la relation de dispersion montre,

$$\sigma^2 = \sigma_p^2 \simeq c^2 k_r^2. \tag{1.8}$$

C'est la limite où se trouve essentiellement les modes de pression ou modes acoustiques uniquement, car seulement la vitesse du son est impliquée dans le terme de droite. On peut constater que la fréquence d'un mode p augmente avec k_r. Dans le cadre de la limite opposée, où $\sigma^2 \ll L_l^2, N^2$, l'équation de dispersion se réduit à:

$$\sigma^2 = \sigma_g^2 \simeq \frac{l(l+1)N^2}{k_r^2 r^2}. \tag{1.9}$$

C'est la limite où se trouve les modes de gravité uniquement, car seulement la fréquence de Brunt-Väisälä est impliquée dans l'expression (pas de terme acoustique). On peut remarquer que la fréquence d'un mode g décroit quand l'ordre radial k_r augmente. Par ailleurs, la fréquence d'un mode g d'un certain ordre radial augmente quand le degré l augmente. Par ailleurs, des modes g avec un degré $l = 0$ n'existe pas ayant une fréquence de zéro. On peut voir un exemple de spectre de périodes à la figure 1.4.

On peut donc résumer ceci, les modes gravito-acoustiques se comportent comme des modes purs de pression à haute fréquence, alors que ils se comportent comme des modes purs de gravité à très basse fréquence. Dans les deux cas, ces limites correspondent à de très larges valeurs d'ordre radial ($k \gg 1$) appelés "limite asymptotique".

Dans le cas des naines blanches, seulement des modes g de bas à moyen ordre ont été observés, alors que les modes p permettraient de sonder le coeur plus en profondeur. La théorie des pulsations non-adiabatiques prédit la présence de modes p excités, mais ils n'ont malheureusement pas encore été détectés à ce jour dans les naines blanches.

1.2.3 Fonction poids

Il a été montré par Lynden-Bell & Ostriker (1967), que les valeurs propres des équations de pulsation adiabatique peuvent être estimées à partir d'une approche variationnelle. Pour un modèle purement sphérique, le carré d'une fréquence propre est donné par:

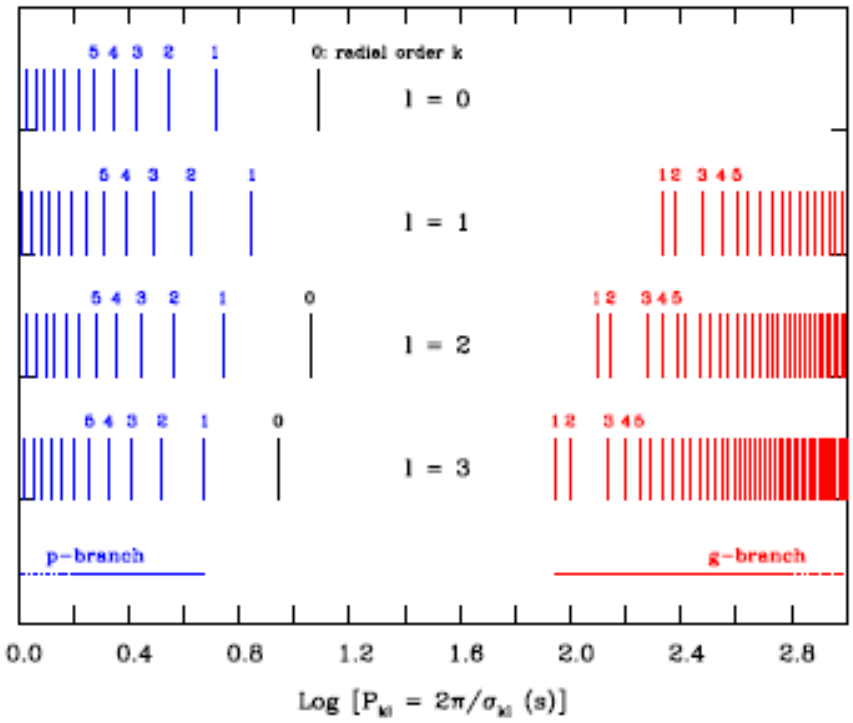

FIGURE 1.4 – Spectre des périodes pour des degrés et ordres bas pour un modèle représentatif d'étoile ZZ Ceti. Les deux familles de modes gravito-acoustiques, les modes p et les modes g sont illustrés ici.

$$\sigma^2 = \frac{D}{A}, \tag{1.10}$$

où D et A sont deux expressions sous forme d'intégrale ayant les fonctions propres de cette fréquence propre. Cette expression peut servir après que la solution du problème des valeurs propres soit obtenue pour dériver un estimé variationnel des fréquences propres qui est une mesure de cohérence interne. D'un plus grand intérêt, par contre, est le fait que l'équation 1.10 utilise des intégrales pour le modèle stellaire. Alors que l'intégrale A apparaissant au dénominateur est simplement proportionnelle à l'énergie cinétique, l'intégrande de l'intégrale D apparaissant au numérateur fournit une mesure de la contribution de chaque couche du modèle stellaire à l'intégrale globale. C'est ainsi que l'intégrande de l'intégrale D pour un mode de pulsation donné est souvent appelé la "fonction poids" de ce mode. Ce concept est très utile pour déterminer quelles régions d'un modèle stellaire contribue le plus à la formation de ce mode, comme on va le voir plus tard à la section suivante lors de l'exercice astérosismologique. L'intégrale D peut s'écrire,

$$D = \int_0^R [\xi_r^2 N^2 + \frac{(P')^2}{\Gamma_1 P \rho} + \Phi'(\frac{P'}{\Gamma_1 P} + \xi_r \frac{N^2}{g})]\rho r^2 dr, \tag{1.11}$$

où deux autres fonctions propres adiabatiques apparaissent explicitement: Φ' (la perturbation Eulérienne du potentiel gravitationnel), et P' (la perturbation Eulérienne de la pression). ξ_r est, elle, la composante radiale du vecteur déplacement Lagrangien.

1.2.4 Le "splitting" rotationnel

L'approche variationnelle mise de l'avant par Lynden-Bell & Ostriker (1967) est ici aussi d'une grande utilité pour l'estimation des effets de la rotation lente sur les spectres des fréquences propres d'une étoile pulsante. En pratique, "rotation lente" veut dire $\Omega \ll \sigma$, où Ω est la fréquence de rotation de l'étoile. La méthode variationnelle permet de traiter la rotation lente comme une perturbation et mène à des corrections des fonctions propres qui sont données sous la forme d'expressions intégrales impliquant les fonctions propres non-perturbées, c'est-à-dire celles venant de la solution du problème de fonctions propres pour un modèle

purement sphérique.

L'effet principal de la rotation lente est de détruire la symétrie sphérique de l'étoile, et de lever la dégénérescence $(2l + 1)$ qui existe pour les fréquences propres d'un mode avec différentes valeurs de m mais appartenant à la même paire (k, l) d'un modèle sans rotation. Si on suppose que la fréquence de rotation angulaire est une simple fonction de la profondeur, $\Omega(r)$, la fréquence d'un mode, maintenant définie par les trois indices k, l, et m, est donnée au premier ordre par la théorie des perturbations par,

$$\sigma_{klm} \simeq \sigma_{kl} - m \int_0^R \Omega(r) K_{kl}(r) dr, \tag{1.12}$$

où σ_{kl} est la fréquence des modes dégénérés (k, l) en l'absence de rotation, et le deuxième terme à droite de l'équation est la correction au premier ordre de cette fréquence, avec m prenant les valeurs $-l, -l + 1, ..., l - 1, l$. La quantité $K_{kl}(r)$ apparaissant dans le terme de la correction est présentée comme le kernel de rotation du premier ordre. Il joue le rôle de fonction poids, de manière très similaire à la fonction poids présentée précédemment, mais cette fois, il fait référence aux régions qui contribuent le plus au splitting de fréquence causé par la rotation. Il est donné par l'expression suivante utilisant les fonctions propres non-perturbées,

$$K_{kl}(r) = \frac{\{\xi_r^2 + [l(l+1) - 1]\xi_h^2 - 2\xi_r \xi_h\}\rho r^2}{\int_0^R \{\xi_r^2 + l(l+1)\xi_h^2\}\rho r^2 dr}. \tag{1.13}$$

Si on émet l'hypothèse que l'étoile tourne de manière rigide, c'est-à-dire que $\Omega \neq \Omega(r)$, on obtient:

$$\sigma_{klm} \simeq \sigma_{kl} - m\Omega(1 - C_{kl}), \tag{1.14}$$

où Ω est la fréquence angulaire de rotation, et C_{kl} est le coefficient de rotation rigide du premier ordre, aussi appelé coefficient de Ledoux. Il est donné par:

$$C_{kl} = \frac{\int_0^R (2\xi_r \xi_h + \xi_h^2)\rho r^2 dr}{\int_0^R (\xi_r^2 + l(l+1)\xi_h^2)\rho r^2 dr}. \tag{1.15}$$

Une fois la solution au problème de valeur propre obtenue pour un mode, on peut ainsi obtenir la valeur du coefficient C_{kl} pour ce mode. La rotation rigide au premier ordre mène à un espacement égal entre les composantes adjacentes en fréquence donné par,

$$\Delta\sigma = \Omega(1 - C_{kl}). \tag{1.16}$$

Comme c'est le cas pour tous les types d'étoiles, les valeurs de C_{kl} pour des modes g tendent vers $1/l(l+1)$ dans la limite asymptotique d'ordre radial élevé, alors que pour les modes p les valeurs deviennent très petites comparées à 1. Les modes g de faible ordre, ceux d'intérêt pour les naines blanches pulsantes, montrent des valeurs de C_{kl} significativement différentes d'un mode à l'autre, permettant ainsi de mieux contraindre l'ordre radial d'un mode plutôt qu'un autre en présence de splitting rotationnel.

1.3 Format de la thèse

Maintenant qu'on a en main certains des outils permettant de comprendre l'analyse de naines blanches pulsantes, il est temps de passer au corps de cette thèse. Celle-ci comprend cinq articles publiés, soumis, ou à soumettre dans le *Astrophysical Journal* et le *Astrophysical Journal Supplement*. Également présentés en annexes, les huit comptes-rendus de conférence au cours desquelles nous avons présenté des résultats. L'ensemble de ces articles et comptes-rendus a comme trame centrale l'exploitation du potentiel sismique des étoiles naines blanches pulsantes.

Le chapitre 2 présente l'analyse des courbes de lumière et l'extraction des fréquences des deux naines blanches, jumelles spectroscopiques, GD 165 et Ross 548, ainsi qu'une révision des paramètres atmosphériques de ces deux étoiles. Cette analyse se base sur des données photométriques de qualité exceptionnelles obtenues au CFHT avec l'instrument LAPOUNE en 1995 et 1991, pour les deux étoiles respectivement, qui n'avaient à ce jour pas été exploitées. Ces deux étoiles présentent des périodes de pulsation assez différentes, malgré le fait qu'elles aient une température effective et une gravité de surface presque identiques.

Le chapitre 3 s'attaque donc à ce problème non résolu en effectuant l'analyse sismologique

complète de ces deux étoiles, dont le spectre de pulsation est relativement simple, vu leur positionnement sur le bord chaud de la bande d'instabilité. La détermination des paramètres principaux et secondaires de GD 165 et Ross 548 est effectuée au travers de cette analyse ainsi que la comparaison avec des paramètres déterminés par des méthodes autres que sismique. L'utilisation du splitting rotationnel permet l'étude du profil de rotation des couches extérieures de GD 165 et Ross 548. L'analyse comparée des deux étoiles permet également la découverte de la sensibilité du cœur sur les périodes de pulsation de Ross 548.

Le chapitre 4 propose une nouvelle paramétrisation du cœur qui a la capacité de mieux reproduire le profil de l'oxygène (et inversement du carbone) obtenu par voie de calculs évolutifs, afin de mieux répondre à la nouvellement découverte sensibilité du cœur sur les pulsations de certaines étoiles. Des tests sont réalisés sur la précision atteignable lors d'un exercice astérosismologique, ainsi que sur la crédibilité de résultats obtenus, en faisant des tests avec des séquences aléatoires. Le dernier (mais non le moindre) ensemble de tests examine la reproductibilité de la stratification chimique ainsi que des paramètres principaux de l'étoile résultants de calculs évolutifs à partir de nos modèles statiques complets et paramétrisés.

Les chapitres 5 et 6 présentent les études sismiques complètes de deux étoiles naines blanches pulsantes, la DBV KIC 08626021 et la DAV GD 1212 respectivement, observées lors des missions spatiales *Kepler* et *Kepler2* avec la nouvelle paramétrisation du cœur présentée au chapitre 4. Les deux analyses sont basées sur des nouvelles analyses de courbes de lumière, au chapitre 5, avec l'ajout d'une nouvelle période au spectre de pulsation par Zong et al. (2016), et pour GD 1212 par une nouvelle ré-analyse en profondeur présentée au chapitre 6. La détermination des paramètres principaux et secondaires est réalisée ainsi que la comparaison avec les paramètres atmosphériques déterminés par la méthode spectroscopique. La sensibilité du cœur est explorée, et la détermination de la stratification chimique entière des deux étoiles est dévoilée. Par ailleurs, l'identification des modes dévoile du splitting rotationnel qui permet l'étude du profil de rotation au creux des deux étoiles KIC 08626021 et GD 1212.

L'article présenté au chapitre 2 expose des données d'observation obtenues par les coauteurs G. Fontaine, P. Bergeron, S. Charpinet, B. Pfeiffer, G. Vauclair. L'analyse est faite dans sa totalité par l'auteure de cette thèse, et la rédaction conjointement avec G. Fontaine,

alors que le support technique est apporté par P. Brassard. En ce qui a trait à l'article présenté au chapitre 3, l'analyse a également été faite dans sa totalité par l'auteure de cette thèse, et la rédaction conjointement avec G. Fontaine, avec le soutien technique de P. Brassard et S. Charpinet. Pour ce qui concerne les articles des chapitres 4, 5, et 6, l'analyse et la rédaction ont été réalisées par l'auteure de cette thèse, en excluant l'analyse des courbes de lumière et l'extraction des fréquences réalisées par S. Charpinet. Le tout avec le soutien technique de G. Fontaine, S. Charpinet et P. Brassard.

Chapitre 2

A New Analysis of the Two Classical ZZ Ceti White Dwarfs GD 165 and Ross 548. I. Photometry and Spectroscopy

N. Giammichele[1], G. Fontaine[1], P. Bergeron[1], P. Brassard[1], S. Charpinet[2], B. Pfeiffer[3], and G. Vauclair[2]

[1] *Département de Physique, Université de Montréal, Succ. Centre-Ville, C.P. 6128, Montréal, QC H3C 3J7, Canada*

[2] *Université de Toulouse, UPS-OMP, IRAP, Toulouse F-31400, France*

CNRS, IRAP, 14 avenue Edouard Belin, F-31400 Toulouse, France

[3] *Department of Physics and Astronomy, Langara College, Vancouver, BC V5Y 2Z6, Canada*

Received 2015 September 9; accepted 2015 November 4; published 2015 December 10

Published in *The Astrophysical Journal*

December 2015, Volume 815, 56

2.1 ABSTRACT

We present the first of a two-part seismic analysis of the two bright, hot ZZ Ceti stars GD 165 and Ross 548. In this first part, we report the results of frequency extraction exercises based on time-series data sets of exceptional quality. We uncovered up to 13 independent pulsation modes in GD 165, regrouped into 6 main frequency multiplets. These include 9 secure (S/N $>$ 4) detections and 4 possible ones (4 $\geq$ S/N $\geq$ 3). Likewise, we isolated 11 independent modes in Ross 548 (9 secure and 2 possible detections), also regrouped into 6 multiplets. The multiplet structure is likely caused by rotational splitting. We also provide updated estimates of the time-averaged atmospheric properties of these two pulsators in the light of recent developments on the front of atmospheric modeling for DA white dwarfs.

2.2 INTRODUCTION

The quest for credible and realistic seismic models for pulsating white dwarfs has been on for more than two decades now. Despite some remarkable early successes (e.g., Winget et al. 1991), progress has been slow, and conflicting results have sometimes been obtained (see, e.g., Section 8.2 of Fontaine & Brassard 2008 for a historical survey of the field through 2008). In particular, reliable and convincing seismic models of the pulsating white dwarfs of the ZZ Ceti type have remained far and few despite the more recent efforts of Bischoff-Kim et al. (2008), Castanheira & Kepler (2009), Romero et al. (2012), and others. The observed periods still cannot be reproduced at a satisfactory level of accuracy, and, consequently, the inferences on the internal structure of these pulsators have remained weak, at best.

The ZZ Ceti stars are low-degree and low- to mid-order g-mode pulsators constituting the most numerous family of pulsating white dwarfs. They are DA (H-line) white dwarfs concentrated in a very narrow instability strip centered on $T_{\rm eff} \simeq 11{,}800$ K in the effective temperature-surface gravity plane (Figure 2 of Green et al. 2015 provides an updated view of that strip). Observationally, the ZZ Ceti stars located near the blue edge of the strip show the simplest behavior, i.e., they exhibit essentially linear (but multi-periodic) light curves made of the superposition of a few very low-order g-modes of low amplitudes. The frequency extraction

analysis in such cases is generally straightforward, even from single-site data provided, in that instance, the S/N is high enough. In contrast, many more modes (of higher order, longer period) are excited in the cooler ZZ Ceti stars, and with amplitudes typically large enough to produce important nonlinear effects in the light curve (harmonics and combination frequencies of the dominant periodicities). In such instances, the frequency extraction exercise can become very touchy and usually requires high-resolution multi-site data to see it through. In addition, several of these high-amplitude, nonlinear pulsators have unstable period spectra, making it difficult, if not impossible, to use in seismic modeling. Hence, even though the cooler ZZ Ceti stars generally exhibit richer period spectra than their hotter counterparts (thus providing in principle more seismic constraints), they remain more difficult to model within the framework of linear pulsation theory. Moreover, having a larger number of detected periods is not, by itself, a guarantee of the superior quality of these constraints. Indeed, there is a lot more seismic information contained in the lowest-order modes of the period spectrum than in the higher-order domain connecting with the asymptotic regime. Finally, to be complete, it should be mentioned that ZZ Ceti stars that have cooled down very near the red edge exhibit again a simple behavior, dominated by only a few excited modes (of high order) with low amplitudes.[1]

With this background in mind, we decided to revisit the problem of the seismic modeling of ZZ Ceti stars using current techniques, typical of those used highly successfully for the class of pulsating hot subdwarf B stars as reviewed and used recently in Charpinet et al. (2013) and Van Grootel et al. (2013a). As a first test, we thought it wise to focus on the simpler pulsators in order to evaluate the potential of these techniques for ZZ Ceti stars in general. In light of the availability of time-series data sets of exceptional quality that some of us gathered years ago at the Canada-France-Hawaii Telescope (CFHT), and which have remained largely unexploited to date, we selected a pair of bright, hot ZZ Ceti stars: GD 165 and Ross 548. This pair is particularly interesting and puzzling from a seismic point of view, because the two stars have been known to be spectroscopic twins since Bergeron et al. (1995), and, yet, are also known to exhibit significantly different dominant pulsation periods (120 s and 192 s in GD 165 vs 213 s and 274 s in Ross 548). The immediate idea that comes to mind is that those

[1]To see this better, the interested reader might enjoy the "journey" through the ZZ Ceti instability strip proposed in Section 6 of Fontaine & Brassard (2008).

two objects, with otherwise comparable atmospheric parameters, may have different internal structures, a possibility that should be testable through seismic modeling.

We present, in this paper, the first part of a detailed seismic analysis of GD 165 and Ross 548, that related to the characterization of the pulsation modes extracted from our available CFHT light curves. To avoid repetition and make some economy of space, we discuss the various steps of the procedure for both stars at the same time, inasmuch as possible. In addition, we also provide updated spectroscopic estimates for both stars in the light of recent progress made on the front of atmospheric modeling for DA white dwarfs as presented by Tremblay & Bergeron (2009) and Tremblay et al. (2013). These estimates represent fundamental independent checks on our eventual seismic models. In a forthcoming publication, we will present the second and final part of our analysis, the seismic modeling per se, including comparisons with past efforts on that front for both stars.

The present work is part of the Ph.D. thesis of the lead author and represents the first step toward establishing the foundations for improved seismic modeling of pulsating white dwarfs. Our ultimate goal in the immediate future is to be able to fully exploit the exquisite data sets gathered with *Kepler* and *Kepler*-2 on ZZ Ceti stars (Greiss et al. 2014; Hermes et al. 2014). Prior to that, our approach has to be fully tested on "simple" bright pulsators such as GD 165 and Ross 548, well observed from the ground, and this fully justifies, we believe, the investigation presented in this short series of two papers.

2.3 THE TWO TARGETS

The variability of GD 165 ($V = 14.32 \pm 0.01$) was first reported by Bergeron & McGraw (1990). This was the first time that the existence of a new ZZ Ceti star had been predicted in advance of photometric monitoring on the basis of spectroscopy. This approach proved to be extremely lucrative, leading over the years to the discovery of a large number of new ZZ Ceti stars (see, e.g., Gianninas et al. 2011 and references therein). GD 165 was also part of the initial sample of 22 ZZ Ceti stars studied in detail by Bergeron et al. (1995) who provided the first quantitative and homogeneous view of the ZZ Ceti instability strip in the spectroscopic HR diagram, including a calibration of the convective efficiency in the atmospheres of those

TABLE 2.1 – Journal of CFHT Observations for GD 165

Run name	Date (UT)	Start time (UT)	Sampling time (s)	Length (s)
CFH-032	20 May, 1995	06:10:10	10	20490
CFH-034	21 May, 1995	05:44:00	10	4250
CFH-035	22 May, 1995	05:40:27	10	27460
CFH-037	23 May, 1995	05:42:46	10	20000
CFH-039	24 May, 1995	05:51:10	10	14470
CFH-041	25 May, 1995	07:31:00	10	13480

stars. Their ML2/α=0.6 results give $T_{\rm eff}$ = 11,980±350 K and log g = 8.06±0.05 for GD 165, close to the blue edge of the ZZ Ceti instability strip.

Bergeron et al. (1993) presented an analysis of a Whole Earth Telescope (WET) campaign carried out on GD 165 in 1990 May. The campaign resulted in some 233 h of broadband "white light" photometric data gathered from six different sites using small telescopes. The formal resolution achieved during the campaign was 1.2 μHz, and the duty cycle was 35%. Despite these considerable efforts, the results turned out to be rather disappointing as only three main periodicities could be detected. Furthermore, it was not possible to decide if the fine structure observed in the two largest peaks (120 s and 192 s) in the Fourier transform of the light curve was due to triplets or quintuplets. In brief, the exercise was defeated by the low signal-to-noise ratio (S/N) of the observations in regard to the relatively low amplitudes of the modes excited in GD 165.

Another broadband photometric campaign on GD 165 was carried out by two of us (G.F. and B.P.) using the CFHT/LAPOUNE[2] combination in 1995 May. The light curve of GD 165 was sampled for a total of 27.9 h over six consecutive nights. The formal resolution achieved was 2.2 μHz and the duty cycle was equal to 22%. A journal of observations is provided in Table 2.1. The conditions on Mauna Kea during that run were superb as can be appreciated from the sample light curve shown in Figure 2.1a. Because of the much improved sensitivity achieved during the CFHT campaign, six statistically significant peaks were detected (as opposed to only three during the WET run) as can be seen in Figure 2.2 displaying the Fourier amplitude

[2]LAPOUNE is the Montréal portable 3-channel photometer that was used often at the CFHT and at Steward Observatory, in particular, to monitor pulsating white dwarfs and hot B subdwarfs from 1990 through 2005. Some details on the instrument and its use can be found in Billères (2000).

spectra of the two campaigns in the 0−10 mHz bandpass.

For its part, Ross 548 ($V = 14.16 \pm 0.01$) is ZZ Ceti itself, the prototype of the class. Bergeron et al. (1995) determined for it the values $T_{\rm eff} = 11{,}990 \pm 350$ K and $\log g = 7.98 \pm 0.05$, virtually the same atmospheric parameters as GD 165 within the measurement errors. Its variability was uncovered by Lasker & Hesser (1971)[3]. It soon became apparent that the period structure of Ross 548 is remarkably stable as noted by Stover et al. (1980). Given this, Ross 548 became a target of choice for attempting to measure its evolutionary timescale through rates of period change measurements. Hence, over the years, Ross 548 was often observed with photometers, notably at McDonald Observatory in the pursuit of the determination of its evolutionary timescale through dP/dt measurements of the dominant pulsation mode at 213.1326 s. This effort culminated recently with the work and result reported in Mukadam et al. (2013; and see also Mukadam et al. 2003 for a progress report). Three of us (P.Be., G.F., and G.V.) contributed modestly to this long-term effort through a 5-day campaign on Ross 548 at the CFHT back in 1991 September. While our observations were used for a seasonal measurement of the drift rate of the main pulsation mode, the information concerning other modes in Ross 548 remained largely unexploited, at least at the public level. The present project gives us the opportunity to remedy the situation. As it turns out, and to our knowledge, our 1991 CFHT data on Ross 548 represent the most sensitive seasonal data set ever gathered on that star.

A journal of observations for our 1991 campaign on Ross 548 is provided in Table 2.3. Ross 548 was observed with LAPOUNE during the last half of each night of the run, except for September 19 when a target of opportunity was looked at instead. The first half of each night was used to monitor GD 385, another bright ZZ Ceti pulsator (Fontaine et al. 1980). The sky conditions above Mauna Kea were again excellent throughout the whole mission. Altogether, the light curve of Ross 548 was sampled for a total of 18.9 h over five nights. The

[3]As correctly stated in Fontaine & Brassard (2008), and contrary to the more recent comment of Mukadam et al. (2013), Ross 548 was indeed the second pulsating DA white dwarf to be discovered. It is not clear to this day why the class was named after it instead of the first pulsator, HL Tau 76, discovered by Landolt (1968). The object mentioned by Mukadam et al. (2013), G44-32, was suspected of being an object similar to HL Tau 76 by Lasker & Hesser (1969), but turned out to be a flare star (Warner, Van Citters, & Nather 1970). McGraw (1977) also ruled out the presence of short-period oscillations characteristic of ZZ Ceti stars. In addition, G44-32 is not a DA white dwarf (it was assigned a spectral type DC), so, by definition, it could not be a ZZ Ceti variable.

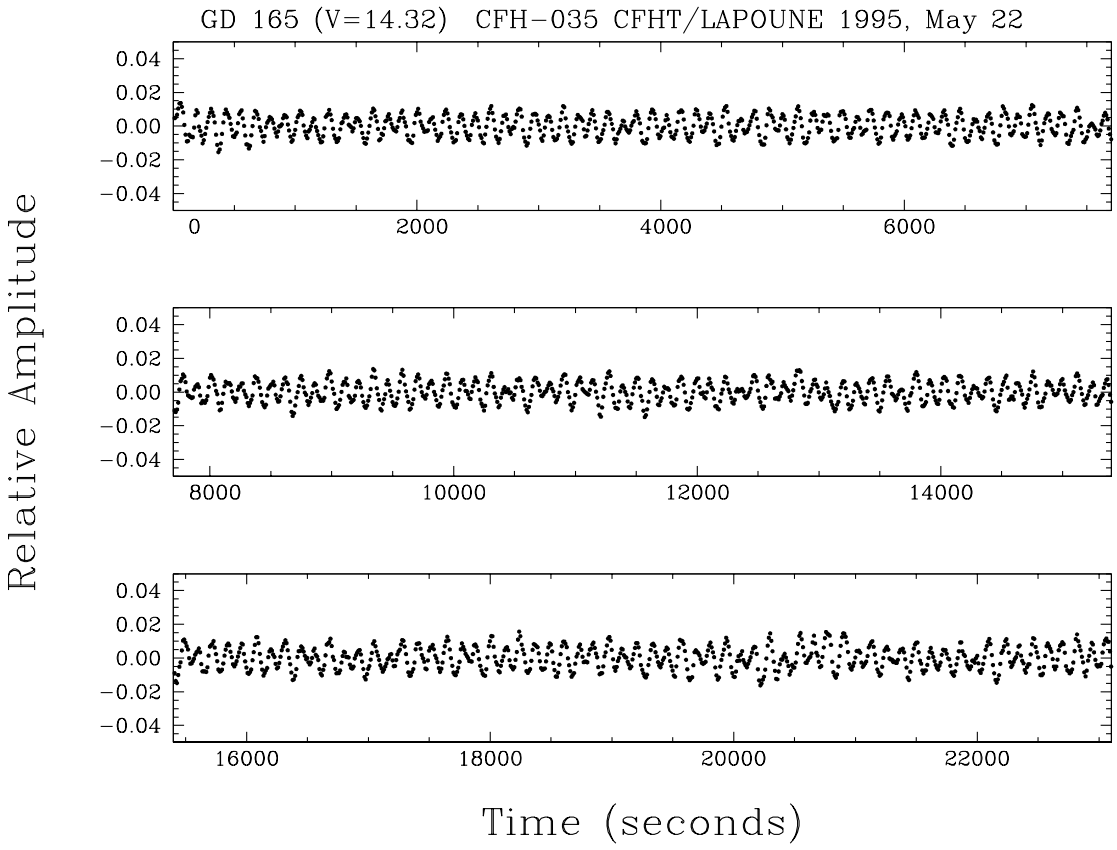

FIGURE 2.1 – (a) Segment of the broadband optical light curve of GD 165 gathered with the CFHT/LAPOUNE combination during one night of our May 1995 six-night run. That segment is representative of the data obtained throughout the run in terms of quality. It is cut short by 4360 s at the end in order to facilitate the comparison with our longest available light curve for Ross 548 (see Fig. 2.1b). The amplitude is expressed in terms of residual intensity relative to the mean brightness of the star. Each plotted point represents a sampling time of 10 s.

TABLE 2.2 – Journal of CFHT Observations for Ross 548

Run name	Date (UT)	Start time (UT)	Sampling time (s)	Length (s)
CFH-011	16 September, 1991	10:58;49	10	15600
CFH-013	17 September, 1991	08:36:45	10	23110
CFH-015	18 September, 1991	11:37:19	10	13120
CFH-020	20 September, 1991	10:59:42	10	16200

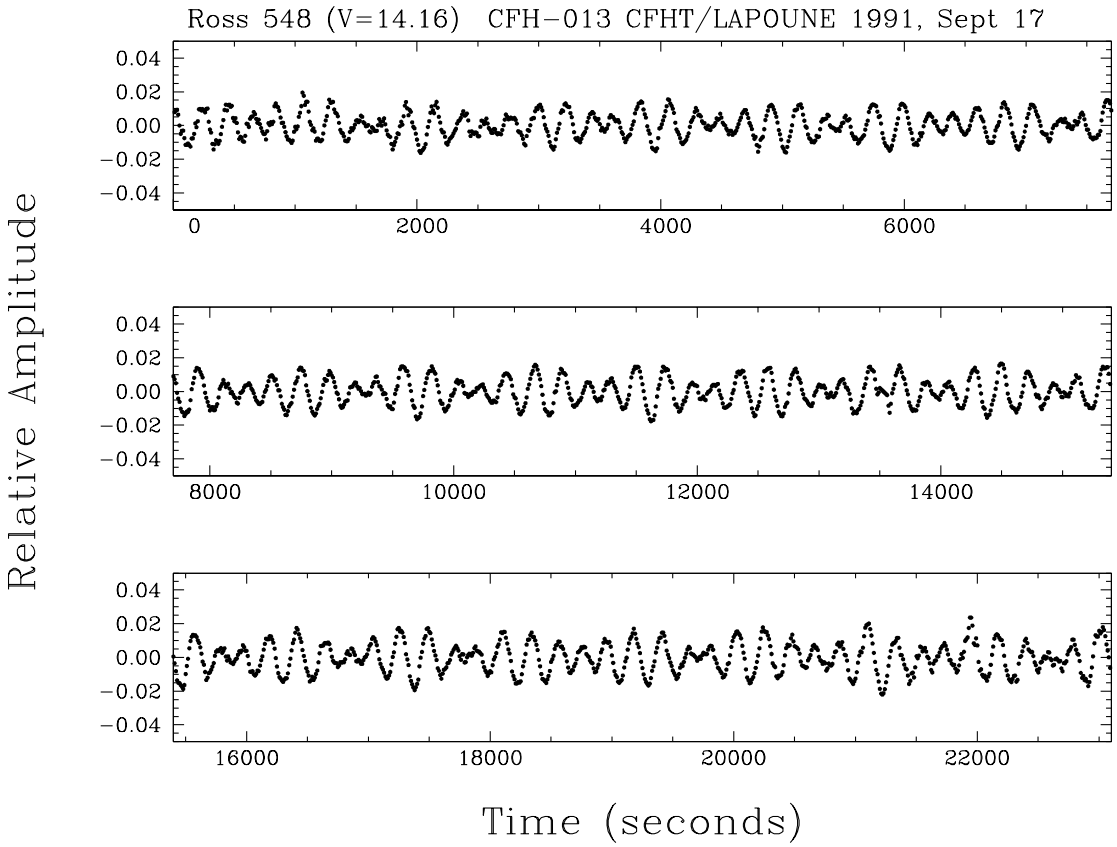

FIGURE 2.1 – (b) Similar to Fig. 2.1a, but for Ross 548 using the exact same format and referring to one night of our five-night mission in September 1991. It is readily apparent that the timescales involved in the multiperiodic pulsations detected in Ross 548 are significantly larger than those seen in its spectroscopic twin GD 165.

formal resolution achieved was 2.8 μHz and the duty cycle was 18.8%. Figure 2.1b shows the superb light curve that we gathered during the night of September 17. It is the longest light curve that we obtained on Ross 548 during the campaign, but is otherwise representative of the whole run quality wise. It is plotted on the exact same scale as Figure 2.1a to ease comparison with the case of GD 165. It is immediately apparent that the timescales involved are significantly longer in Ross 548 than in GD 165. Also, the dominant modes in Ross 548 have larger amplitudes than their counterparts in GD 165. These different behaviors have to be weighted, once again, against the fact that these two objects are very nearly spectroscopic twins.

2.4 LIGHT CURVE ANALYSIS

Standard techniques (Fourier transforms, least-square fits to the light curve, and pre-whitening) were used to extract the frequencies (periods) present in the light curve of both target stars. Some details of our standard approach have been provided in Billères (2000) and Billères et al. (2002). For GD 165, a total of 13 modes were uncovered out of six main peaks – identified as f_1 through f_6 in Figure 2.2 – which include two triplets, three doublets, and a singlet. For Ross 548, we uncovered up to 11 independent pulsation modes regrouped also in six main multiplets (two triplets, one doublet, and three singlets).

The first four columns of Table 2.2 (GD 165) and Table 2.4 (Ross 548) summarize the results of our frequency extraction exercises. It should be noted that the uncertainties on the periods P, the amplitudes A, and the frequencies $\nu = 1/P$ have been estimated with the formalism proposed by Montgomery & O'Donoghue (1999), which is known to be conservative. In comparison, the formal uncertainties on the amplitudes provided by the least-square fits are systematically (and generally significantly) smaller than the values reported in Tables 2.2 and 2.4. They are $\sigma(A) = 0.0039\%$ for GD 165 and $\sigma(A) = 0.0042\%$ for Ross 548, *irrespective of the mode considered*. Since the S/N value for a mode is given by the ratio of the observed amplitude over the amplitude uncertainty $A/\sigma(A)$ times 0.8 (Montgomery & O'Donoghue 1999), it is important to realize that our using the formal least-square fit uncertainties would have led to significantly larger values of the signal-to-noise ratio than those reported in the

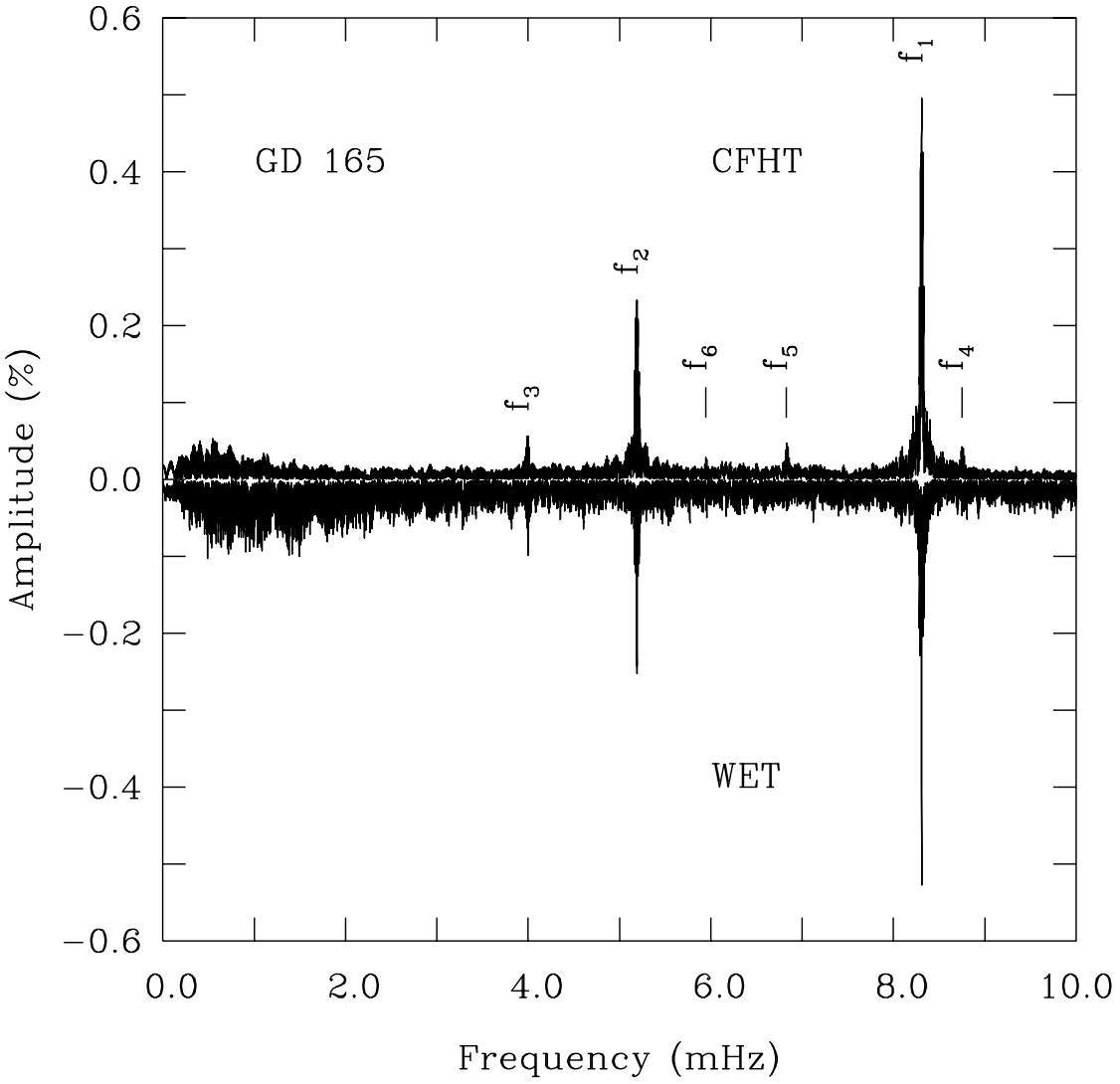

FIGURE 2.2 – Comparison of the Fourier amplitude spectrum of the light curve of GD 165 obtained 1) during the 1995 CFHT run (upper curve), and 2) during the 1990 WET campaign (lower curve plotted upside down). The frequency window depicted here covers the 0-10 mHz range. With an average noise level some 2.5 times higher than that reached during the CFHT run, the signals at f_4, f_5, and f_6 could not be detected on the basis of the WET data.

TABLE 2.3 – Observed properties of the 13 modes detected in GD 165

Period (s)	Amplitude (%)	S/N	Frequency (μHz)	Spacing (μHz)	ID
114.2344±0.0015	0.0428±0.0041	8.4	8753.93±0.12	8.95±0.32	f_4
114.3513±0.0039	0.0167±0.0041	3.3	8744.98±0.30		...
120.3201±0.0006	0.1131±0.0042	21.5	8311.16±0.04	2.47±0.05	...
120.3559±0.0001	0.5070±0.0042	96.6	8308.69±0.01	<2.46±0.03>	f_1
120.3916±0.0005	0.1592±0.0042	30.3	8306.23±0.03	2.46±0.03	...
146.3159±0.0030	0.0439±0.0051	6.9	6834.53±0.14	3.90±0.35	f_5
146.3995±0.0068	0.0191±0.0051	3.0	6830.63±0.32		...
168.1912±0.0081	0.0265±0.0063	3.4	5945.62±0.29		f_6
192.5717±0.0012	0.2311±0.0065	28.4	5192.87±0.03	2.92±0.05	...
192.6801±0.0013	0.2255±0.0065	27.8	5189.95±0.03	<2.92±0.05>	f_2
192.7886±0.0046	0.0631±0.0065	7.8	5187.03±0.12	2.92±0.13	...
250.1589±0.0074	0.0566±0.0056	8.1	3997.46±0.12	2.49±0.30	f_3
250.3150±0.0173	0.0243±0.0056	3.5	3994.97±0.28		...

TABLE 2.4 – Observed properties of the 11 modes detected in Ross 548

Period (s)	Amplitude (%)	S/N	Frequency (μHz)	Spacing (μHz)	ID
186.8740 ±0.0037	0.0877 ±0.0062	11.3	5351.20 ±0.11		f_3
212.7684 ±0.0011	0.4105 ±0.0066	49.8	4699.95 ±0.02	3.93±0.08	...
212.9463 ±0.0033	0.1361 ±0.0066	16.5	4696.02 ±0.07	<4.02±0.05>	f_1
213.1326 ±0.0007	0.6578 ±0.0066	79.7	4691.92 ±0.02	4.11±0.08	...
217.8336 ±0.0146	0.0323 ±0.0066	3.9	4590.66 ±0.31		f_6
274.2508 ±0.0019	0.4299 ±0.0072	47.8	3646.30 ±0.03	3.59±0.10	...
274.5209 ±0.0071	0.1155 ±0.0072	12.8	3642.71 ±0.10	<3.48±0.07>	f_2
274.7745 ±0.0027	0.3107 ±0.0072	34.5	3639.35 ±0.04	3.36±0.10	...
318.0763 ±0.0163	0.0722 ±0.0077	7.5	3143.90 ±0.16	6.80±0.42	f_4
318.7657 ±0.0391	0.0303 ±0.0077	3.1	3137.10 ±0.39		...
333.6447 ±0.0233	0.0621 ±0.0086	5.8	2997.20 ±0.21		f_5

tables. Instead, to be on the safe side before claiming a detection, we evaluated the values of the mean *local* noise on the basis of spectral chunks 2 mHz wide centered on each of the six main frequency peaks in the Fourier domain. This led to values of $\sigma(A)$ that increase with increasing period as can be seen in both tables (except for the 250 s mode in GD 165), in keeping with the expected general trend of increasing noise with decreasing frequency. Within this more conservative framework, we listed in Tables 2.2 and 2.4 all peaks with S/N $\geq$ 3, while warning the reader that that some of the lowest-amplitude periodicities may not be real signals.

In this context, an estimator of the statistical significance of a frequency peak in the Fourier domain is the False Alarm Probability (FAP) formalism put forward by Kepler (1993). This approach leads to an estimate of the probability FAP that a given peak in the Fourier spectrum is due to noise. In that formalism, the probability FAP is known to switch from 0 to 1 in a very narrow range of S/N. For 9 out of 13 periodicities found in GD 165, and for 9 out of 11 in Ross 548, the S/N values are all above 4 and the computed values of FAP are essentially 0 in all cases, so we consider these detections as secure ones. For the lower-amplitude periodicities, found in the range 4 $\geq$ S/N $\geq$ 3, we list here the derived values of FAP. In the case of GD 165 (Table 2.2), we find that FAP = 2.5×10^{-1}, $\sim$ 1.0, 1.2×10^{-1}, and 5.8×10^{-2}, respectively for the low-amplitude peaks 114.3513 s (S/N = 3.5), 146.3995 s (S/N = 3.0), 168.1912 s (S/N = 3.4), and 250.3150 s (S/N = 3.5). For Ross 548 (Table 2.4), we find that FAP = 1.5×10^{-3} and 3.4×10^{-1}, respectively, for the low-amplitude peaks 217.8336 s (S/N = 3.9) and 318.7657 s (S/N = 3.1). Hence, in the strict framework of the FAP formalism, all these extra periodicities may be considered as possible detections (FAP < 0.5), except for the lowest-amplitude peak with 146.3995 s. In the more general context of the seismic analyses to come (and which are carried out with spherically symmetric models), only 2 of these 6 low-amplitude periodicities are of direct relevance as independent pulsation modes. The others are part of multiplet structures caused (presumably) by rotation, and are not used per se in searches for optimal seismic models in parameter space. The two singlet components of interest are the 168.1912 s periodicity in GD 165, and the 217.8336 s periodicity in Ross 548. The former has S/N = 3.4 and FAP = 1.2×10^{-1}, certainly not overwhelming values, but our confidence in the

reality of this signal is boosted by the fact that it has been seen before in an independent data set (see Table 2 of Bergeron et al. 1993). For its part, and to our knowledge, the 217.8336 s periodicity is reported for the first time in this work. It is characterized by S/N = 3.9 and FAP = 1.5×10^{-3}, which suggests that this is a likely detection.

Figure 2.3a provides a comparison of the Fourier transform of the entire CFHT data set for GD 165 with that of the residual light curve obtained after removing the 13 periodicities listed in Table 2.2, which make up the six multiplets identified in the figure. For visualization purposes, the residual is shifted downward by an arbitrary amount in Figure 2.3a. An inspection of that residual readily suggests that the prewhitening procedure must have been successful as no obvious structure stands out significantly above the noise level. We strongly suspect that additional structure must be associated with the incomplete doublets and the singlet identified in Table 2.2, but such structure is likely buried in the noise and cannot be put in evidence from our data. Still, excluding the low-frequency part of the Fourier transform, we find that the mean noise level in the 2−12 mHz range is 0.0062% (67 μmag), which is remarkably small by ZZ Ceti standards (observed from the ground).

We find comparable results for Ross 548 as illustrated in Figure 2.3b. Since the scale of the figure is the same as that of the previous one, one can appreciate, one more time, the fact that the dominant peaks have significantly higher amplitudes than their equivalents in GD 165. In fact, as depicted at the high-frequency end of the plot, the first harmonic of the dominant peak at 213.1326 s is very likely present in the light curve even though its amplitude does not reach S/N = 3. It is the fact that its frequency is *exactly* the double of the frequency of the main mode that is particularly suggestive in that context. We further find from Figure 2.3b that the transform of the residual light curve does not contain obvious leftover structure, a sign that the prewhitening process has also worked well for the Ross 548 data. The mean noise level in the 2−12 mHz bandpass is now 0.0073% (79 μmag). The ratio of that value over the corresponding value for GD 165, 0.0073/0.0062 $\simeq$ 1.2, scales well, as expected for two stars of comparable brightness, with the square root of the inverse ratio of the amounts of time spent on each star, i.e., $\sqrt{(27.9\text{h}/18.9\text{h})} \simeq 1.2$.

Figure 2.4a (2.4b) shows the prewhitening sequences (from top to bottom) for each of

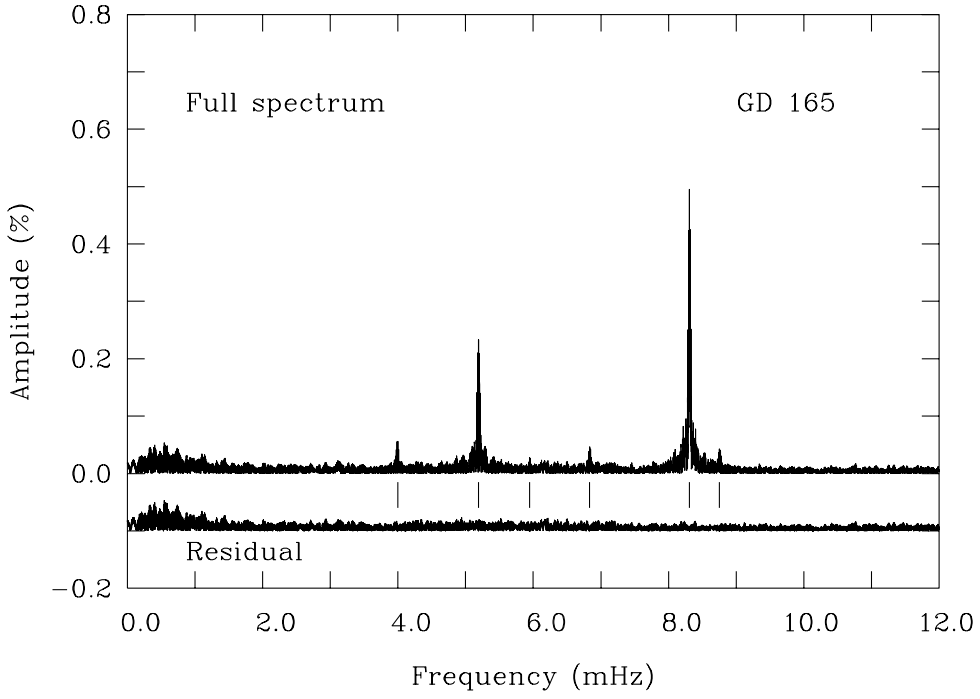

FIGURE 2.3 – (a) Comparison between the Fourier transform of the entire CFHT data set for GD 165 and that of the residual light curve after extraction of 13 periodicities regrouped in 6 distinct frequency multiplets. The frequency range from 12 mHz out to the Nyquist cutoff at 50 mHz is entirely consistent with noise and not shown here. The mean noise level in the 0−12 mHz bandpass is 0.0074% (80 μmag). Excluding the low frequency domain, the mean noise level in the 2−12 mHz range drops to 0.0062% (67 μmag).

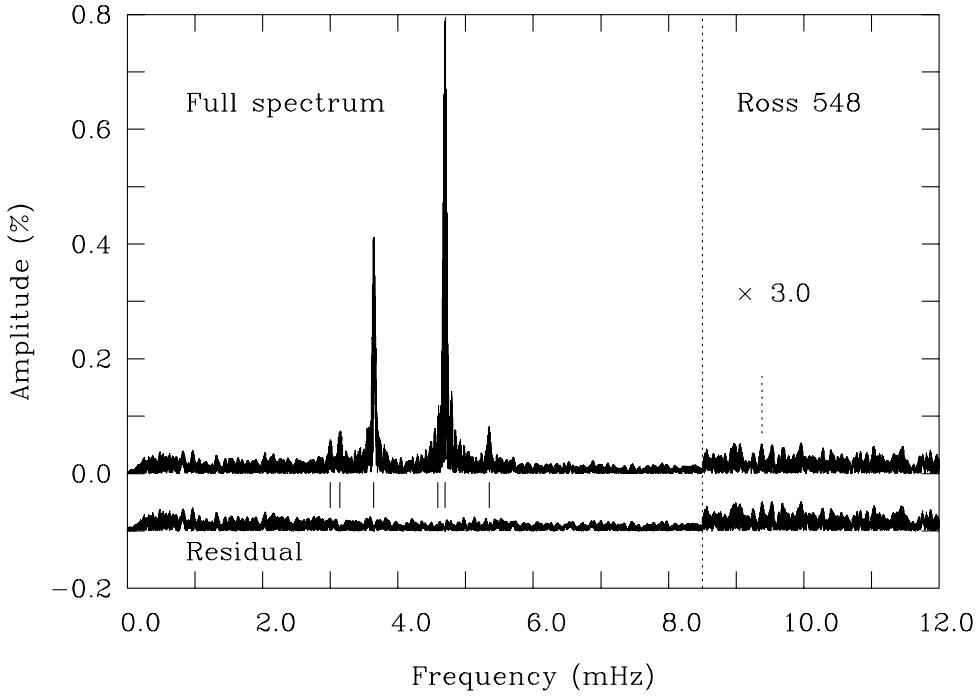

FIGURE 2.3 – (b) Similar to Fig. 2.3a, but for Ross 548 using the same format, except that the higher-frequency part of the domain illustrated has been magnified in amplitude by a factor 3 to help identifying the first harmonic of the dominant periodicity. A total of 11 independent pulsation modes regrouped in 6 frequency multiplets have been uncovered from our CFHT data. The mean noise level in the 0−12 mHz (2−12 mHz) bandpass is 0.0082% (0.0073%).

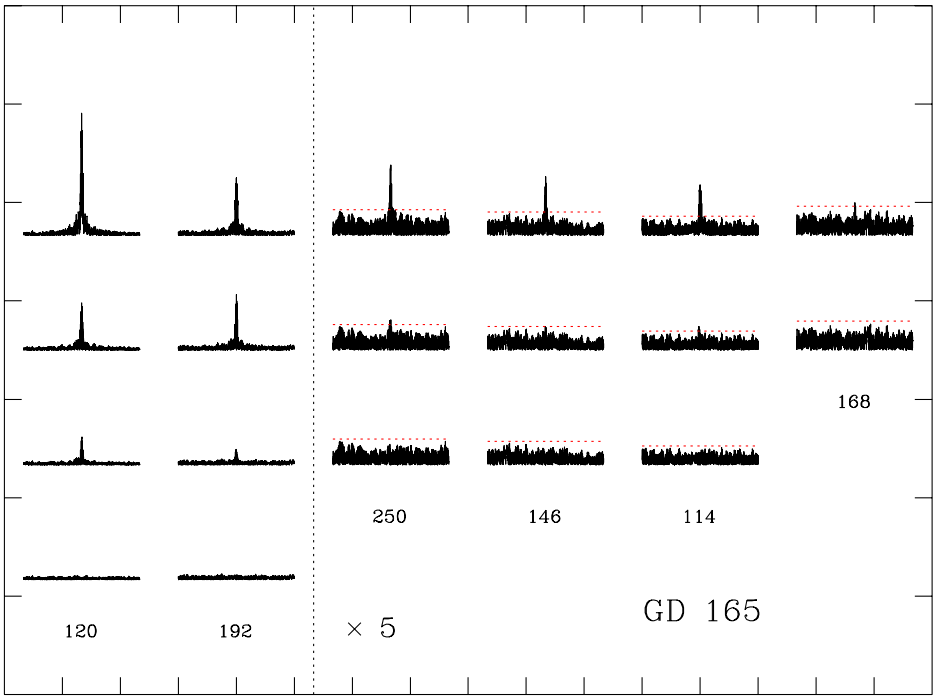

FIGURE 2.4 – (a) Prewhitening sequences for each of the 6 main frequency multiplets detected in the Fourier transform of the GD 165 light curve. The various transforms are shifted vertically for better clarity (from top to bottom) and are identified by their central period (in seconds). One tick mark in abscissa corresponds to 1 mHz, and one in ordinate to 0.2%. For the 4 lower-amplitude multiplets, the amplitude has been magnified by a factor 5, and a detection threshold, corresponding to 3 times the mean noise level in each of the 2 mHz-wide spectral chunks is illustrated by a horizontal red dotted line.

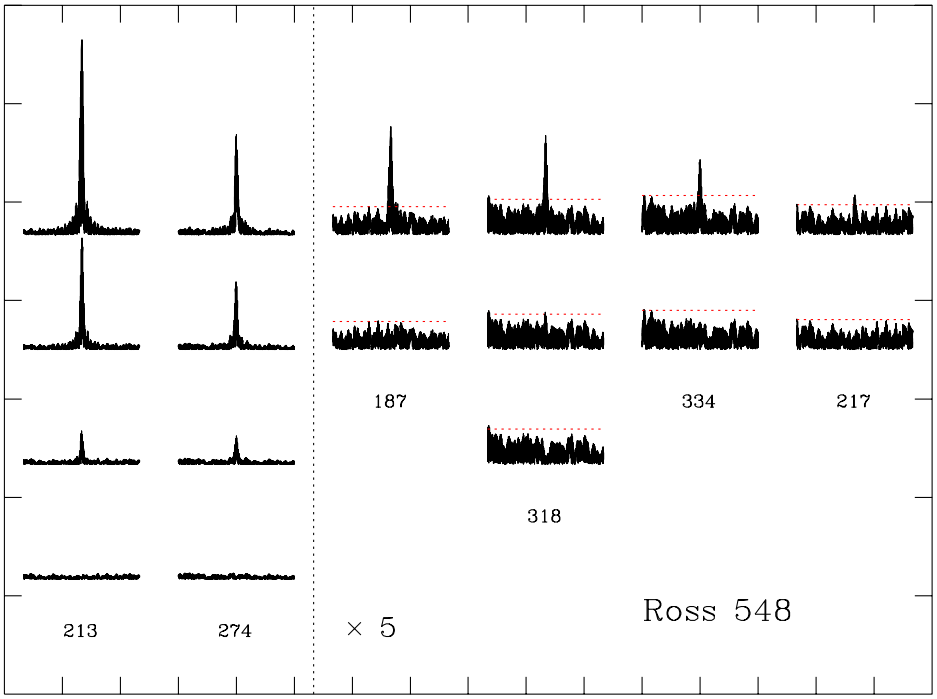

FIGURE 2.4 – (b) Similar to Fig. 2.4a, but for Ross 548 using the same format.

the six significant peaks that appear in the Fourier amplitude spectrum of GD 165 (Ross 548). The segments of the Fourier transform are displaced, both vertically and horizontally, for visualization purposes. Each column illustrates, from top to bottom, the prewhitening sequence obtained for a given peak identified by its approximate central period (in s). One can distinguish the 13 (11) independent pulsation modes that we uncovered in our data for GD 165 (Ross 548). As pointed out just above, it is very likely that the incomplete multiplets contain additional components, but with amplitudes too small to be detectable in our data sets. In contrast, the dominant peaks are likely complete triplets. The series of Figures 2.5 through 2.8 provides an interesting zoomed-in view of each of the two dominant structures found in each star. Note, in particular, the very low level of noise reached in the lower curve and the lack of significant residual structure within it. Note also how the Fourier transform of the reconstructed light curve (the red dotted curve at the top of the plot) matches extremely well the transform of the actual observed light curve. This is in line with the proposition that these dominant structures are likely *complete* triplets in Fourier space, as opposed to complexes with unseen components.

The most likely cause for the observed multiplet structures in both target stars is rotational splitting[4]. We will exploit this avenue in the second paper of this short series. For the time being, we report in the fifth column of both Tables 2.2 and 2.4 the computed frequency spacings between adjacent multiplet components detected in our light curves. Within the measurement uncertainties, the four dominant triplets show a symmetric structure in frequency space, although, as usual, the amplitude structure is not at all symmetric, a characteristic usually ascribed to unknown nonlinear physics. We also note that the frequency spacings are significantly different from one mode to another for a given star. This is an important bonus of studying the hot ZZ Ceti pulsators, which show low-order excited modes, well away from the asymptotic regime of high-order modes for which the spacings tend to be the same and proportional to $[1 - 1/(\ell^2 + \ell)]$. These differences represent additional constraints on an eventual mode identification in a seismic exercise. Knowing that the modes that have been

[4]It seems appropriate to recall here that, for a long time, Ross 548 was often presented as the archetype of a pulsator showing multiplet structures caused by $\ell + 1$ magnetic splitting instead of $2\ell + 1$ rotational splitting. This was because the early observations had revealed only a pair of doublets at 213 s and 274 s, and not the lower-amplitude central components. For more details, please see Section 7.3 of Fontaine & Brassard (2008).

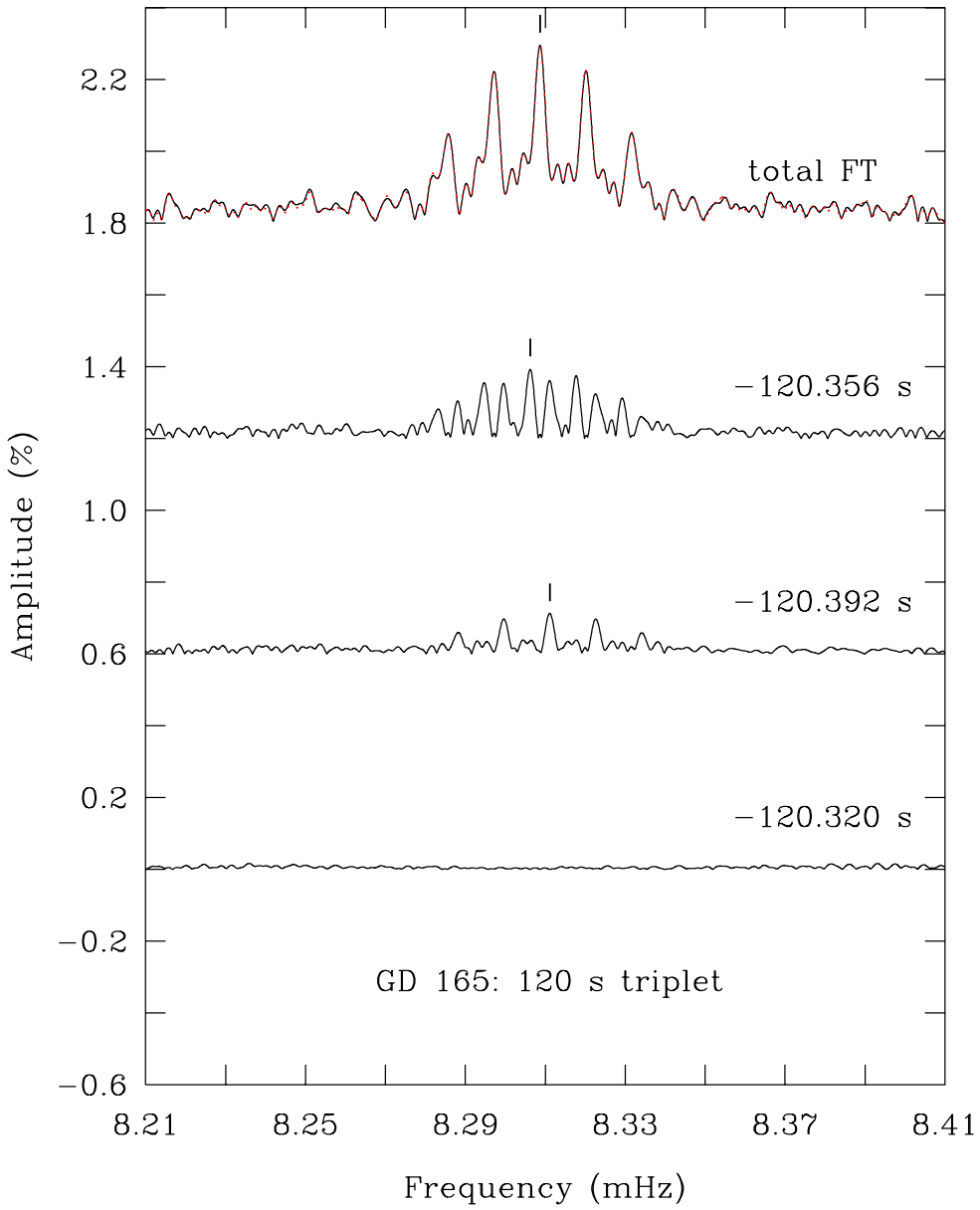

FIGURE 2.5 – Zoomed-in view and details of the prewhitening sequence for the dominant 120 s structure detected in the light curve of GD 165. The red dotted curve at the top illustrates the Fourier amplitude transform of the reconstructed light curve. The match with the actual transform is excellent. The triplet nature of this structure clearly stands out.

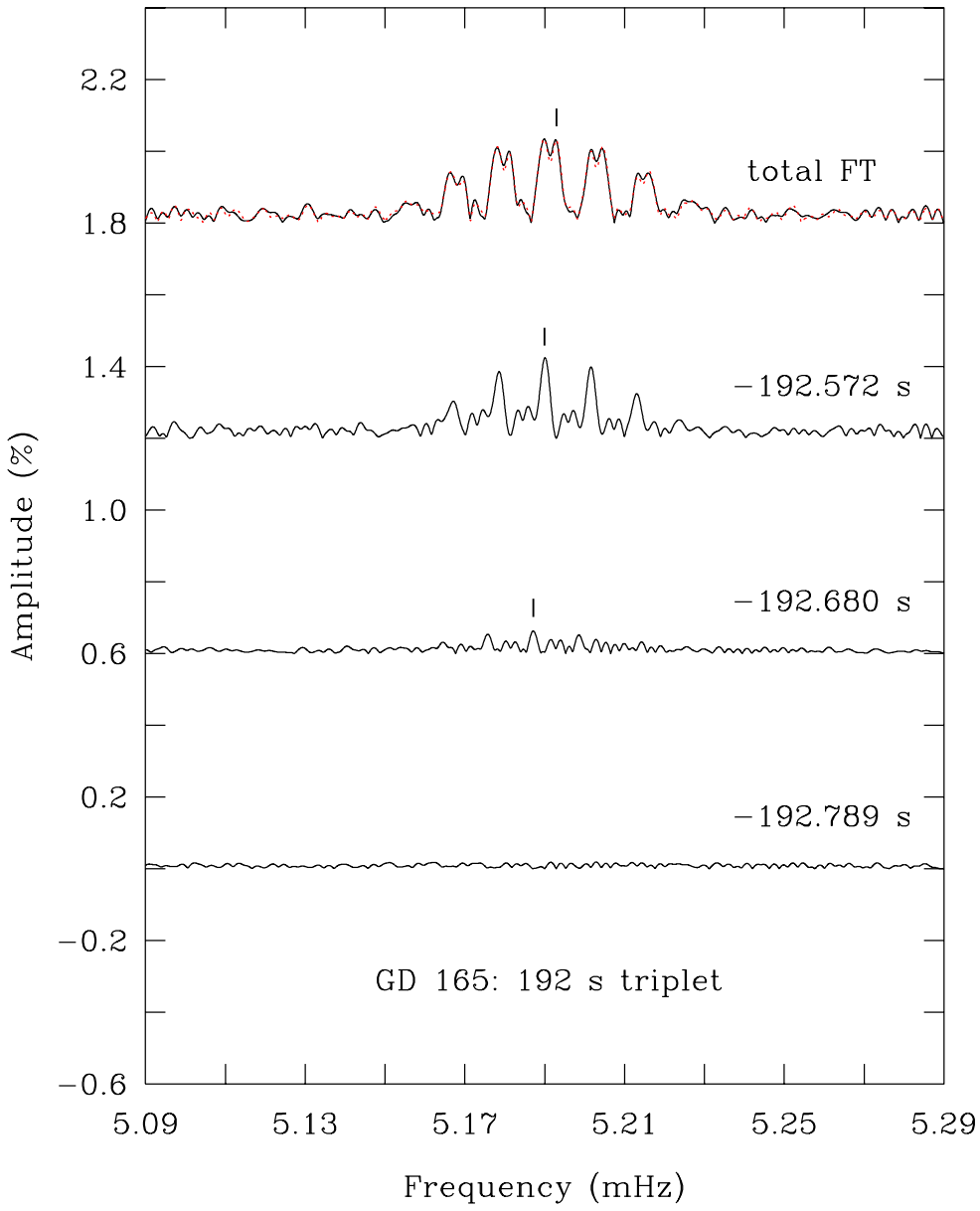

FIGURE 2.6 – Similar to Fig. 2.5, but for the second-highest amplitude multiplet in the light curve of GD 165. The triplet nature of this feature is again evident.

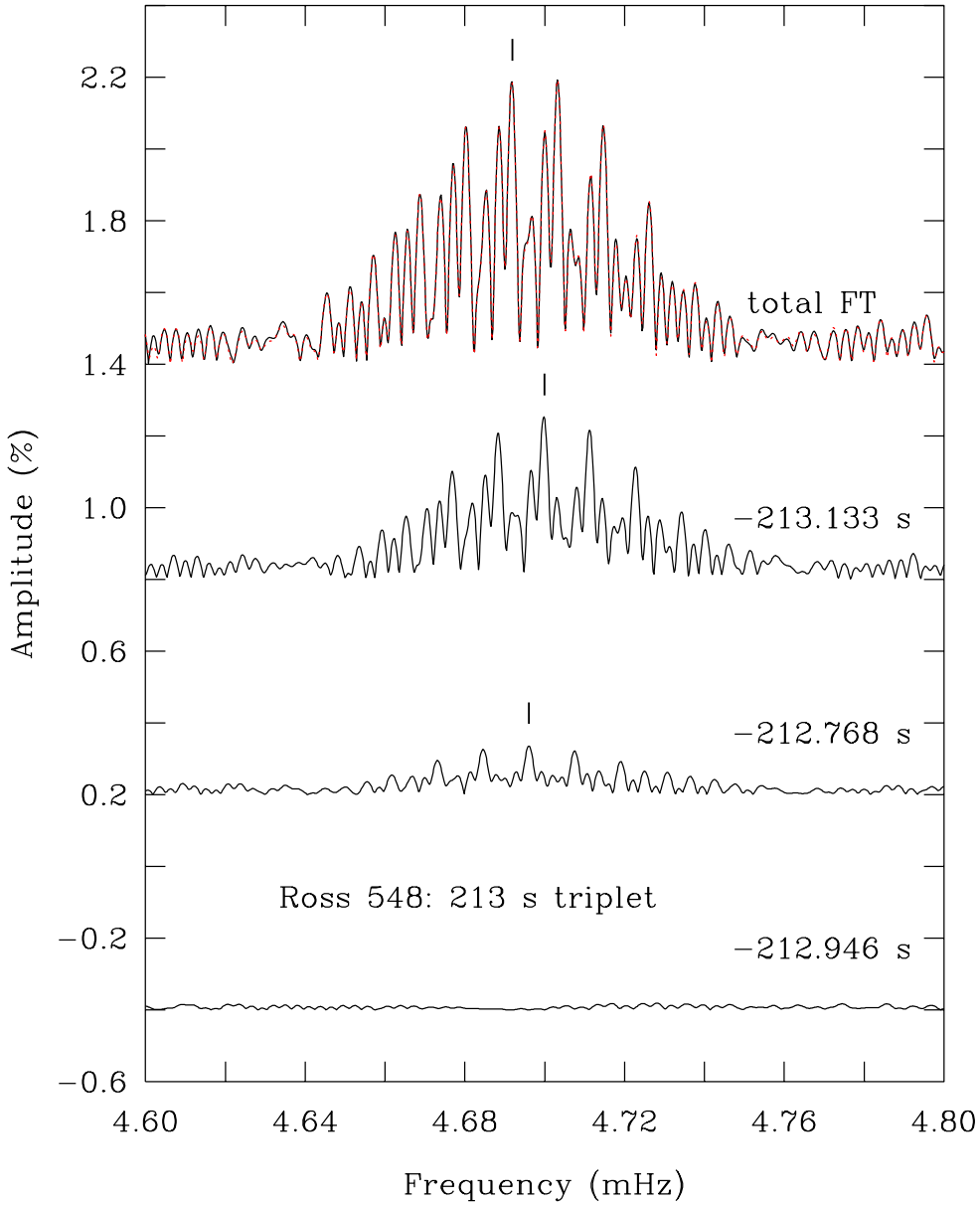

FIGURE 2.7 – Zoomed-in view and details of the prewhitening sequence for the dominant 213 s structure detected in the light curve of Ross 548. The triplet nature of this structure clearly stands out. To ease comparison with Figs. 2.5 and 2.6, the amplitude scale has been kept the same.

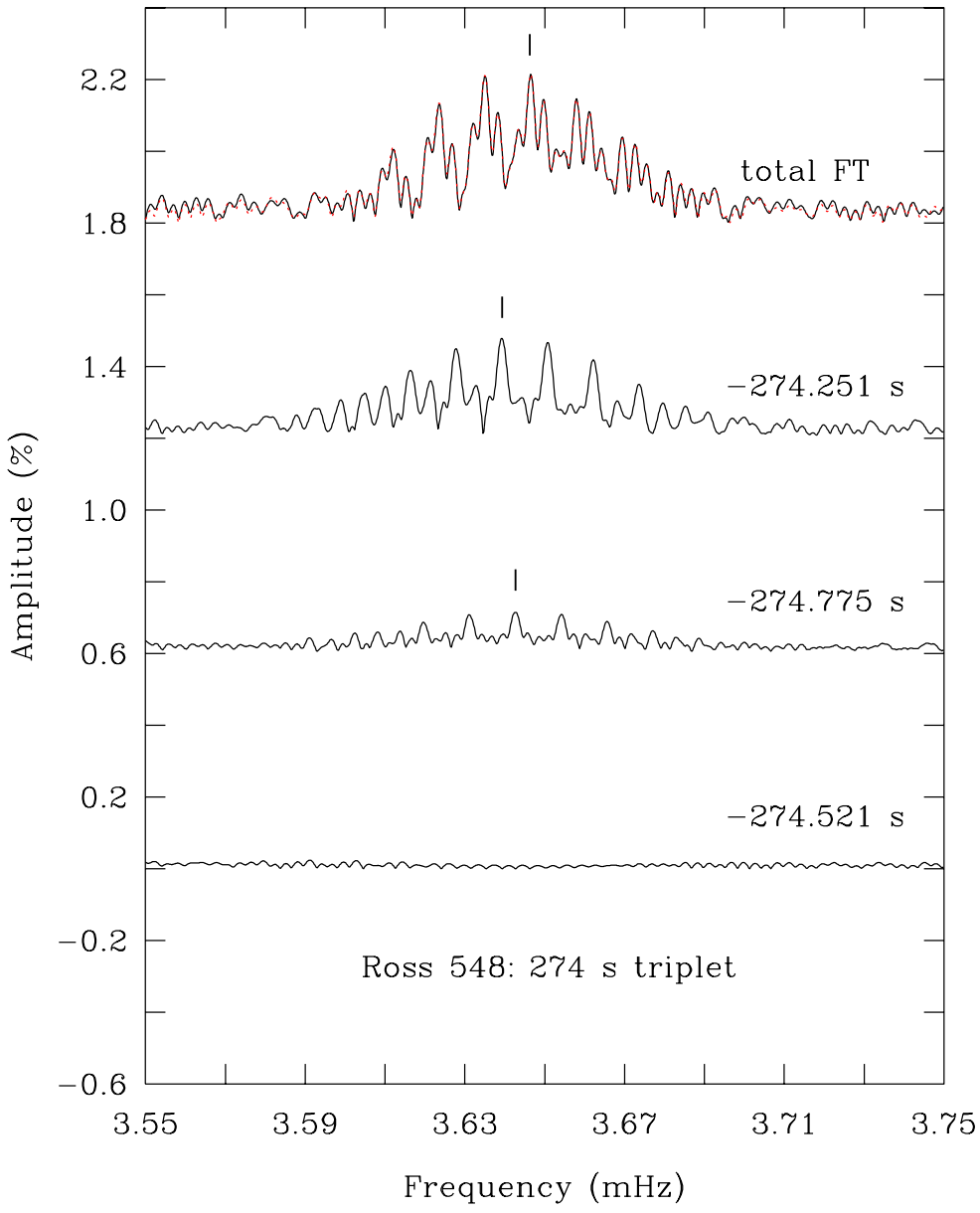

FIGURE 2.8 – Similar to Fig. 2.7, but for the second-highest amplitude multiplet in the light curve of Ross 548. Another obvious triplet.

unambiguously identified previously in ZZ Ceti stars belong to $\ell = 1$ and $\ell = 2$, and taking at face value the very strong indication that the triplets seen in our data are truly dipole ($\ell = 1$) modes, we can deduce from Table 2.2 that the complexes at 120 s, 192 s, and 250 s in GD 165 are very likely dipole modes, while the 114 s and 146 s multiplets, with their larger frequency spacings, are rather quadrupole modes. Likewise, the two triplets at 213 s and 274 s are very likely dipole modes, while the 318 s structure could be either a quadrupole mode if the two components are adjacent, or a dipole modes if the two detected frequencies are the $m = +1$ and $m = -1$ components of a triplet (with a basic spacing of $6.80/2 = 3.40$ mHz). Of course, these inferences can only be considered as suggestions at this stage, and only a detailed seismic analysis can confirm (or infirm) them.

The last step of our standard frequency extraction procedure is to compute a noise-free model light curve and compare it quantitatively with the observed light curve. This provides us with another measure of the relative success (or failure) of the exercise. The reconstructed light curve is obtained by adding together sinusoidal signals with the amplitudes, frequencies (periods), and phases (the latter not listed in Tables 2.2 and 2.4 since they are not directly relevant for seismic modeling) derived previously and sampled in *exactly* the same way as the actual observations. In this connection, Figure 2.9a compares the Fourier amplitude spectrum of our light curve of GD 165 with that of the model light curve (the latter plotted upside down). The point-by-point difference between these two curves is also illustrated in the figure. Note that this residual is obtained in frequency space, while that shown in Figure 2.3a, for example, comes from the time domain, thus providing a complementary way for evaluating the success of the procedure. The fact that there is no statistically significant residual structure left in the lower curve depicted in Figure 2.9a is both reassuring and encouraging. The standard deviation (about 0) in that curve is 49 μmag only, which is very small for ZZ Ceti stars observed from the ground. Similar results are illustrated in Figure 2.9b referring, this time, to Ross 548. In that latter case, as expected from above, the noise level is somewhat higher, showing a standard deviation of 69 μmag, but this is still quite remarkable by ZZ Ceti star standards. We thus believe that our frequency extraction exercises have been successful and, thus, suggest that the period data provided here in Tables 2.2 and 2.4 are quite reliable for

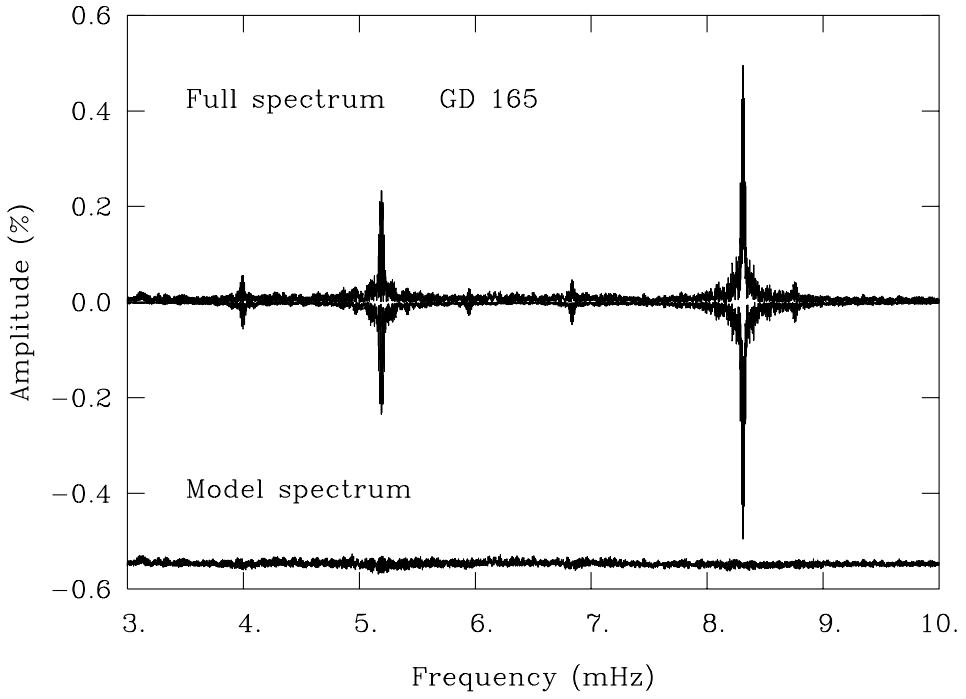

FIGURE 2.9 – (a) Comparison between the Fourier transform of the light curve of GD 165 in the 3−10 mHz bandpass with the transform, plotted upside down, of the reconstructed noise-free light curve on the basis of the 13 detected periodicities. The point-by-point difference between the two curves is also illustrated and shifted at the bottom of the plot. It provides another measure of the quality of our frequency extraction exercise. The standard deviation of that curve about the mean value of ∼0 is 0.0045%.

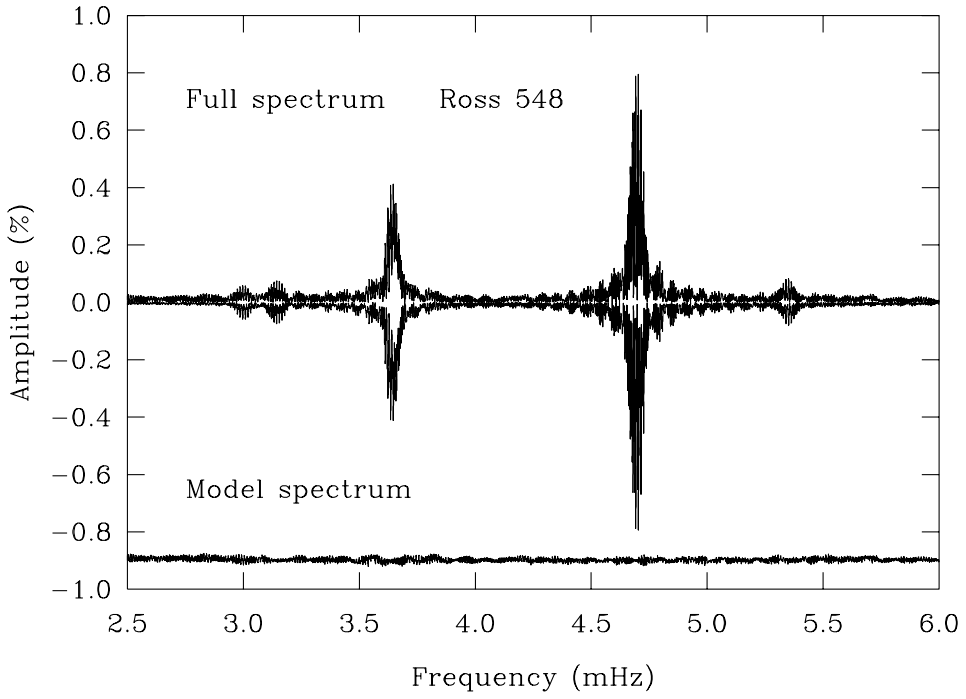

FIGURE 2.9 – (b) Similar to Fig. 2.9a, but for Ross 548 and on another scale in both amplitude and frequency. In the present case, 11 detected modes have been used in the construction of the model Fourier spectrum. The standard deviation of the lower curve about the mean value of ∼0 is 0.0064%.

seismic modeling.

2.5 COMPARISON WITH OTHER STUDIES

We have searched the published literature for earlier studies of the light curves of our two target stars for comparison purposes. For GD 165, we found no previous extensive study of its light curve other than the WET paper of Bergeron et al. (1993) already alluded to above. Their Table 2.4 summarizes their best results pertaining to the two triplets at 120 s and 192 s. Within the measurement uncertainties, our periods for these six pulsation modes (see Table 2.2) agree perfectly with their results. The relative amplitude structure within each of these triplets is also approximately the same, notably concerning the dominant role of the central component of the 120 s multiplet. In addition, Bergeron et al. (1993) reported the detection of a third frequency peak with a single component at 250.1864 s, which is at least consistent with our doublet having components at 250.1589 s and 250.3150 s.

In the case of Ross 548, the most extensive analysis that we found is that of Mukadam et al. (2013) reporting on their long-term project aimed at measuring the evolutionary timescale of that star. Comparing our Table 2.4 with their Table 2, we find that 8 of the modes we detected out of 11 have periods perfectly compatible with their results, again well within our measurement errors (which are significantly larger than theirs based on a huge timebase). This boosts greatly our confidence in the reliability of these periods for seismic analyses. The exceptions are 1) the value of the dominant period of the 186 s complex which we find at 186.8740±0.0037 s, some 5σ away from the value of 186.8557329±0.0000085 s reported by Mukadam et al. (2013), 2) our detection of a signal (S/N = 3.9) at 217.8336±0.0146 s not reported in the study of Mukadam et al. (2013), and 3) our suggestion of a second component in the 318 s complex with a period of 318.7657±0.0391 s, a S/N = 3.1 result in conflict with the interpretation of the multiplet structure of the 318 s peak proposed by the same authors. To put things in perspective, however, we note that these latter differences, save for the reality of the 217 s peak, are not at all critical for seismic analyses at this stage since current models cannot yet reproduce observed periods within a fraction of a second. Nevertheless, we took a closer look at the lower-amplitude peaks at 186 s, 318 s, and 334 s (no comparison being

possible for the 217 s structure) from the two studies. Obviously, we cannot rival the resolution reached in the Mukadam et al. (2013) work, but we have on our side an exceptional sensitivity combined with a very simple window function compared to the very complicated multi-year equivalent in their study.

The lower half of Figure 2.10 provides a zoomed-in view of the Fourier transform of our light curve centered on the 186 s peak (upper solid curve marked with our derived frequency of 5.3512 mHz), the Fourier transform of the residual light curve after removing that single component (the lower solid curve just above the horizontal dotted line), and the transform of the reconstructed light curve (the red dotted curve). Given the shapes of the transforms of the residual as well as the reconstructed light curve, we cannot reasonably extract more information from our data on the 186 s peaks, to which we assign a singlet. In other words, at the limit of sensitivity of our observations, the usual criteria for a satisfactory extraction procedure have been met. Again, however, we suspect the presence of other 186 s components being excited in Ross 548, but they are not detectable in our data set.

In comparison, the upper half of Figure 2.10 shows the results of a similar calculation but, this time, when forcing on our data the three periods from the asymmetric triplet proposed by Mukadam et al. (2013) for the 186 s structure. The 5σ frequency discrepancy referred to above is readily apparent in the misalignment of the lower frequency component of the triplet with the maximum of the dominant peak in the observations. By forcing three components instead of removing a single sine wave, the residual transform is naturally further lowered in the frequency range of interest, to the point where it is not flat as it should be in an ideal situation. Furthermore, there is another sign that things are not well, and that is the shape of the transform of the reconstructed light curve which is clearly worse for the triplet hypothesis (upper half of Figure 2.10) than its counterpart for our singlet solution (lower half of Figure 2.10). We conclude from this, that the triplet structure proposed by Mukadam et al. (2013) to account for the 186 s multiplet cannot explain our data.

A comparable situation is encountered for the 318 s structure as can be seen in Figure 2.11, which is similar in format to the previous one. Here, the triplet solution proposed by Mukadam et al. (2013) fares a lot worse than our doublet solution, both in terms of the transform of

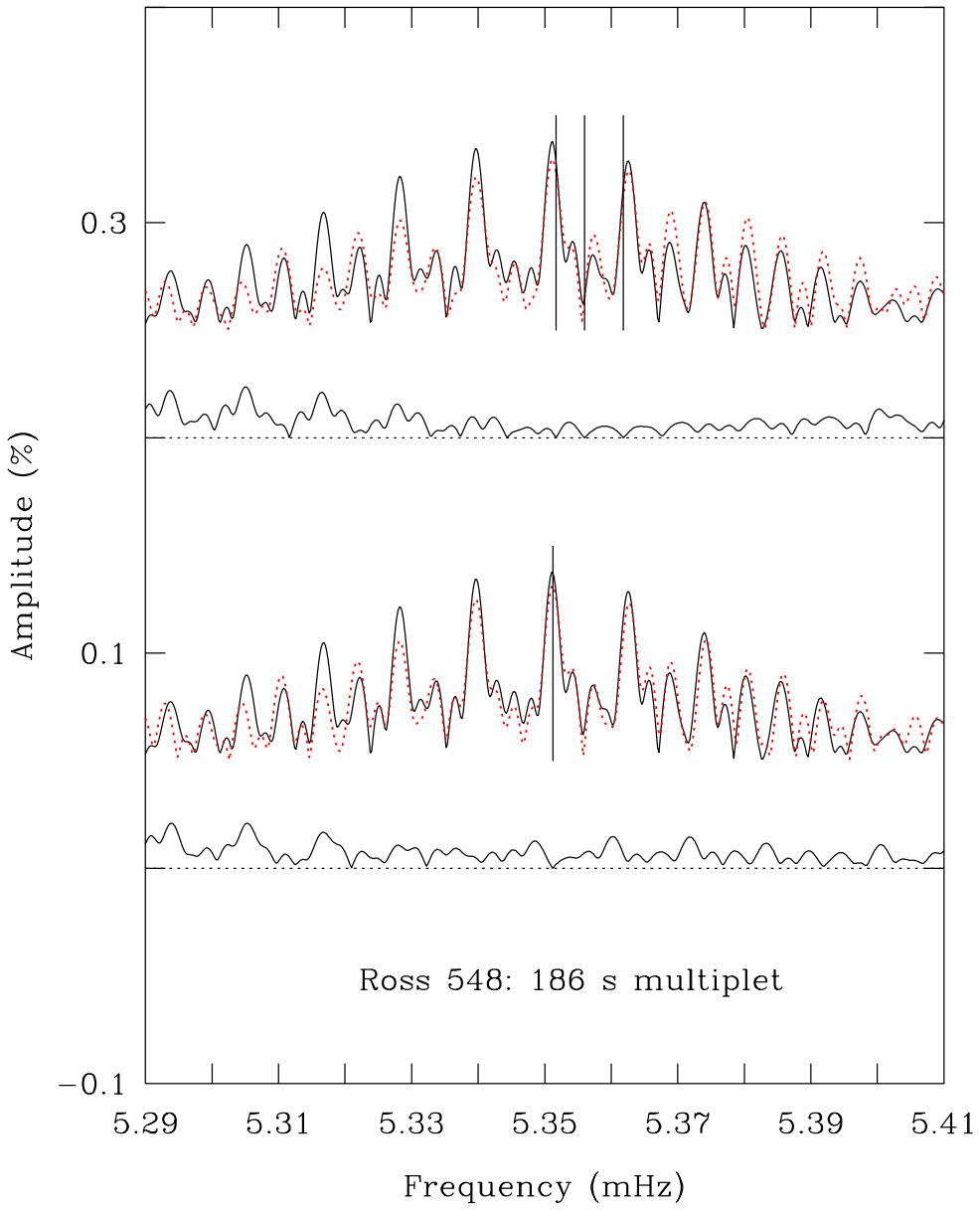

FIGURE 2.10 – *Lower panel:* Extreme zoomed-in view of the Fourier transform of the light curve of Ross 548 centered on the 186 s structure (upper solid curve). The lower solid curve depicts the transform of the residual after prewhitening the light curve of a single component (vertical line segment) with a period of 186.8740 s. The red dotted curve shows the transform of the reconstructed noise-free light curve on the basis of that single periodicity. *Upper panel:* Similar, but obtained by forcing on our data the 3 periods suggested by Mukadam et al. (2013) for the 186 s complex. The various transforms have been shifted arbitrarily in the vertical direction for visualization purposes.

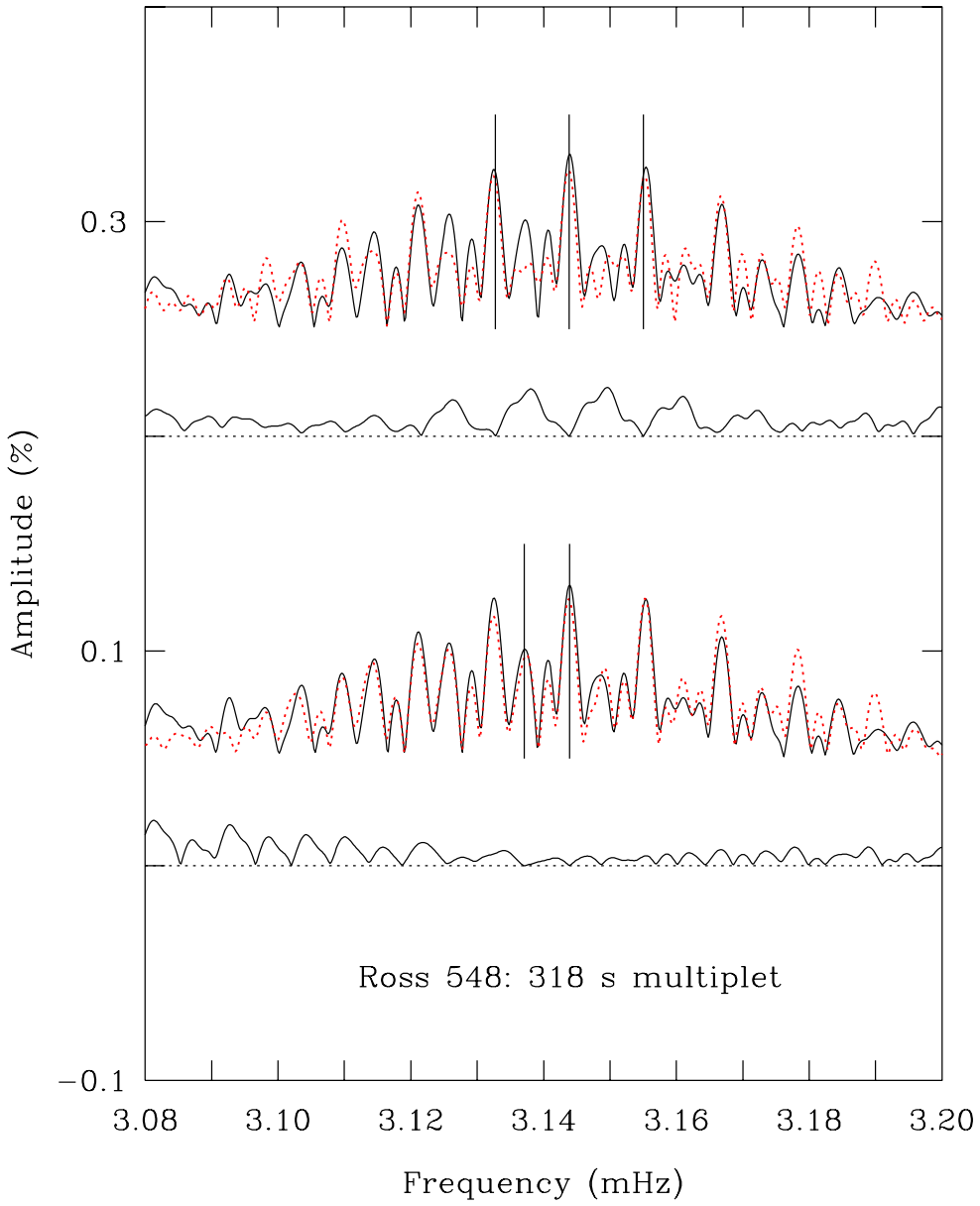

FIGURE 2.11 – Similar to Fig. 2.10, but for the 318 s multiplet. Our best solution (lower panel), involving 2 periods at 318.0763 s and 318.7657 s is compared to the forced solution (upper panel) involving the 3 periods proposed by Mukadam et al. (2013).

the residual light curve and that of the reconstructed light curve. We strongly suspect that the fact that the three components in the suggested triplet nearly align with daily aliases of the same periodicity undermines completely that model. Again, we conclude that the triplet structure proposed by Mukadam et al. (2013) to explain the 318 s multiplet is incompatible with our data. And the same is true for the 334 s complex as can be appreciated from Figure 2.12. In that case, we find that our singlet solution is preferable to the quadruplet structure (two components of which are daily aliases of the same periodicity) discussed by the same authors.

2.6 SPECTROSCOPY

Bergeron et al. (1995) provided the very first homogenous quantitative study of the class properties of the ZZ Ceti stars using optical spectroscopy, optical photometry, and UV spectrophotometry. These authors considered the full sample of 22 ZZ Ceti stars that were known at the time. Among other important results, they were able to "calibrate" the version of the mixing-length theory used to describe convection in the atmospheric layers of these stars by finding out which one provides the best internal consistency between optical measurements, UV observations, parallax determinations, and gravitational redshift measurements (when available). Since that time, and until recently, the so-called ML2/α=0.6 version of the mixing-length theory (where α is the ratio of the mixing length over the local pressure scale height) has been used by all other modelers in the field and has been considered as the standard.

After this was established, Bergeron and colleagues found out that high S/N ratio optical spectroscopy alone (analyzed with ML2/α=0.6 synthetic spectra) would provide reliable estimates of the atmospheric parameters of ZZ Ceti stars. Two essential rules were imposed, 1) gathering optical spectra with S/N ratios generally above 100 and never below 80, and 2) choosing exposure times to cover several pulsation cycles in order to obtain meaningful time-averaged data. The last point is particularly important for long-period, large-amplitude pulsators since observing during only part of a cycle can only skew the inferred atmospheric parameters. This spectroscopic program has been very successful and has led to the disco-

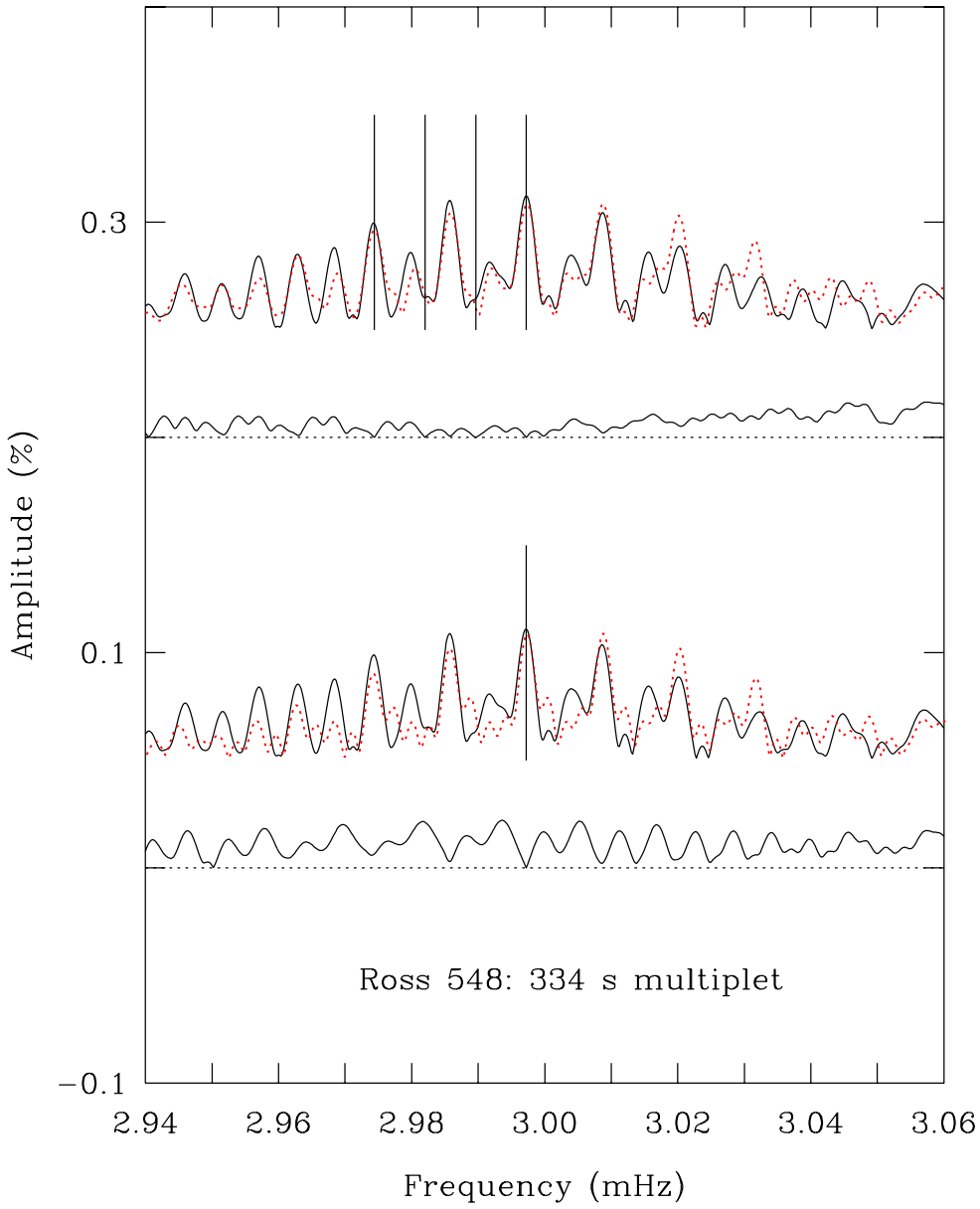

FIGURE 2.12 – Similar to Fig. 2.10, but for the 334 s structure. Our best solution (lower panel), involving a single period at 333.6447 s is compared to the forced solution (upper panel) involving the quadruplet proposed by Mukadam et al. (2013).

very of many new ZZ Ceti stars. Furthermore, it has provided an ever growing source of time-averaged data with which to discuss the class properties of these stars. An outstanding example of this is the discussion of the ZZ Ceti instability strip presented recently by Van Grootel et al. (2013b).

As indicated above, both our target stars belong to the original sample of 22 ZZ Ceti stars examined by Bergeron et al. (1995). The derived atmospheric parameters, under the assumption of ML2/α=0.6 convection, are reported in Table 2.5 for both objects. Note that only the formal fit errors are listed in that table. Those are rather small compared to the external errors which were conservatively estimated at the time to be around $\Delta T_{\rm eff} = \pm 350$ K and $\Delta \log g = \pm 0.05$ on the basis of multiple observations of the same objects during different nights. An important breakthrough was made recently on the modeling front by Tremblay & Bergeron (2009) who provided new calculations of the line broadening parameters of the Balmer and Lyman series for hydrogen to improve upon the older calculations of Lemke (1977) on which synthetic spectra of DA white dwarfs were previously based. This improvement led to a reanalysis of all of the high S/N DA spectra available in Montréal, including a recalibration of the convective efficiency most appropriate for usage in DA white dwarf atmospheres. The outcome of this reanalysis, now based on a new grid of model atmospheres using the ML2/α=0.8 efficiency, was presented in Gianninas et al. (2011). The inferred parameters for our two stars of interest that came out of that work are reported in Table 2.5. More recently, one of us (P.Be.) reexamined critically the new calibration of the convective efficiency and came to the conclusion that the adoption of the ML2/α=0.8 version actually overcorrects for the effects of the new line profiles and realized that an intermediate efficiency, termed ML2/α=0.7, is more appropriate. The details of that work will be discussed elsewhere, but we report our most recent estimates of the atmospheric parameters of our two targets on the basis of that newer calibration in Table 2.5. Figure 2.13 provides a view of the spectral fits we have obtained in that context. We emphasize, once again, the twin spectroscopic nature of GD 165 and Ross 548.

Another important breakthrough on the front of atmosphere modeling for DA white dwarfs was presented most recently by Tremblay et al. (2013) who finally succeeded at providing a

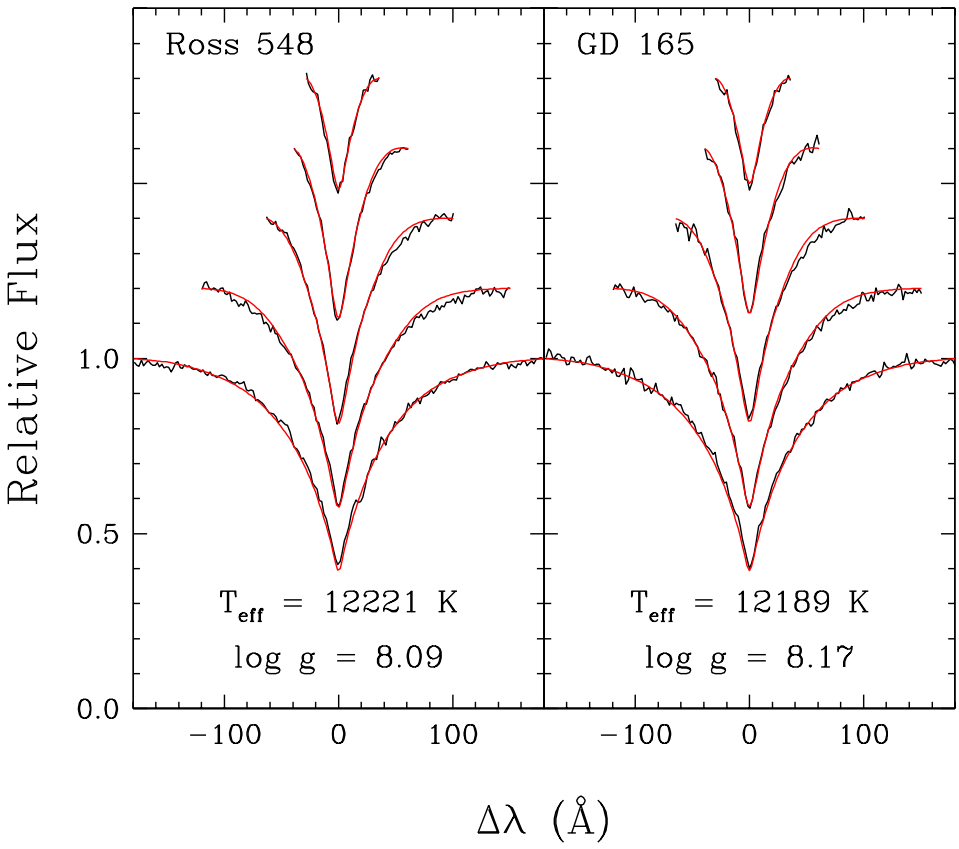

FIGURE 2.13 – Model fits to our high S/N blue optical spectra of Ross 548 (left panel) and GD 165 (right panel). The modeled lines are H8 through Hβ, from top to bottom. The atmospheric parameters are based on a new grid of model atmospheres and synthetic spectra for DA white dwarfs using the so-called ML2/α=0.7 convective efficiency. The formal uncertainties of the fits are listed in Table 2.5.

TABLE 2.5 – Derived Atmospheric Parameters with Formal Fit Errors Only

Name	Convection	TB09 profiles	$T_{\rm eff}$ (K)	Log g (cm s^{-2})	Reference
Ross 548	ML2/α=0.6	No	11985±54	7.978±0.021	Bergeron et al. 1995
	ML2/α=0.8	Yes	12479±117	8.053±0.028	Gianninas et al. 2011
	ML2/α=0.7	Yes	12218±69	8.088±0.022	This work
GD 165	ML2/α=0.6	No	11977±56	8.064±0.021	Bergeron et al. 1995
	ML2/α=0.8	Yes	12436±118	8.136±0.028	Gianninas et al. 2011
	ML2/α=0.7	Yes	12188±70	8.168±0.023	This work

TABLE 2.6 – Adopted Atmospheric Parameters with Estimates of External Errors

Name	Convection	TB09 profiles	$T_{\rm eff}$ (K)	Log g (cm s^{-2})	T13 1D/3D corrections
Ross 548	ML2/α=0.7	Yes	12218±162	8.088±0.044	No
	ML2/α=0.7	Yes	12276±190	8.006±0.048	Analytic fits
	ML2/α=0.7	Yes	12204±190	8.012±0.048	Direct interpolation
GD 165	ML2/α=0.7	Yes	12188±162	8.168±0.044	No
	ML2/α=0.7	Yes	12238±190	8.073±0.048	Analytic fits
	ML2/α=0.7	Yes	12165±190	8.082±0.048	Direct interpolation

credible explanation for the old puzzle of the apparent increase of the surface gravity with decreasing effective temperature for DA white dwarfs cool enough to have convective layers in their atmospheres ($T_{\rm eff} \simeq 14{,}000$ K and less). Their main results were based on the first detailed 3D hydrodynamic simulations of convection in DA white dwarfs. Among other important results, Tremblay et al. (2013) provided a correction scheme to be applied to the estimates of atmospheric parameters coming from standard 1D model atmospheres (still the only practical way to carry out spectroscopic analyses on a large scale). For a given convective efficiency, among the three versions already mentioned, the 1D/3D correction scheme came either in terms of tables (a grid over the log g-$T_{\rm eff}$ plane), or in terms of more practical analytic fits. In this context, we first listed in Table 2.6 our previous ML2/α=0.7 values of the atmospheric parameters of GD 165 and Ross 548, but incorporating more realistic estimates of the external errors that we added in quadrature with the formal errors of the fit. The estimates of the external errors are now based on the results of Liebert, Bergeron, & Holberg (2005) who found $\Delta T_{\rm eff} = 1.2\% T_{\rm eff}$ and $\Delta \log\, g = \pm 0.038$ in the more general context of the now well-known spectroscopic method first put forward by Bergeron, Saffer, & Liebert (1992). In addition, Pier-Emmanuel Tremblay (private communication) suggested that his 1D/3D correction scheme likely suffers from some uncertainties, which he estimates to be around $\Delta T_{\rm eff} \simeq \pm 100$ K and $\Delta \log\, g = \pm 0.02$, typically. Hence, we added this additional source of uncertainties (again in quadrature) when we applied the 1D/3D corrections of Tremblay et al. (2013). This led to the second and third entries in our Table 2.6. They differ in that one is based on the correction scheme using analytic fits, while the other is based on a direct double linear interpolation in the ML2/α=0.7 tables of Tremblay et al. (2013). Those two entries correspond to our best estimates of the atmospheric parameters of GD 165 and Ross 548. They constitute important independent constraints on future (and past) seismic modeling of these stars.

2.7 CONCLUSION

We have presented in this paper the first of a two-part seismic analysis of the two classical, bright, hot ZZ Ceti stars GD 165 and Ross 548. Those were selected on the basis of the simplicity of their pulsation properties, a general characteristic of stars located near the blue

edge of the ZZ Ceti instability strip in the spectroscopic HR diagram. In this project, we took advantage of the availability of two time-series data sets of exceptional sensitivity. Those were gathered many years ago by some of us using the photometer LAPOUNE attached to the CFHT, but they had remained largely unexploited until recently. Our selection of GD 165 and Ross 548 finds further justification in the fact that these are known to be nearly spectroscopic twins, yet they show significantly different dominant pulsation periods. This presents an interesting challenge from a seismic point of view. In our quest to revisit the problem of the seismic modeling of ZZ Ceti stars using the most recent techniques, we thought it appropriate to focus our efforts first on those two "simple" pulsators and solve this puzzle if possible. This is also to be considered as a benchmark for future studies of more complicated ZZ Ceti's, notably GD 1212, an object near the red edge which has been observed in short-cadence mode by $Kepler-2$. We will report the results of our efforts on the front of the seismic modeling of GD 165 and Ross 548 in a forthcoming paper, which constitutes the second part of our two-prong project.

The most important results of this article are presented in Table 2.2 (GD 165) and Table 2.4 (Ross 548) which summarize the outcome of our frequency extraction exercises, and also in Table 2.6 where our best estimates of the atmospheric parameters of the two stars are listed.

This work was supported in part by the NSERC Canada through a doctoral fellowship awarded to Noemi Giammichele, and through a research grant awarded to Gilles Fontaine. The latter also acknowledges the contribution of the Canada Research Chair Program.

2.8 REFERENCES

Bergeron, P., & McGraw, J.T. 1990, ApJ, 352, L45

Bergeron, P., Saffer, R.A., & Liebert, J. 1992, ApJ, 394, 228

Bergeron, P., Wesemael, F., Lamontagne, R., Fontaine, G., Saffer, R.A., & Allard, N. 1995, ApJ, 449, 258.

Bergeron, P., Fontaine, G., Brassard, P., et al. 1993, AJ, 106, 1987

Billères, M. 2000, Ph.D. thesis, Université de Montréal

Billères, M., Fontaine, G., Brassard, P., & Liebert, J. 2002, ApJ, 578, 515

Bischoff-Kim, A., Montgomery, M.H., & Winget, D.E. 2008, ApJ, 675, 1505

Castanheira, B.G., & Kepler, S.O. 2009, MNRAS, 396, 1709

Charpinet, S., Van Grootel, V., Brassard, P., Fontaine. G., Green, E.M., & Randall, S.K. 2013, EPJ Web of Conferences, Vol. 43, 04005

Fontaine, G., & Brassard, P. 2008, PASP, 120, 1043

Fontaine, G., McGraw, J.T., Coleman, L., Lacombe, P., Patterson, J., & Vauclair, G. 1980, ApJ, 239, 898

Gianninas, A., Bergeron, P., & Ruiz, M.T. 2011, ApJ, 743, 138

Green, E.M., Limoges, M.-M., Gianninas, A., et al. 2015, in Proc. 19th European Workshop on White Dwarfs, ed. P. Dufour, P. Bergeron, & G. Fontaine (San Franciso: ASP), 493, 237

Greiss, S., Gänsicke, B.T., Hermes, J.J., et al. 2014, MNRAS, 438, 3086

Hermes, J.J., Charpinet, S., Barclay, T., et al. 2014, ApJ, 789, 85

Landolt, A.U. 1968, ApJ, 153, 151

Lasker, B.M., & Hesser, J.E. 1969, ApJ, 158, L171

Lasker, B.M., & Hesser, J.E. 1971, ApJ, 163, L89

Lemke, M. 1977, A&AS, 122, 285

Liebert, J., Bergeron, P., & Holberg, J.B. 2005, ApJS, 156, 47

McGraw, J.T. 1977, Ph.D. thesis, University of Texas at Austin

McGraw, J.T. 1979, ApJ, 229, 203

Montgomery, M.H., & O'Donoghue, D. 1999, Delta Scuti Star Newsletter, 13, 28

Mukadam, A.S., Kepler, S.O., Winget, D.E., et al. 2003, ApJ, 594, 961

Mukadam, A.S., Bischoff-Kim, A., Fraser, O., et al. 2013, ApJ, 771, 17

Romero, A.D.,Corsico, A.H., Althaus, L.G., et al. 2012, MNRAS, 420, 1462

Stover, R.J., Hesser, J.E., Lasker, B.M., Nather, R.E., & Robinson, E.L. 1980, ApJ, 240, 865

Tremblay, P.-E., & Bergeron, P. 2009, ApJ, 696, 1755, (TB09)

Tremblay, P.-E., Ludwig, H.-G., Steffen, M., & Freytag, B. 2013, A&A, 559, A104, (T13)

Van Grootel, V., Charpinet, S., Brassard, P., Fontaine, G., & Green, E.M., 2013a, A&A, 553, A97

Van Grootel, V., Fontaine, G., Brassard, P., & Dupret, M.-A. 2013b, ApJ, 762, 57

Warner, B., Van Citters, C.W., & Nather, R.E. 1970, Nature, 226, 67

Winget, D.E., Nather, R.E., Clemens, J.C., et al. 1991, ApJ, 378, 326

Chapitre 3

A New Analysis of the Two Classical ZZ Ceti White Dwarfs GD 165 and Ross 548. II. Seismic Modeling

N. Giammichele[1], G. Fontaine[1], P. Brassard[1], and S. Charpinet[2]

[1] *Département de Physique, Université de Montréal, Succ. Centre-Ville, C.P. 6128, Montréal, QC H3C 3J7, Canada*

[2] *Université de Toulouse, UPS-OMP, IRAP, Toulouse F-31400, France*

CNRS, IRAP, 14 avenue Edouard Belin, F-31400 Toulouse, France

Received 2015 December 27

Submitted to *The Astrophysical Journal Supplement*

3.1 ABSTRACT

We present the second of a two-part seismic analysis of the bright, hot ZZ Ceti stars GD 165 and Ross 548. In this second part, we report the results of detailed searches in parameter space for identifying an optimal model for each star that can account well for the observed periods, while being consistent with the spectroscopic constraints derived in our first paper. We use a forward seismic approach similar to that applied quite successfully for pulsating hot B subdwarfs in recent years. The equilibrium stellar structures are full, static, spherically symmetric parametrized models of DA white dwarfs. Five basic parameters are varied: the composition of the C-O core (assumed homogeneous), the surface gravity, the effective temperature, the mass contained in the He mantle surrounding the C-O core, and the mass of the H outermost layer sitting on top of that mantle. We find optimal models for each target that reproduce the six observed periods well within $\sim$0.3% on the average, which is comparable to the best results achieved so far in asteroseismology. We also find that there is a sensitivity to the core composition for Ross 548, while there is practically none for GD 165. This a priori puzzling difference, along with the fact that the observed periods are significantly longer in Ross 548 than in GD 165 (which are otherwise near spectroscopic twins), may find a natural explanation in that the internal structures of the two stars differ in one significant aspect: Ross 548 has a relatively thin outer envelope, while GD 165 likely has a rather thick one. A thinner envelope leads to a longer period for a given g-mode, all other things being the same, and it may allow for more efficient trapping/confinement properties. Our optimal model of Ross 548 indeed shows weight functions for some confined modes that extend relatively deep into the interior, thus explaining the sensitivity of the period spectrum to the core composition in that star. In contrast, our optimal seismic model of its spectroscopic sibling, GD 165 with its thick envelope, does not trap/confine modes very efficiently, and we find weight functions for all six observed modes that do not extend into the deep core, hence accounting for the lack of sensitivity in that case. On the basis of our seismic modeling, we present a number of inferences on Ross 548 and GD 165. Furthermore, we exploit after the fact the observed multiplet structure which we ascribe to rotation. We are able to map the rotation profile in GD 165 (Ross 548) over the outermost $\sim$20% ($\sim$5%) of its radius, and find

that the profile is consistent with solid body rotation. Both ZZ Ceti stars rotate extremely slowly by stellar standards, at least in the layers – the outermost ones – that can be probed on the basis of the available rotationally-split multiplet data.

3.2 INTRODUCTION

In the first part of this short series of two papers dedicated to a detailed seismic analysis of the two bright, hot ZZ Ceti stars GD 165 and Ross 548, Giammichele et al. (2015a; hereafter referred to as Paper I) presented the results of frequency extraction exercises based on time-series data sets of exceptional quality. A total of up to 13 independent pulsation modes, regrouped into six main frequency multiplets, were uncovered in GD 165. Likewise, up to 11 independent modes, also regrouped into six multiplets, were isolated in Ross 548. The most likely cause of the multiplet structure is rotational splitting, and we will explore that avenue in some details below. For the purpose of comparing the observed pulsation periods with those of spherically symmetric (non-rotating) stellar models, each multiplet must be considered as a single degenerate mode, so there are, in fact, six "main" modes useful for that purpose for each star. We note that Paper I has revealed the existence of two more of these main modes than previously known for GD 165, and an additional one for Ross 548, thus providing welcome and significant additional constraints in the seismic modeling of these two pulsators. Further independent constraints were also provided in Paper I with the release of updated estimates of the time-averaged atmospheric parameters of each star in the light of recent developments on the front of atmospheric modeling for DA white dwarfs. Given the proven and widely acknowledged reliability of the spectroscopic method developed by our colleague Pierre Bergeron at Université de Montréal (Bergeron et al. 1992), we view these as fundamental additional constraints. Indeed, any seismic model leading to estimates of the effective temperature and the surface gravity that would be in serious conflict with the values obtained independently by high-quality spectroscopic modeling should be disqualified.

We selected GD 165 and Ross 548 on the basis of the simplicity of their pulsation properties, a general characteristic of stars – such as those two – located near the blue edge of the ZZ Ceti instability strip in the spectroscopic HR diagram. Our selection finds further

justification in the fact that these are known to be near spectroscopic twins, yet they show significantly different dominant pulsation periods. This presents an interesting challenge from a seismic point of view. In our quest to revisit the problem of the seismic modeling of ZZ Ceti stars using the most recent techniques, we thought it appropriate to focus our efforts first on those two "simple" pulsators and solve this puzzle if possible. The current work is also to be considered as a benchmark for future studies of more complicated ZZ Ceti's, notably GD 1212, an object near the red edge which has been observed in short-cadence mode with *Kepler-2*. Hence, we seek credible seismic models for both GD 165 and Ross 548, able to account for the six observed periods[1] at a level of accuracy comparable to the best currently achieved in the field of asteroseismology. To our knowledge, the best quantitative results on that front have been obtained from hot subwarf seismology, leading to typical average dispersions in the range 0.15−0.30% in fitted periods (see, e.g., Charpinet et al. 2008, 2011, and Van Grootel et al. 2010a, 2010b).

The credibility of a seismic model not only rests on its ability to reproduce simultaneously all of the observed periods at the highest possible accuracy, but also on the statistical significance of the solution. Typically, in seismic searches for an optimal model in parameter space, a merit function that measures the quality of the fit between the observed and theoretical periods for a given model is optimized. To establish the statistical validity of an optimal solution, it is then essential that the vicinity of that solution in parameter space be thoroughly explored. Furthermore, a credible seismic model should be compatible with the expectations of pulsation theory. In particular, for pulsating ZZ Ceti white dwarfs (see, e.g., Fig. 7c of Van Grootel et al. 2012), linear nonadiabatic theory predicts that a range of modes with consecutive values of the radial order k should be excited (for a given value of the degree l). In other words, the mode identification inferred from a seismic model must be in tune with such expectations if the model is to be considered as acceptable. In addition, a credible seismic model must be compatible with external independent constraints such as estimates of the atmospheric parameters derived from time-averaged spectroscopy (as mentioned above), estimates of distances provided by parallax measurements or spectroscopy, and previous mode identification of the

[1]Those are labelled f_1 through f_6 in Table 2.3 of Paper I for GD 165, and in Table 2.4 for Ross 548.

degree index l obtained through multicolor measurements or time-dependent spectroscopy, if available. In the following, we apply these principles in our search for optimal seismic models for GD 165 and Ross 548.

3.3 METHOD

3.3.1 Search for Optimal Seismic Models in Parameter Space

Our method is based on the forward modeling approach which consists in finding the best possible match between a set of oscillation periods detected in a given star and the periods computed from stellar models. Our original strategy along this avenue has been presented by Brassard et al. (2001) in the context of pulsating hot subdwarf stars. This strategy has since been considerably improved as discussed, in particular, by Charpinet et al. (2005) and Van Grootel et al. (2013a). The most recent discussion of our continuing quest for an objective approach to quantitative asteroseismology, with application to white dwarf stars in particular, has been presented by Charpinet et al. (2015).

Our technique relies on a double-optimization scheme that, first, best fits the six – in the case of both GD 165 and Ross 548 – observed periods (denoted $P_{\rm obs}$ in what follows) with six periods (denoted $P_{\rm th}$) belonging to the spectrum of a given model (note that the match might be quite poor if the model has properties quite different from those of the real star) and, second, searches for the best-matching model in parameter space. No a priori mode identification is imposed on the observed periods, except that they have to belong to degree index $l = 1$ or $l = 2$ in keeping with what is known about identified modes in white dwarfs (see, in this regard, Section 7 of Fontaine & Brassard 2008). For a given model, theoretical periods are computed in a window that encompasses the range of observed periods for modes with $l = 1$ and 2. For the present purposes, sufficiently accurate periods may be computed in the adiabatic approximation, so this is adopted as a major time-saving measure. The quality of the match between the observed and computed periods is measured quantitatively with a merit function defined by,

$$S^2 = \sum_{i=1}^{N_{\rm obs}} \left(P^i_{\rm obs} - P^i_{\rm th} \right)^2 , \tag{3.1}$$

where $N_{\rm obs} = 6$ in the present case. The goal of the exercise is to find, if possible, the minimum of S^2 in parameter space and, hopefully, a minimum that identifies a good and credible optimal model. To objectively and automatically carry out this search for the optimal model in parameter space requires considerable computing resources. Currently, a typical exercise of this kind for white dwarfs necessitates the computations of several million models and of their period spectra. In the present application, we have used the optimization package LUCY developed by one of us (S.C.) in Toulouse in order to handle this demanding numerical problem. This code is a massively parallel hybrid genetic algorithm capable of multimodal optimization and offers several advantages. It does not rely on model grids, as parameter space is explored essentially continuously. This leads to much higher computational efficiency and, in addition, the approach avoids grid resolution limitations. The code is also particularly robust at finding the best-fit solution, as well as all potentially interesting secondary optima. Some illustrations of the capabilities of the code, as well as additional details can be found in Charpinet et al. (2015).

3.3.2 Need for Parametrized Models

When some of us started investigating the application of the forward asteroseismological method to pulsating hot subdwarf and white dwarf stars more than a decade ago (see, e.g., Brassard et al. 2001 or Fontaine & Brassard 2002), we realized at the outset that the most practical way to do that would be through the use of parametrized static models. It has been our assertion since that parametrized models, as compared to full evolutionary models, provide the best, if not the only way, to thoroughly search in parameter space for an optimal seismic model. In principle, state-of-the-art evolutionary models provide the best physical description of stars. However, they suffer from two important drawbacks in the context of searching for the best seismic model.

The first of these shortcomings is their lack of flexibility. It is indeed nearly impossible, even with large computer clusters, to cover finely all of the relevant domains of parameter space with evolutionary sequences; it would take too much computing time. The practical consequence is that evolutionary sequences, necessarily limited in number, may actually miss

the "correct" region of parameter space where resides the best seismic model. In that context, it is virtually impossible to ensure that a potentially acceptable seismic model is the best one available from the traditional evolutionary approach.

The second drawback is that, by construction, it is implicitly assumed that the constitutive physics used in the construction of state-of-the-art evolutionary models is "perfect". Of course, this cannot be the case, especially in domains of the phase diagram corresponding to extreme physical conditions, such as those, for example, encountered in white dwarf stars. It may very well be the case in these circumstances that the input constitutive physics is not realistic enough and, consequently, that the observed pulsation periods cannot be accounted for at an acceptable level of accuracy on the basis of such evolutionary models.

In contrast, parametrized static models, even though they are cruder structures than evolutionary ones, offer maximum flexibility and speed for searching in parameter space. They can also compensate partly for uncertain input physics, and are particularly useful at that level for identifying the part of the input physics that needs improvement. They thus are most useful for providing feedback on the constitutive physics itself. Ultimately, they must of course be validated by improved evolutionary models. Successful examples of this type of feedback from parametrized seismology have been discussed recently by Charpinet et al. (2013). We further note that the method has proven itself in a rather remarkable way in the case of the pulsating hot B subdwarf component of the close eclipsing binary system PG 1336−018, which has turned out to be a true "Rosetta Stone" of hot subdwarf seismology (Charpinet et al. 2008; Van Grootel et al. 2013a).

In the case of white dwarf stars, extra care should be taken when using evolutionary models in a seismological context, particularly the more detailed ones that begin on the ZAMS. This is because they pile up numerous uncertainties and numerical noise by the time the modeled star becomes a white dwarf. These defects, often observed as very tiny bumps and discontinuities in the profile of the Brunt-Väisälä frequency in the final white dwarf model, have no importance for the evolution itself, but may play havoc with the period spectrum and the merit function. This is especially true for those pulsation modes with weight functions extending into the deep C-O core where diffusion has not enough time to erase these defects. Hence, relying on

such models for accurate seismic analyses of individual white dwarfs can be misleading. It has been our experience that extreme smoothness in all the variables of interest is a sine qua non condition for successful quantitative asteroseismology. We thus prefer the smoothness and flexibility provided by parametrized static models. Even though they constitute more approximate structures, they do not suffer from accumulated numerical noise which tends to destroy the shape of the S^2 hypersurface in parameter space.

3.3.3 Parametrized Models

To define a full (but static) ZZ Ceti white dwarf model, it is necessary to specify the surface gravity (or the mass via the mass-radius relation),[2] the effective temperature, the envelope layering, the core composition, and the convective efficiency via one flavor or another of the mixing-length theory. Quite realistic static models of white dwarfs can be computed (as compared to full evolutionary models) since in these cooling bodies the approximate relationship between the local luminosity and integrated mass, $L(r) \propto M(r)$, becomes quite accurate and, thus, may be used to provide an excellent estimate of the luminosity profile. Section 8 of the review paper of Fontaine & Brassard (2008) provides a detailed discussion of how the periods of pulsating white dwarfs depend on these structural parameters.

In particular, with respect to the convective efficiency to be used in the model-building phase, Figure 42 of Fontaine & Brassard (2008) shows that the periods of low-order g-modes in ZZ Ceti star models practically do not depend on the choice of the assumed convective efficiency, so it is justified here to adopt one version of the mixing-length theory and not worry further about it. This is especially justified in stars like GD 165 and Ross 548, which show rather short periods in the range from $\sim$114 s to $\sim$334 s, because such periods *have* to be associated with low-order modes. In the present asteroseismological exercise, the so-called ML2/α=1.0 version of the mixing length theory was therefore adopted following the calibration derived in Van Grootel et al. (2013b).

Concerning the core composition, it is well known that the exact chemical profile in the C-O core of a typical white dwarf is uncertain (see, e.g., the brief discussion in Giammichele

[2]We prefer to use the surface gravity rather than the mass in our approach because this allows a direct comparison with atmospheric parameters derived from spectroscopy.

et al. 2015b). Furthermore, characterizing such a detailed profile would require several free parameters. Given the limited number of constraints available in the present context, we decided instead to opt for homogeneous cores with the C/O ratio as the single free parameter. The assumption of core homogeneity is admittedly a rather crude approximation, but, in this way, at least the *bulk core composition* can potentially be probed (see, e.g., Giammichele et al. 2013). Figure 3.1 illustrates the small but significant differences that exist in the profile of the Brunt-Väisälä frequency in the core of three ZZ Ceti models that are otherwise the same, except for their homogeneous core composition (pure C, mixture of C and O in equal proportions by mass, pure O). One can expect a priori that these differences would affect the periods of gravity modes, at least for those modes with weight functions reaching down into the core with significant amplitudes.

The question of envelope layering deserves also some comments. It is specified not only by the total amount of mass there is in the helium mantle, $M(\mathrm{He})$, and the total amount of mass there is in the hydrogen outer envelope, $M(\mathrm{H})$, but also by the actual composition profiles in the transition zones themselves. This is because mode trapping/confinement, which has a very significant effect on the g-mode period spectrum in a white dwarf, is very sensitive to the conditions encountered in the composition transition zones (see, e.g., Section 4 in Brassard et al. 1992a). One standard assumption, based on physics as opposed to using some arbitrary profiles at the composition interfaces, has been to invoque diffusive equilibrium in order to compute the chemical distributions in the transition zones. The experiments reported by Brassard & Fontaine (2006) have been quite enlightening in this respect, in that they have shown that the assumption of diffusive equilibrium does not hold in GD 165. Indeed, this assumption leads, after a search in parameter space, to a rather poor optimal model characterized by a merit function of $S^2 \simeq 140.7$, a value that is not at all impressive compared to those that have been reached in other pulsating white dwarfs.

The optimal model found by Brassard & Fontaine (2006), although giving a poor match to the six periods observed in GD 165, still suggested the presence of a rather thick hydrogen layer in that star, a result consistent with the earlier independent arguments put forward by Fontaine et al. (1992). If true, then the assumption of diffusive equilibrium had to be ques-

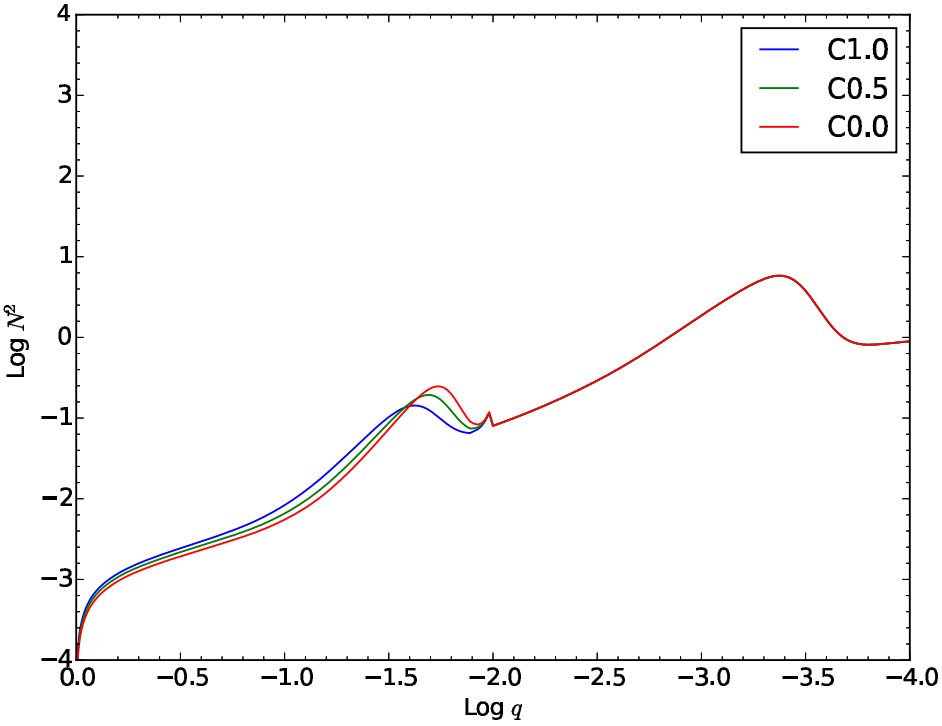

FIGURE 3.1 – Comparison of the profile of the square of the Brunt-Väisälä frequency versus fractional mass depth in the core of three representative ZZ Ceti star models that differ only in their core composition. One model has a pure carbon core, the second a mixed, homogeneous C and O core in equal proportions by mass, and the third has a pure O core. The other defining characteristics of these models are $T_{\rm eff} = 12{,}000$ K, $\log g = 8.0$, $\log M({\rm He})/M_* = -2.0$, and $\log M({\rm H})/M_* = -4.0$. The different composition is expected to perturb the periods of g-modes, at least for those modes that have weight function amplitudes that are nonnegligible in the core.

tioned. Indeed, one could argue that, at the depths corresponding to the base of a rather thick envelope, diffusion may not have had the time to reach equilibrium (the diffusion timescale increases rapidly with increasing depth in white dwarfs). This proposition was verified explicitly by Brassard & Fontaine (2006) who carried out detailed evolutionary calculations including diffusion at the composition interfaces. They were able to conclude that diffusive equilibrium is indeed not reached at the composition interfaces in a ZZ Ceti star model with thick hydrogen and helium layers. More importantly for the present purpose, they were able to "calibrate" the steepness of the composition profiles in a model of GD 165, and it is this calibration that is used here. To keep the number of free parameters to a minimum and to ensure that the exact same search procedure is used for Ross 548 as well, we assume, without further justification, that this calibration is also valid for models of that star.

With the convective efficiency chosen and two transition zone parameters calibrated (H/He and He/C-O interfaces), the search for the optimal model in parameter space boils down to a 5D exercise in terms of $X(\mathrm{O})$ (the mass fraction of oxygen in the C-O core), T_{eff}, $\log g$, $\log M(\mathrm{He})/M_*$, and $\log M(\mathrm{H})/M_*$, still a formidable numerical challenge. In order to include at the outset the independent constraints derived from spectroscopy, the search was confined to a range of T_{eff} and a range of $\log g$ corresponding to the 4σ "spectroscopic box" defined by the published values of these atmospheric parameters and their uncertainties. From Paper I, this corresponds to $T_{\mathrm{eff}} = 12165\pm760$ K and $\log g = 8.082\pm0.192$ for GD 165, and to $T_{\mathrm{eff}} = 12204\pm760$ K and $\log g = 8.012\pm0.192$ for Ross 548. Given the confidence we have on the reliability of these spectroscopic determinations, we choose to accept an optimal seismic model only if it falls within this 4σ box in the $\log g$-T_{eff} plane. For its part, the mass of the helium mantle was allowed to vary in the range $-4.0 \lesssim \log M(\mathrm{He})/M_* \lesssim -1.5$, while the mass of the hydrogen envelope was allowed to vary in the range $-9.0 \lesssim \log M(\mathrm{H})/M_* \lesssim -4.0$, with the condition $M(\mathrm{He})/M_* > M(\mathrm{H})/M_*$. The composition of the (homogeneous) core was searched in the full range of $X(\mathrm{O})$, from 0.0 to 1.0.

3.4 RESULTS

3.4.1 Optimal Seismic Models in Parameter Space

The results of our searches in parameter space turned out to be most encouraging as we found best-fit solutions with values of the surface gravity and the effective temperature well within the 4σ spectroscopic box for both stars of interest. In this context, we point out that there is never any guarantee at the outset that a minimum of the merit function S^2 will be found within the spectroscopic box. This is the kind of consistency that gives credibility to a seismic solution. Figure 3.2 shows a map of the merit function S^2 projected onto the surface gravity-effective temperature plane. Note the logarithmic scale used in the color coding. For each pair ($\log g$, $T_{\rm eff}$), the value given is the minimum of $\log S^2$ that can be found among the values obtained by varying the other parameters, i.e., $\log M(\mathrm{H})/M_*$, $\log M(\mathrm{He})/M_*$, and $X(\mathrm{O})$.

The left panel of Figure 3.2, which refers to GD 165, shows a small white cross which indicates the best-fit solution that we found for that star. It is located about 0.9σ away from the formal spectroscopic values at the center of the plot. The white dotted contours show regions where the period fits have S^2 values within the 1σ, 2σ, and 3σ confidence levels relative to that best-fit solution. Judging from their shapes, our optimal seismic model for GD 165 belongs to a family of solutions defining a rather long valley along the effective temperature axis, meaning that the observed pulsation modes in GD 165 do not constrain very tightly that parameter.

In contrast, the right panel of Figure 3.2 referring to Ross 548, indicates two rather well-defined minima corresponding to two possible solutions with comparable values of the merit function S^2. Those two solutions differ in the thickness of their H-He envelope, the upper one having a relatively thin envelope while the lower one having a thick one. This difference is associated with a shift of the radial index from k to $k-1$ for all six fitted modes from the thin-envelope to the thick-envelope model. Even though the thin-envelope solution is located farther away from the formal spectrocopic values at the center of the diagram than the thick-envelope solution (2.3σ versus 1.6σ), we argue below that it should be the preferred model

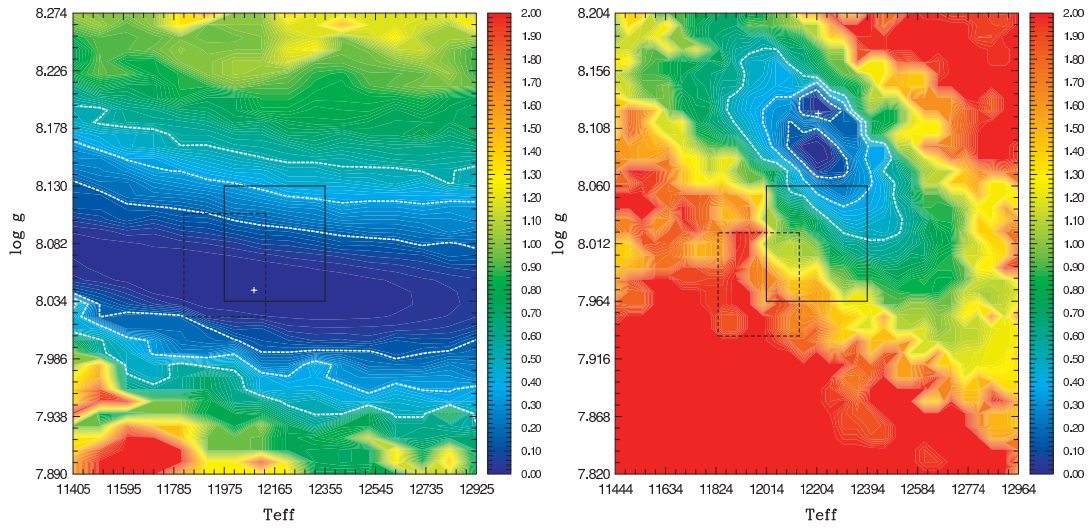

FIGURE 3.2 – *Left Panel:* Map of the 5D merit function S^2 projected onto the log g – $T_{\rm eff}$ plane for models of GD 165. The merit function is shown on a logarithmic scale (base 10). The location of the optimal model in this plane is indicated by a white cross. The white dotted curves delimit the regions where the merit function has values within the 1σ, 2σ, and 3σ confidence levels relative to the best-fit solution. By construction, the search domain in this plane is centered on the spectroscopic box (solid lines) and covers 4 times the spectroscopic uncertainties in both directions. The dashed lines define another spectroscopic box based on an earlier determination by Bergeron et al. (1995). *Right Panel:* Similar to the left panel, but for models of Ross 548. In contrast to the GD 165 case showing an optimal solution at the bottom of a relatively shallow S^2 valley, there are two well-defined minima here corresponding to a best-fit model with a thin envelope (upper minimum) and one with a thick envelope (lower minimum).

TABLE 3.1 – Defining parameters for the seismic models found for GD 165 and Ross 548

Model	$T_{\rm eff}$ (K)	$\log g$ (cm s^{-2})	D(H)	D(He)	X(O)	S^2 (s^2)	s^2 (s^2)
GD 165	12087.27	8.0432	−4.9490	−2.3311	0.000	1.918	0.320
Ross 548 (thin)	12209.31	8.1205	−8.3113	−3.5719	0.673	2.112	0.352
Ross 548 (thick)	12179.57	8.0885	−5.4300	−3.0967	0.448	2.086	0.348

and, consequently, we identified it with a small white cross in the figure.

Figure 3.3 is similar in format to the previous plot, but it refers to the D(He)−D(H) plane. These quantities used in the model building code are directly related to the mass contained in the He mantle and the mass contained in the H outer envelope, respectively, through the relation $\log M(\mathrm{He})/M_* \simeq D(\mathrm{He}) + 0.7$ and $\log M(\mathrm{H})/M_* \simeq D(\mathrm{H}) + 0.8$. For GD 165 (left panel), the optimal seismic model is rather well localized in this plane. The derived values of D(He) and D(H) imply thick envelope layers for GD 165. In comparison, the two solutions found for Ross 548 clearly stand out in the right panel and are even more localized than the GD 165 solution. Note as well that the thin-envelope solution is more sharply defined in this diagram.

Figure 3.4 refers to the fifth free parameter in our approach, the core composition – assumed homogeneous in this work – as measured by the oxygen mass fraction X(O). The plot illustrates the behavior of S^2 versus X(O). In the case of GD 165, the curve is rather flat, indicating a lack of sensitivity of the period fits on the core composition. The smallest value of S^2 obtained in that case is for $X(\mathrm{O}) = 0.0$, which corresponds to the core composition of the optimal model discussed above. This finding, i.e., the flatness of the curve, implies that the modes detected in GD 165 are not very sensitive to the core composition and, consequently, cannot be used to constrain it accurately. In sharp contrast, there is a clear sensitivity of the period fits on the core composition for Ross 548, with a relatively well-defined minimum in S^2 at $X(\mathrm{O}) \simeq 0.7$. Given that the two stars are near spectroscopic twins, this is a puzzling and interesting difference. Somehow, the modes detected in Ross 548 must be more sensitive to the core composition than are those found in GD 165. We come back to that problem below.

Table 3.1 lists the values of the five defining parameters needed in the construction of the

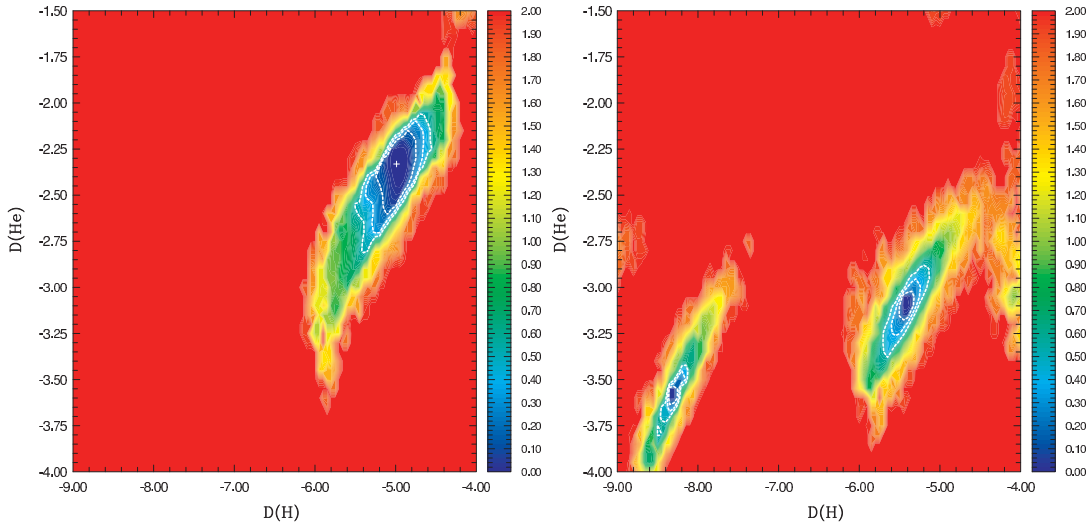

FIGURE 3.3 – *Left Panel:* Map of the 5D merit function S^2 projected onto the D(He) – D(H) plane for models of GD 165. The merit function is shown on a logarithmic scale. The location of the optimal model in this plane is indicated by a white cross. The white dotted curves delimit the regions where the merit function has values within the 1σ, 2σ, and 3σ confidence levels relative to the best-fit solution. Contrary to Fig. 3.2a, the optimal model corresponds to a relatively well-defined minimum in this plane. The parameters D(H) and D(He) used in the model building code are directly related to the mass fractions of hydrogen and helium through $\log M(\mathrm{H})/M_* \simeq D(\mathrm{H}) + 0.8$ and $\log M(\mathrm{He})/M_* \simeq D(\mathrm{He}) + 0.7$. The optimal model for GD 165 has rather thick H and He layers by white dwarf standards. *Right Panel:* Similar to the left panel, but for models of Ross 548. There are two very well-defined minima corresponding to a best-fit model with a relatively thick He and H envelope (lower right) and one with a thin envelope (lower left). The mode identification for the thick-envelope model is the same as for the thin-envelope model, except for the important fact that the radial index k is shifted to $k - 1$ for all 6 modes from the latter to the former.

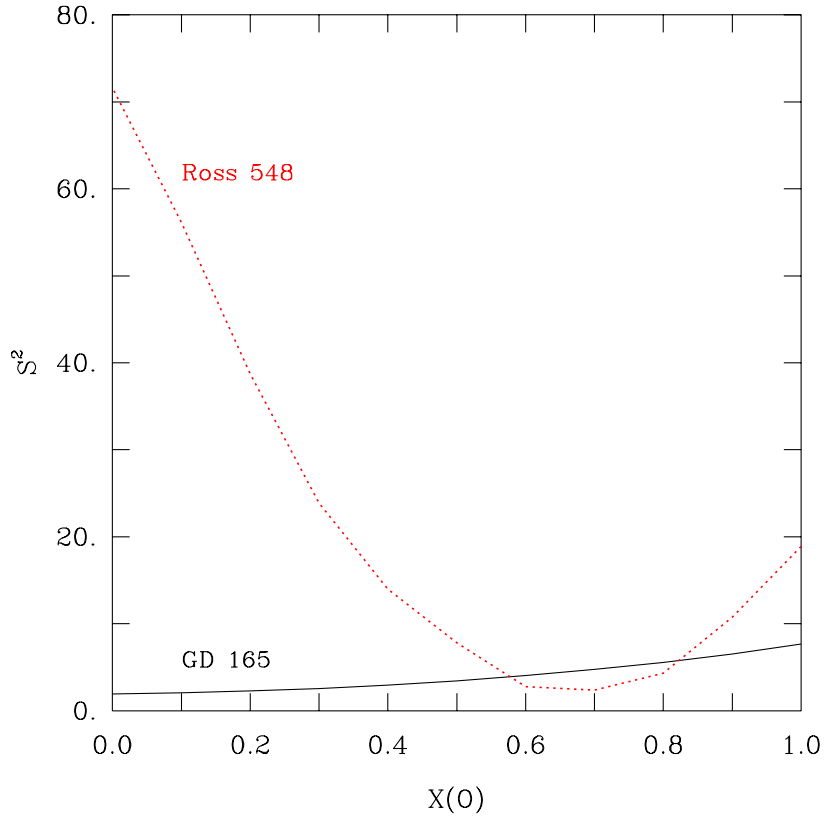

FIGURE 3.4 – Behavior of the merit function S^2 in terms of the core composition – measured by the oxygen mass fraction $X(\mathrm{O})$ – for the family of optimal models associated with each target star. This is obtained by fixing the core composition and searching for the best-fit solution in 4D space. The process is repeated for 11 values of $X(\mathrm{O})$ from 0.0 to 1.0, in steps of 0.1. While S^2 shows a well-defined minimum for $X(\mathrm{O}) \simeq 0.7$ in the case of Ross 548, there is practically no sensitivity on the core composition for GD 165. This implies that, contrary to Ross 548, the modes detected in GD 165 do not probe the deep core.

TABLE 3.2 – Mode identification and details of the period fit obtained for the optimal solution ($S^2 = 1.918$, $s^2 = 0.320$) for GD 165. The mean relative dispersion of the fit is $\overline{\Delta X/X} = 0.26\%$ (or $\overline{\Delta P} = 0.43$ s and $\overline{\Delta\nu} = 16.858$ μHz).

l	k	$\nu_{\rm obs}$ (μHz)	$\nu_{\rm th}$ (μHz)	$P_{\rm obs}$ (s)	$P_{\rm th}$ (s)	$\Delta X/X$ (%)	ΔP (s)	$\Delta\nu$ (μHz)	log $E_{\rm kin}$ (erg)	$A_{\rm obs}$ (%)	ID
1	−1	8308.691	8324.524	120.36	120.13	+0.19	+0.23	−15.833	46.55	0.507	f_1
1	−2	5189.950	5187.720	192.68	192.76	−0.04	−0.08	+2.230	47.51	0.231	f_2
1	−3	3997.459	3983.975	250.16	251.01	−0.34	−0.85	+13.484	45.31	0.057	f_3
1	−4	...	3456.083	...	289.34	...	...	...	45.09	...	
2	−1	...	14409.838	...	69.40	...	...	...	46.55	...	
2	−2	8753.931	8768.477	114.23	114.04	+0.17	+0.19	−14.546	47.41	0.043	f_4
2	−3	6834.527	6883.292	146.32	145.28	+0.71	+1.04	−48.764	45.30	0.044	f_5
2	−4	5945.614	5951.902	168.19	168.01	+0.11	+0.18	−6.288	45.07	0.027	f_6
2	−5	...	4858.771	...	205.81	...	...	...	44.44	...	
2	−6	...	4449.892	...	224.72	...	...	...	44.34	...	
2	−7	...	4170.575	...	239.78	...	...	...	44.24	...	
2	−8	...	3716.483	...	269.07	...	...	...	43.62	...	
2	−9	...	3449.181	...	289.92	...	...	...	43.52	...	

optimal models obtained from our detailed searches in parameter space. It is to be understood that the inferred value of X(O) can only be considered as an estimate of the bulk core composition in regions actually probed by the modes available. The last two columns give the value of the merit function S^2 for these optimal models, and of the normalized merit function s^2. The latter is simply defined as the merit function divided by the number of fitted periods (six for both stars in the present case), and will be used below for comparison purposes with the results of other investigators.

3.4.2 Mode Identification and Other Properties

Our search method yields automatically the mode identification (in terms of the indices l and k for spherical models) consistent with the best S^2 value as output.[3] Table 3.2 summarizes the period match obtained and the mode identification inferred for the optimal model found for GD 165. It gives the results both in terms of the period P and the frequency $\nu = 1/P$. In addition, the last three columns of the table give, respectively, the kinetic energy for each model mode listed (useful for recognizing trapped and/or confined modes; see below), the observed Fourier amplitude of each detected mode (actually, the amplitude of the largest component within a multiplet, if applicable), and an identification giving the ranking in terms

[3]Note that we adopt here the convention that negative values of the radial order index k refer to g-modes.

TABLE 3.3 – Mode identification and details of the period fit obtained for the retained optimal solution ($S^2 = 2.112$, $s^2 = 0.352$) for Ross 548. The mean relative dispersion of the fit is $\overline{\Delta X/X} = 0.22\%$ (or $\overline{\Delta P} = 0.48$ s and $\overline{\Delta\nu} = 9.915$ μHz).

l	k	$\nu_{\rm obs}$ (μHz)	$\nu_{\rm th}$ (μHz)	$P_{\rm obs}$ (s)	$P_{\rm th}$ (s)	$\Delta X/X$ (%)	ΔP (s)	$\Delta\nu$ (μHz)	log $E_{\rm kin}$ (erg)	$A_{\rm obs}$ (%)	ID
1	−1	4696.019	4690.631	212.94	213.19	−0.11	−0.24	+5.387	46.51	0.658	f_1
1	−2	3642.709	3637.563	274.52	274.90	−0.14	−0.39	+5.146	43.92	0.430	f_2
1	−3	3140.496	3143.119	318.42	318.15	+0.08	+0.26	−2.622	45.00	0.072	f_4
1	−4	2997.200	2996.045	333.64	333.77	−0.03	−0.12	+1.154	45.04	0.062	f_5
1	−5	...	2327.315	...	429.67	...	...	...	44.58	...	
2	−1	...	8096.161	...	123.51	...	...	...	46.48	...	
2	−2	...	6299.070	...	158.75	...	...	...	43.92	...	
2	−3	5351.199	5329.143	186.87	187.64	−0.41	−0.77	+22.055	44.76	0.088	f_3
2	−4	4590.660	4567.538	217.83	218.93	−0.50	−1.10	+23.121	45.75	0.032	f_6
2	−5	...	3921.390	...	255.01	...	...	...	44.26	...	
2	−6	...	3504.982	...	285.30	...	...	...	43.79	...	
2	−7	...	3266.365	...	306.15	...	...	...	42.61	...	
2	−8	...	3035.180	...	329.46	...	...	...	42.84	...	
2	−9	...	2789.663	...	358.46	...	...	...	43.16	...	

of observed amplitude, from f_1 through f_6, as also given in Paper I. Table 3.3 uses the same format for presenting the equivalent data for the optimal model of Ross 548 that we retained, the one with a thin envelope. We point out that the mean relative dispersions of the global fits in period or frequency, $\Delta X/X = 0.26\%$ for GD 165 and $\Delta X/X = 0.22\%$ for Ross 548, are comparable to the best results obtained in recent years in the fields of white dwarf and hot subdwarf seismology. From this point of view, each fit is quite satisfactory. In the worst case for GD 165 (the 146.32 s mode), there is a difference of +0.71% between the observed period and the theoretical period of the assigned $l = 2$, $k = -3$ mode in the optimal model. The counterpart for Ross 548 is the 217.83 s pulsation, identified with a $l = 2$, $k = -4$ mode, for which a difference of −0.50% is found. Figure 3.5 provides a graphic representation of these excellent overall fits. Note that we use the reduced period, $P[l(l+1)]^{0.5}$, as the abcissa in order to have a tighter diagram.

It may be significant that the search exercise has assigned the three largest amplitude oscillations in GD 165 to $l = 1$ modes, and the three smallest amplitude ones to $l = 2$ modes. But for one mode (f_3), this behavior is also observed in Ross 548. This is indeed the expected hierarchy in view of geometrical cancellation effects, but this argument should be used with some caution as there are known cases of pulsating stars (including white dwarfs) that show

$l = 2$ modes with larger amplitudes than $l = 1$ modes.[4] Nevertheless, we do point out that the light curve of each star is dominated by two relatively large oscillations (f_1 and f_2), both of which showing a clear triplet structure when viewed at very high resolution (see Figs. 2.5 through 2.8 in Paper I). This certainly reinforces their assigment in Tables 3.2 and 3.3 to dipole modes. Furthermore, for both GD 165 and Ross 548, the largest of the two oscillations is identified with the radial order $k = -1$, while the other one is identified with the value of $k = -2$, so there is a common pattern here. It is also of interest to point out that the assigned modes in Table 3.2 have consecutive values of the radial order; from $k = -1$ to $k = -3$ for the dipole modes, and from $k = -2$ to $k = -4$ for the quadrupole modes. Likewise, in the case of Ross 548 as can be seen in Table 3.3, the four oscillations assigned to dipole modes have consecutive values of the radial order, from $k = -1$ to $k = -4$. The two other pulsations, identified with quadrupole modes, have also consecutive values of the radial order with $k = -3$ and $k = -4$. This is again circumstantial evidence that adds to the credibility of our optimal models because nonadiabatic theory (see below) usually predicts that pulsation modes should be excited in a band of Δk modes in radial order, for a given value of l.

We have verified explicitly that the mode identification proposed for GD 165 in Table 3.2 remains the same whatever the assumed core composition. That is, it does not change along the flat curve illustrated in Figure 3.4 above. In retrospect, this is not at all surprising since the modes detected in GD 165 seem to hardly probe the core at all and, consequently, their periods are not very sensitive to a change in core composition. The mode identification in such a case must rest mostly with the response of the pulsation periods upon varying the other parameters. Interestingly, even though the pulsation periods do depend on the core composition in models of Ross 548, we find that the mode assignment in Table 3.3 is rather robust, as it does not change in a rather wide interval $0.2 \lesssim X(\mathrm{O}) \leq 1.0$ along the dotted curve in Figure 3.4. For values of $X(\mathrm{O})$ smaller than $\simeq 0.2$, the mode identification loses its coherence as the assigned modes no longer show consecutive values of k for given l.

We also point out that the second optimal model found for Ross 548, the one with a thick

[4]The case of the crystallized ZZ Ceti star BPM 37093 is interesting in that respect in that only one mode has been assigned a value of $l = 1$, while the seven other detected pulsations have been identified with $l = 2$ modes (Metcalfe et al. 2004; Brassard & Fontaine 2005). It may be that the solid core in that object has an incidence on the preferred excitation of quadrupole modes in that particular case.

envelope, differs in its mode identification from the model we retained in Table 3.3 in that all of the six modes of interest have values of their radial order decreased by 1 unit. Hence, the dominant observed pulsation at 212.94 s is now assigned to a mode characterized by $l = 1$ and $k = -2$, the second-largest oscillation at 274.52 s is assigned to a mode with $l = 1$ and $k = -3$, and so on. This leaves a $l = 1$ and $k = -1$ mode (with a period of 131.11 s) in that optimal model that has no observed counterpart. In our view, this undermines somewhat the credibility of that model. Nevertheless, on the sole basis of the value of S^2, both optimal models for Ross 548 are equally acceptable. A comparison with the spectroscopic values of log g and $T_{\rm eff}$ even suggests that the thick-layer solution is somewhat better, but the improvement over the thin-layer solution is only marginal in that respect. We do prefer the thin-layer optimal model for two principal reasons.

First, linear nonadiabatic theory shows that the 131.11 s $l = 1$, $k = -1$ mode in the thick-layer optimal model is as strongly driven as the 212.73 s $l = 1$, $k = -2$ mode in that model. The growth rates and the kinetic energies of the two modes are indeed quite comparable, meaning that both modes have the same chances of growing an observable amplitude. In other words, both modes should be detectable if one is observed. As this is not the case, we propose that the 213 s mode is more likely a $l = 1$, $k = -1$ mode, in which case it would have the largest amplitude, similarly to the 120 s dominant pulsation in GD 165 identified above as a $l = 1$, $k = -1$ mode. And indeed, as already mentioned previously, the 213 s pulsation has the largest observed amplitude in the light curve of Ross 548. If our proposed mode identification is correct ($l = 1$, $k = -1$), then the thin-layer solution must apply (see Fontaine et al. 1992).

Second, in the light of what is known about rotation in the pulsating pre-white dwarfs of the GW Vir type (Charpinet et al. 2009; Fontaine et al. 2012), it is very likely that isolated white dwarfs, as a group, rotate extremely slowly and as solid bodies. If this is true, then the 1st-order rotation coefficient C_{kl} (see Appendix A) can be used to verify the mode identification in presence of rotational-splitting data. We find in this regard that the thick-layer solution is characterized by values of C_{kl} for the two dominant triplets (213 and 274 s) that are in conflict with the observed frequency spacings in the multiplet data. In particular, that solution leads

to the prediction that the frequency spacing should be smaller in the 213 s multiplet than in the 274 s complex, in direct contradiction with the observations. In contrast, the thin-layer model predicts frequency spacings that go in the same sense as the observations. For those two reasons, we propose the thin-layer optimal model for Ross 548 as the more appropriate one. In the rest of this paper, we concentrate on that latter model for Ross 548.

Given that our adopted seismic model for Ross 548 is characterized by a much thinner H-He envelope than our seismic model for GD 165, we find a natural explanation for the fact that the dominant pulsation periods are significantly longer in Ross 548 (213 and 274 s) than in GD 165 (120 and 192 s), even though, once again, those two stars are near spectroscopic twins. Indeed, all other things being the same, the period of a g-mode – specified by the pair of indices l and k – increases with decreasing envelope mass. This is very well explained in the detailed study of the adiabatic properties of models of ZZ Ceti stars presented by Brassard et al. (1992a; see, in particular, their Tables 3, 4, and 5 and related text). Likewise, we find a natural explanation for the fact that our optimal model of GD 165 shows only a weak sensitivity on the core composition, while that of Ross 548 shows a much stronger dependence. Indeed, an examination of the weight functions of each of the assigned modes as shown in Figure 3.6 reveals that all six modes in the GD 165 model (left panel) have weight functions that do not extend into the deep core and, consequently, their periods are not sensitive to a variation of the core composition in that region. At best, these modes probe the outermost region of the core which is expected to be C-dominated, and it may therefore be significant that our seismic model suggests a value of $X(\mathrm{O}) = 0.0$ in that case. In comparison, three of the six modes in the Ross 548 model are partly confined below the thin envelope and, therefore and a contrario, have a strong sensitivity to the core composition. It has been shown, in this context, that thinner envelopes in models of ZZ Ceti stars have generally better capacities for trapping and confining g-modes (Brassard et al. 1992b).[5] We submit that this remarkable internal consistency bodes well in favor of the credibility of our seismic models for these spectroscopic look-alikes.

[5]In the nomenclature suggested by Brassard et al. 1992b, a mode is said to be trapped above a composition transition layer if its amplitude and weight function are negligible below that layer. Conversely, a mode is said to be confined below a composition transition layer if its amplitude and weight function are negligible above that layer.

TABLE 3.4 – Mode identification, observed multiplet structures in GD 165, and inferred rotation period under the assumption of solid body rotation.

l	k	m	C_{kl}	log $E_{\rm kin}$ (erg)	$A_{\rm obs}$ (%)	$P_{\rm obs}$ (s)	$\nu_{\rm obs}$ (μHz)	$\delta\nu_{\rm obs}$ (μHz)	$P_{\rm rot}$ (h)
1	−1	−1			0.1131±0.0042	120.3201±0.0006	8311.16±0.04	2.47±0.05	
1	−1	0	0.491	46.55	0.5070±0.0042	120.3559±0.0001	8308.69±0.01	<2.46±0.03>	57.43±0.70
1	−1	+1			0.1592±0.0042	120.3916±0.0005	8306.23±0.03	2.46±0.03	
1	−2	−1			0.2311±0.0065	192.5717±0.0006	5192.87±0.03	2.92±0.05	
1	−2	0	0.399	47.51	0.2255±0.0065	192.6801±0.0001	5189.95±0.03	<2.92±0.05>	57.20±0.98
1	−2	+1			0.0631±0.0065	192.7886±0.0046	5187.03±0.12	2.92±0.13	
1	−3	0	0.486	45.32	0.0566±0.0056	250.1589±0.0074	3997.46±0.12	2.49±0.30	57.30±6.90
1	−3	+1			0.0243±0.0056	250.3150±0.0173	3994.97±0.28		
2	−2	0	0.084	47.41	0.0428±0.0041	114.2344±0.0015	8753.93±0.12	8.95±0.32	56.88±2.04
2	−2	+2			0.0167±0.0041	114.3513±0.0039	8744.98±0.30		
2	−3	0	0.155	45.30	0.0439±0.0051	146.3159±0.0030	6834.53±0.14	3.90±0.35	60.16±5.40
2	−3	+1			0.0191±0.0051	146.3995±0.0068	6830.63±0.32		

We finally draw the attention of the reader on the correlation that exists between the behavior of the weight function of a pulsation mode and its global kinetic energy. A mode that extends deep into a model has a relatively large kinetic energy ($E_{\rm kin} = 0.5 \int_0^V \rho v^2 dV$) because the density increases with depth. Conversely, a mode that would be trapped in the outermost layers of a model would show a much reduced value of its kinetic energy. For example, Tables 3.2 and 3.3, in conjunction with Figure 3.6, show that the f_2 mode in Ross 548 is completely trapped above the H/He composition transition layer and has a low value of log $E_{\rm kin} = 43.92$, while the f_2 mode in GD 165, with log $E_{\rm kin} = 47.51$, is largely confined to the He mantle in that model. Another example is the f_6 mode in Ross 548 which extends deep into the core and, consequently, show a maximum in kinetic energy (log $E_{\rm kin} = 45.75$) compared to its adjacent $l = 2$ neighbors. This mode is largely confined below the thin H-He envelope.

3.4.3 Multiplet Structure and Rotation

On the basis of our optimal seismic models, we next analyze the multiplet structures detected in the light curves of GD 165 and Ross 548, which we ascribe to rotation. In the case of GD 165 (Ross 548), five (three) of the six main modes show multiplet structure. This is summarized in Table 3.4 (Table 3.5) where we provide the detailed mode identification

TABLE 3.5 – Mode identification, observed multiplet structures in Ross 548, and inferred rotation period under the assumption of solid body rotation.

l	k	m	C_{kl}	log $E_{\rm kin}$ (erg)	$A_{\rm obs}$ (%)	$P_{\rm obs}$ (s)	$\nu_{\rm obs}$ (μHz)	$\delta\nu_{\rm obs}$ (μHz)	$P_{\rm rot}$ (h)
1	−1	−1			0.4105±0.0066	212.7684±0.0011	4699.95±0.02	3.93±0.08	
1	−1	0	0.468	46.51	0.1361±0.0066	212.9463±0.0033	4696.02±0.07	<4.02±0.05>	36.73±0.46
1	−1	+1			0.6578±0.0066	213.1326±0.0007	4691.92±0.02	4.11±0.08	
1	−2	−1			0.4299±0.0072	274.2508±0.0019	3646.30±0.03	3.59±0.10	
1	−2	0	0.498	43.92	0.1155±0.0072	274.5209±0.0071	3642.71±0.10	<3.48±0.07>	40.09±0.81
1	−2	+1			0.3107±0.0072	274.7745±0.0027	3639.35±0.04	3.36±0.10	
1	−3	−1	0.399	45.00	0.0722±0.0077	318.0763±0.0163	3143.90±0.16	6.80±0.42	49.11±3.03
1	−3	+1			0.0303±0.0077	318.7657±0.0391	3137.10±0.39		

in terms of the set of indices (k,l,m) for each of the detected multiplet components (12 for GD 165 and 8 for Ross 548). Using data from Paper I, we also provide the observed Fourier amplitude $A_{\rm obs}$, the observed period $P_{\rm obs}$, and the observed frequency $\nu_{\rm obs}(= 1/P_{\rm obs})$ for each of these independent pulsation modes, as well as the frequency spacings $\delta\nu_{\rm obs}$ between multiplet components.

Under the assumption of slow, solid body rotation, one can use each multiplet structure in conjunction with a seismic model in order to obtain an independent estimate of the rotation period of a star. From the details provided in Appendix A, the solid body rotation period may be obtained from the following equation (based on equation (A5) while remembering that $\sigma = 2\pi\nu$ and $\Omega_{\rm rot} = 2\pi/P_{\rm rot}$),

$$P_{\rm rot} = (1 - C_{kl})/\delta\nu_{\rm obs} \ , \tag{3.2}$$

where C_{kl} is the first-order solid body rotation coefficient. This quantity depends only on the unperturbed adiabatic eigenfunctions ξ_r and ξ_h associated with our purely spherically symmetric seismic models. Its value is provided for each multiplet structure listed in Tables 3.4 and 3.5.[6]

In the case of GD 165, each of the five detected multiplet structures provides a very similar

[6] As can be seen in these tables, there exists a strong correlation between the value of the first-order solid body rotation coefficient and the kinetic energy of a g-mode, in the sense that a mode trapped in the outermost H layer tends to have a relatively large value of C_{kl} and a small value of log $E_{\rm kin}$; conversely for a confined mode. The interested reader will find a detailed discussion of that behavior in Brassard et al. 1992a; see their Fig. 18, in particular.

estimate of the rotation period as given in the last column of Table 3.4. These estimates are quite coherent with the a priori assumption of slow, solid body rotation, at least in those regions actually probed by the available modes. This internal coherency provides us with a strong test of the mode identification achieved previously in our objective and automatic search for an optimal seismic model in parameter space. Indeed, we note that the value of C_{kl} coming from our seismic model of GD 165 varies significantly from mode to mode. This is because we are dealing with very low-order g-modes, well away from the asymptotic regime of high-order modes for which the values of the first-order solid body rotation coefficient reduces to $1/(l(l+1))$, independent of the index k (see Appendix A). Quite on the contrary for low-order modes, slow and rigid rotation leads to k-specific frequency spacings for a given value of the degree l. Hence, the observed frequency spacings $\delta\nu_{\rm obs}$ bear the signature of both the l and k indices. We find that the results presented in Table 3.4 for GD 165 confirm remarkably well the mode identification obtained in Subsection 3.2 for the five modes showing rotational splitting.

For Ross 548, we find that the three independent estimates of the rotation period listed in the last column of Table 3.5 are formally inconsistent with the hypothesis of rigid rotation. Taken at face value, these different estimates imply some mild differential rotation between the different regions of the star actually probed by the three multiplets of interest. If true, we cannot use the observed frequency spacings to test the mode identification because the (differential) rotation law is unknown in that case. Before adopting that conclusion, however, it is well to take a critical look at each of these three multiplets. While the existence of the two triplets at 213 and 274 s cannot be questionned, we recall that the multiplet centered on 318 s may not be a real detection. Indeed, as discussed in Paper I, the low-amplitude component of that doublet, the one with a period of 318.7657 s, is only a possible detection with a value of S/N = 3.1, and a False Alarm Probability value of 0.34, formally smaller than the "passing value" of 0.5, but not by very much. Removing the 318 s doublet from Table 3.5 goes a long way toward improving the consistency of the two remaining estimates of $P_{\rm rot}$, within the hypothesis of rigid rotation, since these estimates overlap within 2.7σ and are based on the implicit assumption in equation (2) that our values of C_{kl} have no uncertainties. Given

that our optimal model of Ross 548 is certainly perfectible, we submit that the hypothesis of rigid rotation is still viable for Ross 548. As briefly alluded to above, slow and rigid rotation is generally expected in a cool, isolated white dwarf such as Ross 548. If we adopt that point of view, we find that the observed frequency spacings in the 213 and 274 s triplets are, in fact, consistent with their respective identification as $k = -1,\ l = 1$ and $k = -2,\ l = 1$ multiplets. In particular, and contrary to GD 165, the frequency spacings are predicted (and observed) to be larger in the $k = -1,\ l = 1$ triplet than in the $k = -2,\ l = 1$ triplet. In a paragraph above, we used the fact that this coherency is not found in the thick-envelope model for Ross 548 as an argument to discredit it.

It is highly instructive to locate the region of a seismic model that is actually probed for rotation, given a specific multiplet structure. In the regime of slow rotation, that information is contained in the so-called first-order rotation kernel, K_{kl}, discussed in Appendix A. That depth-dependent function is computed from the eigenfunctions ξ_r and ξ_h associated with the degenerate mode (k,l) identified, in the (non-rotating) seismic model, with the multiplet structure. From equation (A2), K_{kl} clearly plays a role similar to the weight functions encountered above, as it indicates, in the present case, the layers contributing most to the integral giving the frequency spacing between multiplet components.

Figure 3.7 (left panel) shows the relevant quantities for the five modes from our seismic model associated with multiplets in the light curve of GD 165. In the case of Ross 548 (Figure 3.7, right panel), based on the discussion just above, we retained only the two secure triplets at 213 and 274 s. In the upper part of each panel, we plotted the first-order rotation kernel for each of the mode of interest. To compare properly the kernel distribution associated with one mode with that associated with another mode, we plotted the *relative rotation kernels*, after having normalized arbitrarily the largest amplitude of all kernels involved to 1.0. We illustrate the outermost 20% of the normalized radius for both seismic models because, as it turns out, the rotation kernels have non-negligible amplitudes only in those outer layers.

In order to best identify the region over which rotation can be probed, we computed the weighted sum of kernels, which is shown by the dashed curve in the lower subpanel of each plot. The weighted sum takes into account the number of splittings observed in a given multiplet.

Hence, the rotation kernels for the 120 and 192 s modes in GD 165 were multiplied by a weight of 2 in the sum because two frequency spacings were detected in their case (see Table 3.4). In comparison, a weight of 1 was assigned to the 250, 114, and 146 s doublets in that same sum. We thus find that rotation can be probed in GD 165 over approximately the outer 20% of its radius. In comparison, from the weighted sum of the kernels of the 213 and 274 s triplets in Ross 548, rotation can be probed in a more restricted region covering, approximately, the outer 5% of the radius in that case. In both instances, the coverage corresponds to the H-He envelope.

It is unfortunate, in this context, that the three confined modes sensitive to the core composition in Ross 548 (see Fig. 3.6, right panel) have rather small amplitudes with no detected (218 and 333 s) or unreliable (318 s) multiplet structure. Indeed, the coverage of the weight function of a mode and that of its first-order rotation kernel are comparable, meaning that the internal dynamics of the core of Ross 548 *could* have been tested, had those modes revealed rotational splitting. In comparison, even though five of the six main modes observed in GD 165 have secure multiplet structures, none of them have weight functions or rotation kernels extending down into the core according to Figures 3.6 and 3.7. The low-amplitude singlet at 168 s is also restricted to the H-He envelope according to Figure 3.6 (left panel). This implies that the potential for sounding the rotation in the core of GD 165 does not exist on the basis of the available data and of our seismic model.

3.4.4 Formal Analysis of the Multiplet Data

In this subsection, we use and develop further the formal approach that was introduced by Charpinet et al. (2008, 2009) for exploiting quantitatively the fine structure caused by rotational splitting in seismic data. The method consists in analyzing *simultaneously* the available rotational data under the assumptions that (1) the star rotates slowly, and (2) it rotates as a solid body. The inferred uniform rotation period, $P_{\rm rot}$, can be used after the fact to verify if the star indeed rotates slowly, in which case $P_{\rm rot}$ should be much larger than the periods of the pulsation modes of interest and first-order perturbation theory should apply. The hypothesis that the star rotates as a rigid body is next verified through stringent tests

based on the theory summarized in Appendix A. To insure success, reliable multiplet data must be available, the modes must have been identified correctly, and a credible seismic model with appropriate eigenfunctions (rotation kernels) must be on hand.

It should be clear, at the outset, that testing for rigid rotation requires the availability of at least two multiplets, and preferably many more, as each main mode probes a specific region of the star as seen in Figure 3.7 above, for example. In this regard, the lowest-order modes contain much more information than high-order modes which tend to show very similar rotation kernels. The sensitivity of the tests for rigid rotation proposed below rests heavily on the diversity of the applicable rotation kernels. We consider first the case of GD 165, which is outstanding in that seven well-measured frequency spacings belonging to five well-identified low-order modes are available (see Table 3.4), along with a credible seismic model that accounts remarkably well for the seismic and spectroscopic data on hand.

Under the a priori assumption that GD 165 spins slowly and rigidly, the rotational data is best explained globally with a value of the rotation period $P_{\rm rot} = 57.294 \pm 0.338$ h. This is obtained by minimizing the merit function given in equation (3.14) (with $N_{\rm obs} = 7$) in conjunction with equations (3.12) and (3.13) for solid-body rotation. In this particular case, the optimization problem is a simple 1D exercise featuring the behavior of the merit function S^2 (not to be confused with the merit function above related to period matching) in terms of the uniform rotation period $P_{\rm rot}$. The result of the procedure is shown in the upper left panel of Figure 3.8. Not surprisingly, the derived value is perfectly consistent with the individual estimates listed in the last column of Table 3.4, and indicates that GD 165 indeed rotates very slowly. For instance, in comparison to 57.294 h, the detected pulsation periods have very low values, between 114 and 250 s.

The second hypothesis, that the star rotates as a solid body (at least in the region where the weighted sum of the rotation kernels has a non-negligible amplitude), is also nicely verified here through the results of three different tests as shown in the other panels of Figure 3.8. Test #1 relies on the assumption that the rotation law, $\Omega_{\rm rot}(r)$, is linear with the radial coordinate and is defined by two free parameters, $P_{\rm c}$ the central rotation period, and $P_{\rm s}$ the superficial rotation period. The merit function S^2 given by equation (3.14), in conjunction this time with

equations (3.9) and (3.10), is now a quantity that must be optimized in 2D, as a function of $P_{\rm c}$ and $P_{\rm s}$. Hence, *if GD 165 rotates as a rigid body, the merit function must show a minimum when* $P_{\rm c} = P_{\rm s} = P_{\rm rot}$. This is precisely what the 2D map shown in the upper right panel of Figure 3.8 indicates. Note here that no use has been made of the fact that the rotation kernels are concentrated in amplitude in the outer layers; the computations took into account the full kernel distributions, from the center to the surface. The very small amplitudes of the rotation kernels in the core explain, a posteriori, why the central rotation period is much less constrained than the superficial rotation period is in that test. Nevertheless, the results are consistent with the original hypothesis of rigid rotation.

Test #2 uses a fixed step rotation law, i.e., one supposes that the star is divided into two zones, an inner one assumed to rotate rigidly with a period $P_{\rm i}$, and an outer one assumed to rotate rigidly and independently with a period $P_{\rm o}$. The location of the transition between the two zones must be chosen at some suitable fixed depth. A sensible choice is given by the location of the vertical dotted line in the lower plot of Figure 3.7 (left panel), which divides the integral of the weighted sum of kernels into two equal parts. In this way, the information that the overall kernel distribution is concentrated in the outer region of the star is built in Test #2. The 2D merit function S^2 must now be optimized as a function of $P_{\rm i}$ and $P_{\rm o}$. Hence, *if GD 165 rotates as a rigid body, the merit function must show a minimum when* $P_{\rm i} = P_{\rm o} = P_{\rm rot}$. The lower left panel of Figure 3.8 illustrates superbly that the hypothesis of solid-body rotation is verified (in the region where the kernels have sensible amplitudes).

Finally, Test #3 is designed after a variable step rotation law, i.e, one supposes again that the star is divided into two zones, an inner one assumed to rotate rigidly with a period $P_{\rm i}$ that may be varied, and an outer one assumed to rotate rigidly with the fixed uniform period $P_{\rm rot}$, but, this time, the location of the transition between the two zones is allowed to freely vary from the center to the surface on a normalized radius scale, r/R. The 2D merit function S^2 must now be optimized as a function of $P_{\rm i}$ and r/R. Hence, *if GD 165 rotates as a rigid body, the merit function must show a minimum when* $P_{\rm i} = P_{\rm rot}$, *irrespective of the depth* r/R. This is exactly what the lower right panel of Figure 3.8 illustrates, at least down to depths beyond which the method loses its sensitivity due to the fact that the amplitudes

of the rotation kernels plunge to very small values (below the outermost ∼20% of the radius in the present case). Test #3 is probably the most useful one in terms of presentation, since it indicates explicitly and visually the region over which the hypothesis of rigid rotation is effectively tested.

In the case of Ross 548, we dispose only of two secure triplets ($N_{\rm obs} = 4$), the minimum required for testing for rigid rotation. Following an approach similar to that used for GD 165, we find the results summarized in Figure 3.9. Thus, under the assumption that Ross 548 spins slowly and rigidly, the available rotational data is best explained if the uniform rotation period takes the value $P_{\rm rot} = 37.836 \pm 1.991$ h. Quite noticeably in the upper right panel of Figure 3.9, we find that Test #1 fails, in the sense that the central rotation period is left unconstrained. In retrospect, this is not at all surprising given the concentration of kernel amplitude in the outermost 5% of the radius as already observed in the right panel of Figure 3.7 above. On the other hand, the results of Test #2 and Test #3 are perfectly consistent with the proposition of solid body rotation over that outermost region in Ross 548. Again, it is unfortunate that the three modes detected in that star which extend into the deep core (those with periods of 318, 333, and 218 s), have amplitudes too small to reveal their multiplet structure. Those hold the potential for probing the rotation rate in very deep layers in Ross 548.

The final "product" of our formal approach designed to exploit quantitatively rotational splitting data is presented in Figure 3.10, which compares the observed (in red) and calculated (in blue) rotational splittings in GD 165 (left panel) and in Ross 548 (right panel). The calculated values are based on the optimal seismic model retained for each star, in conjunction with the assumption of slow, rigid rotation with a period of 57.294 ± 0.338 h for GD 165, and 37.836 ± 1.991 h for Ross 548. The uncertainties on the calculated values of the frequency of the components are based on the uncertainty of 0.338 h (1.991 h) on the rotation period, while the central component (not affected by rotation in the context of our approach) is assumed to be known to perfect accuracy. The width of each of the blue boxes corresponds to the uncertainty on the calculated frequency of the multiplet components, expressed in units of microhertz. In comparison, the uncertainties on each of the detected (red) frequency

components are the actual measured values coming out of the analysis presented in Paper I.

Not all of the multiplet components have been detected owing to the finite sensitivity of the available observations. This is a rather common situation encountered in pulsating white dwarfs and reflects the fact that the amplitudes of the components vary significantly from mode to mode. There are five multiplets of interest in GD 165 (3 dipole and 2 quadrupole modes). A total of seven individual spacings has been found in the available data. In comparison, two triplet structures (both of which being dipole modes) have been exploited for Ross 548. It is striking that the two dominant periodicities in both stars (120 and 192 s in GD 165; 213 and 274 s in Ross 548) have opposite behavior in the sense that the ($l = 1$, $k = -1$) multiplet shows smaller frequency spacings than the ($l = 1$, $k = -2$) multiplet for GD 165, while the opposite is true for Ross 548. As discussed above, this underlines the strong potential of frequency splitting for testing the mode identification. Figure 3.10 argues strongly in favor of the proposition that slow, solid body rotation is indeed at work in both stars, at least in the regions probed by the rotation kernels.

3.4.5 Statistical Analysis and Inferred Properties

An essential component of our approach to quantitative seismology is the requirement that the neighborhood of an optimal model in parameter space be throroughly explored in order to assess the statistical significance of the solution. That information is contained in the shape of the merit function S^2 in parameter space.[7] We thus seek to statistically estimate the value of each parameter of interest as well as its uncertainty, given a best-fit seismic model. This is best done using a new procedure introduced in Van Grootel et al. (2013a) where details can be found. In a nutshell, however, we calculate the likelihood function in 5D parameter space (in the present case),

$$\mathcal{L}(a_1, a_2, a_3, a_4, a_5) \propto e^{-\frac{1}{2}S^2} \ , \tag{3.3}$$

from the merit function, $S^2(a_1, a_2, a_3, a_4, a_5)$, which has been sampled by the optimization code during the search for the best-fit models, along with additional grid calculations covering the regions of interest in parameter space. For each parameter of interest, say a_1, this function is

[7] We refer here to the merit function defined by equation (1).

integrated over the full parameter range covered by the other free parameters, thus defining a density of probability function for the chosen parameter,

$$\mathcal{P}(a_1)\mathrm{d}a_1 \propto \mathrm{d}a_1 \int \mathcal{L}(a_1, a_2, a_3, a_4, a_5)\mathrm{d}a_2\mathrm{d}a_3\mathrm{d}a_4\mathrm{d}a_5 \ . \tag{3.4}$$

This density of probability function is then normalized assuming that the probability that the value of a_1 is in the range specified for the search of a solution is equal to 1. In other words, the normalization factor is such that,

$$\int \mathcal{P}(a_1)\mathrm{d}a_1 = 1 \ , \tag{3.5}$$

over the allowed parameter range. This method permits the construction of histograms for the probability distribution of each primary model parameter. Secondary model parameters, such as the total mass M_*, the radius R_*, the luminosity L_*, and others, can also be evaluated in a similar way. For instance, let b_1 be one of these secondary parameters. The density probability function is then,

$$\mathcal{P}(b_1)\mathrm{d}b_1 \propto \mathrm{d}b_1 \int\limits_{b\in[b_1, b_1+\mathrm{d}b_1]} \mathcal{L}(a_1, a_2, a_3, a_4, a_5; b)\mathrm{d}a_1\mathrm{d}a_2\mathrm{d}a_3\mathrm{d}a_4\mathrm{d}a_5 \ , \tag{3.6}$$

where the integration is done with the additional constraint that for a given set of primary parameters, the corresponding value b of the secondary parameter considered must be within b_1 and $b_1 + \mathrm{d}b_1$. Again, the density of probability for the secondary parameters is normalized such that,

$$\int \mathcal{P}(b_1)\mathrm{d}b_1 = 1 \ . \tag{3.7}$$

The series of Figures 3.11a through 3.11f summarizes the results of the statistical analysis carried out in parameter space about our optimal seismic model for GD 165. The derived density of probability for each retained model parameter is illustrated as an histogram. The red-hatched region between the two red vertical solid lines defines the statistically acceptable range containing 68.3% of the distribution. For each parameter, it can be verified that the

optimal model value, indicated in a panel by the blue vertical dashed line, belongs to that population as it ideally should. Since all values of a parameter within the $\pm 1\sigma$ interval are equally acceptable, we adopt for simplicity, and as our best final estimates of that quantity, the central value of that interval as indicated in red in each plot.

In the case of GD 165, four of the five primary parameters are illustrated, (1) $\log g$ (Fig. 3.11a), (2) $T_{\rm eff}$ (Fig. 3.11b), (3) $\log M({\rm H})/M_*$ (Fig. 3.11c), and (4) $\log M({\rm He})/M_*$ (Fig. 3.11d). Since we found no sensitivity of the pulsation periods on the core composition for our seismic model of GD 165, we did not compute the probability distribution for $X({\rm O})$, the fifth primary quantity. The latter would have been quite flat and uninteresting. We also note that the effective temperature of GD 165 is relatively less constrained than the other parameters as can be appreciated from Figure 3.11b in comparison to the others. This was noticed above and should come as no surprise. Indeed, looking back at Figure 3.2 (left panel), one observes an elongated "valley" along the $T_{\rm eff}$ axis in that S^2 map, so, clearly, the available seismic data (the six periods of Table 3.2) do not constrain that quantity well. To depict the behavior of some secondary parameters in this approach, we also provide in Figures 3.11e and 3.11f the histograms related to the total mass and total radius, respectively.

The results of our statistical analysis for Ross 548 are presented in a series of similar figures (Figs. 3.12a through 3.12f), to which we have added Figure 3.12g pertaining to the probability distribution associated with the fifth parameter, $X({\rm O})$. As indicated above, contrary to the case of GD 165, the pulsation periods in our seismic model for Ross 548 are sensitive to a variation of the core composition. The statistical exploration of parameter space in that direction leads to our best estimates of the composition of the C-O core (supposed homogeneous) for that star, i.e., $X({\rm O}) = 0.70 \pm 0.06$.

TABLE 3.6 – Inferred properties of GD 165 on the basis of asteroseismology.

Quantity	Estimated value
$\log g$ (cm s^{-2})	8.052±0.035
$T_{\rm eff}$ (K)	12130±450
$\log M(\mathrm{H})/M_*$	−4.23±0.15
$\log M(\mathrm{He})/M_*$	−1.70±0.13
$X(\mathrm{O})$	0.0 (outer core)
$M_*/\,M_\odot$	0.64±0.02
$R_*/R_\odot$	0.0124±0.0003
$L_*/L_\odot$	0.0030±0.0006
$P_{\rm rot}$ (h)	57.29±0.34
$V_{\rm eq}$ (km s^{-1})	0.263±0.008
J (kg m^2 s^{-1})[a]	4.88±0.03×10^{38}
$J/J_\odot$	1/393
M_V[b]	11.73±0.12
d (pc)	33.0±2.0
$\dot{P}_{120}$ (s/s)	6.98−7.96×10^{-16}
$\dot{P}_{192}$ (s/s)	2.47−2.71×10^{-15}

[a] Assuming solid body rotation throughout the star.

[b] Based on a model atmosphere with the seismic values of $\log g$, $T_{\rm eff}$, and M_*.

TABLE 3.7 – Inferred properties of Ross 548 on the basis of asteroseismology.

Quantity	Estimated value
$\log g$ (cm s^{-2})	8.108±0.025
$T_{\rm eff}$ (K)	12281±125
$\log M({\rm H})/M_*$	−7.45±0.12
$\log M({\rm He})/M_*$	−2.92±0.10
$X({\rm O})$	0.70±0.06
$M_*/\,M_\odot$	0.65±0.02
$R_*/R_\odot$	0.0118±0.0002
$L_*/L_\odot$	0.0029±0.0002
$P_{\rm rot}$ (h)	37.84±1.99
$V_{\rm eq}$ (km s^{-1})	0.379±0.020
J (kg m^2 s^{-1})[a]	7.18±0.38×10^{38}
$J/J_\odot$	1/267
M_V[b]	11.78±0.06
d (pc)	30.0±0.9
$\dot{P}_{213}$ (s/s)	2.87−2.91×10^{-15}
$\dot{P}_{274}$ (s/s)	1.41−1.51×10^{-15}

[a] Assuming solid body rotation throughout the star.

[b] Based on a model atmosphere with the seismic values of $\log g$, $T_{\rm eff}$, and M_*.

We have assembled in Table 3.6 (Table 3.7) the values of the parameters and properties that define GD 165 (Ross 548) as inferred from our asteroseismological exercises. The first

five entries correspond to the values of our standard primary parameters as derived from the statistical approach described just above. To those, we added the related values of three interesting secondary parameters, i.e, the total mass, the radius, and the luminosity, all in solar units. Using next the results of our multiplet analysis, we also listed the derived uniform rotation period $P_{\rm rot}$, which, combined to the radius R_*, leads to an estimate of the equatorial velocity $V_{\rm eq}$.

Another interesting quantity may be derived if we make the important assumption that both stars rotate rigidly *throughout* their interior. We recall that this is an inference that could not be made, given that the available multiplet data limited the coverage of the internal rotation profile to the outer 20% of the radius of GD 165, and only to the outer 5% in the case of Ross 548. Nevertheless, *if* the hypothesis of rigid rotation is adopted, an estimate of the total angular momentum J of each pulsator is obtained by combining the value of the uniform period $P_{\rm rot}$ with a numerical integration over the structure of the seismic model. This leads to the value of J reported in each table, as well as the particularly interesting ratio, $J/J_\odot$, i.e., the value of the global angular momentum with respect to that of the Sun. These very small values of $J/J_\odot$ suggest very strongly that these isolated ZZ Ceti stars have very likely shed essentially all of their initial angular momentum. This is in line with what has been found previously by Charpinet et al. (2009) and Fontaine et al. (2013) in the very hot pulsating white dwarfs of the GW Vir type.

The DA model atmospheres of Pierre Bergeron (private communication) may also be used to estimate the value of the absolute magnitude in the V band, given the seismic values of the surface gravity, the effective temperature, and the mass (or radius). We thus find $M_V = 11.73 \pm 0.12$ for GD 165 and $M_V = 11.78 \pm 0.06$ for Ross 548. The larger uncertainty in M_V for the former object is due mostly to the less accurate value of the effective temperature derived in that case. The combination of M_V with the observed visual magnitude V ($V = 14.32 \pm 0.01$ for GD 165; $V = 14.16 \pm 0.01$ for Ross 548) then leads to the "seismic" distance d listed as an additional entry in both Tables 3.6 and 3.7. No reddening was considered in the derivation of the distance, an approximation that is fully justified over the very short distances involved.

Finally, our seismic models may also be used to provide estimates of rates of period change

of various pulsation modes due to cooling, which, at least in principle, are observables. To do this requires the computations of suitable evolutionary sequences, and we describe such efforts in the next Subsection. At this point, we simply report in the last two lines of Table 3.6 (Table 3.7) our best estimates of the rates of period change for the two largest-amplitude modes present in the light curve of GD 165 (Ross 548), i.e., the 120 and 192 s (213 and 274 s) main periodicities. The rates should be easier to determine for the larger amplitude pulsations due to their higher S/N. The range of values reported in the tables simply refers to the variation associated with a change of core composition, from pure C to pure O, and not to a detailed error analysis involving the uncertainties of all the other parameters that may have an impact on these values. For our present needs, the tabulated estimates are amply sufficient. We recall that the rate of period change is mode-specific, i.e., it bears the signature of the k and l indices (and see Section 8.3 of Fontaine & Brassard 2008 for more details). In this context, it is interesting to point out here that $\dot{P}_{120} < \dot{P}_{192}$ in GD 165, while $\dot{P}_{213} > \dot{P}_{274}$ in Ross 548, as an illustration of the effects of different chemical layering and trapping/confinement properties in the two seismic models.

The results reported in Tables 3.6 and 3.7 represent the main outcome of this paper. In that context, it is quite fortunate that the values of some of the listed parameters have been estimated by means totally independent of asteroseismology, as we can use them to test further the credibility and validity of our seismic models. In particular, independent estimates of the surface gravity and of the effective temperature have been derived from the spectroscopic study reported in Paper I. Likewise, estimates of the absolute visual magnitude and of the distance for both stars have been presented in the very detailed spectroscopic analysis of DA white dwarfs presented by Gianninas et al. (2011). Also, a very reliable estimate of the distance to GD 165 through a parallax measurement has been reported by Kirkpatrick (2005) in his review of the properties of brown dwarfs (including GD 165B orbiting around the pulsating ZZ Ceti GD 165A). A much less reliable estimate of the distance to Ross 548, based on an old ground-based parallax measurement, is also available from Bergeron et al. (1995). And last, but not least, Mukadam et al. (2013) have summarized some 41 years of efforts to derive a value of the rate of period change of the dominant 213 s pulsation mode (more precisely, of

the largest-amplitude component in that triplet) in the light curve of Ross 548. They found $\dot{P}_{213} = 3.3 \pm 1.1 \times 10^{-15}$ s/s through the $O-C$ technique.

TABLE 3.8 – Comparison with parameters obtained independently.

Star	Quantity	Seismology	Spectroscopy	Parallax	$O-C$
GD 165	$\log g$ (cm s^{-2})	8.052±0.035	8.082±0.048[a]	...	...
	$T_{\rm eff}$ (K)	12130±450	12165±190[a]	...	...
	M_V	11.73±0.12	11.80[b]	...	...
	d (pc)	33.0±2.0	32.0[b]	31.5±2.5[c]	...
Ross 548	$\log g$ (cm s^{-2})	8.108±0.025	8.012±0.048[a]	...	...
	$T_{\rm eff}$ (K)	12281±125	12204±190[a]	...	...
	M_V	11.78±0.06	11.68[b]	...	...
	d (pc)	30.0±0.9	31.0[b]	67.1±9.0[d]	...
	$\dot{P}_{213}$ (s/s)	$2.87-2.91\times10^{-15}$	...	...	$3.3\pm1.1\times10^{-15}$[e]

[a] Paper I

[b] Gianninas et al. (2011)

[c] Kirkpatrick (2005)

[d] Bergeron et al. (1995)

[e] Mukadam et al. (2013)

We compare these estimates in Table 3.8. First, we find remarkable agreement between the seismic and spectroscopic estimates of the surface gravity and of the effective temperature. These values overlap within their 1σ uncertainties, except for the surface gravity of Ross 548 which is still only 1.3σ away from its spectroscopic counterpart. We see this as a very important and significant test of the reliability of our seismic models. Second, the spectroscopic values of the absolute magnitude and of the distance obtained by Gianninas et al. (2011) are entirely consistent with our derived seismic values, and this is true for both stars. We note also the excellent agreement between our seismic distance to GD 165 and that based on the parallax

TABLE 3.9 – Defining parameters for the evolutionary models for GD 165 and Ross 548.

Model	$M_*/\,M_\odot$	$\log M(\mathrm{H})/M_*$	$\log M(\mathrm{He})/M_*$	$X(\mathrm{O})$
GD 165	0.6315	−4.1402	−1.6368	0.0
Ross 548	0.6571	−7.5125	−2.9376	0.6732

value of Kirkpatrick (2005). In contrast, the only parallax measurement available for Ross 548 indicates a distance much larger than that obtained through the spectroscopic method (d = 31.0 pc) or the seismic method ($d = 30.0 \pm 0.09$ pc). As pointed out originally by Bergeron et al. (1995), there is very likely a problem with the old parallax value for Ross 548. The problem has also been commented on in an asteroseismological context by Bradley (1998). It is hoped that the issue will be settled with the release of appropriate data from *Gaia*. The last entry of Table 3.8 demonstrates rather nicely that our proposed mode identification and seismic model for Ross 548 passes another major test. Indeed, it shows that our computed rate of period change for the dominant 213 s mode is in perfect agreement with the observed value of Mukadam et al. (2013).

3.4.6 Evolutionary Calculations and Rates of Period Change

In Subsection 2.2 above, we discussed the need for and the use of parametrized static models for quantitative seismology. Having identified and characterized seismic models in this way for our target stars, it is essential at this stage to verify if they can be reproduced by full evolutionary calculations. In other words, are our static models artificial structures that cannot be computed from evolutionary calculations or, on the contrary, are they compatible with traditional evolutionary models? We show, in this subsection, that the latter alternative is the correct one, and that our static seismic models also pass this important additional test. We then take advantage of the evolutionary sequences computed in this context to obtain reliable estimates of the rates of period change for the two dominant modes in the light curves of both GD 165 and Ross 548, as reported above.

We used the Montréal evolutionary code to first compute a model sequence with defining parameters compatible with those inferred from our optimal seismic model of GD 165. We also computed a similar sequence for Ross 548. Those defining parameters are summarized in

Table 3.9. Hence, for full evolutionary models, the total mass M_*, the fractional mass in the H envelope $\log M(\mathrm{H})/M_*$, the fractional mass in the He mantle $\log M(\mathrm{He})/M_*$, as well as the oxygen mass fraction $X(\mathrm{O})$ in the (assumed) homogeneous core must be specified. Likewise, for the purpose of comparing with our static models, the same version of the convective efficieny (ML2/α = 1.0) was employed, and we used also the same calibration of the composition transition zone profiles as discussed above.

The sequences we computed all started as purely contracting, very hot models of the former nuclei of red giant stars. No residual thermonuclear burning was allowed, but neutrino cooling, which is significant in the hot phases of the evolution, was included. No connection was made with previous evolutionary phases. Since the time stepping is controled by an internal algorithm that checks the convergence of each model, we end up with values of the effective temperature that cannot be predicted in advance. Hence, in the case of GD 165, we ended up with three adjacent models with $T_{\rm eff}$ values of 12218.55, 12015.36, and 11823.38 K, in the vicinity of that characterizing our seismic model for that star, that is, $T_{\rm eff}$ = 12087.27 K (see Table 3.1). Note that we could have slowed down the evolutionary calculations on purpose to obtain a better resolution in effective temperature, but, in any case, this underlines the lack of flexibility that we pointed out above (Subsection 3.2.2) concerning full evolutionary calculations as opposed to static models.

We have explicitly compared the S^2 values associated with those three evolutionary models against the values obtained from dedicated static models computed with exactly the same effective temperatures and other relevant parameters. Comparing the values of the merit function indeed represent the most stringent test that we could come up with in this exercise. We find that the ratio $S^2_{\rm evol}/S^2_{\rm static}$ varies from about 1.25 to 1.75 over these three models, which is not perfect (the ideal ratio is 1), but nevertheless extremely gratifying. We also find, using parabolic interpolation in conjunction with the values of S^2 and $T_{\rm eff}$ associated with the three evolutionary models, that the minimum of the merit function occurs for $T_{\rm eff}$ = 12094.47 K, only 7.2 K away from our seismic model. Likewise, on the basis of a similar sequence for Ross 548, we isolated the three consecutive evolutionary models in the neighborhood of our seismic model in terms of effective temperature, i.e., $T_{\rm eff}$ = 12447.99, 12226.41, and 12021.01

K, compared to the seismic value of 12209.31 (Table 3.1). In that case, the ratio $S^2_{\rm evol}/S^2_{\rm static}$ varies from 1.02 to 1.49, and the minimum in S^2 is found at 12193.23 K (only 16.08 K away from the seismic value of 12209.31 K).

We thus find that our seismic models are extremely well reproduced from evolutionary calculations, but not perfectly. And there is a reason why perfection cannot be achieved here. Indeed, as we found out long ago, it is is impossible to implement in *exactly* the same way the composition transition profiles in an evolutionary and a static model. To illustrate the consequences of this technicality, as well as to impress upon the reader the notion that the resulting effects are particularly small, we provide in Figure 3.13 a comparison of the profile of the Brunt-Väisälä frequency of an evolutionary model culled from the GD 165 sequence above (the one with $T_{\rm eff}$ = 12015.36 K) with that of its static counterpart. We do point out, in this context, that the run of this quantity (as compared to others such as density, pressure, adiabatic exponents, etc.) bears the strongest signature on the g-mode period spectrum. Hence, a small difference between the two curves necessarily implies a small difference in the period spectrum. On the scale of the upper panel of Figure 3.13, the tiny differences that exist between the evolutionary and static model cannot be seen. In the zoomed-in view presented in the lower panel, however, one can notice very small differences in the upper part of the H/He transition zone (the right side of the upper bump) and even smaller differences again in the upper part of the He/C transition zone (the right side of the lower bump). As pointed out just above, a technical reason is the culprit for this state of affair. In principle, these tiny differences could be compensated, at least partly, by moving so slightly around in parameter space. We submit that, in fact, such related evolutionary models could be found with values of the merit function getting very close to our above value of $S^2 = 1.918$ for GD 165. The price to pay, however, would be to compute a large (and still undefined) number of full sequences, a very time consuming and totally impractical way to prove our point.

We end this Subsection by mentioning that we took advantage of the two evolutionary sequences described here, as well as supplementary ones (a pure O core sequence for GD 165, a pure C core sequence and another one with a pure O core for Ross 548) to derive estimates

of the rates of period change associated with the two-largest amplitude modes of both stars. These values are reported at the bottom of Tables 3.6 and 3.7. They were obtained by simply taking the ratio of the period difference over the age difference for two adjacent models that would sandwich the seismic model in effective temperature. For ZZ Ceti pulsators, cooling leads to a systematic (and mode-specific) increase of the period of a g-mode, so the expected values of the rates of period change are all positive.

3.4.7 Nonadiabatic Considerations

It is instructive to analyze each of the optimal model we retained for GD 165 and Ross 548 with a nonadiabatic pulsation code to verify if the modes identified with the observed ones are indeed predicted to be unstable. This provides a last consistency check and, if successful, adds further credibility to these seismic models. As stated previously, the periods of the low-order modes found in GD 165 and Ross 548 are quite insensitive to the choice of the convective efficiency that has been made in the model-building phase. However, the question of the stability of the modes *does* depend sensitively on the choice of the assumed convective efficiency as has been known for a long time (see, e.g., Tassoul et al. 1990). The models that were built in the present search exercise used the ML2/α=1.0 version of convection which, not by accident, is the version that was most recently "calibrated" by matching the theoretical with the empirical blue edge of the ZZ Ceti instability strip (Van Grootel et al. 2013). This calibration is based on the use of the Liège nonadiabatic code MAD, which takes properly into account the perturbations of the convective flux, unlike all other nonadiabatic codes employed in a white dwarf context (see Van Grootel et al. 2012 for details).

Table 3.10 (GD 165) and Table 3.11 (Ross 548) provide some of the results obtained with MAD in the present context. Along with the mode identification provided by the set of indices (l,k), a mode is characterized in these tables by the value of its period P, the values of the real and imaginary parts of the complex frequency of the mode σ_R ($= 2\pi/P$) and σ_I, as well as the e-folding timescale τ_e ($= 1/\sigma_I$). An excited (stable) mode has a negative (positive) value of σ_I. Hence, the tables immediately reveal that the modes identified with the observed ones in both GD 165 and Ross 548 are indeed excited in their respective optimal models. In fact,

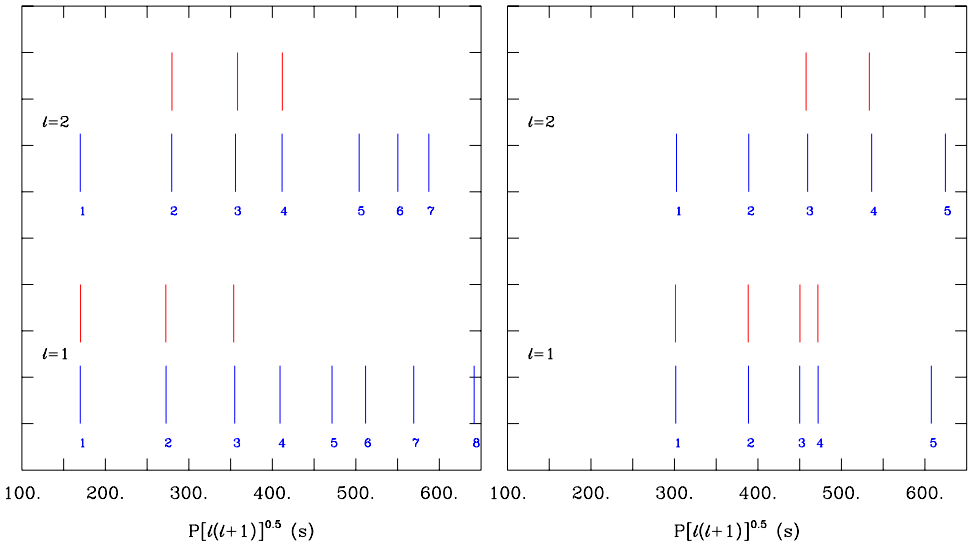

FIGURE 3.5 – *Left Panel:* Comparison of the six observed periods in GD 165 (red) with the theoretical g-mode spectrum of the optimal model (blue). The dipole (quadrupole) modes are illustrated in the lower (upper) half of the plot and the radial order of each mode is indicated. The "reduced" period is used as the abcissa in order to have comparable values for both dipole and quadrupole modes. *Right Panel:* Similar to the left panel, but for Ross 548.

TABLE 3.10 – Nonadiabatic properties of the optimal model for GD 165

l	k	P (s)	σ_R (rad/s)	σ_I (rad/s)	τ_e (yr)
1	−1	120.127	5.23×10^{-2}	-1.18×10^{-13}	2.69×10^{5}
1	−2	192.763	3.26×10^{-2}	-1.64×10^{-13}	1.93×10^{5}
1	−3	251.006	2.50×10^{-2}	-5.61×10^{-11}	5.65×10^{2}
1	−4	289.345	2.17×10^{-2}	-2.05×10^{-10}	1.55×10^{2}
2	−1	69.397	9.05×10^{-2}	-1.21×10^{-13}	2.62×10^{5}
2	−2	114.045	5.51×10^{-2}	-2.48×10^{-13}	1.28×10^{5}
2	−3	145.279	4.32×10^{-2}	-6.66×10^{-11}	4.76×10^{2}
2	−4	168.013	3.74×10^{-2}	-2.38×10^{-10}	1.33×10^{2}
2	−5	205.813	3.05×10^{-2}	-2.16×10^{-9}	1.47×10^{1}
2	−6	224.724	2.80×10^{-2}	-1.85×10^{-9}	1.71×10^{1}
2	−7	239.775	2.62×10^{-2}	-1.08×10^{-8}	2.93×10^{0}
2	−8	269.072	2.34×10^{-2}	-3.02×10^{-8}	1.05×10^{0}
2	−9	289.924	2.17×10^{-2}	-7.15×10^{-8}	4.43×10^{-1}

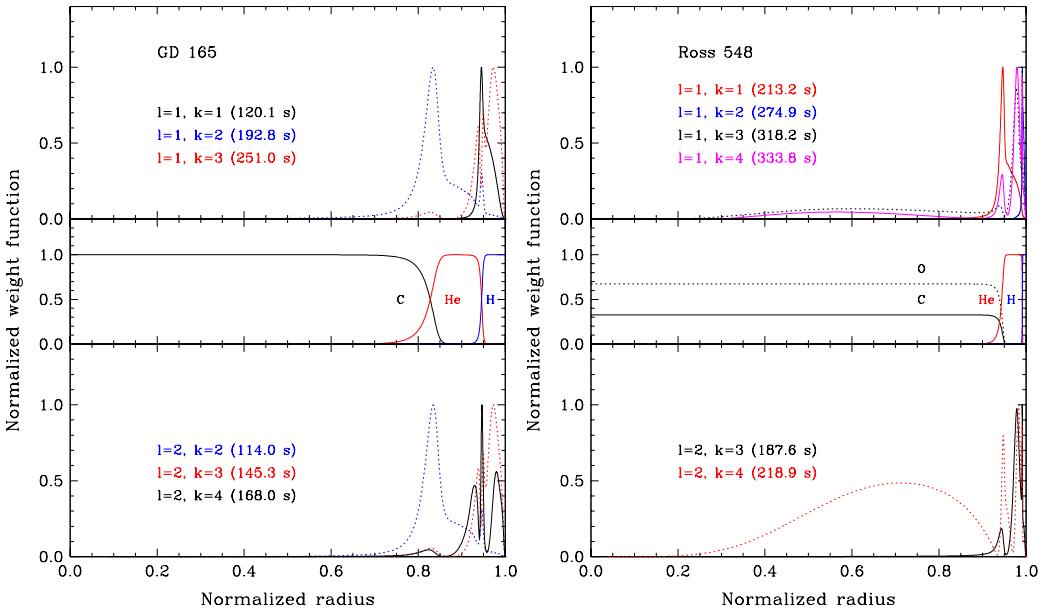

FIGURE 3.6 – *Left Panel:* Normalized weight function versus normalized radius for the six modes of the retained seismic model for GD 165 identified with the six pulsations detected in that star. Each individual weight function is normalized to a maximum value of 1.0. The weight function of a mode indicates the layers contributing most to the integral giving the frequency of the mode according to a well-known variational principle in linear pulsation theory (see, e.g., Unno et al. 1989). The middle subpanel illustrates the chemical stratification of the model. All of the weight functions have negligible amplitudes below a normalized radius of 0.6 (containing some 74% of the total mass of the star) and, consequently, cannot probe the chemical composition in that region. *Right Panel:* Similar to the left panel, but for the retained best-fit seismic model for Ross 548. In contrast to the case of GD 165, three of the six identified modes have nonneglible values of their weight functions below a normalized radius of 0.6 (containing some 72% of the total mass of the star in this case). The periods of these modes are therefore sensitive to the chemical composition in the inner core.

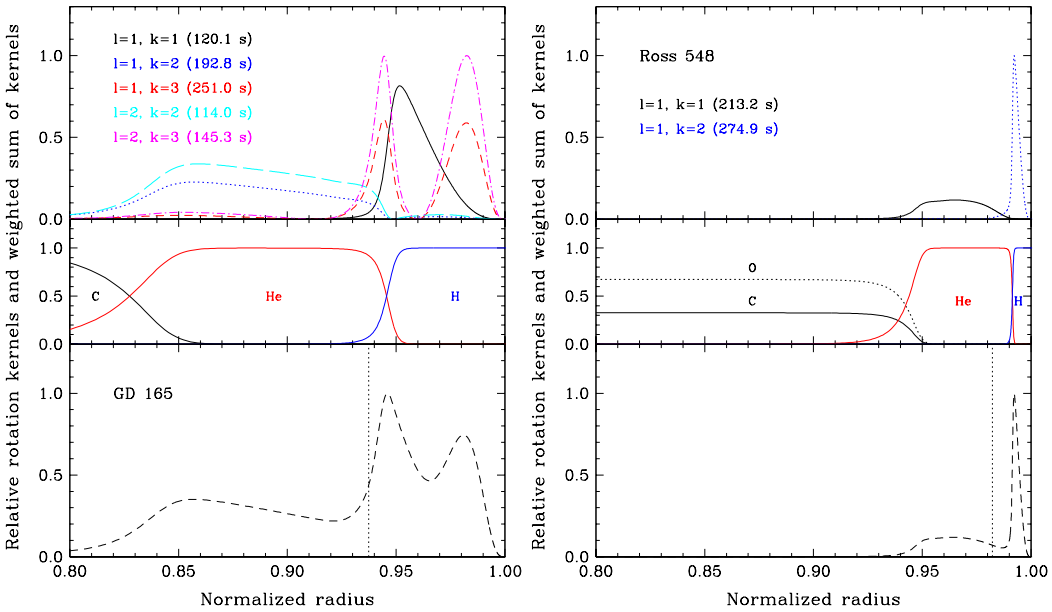

FIGURE 3.7 – *Left Panel:* Relative rotation kernels versus normalized radius for the five modes of the optimal model of GD 165 identified with the five multiplet structures observed in the light curve of that star (upper subpanel). Chemical stratification of the model (middle subpanel). Weighted sum of the kernels versus normalized radius (lower subpanel). The region over which the rotation profile can be probed corresponds to those layers where the weighted sum has a nonnegligible amplitude, i.e., approximately over the outer 20% of the radius of the model in the present case. The vertical dotted line in the lower subpanel defines the layer where half of the running integral of the weighted sum is below, and the other half above. *Right Panel:* Similar to the left panel, but pertaining to the retained optimal seismic model of Ross 548 and the two triplet structures observed in the light curve of that star. In this other case, the rotation profile can be probed over only the outermost ∼5% of the radius.

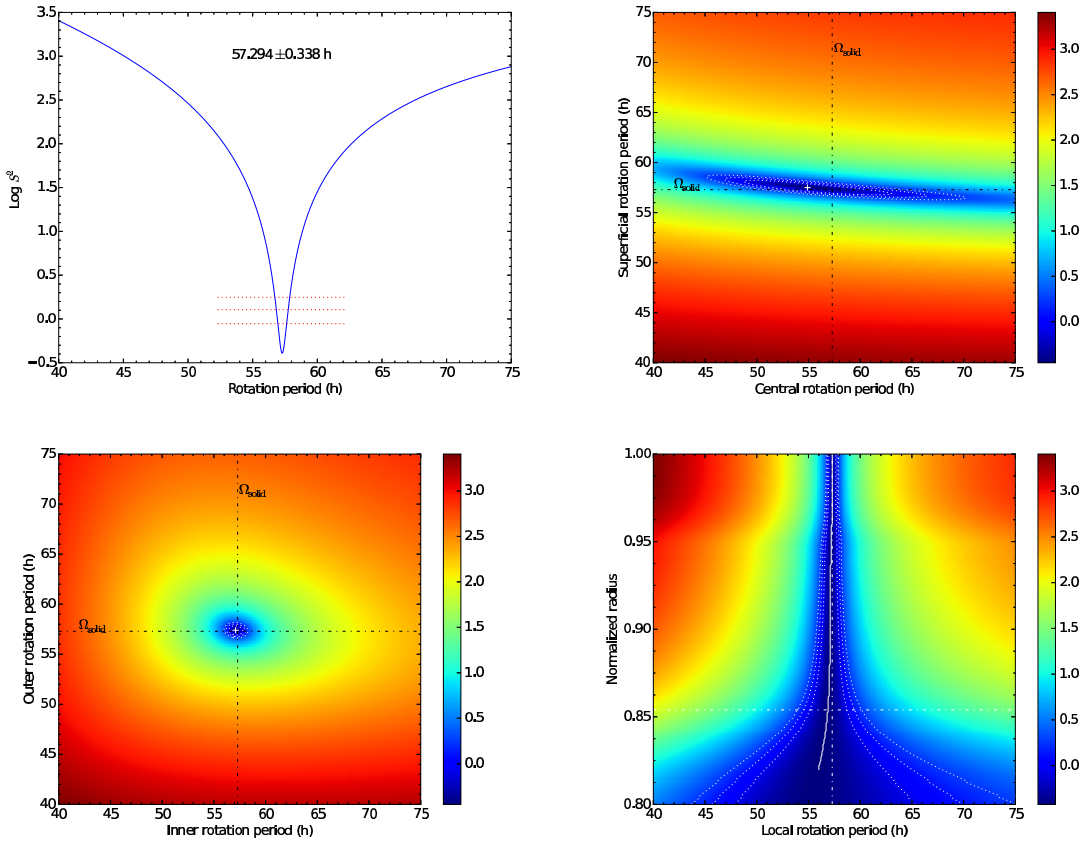

FIGURE 3.8 – *Upper Left Panel:* Result of the optimization procedure under the hypothesis that GD 165 rotates slowly and rigidly. This shows the behavior of the merit function S^2 in terms of the assumed rotation period. The merit function exhibits a very well defined minimum, corresponding to a rotation period of 57.294 ± 0.338 h. The dotted horizontal lines correspond, from bottom to top, to the 1σ, 2σ, and 3σ limits. *Upper Right Panel:* Result of Test #1 for solid body rotation using a linear rotation law. This is a contour plot of the 2D merit function associated with that particular test. Note the logarithmic scale (base 10) used for that function, indicating a relatively well defined optimal solution. The latter is depicted by a small white cross in that plane, well within the 1σ, 2σ, and 3σ confidence levels illutrated by the dotted white curves. *Lower Left Panel:* Result of Test #2 for solid body rotation using a fixed step rotation law. This is similar in format to the panel associated with Test #1, but note the more localized and better defined minimum obtained with that different approach. This provides a more stringent test of the hypothesis of rigid rotation. *Lower Right Panel:* Result of Test #3 for solid body rotation using a variable step rotation law. This is a contour map indicating the behavior of the 2D merit function S^2 in terms of depth (expressed in fractional radius) and in terms of the rotation period of the inner region of our two-zone approach. Again, the scale used for S^2 indicates a very well defined solution. That solution is illustrated by the nearly vertical white curve and the dotted white curves depicting its associated 1σ, 2σ, and 3σ contours. The fact that these contours diverge out at the larger depths considered here indicates that the rotationally-split gravity modes available in the present case lose their capacity at measuring the local rotation rate there. The horizontal dot-dashed line indicates the layer above which there is 1% of the mass of the star.

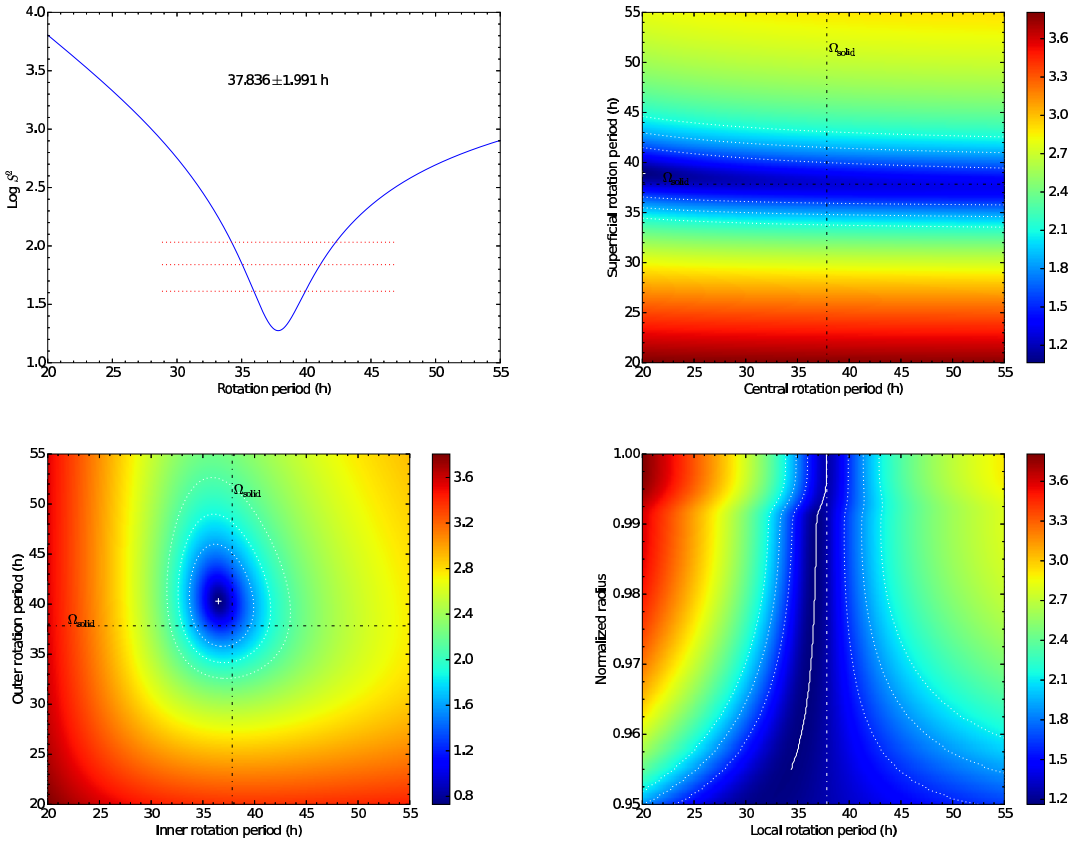

FIGURE 3.9 – Similar to Fig. 8, but for Ross 548 and based on two multiplet structures only compared to five in the case of GD 165. With an estimate of the rotation period of 37.836 ± 1.991 h, the hypothesis of slow, rigid rotation is generally verified, although the test with the linear rotation law (upper right panel) is inconclusive. In addition, the available rotation data can be used to sample only the outer ∼5% of the radius.

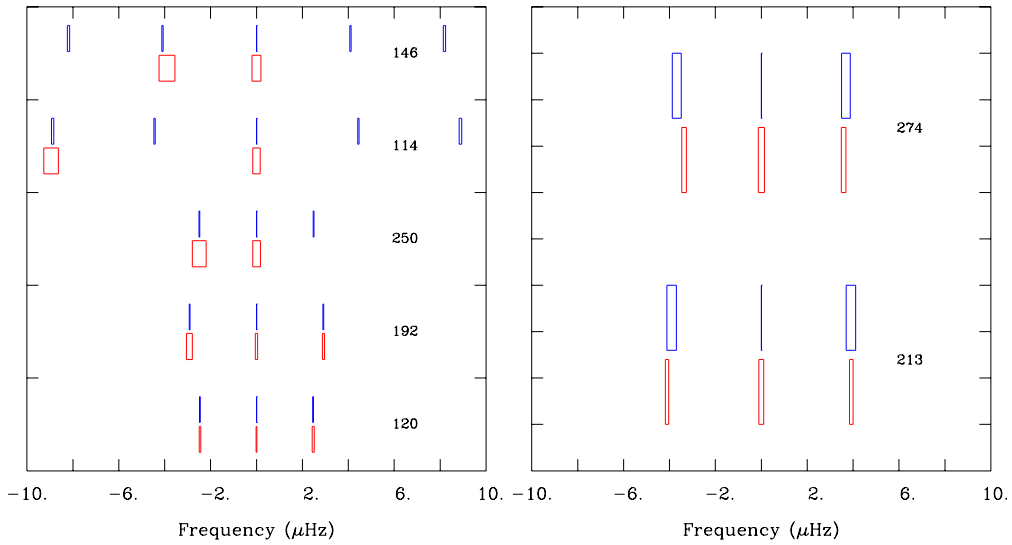

FIGURE 3.10 – *Left Panel:* Observed and calculated rotational splittings in GD 165. This shows the comparison of the observed multiplet structures (in red) with those predicted (in blue) on the basis of the optimal seismic model assuming solid body rotation with a period of 57.294 ± 0.338 h. There are five multiplets of interest in GD 165 (3 dipole and 2 quadrupole modes). *Right Panel:* Similar to the left panel, but pertaining to the two triplet structures (both of which being dipole modes) detected in Ross 548. The calculated rotational splittings are based on the assumption of slow, rigid rotation with a period of 37.836 ± 1.991 h.

TABLE 3.11 – Nonadiabatic properties of the optimal model for Ross 548

l	k	P (s)	σ_R (rad/s)	σ_I (rad/s)	τ_e (yr)
1	−1	213.191	2.95×10^{-2}	-1.81×10^{-11}	1.75×10^{3}
1	−2	274.909	2.29×10^{-2}	-3.52×10^{-9}	9.00×10^{0}
1	−3	318.155	1.97×10^{-2}	-3.53×10^{-9}	8.98×10^{0}
1	−4	333.773	1.88×10^{-2}	-9.91×10^{-10}	3.20×10^{1}
1	−5	429.679	1.46×10^{-2}	-3.09×10^{-10}	1.03×10^{2}
2	−1	123.515	5.09×10^{-2}	-2.04×10^{-12}	1.55×10^{4}
2	−2	158.753	3.96×10^{-2}	-4.07×10^{-9}	7.79×10^{0}
2	−3	187.647	3.35×10^{-2}	-1.07×10^{-9}	2.96×10^{1}
2	−4	218.936	2.87×10^{-2}	-2.45×10^{-10}	1.29×10^{2}
2	−5	255.011	2.46×10^{-2}	-4.29×10^{-9}	7.39×10^{1}
2	−6	285.308	2.20×10^{-2}	-2.36×10^{-8}	1.34×10^{0}
2	−7	306.150	2.05×10^{-2}	-2.49×10^{-7}	1.27×10^{-1}
2	−8	329.469	1.91×10^{-2}	-7.85×10^{-7}	4.03×10^{-2}
2	−9	358.466	1.75×10^{-2}	-2.77×10^{-7}	1.14×10^{-1}

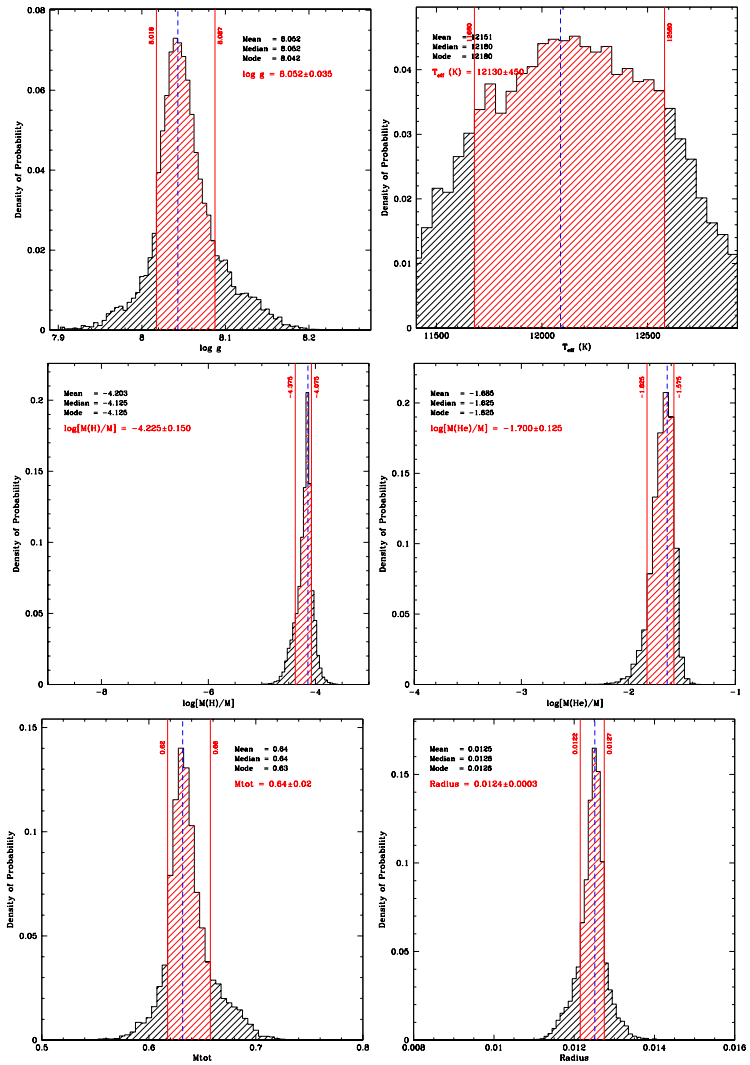

FIGURE 3.11 – Results of the statistical analysis carried out in parameter space about the optimal seismic model for GD 165. Each histogram shows the derived probability density function for a given model parameter. The red-hatched region between the two vertical solid red lines defines the $\pm 1\sigma$ range, containing 68.3% of the distribution. The blue vertical dashed line indicates the value of the parameter of the optimal model solution. The mean, median, and mode values are also indicated. The final adopted estimate of the parameter of interest is listed in red, and corresponds to the central value of the $\pm 1\sigma$ interval. The various panels correspond to the following model parameters, (11a) surface gravity, (11b) effective temperature, (11c) mass fraction in the hydrogen envelope, (11d) mass fraction in the helium mantle, (11e) total mass, and (11f) total radius.

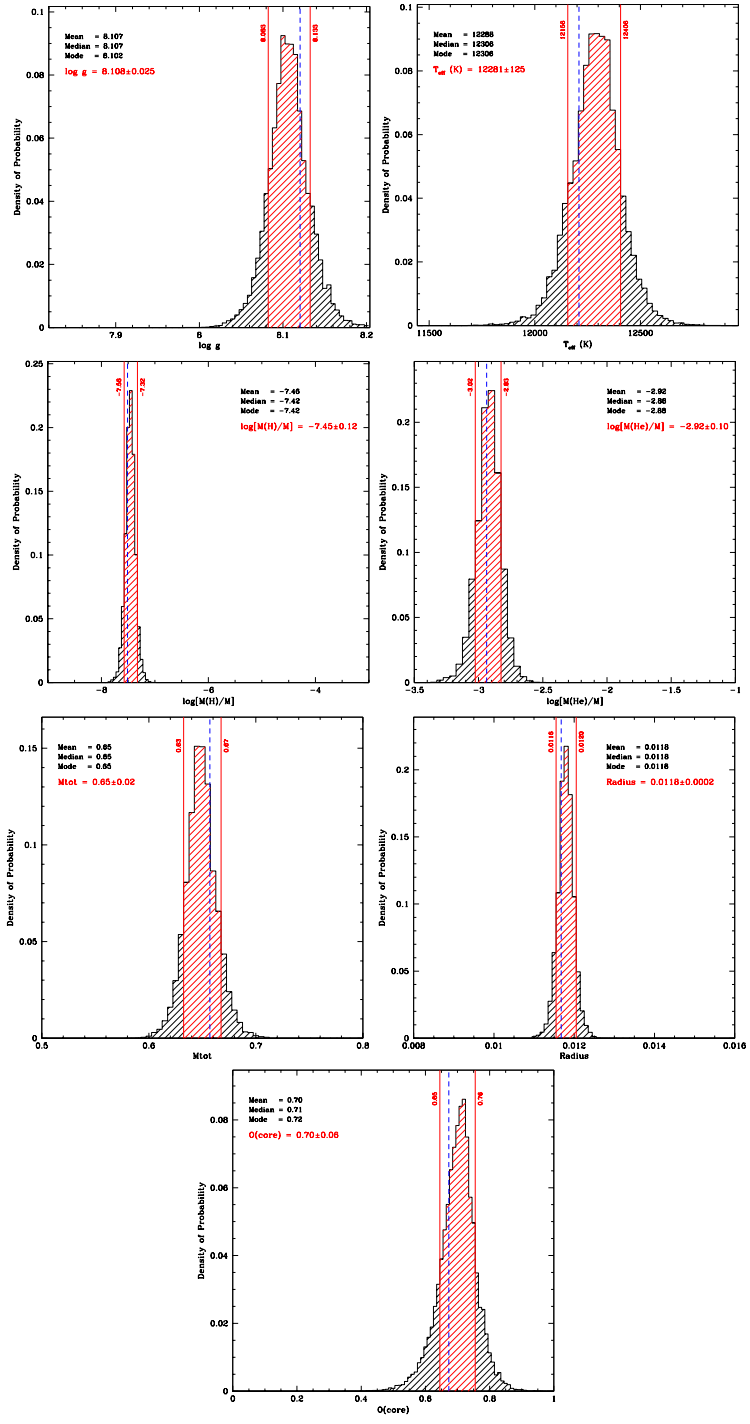

FIGURE 3.12 – Similar to Fig. 3.11, but for the optimal seismic model for Ross 548, with the addition of panel (3.12g) referring to the oxygen mass fraction in the core.

all dipole g-modes with radial order between $k = 1$ and $k = 13$, and all quadrupole modes with radial order between $k = 1$ and $k = 17$ are predicted to be driven in the optimal model of GD 165, as well as many low-order p-modes, including radial modes. A similar situation is encountered for Ross 548 which indicates that all dipole modes with radial order between $k = 1$ and $k = 9$, and all quadrupole modes with radial order between $k = 1$ and $k = 12$ are predicted to be driven. This is a fairly common situation in nonadiabatic linear physics which tends to predict wider bands of excited periods than those observed. But the important test here is that the modes in the optimal models assigned to the observed modes in GD 165 and Ross 548 are indeed predicted to be excited. Doubts could justifiably have been cast on the credibility of the seismic models if they had failed that test.

The tables also indicate that, for all modes considered, $|\sigma_R| \gg |\sigma_I|$, which is consistent with an earlier remark made above concerning the justification for using the adiabatic approximation to compute sufficiently accurate periods. Indeed, the imaginary part is so small compared to the real part that nonadiabatic effects have negligible impact on the values of the oscillation period in the stars of interest. In addition, the e-folding timescales listed in Tables 3.10 and 3.11 are all much smaller than the evolutionary timescales,[8] which is a sine qua non condition for mode observability since the predicted unstable modes must have enough time to develop a detectable amplitude. This is clearly the case here. For instance, at its current cooling rate according to our evolutionary calculations, GD 165 needs to cool only by a further 2.9 K in order to cover 2.69×10^5 yr, the e-folding timescale associated with the dominant 120 s mode in that star. Likewise, a tiny drop of 0.016 K in the effective temperature of Ross 548 is sufficient to cover 1.75×10^3 yr, the e-folding time associated with the dominant 213 s mode in that other star.

Figure 3.14 summarizes the situation by illustrating the bands of detected periods in relation to the bands of predicted unstable modes. It should be pointed out that linear nonadiabatic pulsation theory is unable to predict which of the unstable modes will grow to observable amplitudes. This is rather in the realm of nonlinear theory, which is still being developed. Hence, it is not possible to offer an explanation for the fact that there seems to be

[8] It takes $1 - 3 \times 10^8$ yr for a typical H-atmosphere white dwarf to cross the ZZ Ceti instability strip.

a shift in radial order from the dipole to the quadrupole modes that are effectively detected in GD 165 and Ross 548. In particular, the lowest-order quadrupole modes (those with $k = 1$ in GD 165 and $k = 1$ and 2 in Ross 548) are not detected, and no credible explanation can be offered other than invoking unknown nonlinear processes. On the other hand, it is possible to narrow down the widths of the bands of predicted unstable periods by decreasing the convective efficiency used in the nonadiabatic modeling, but this needs to be justified in view of the results of Van Grootel et al. (2013) showing that the blue edge of the ZZ Ceti instability strip is very well explained using a convective efficiency defined by ML2/$\alpha = 1.0$. Given also that both GD 165 and Ross 548 are located near the blue edge, it is difficult to see how the convective efficiency could be significantly decreased in those two particular stars.

In this context, it is quite appropriate to mention the recent work of Tremblay et al. (2015) who provided a calibration of the mixing-length parameter to be used in 1D models of DA white dwarfs (such as those used here) on the basis of detailed 3D hydrodynamics calculations. These authors provided effective temperature- and surface gravity-dependent values of the parameter α (the ratio of the mixing length to the local pressure scale height) to be used within the ML2/α framework of the mixing-length theory employed in white dwarf models. An examination of their Table 3.2, taking into account the values of $T_{\rm eff}$ and $\log g$ of both stars, indicates that the effective value of α that should be used for modeling the flux is, in fact, rather close to 1.0 in both cases. This implies that the predictions of linear nonadiabatic pulsation theory presented in Figure 3.14 remain essentially unchanged.

3.5 COMPARISON WITH PREVIOUS STUDIES

There have been a few previous seismic analyses concerning the classical ZZ Ceti stars GD 165 and Ross 548, and it is of interest to compare the results of these independent studies with our own. In the case of GD 165, Bradley (2001) presented the first seismic model of that star using parametrized evolutionary models computed with the Rochester code WDEC. More recently, Romero et al. (2012) carried out a general seismic survey of some 44 ZZ Ceti stars, including GD 165 (and Ross 548). Their approach is characterized by the use of evolutionary models with a full history from the ZAMS. In the case of Ross 548, along with the Romero

TABLE 3.12 – Observed periods, mode identification, and normalized merit function for past seismic studies of GD 165 in comparison to the present work.

Mode	120.36 (s)	192.68 (s)	250.16 (s)	114.23 (s)	146.32 (s)	168.19 (s)	s^2 (s^2)	Reference
l	1	1	1	2	2	2	0.32	This work
$-k$	1	2	3	2	3	4		
l	1	1	1	2	...	...	0.83−4.68	Bradley 2001
$-k$	1	2	4	2	...	...		
l	1	1	1	2	...	...	1.71	Romero et al. 2012
$-k$	1	2	3	2	...	...		

et al. (2012) paper, seismic models have been proposed by Bischoff-Kim et al. (2008a) and Castanheira et al. (2009), both of which using parametrized evolutionary models from WDEC.

TABLE 3.13 – Observed periods, mode identification, and normalized merit function for past seismic studies of Ross 548 in comparison to the present work.

Mode	212.94 (s)	274.52 (s)	318.42 (s)	333.64 (s)	186.87 (s)	217.83 (s)	s^2 (s^2)	Reference
l	1	1	1	1	2	2	0.35	This work
$-k$	1	2	3	4	3	4		
l	1[a]	1[a]	1	2	2	...	Not given[b]	Bischoff-Kim et al. 2008a
$-k$	1	2	4	8	4	...		
l	1	1	1	2	2	...	6.96	Castanheira et al. 2009
$-k$	1	2	3	9	3	...		
l	1[a]	1[a]	2	2	1	...	11.72	Romero et al. 2012
$-k$	2[a]	3	8	9	1	...		

[a] Fixed a priori.

[b] The authors use a different merit function than ours, $\Phi = \sum_{i=1}^{N_{\rm obs}} |P^i_{\rm obs} - P^i_{\rm th}|/N_{\rm obs}$, and state that they find a minimum value around $\lesssim$ 1.5. Translated into their merit function, our results for the five periods in commun give a value of $\Phi = 0.36$.

Table 3.12 (Table 3.13) indicates the mode identification and normalized merit function inferred in the past available seismic studies of GD 165 (Ross 548) in comparison to the present work. We recall that the normalized merit function, s^2, is obtained by dividing our usual merit function (equation(3.1)) by the number of fitted periods in order to put the different studies on the same footing. We also point out, in this context, that Paper I has revealed two more main modes than previously known for GD 165, and an additional one for Ross 548. These additions are quite significant, especially for low-order modes such as those involved here, because they contain extra seismic information about the pulsating star. At the same time, the challenge of fitting simultaneously all of the observed periods increases greatly,[9] which is, again, particularly true for low-order modes. Despite this, Tables 3.12 and 3.13 reveal that our approach leads to significantly better values of s^2 than in all previous studies, and sometimes by very large margins. This should not be overly surprising given that our use of parametrized static models allows us to explore parameter space much more finely than before.

TABLE 3.14 – Main inferred parameters for past seismic studies of GD 165 in comparison to the present work.

$\log g$ (cm s^{-2})	$T_{\rm eff}$ (K)	$M_*/M_\odot$	$\log M({\rm H})/M_*$	$\log M({\rm He})/M_*$	$X({\rm O})$	Reference
8.052±0.035	12130±450	0.64±0.02	−4.23±0.15	−1.70±0.13	Unrestricted	This work[a]
∼8.06	∼12,190	0.65−0.68	−3.8,−4.0	−1.8,−2.0	∼0.80	Bradley 2001[b]
8.05±0.07	11635±330	0.632±0.014	−4.17±0.21	−1.76	0.76	Romero et al. 2012[c]

[a] Parametized static models.

[b] Parametized evolutionary models.

[c] Evolutionary models from the ZAMS.

With respect to mode identification, our automatic and blind procedure leads to results that are sometimes at odds with previous analyses, especially for Ross 548. For GD 165, the comparison is rather positive since our mode identification for the four fitted periods in common with Romero et al. (2012) gives the same results, while there is a difference with

[9] A clear indication of this is provided in Romero et al. (2012), from which we can deduce that their average merit function $< \Phi >$ degrades quite significantly from a value of 0.57 for the objects in their sample with four or less fitted periods (about half of the sample) to 1.69 for the pulsators with more than 4 fitted periods. This different merit function is defined by $\Phi = \sum_{i=1}^{N_{\rm obs}} |P^i_{\rm obs} - P^i_{\rm th}|/N_{\rm obs}$.

Bradley (2001) for the 250 s period. Things are not so well for Ross 548, since we differ from Bischoff-Kim et al. (2008a) for three modes out of five, from Castanheira et al. (2009) for two modes out of five, and from Romero et al. (2012) for all five modes. We point out that in some of the previous studies, the values of k and l for some modes were fixed a priori. We further note that our mode identification has the clear advantage of boosting consecutive values of k for given value of l for both stars, which is the expected behavior from nonadiabatic theory as discussed above.

TABLE 3.15 – Main inferred parameters for past seismic studies of Ross 548 in comparison to the present work.

$\log g$ (cm s^{-2})	$T_{\rm eff}$ (K)	$M_*/M_\odot$	$\log M({\rm H})/M_*$	$\log M({\rm He})/M_*$	$X({\rm O})$	Reference
8.108±0.025	12281±125	0.65±0.02	−7.45±0.12	−2.92±0.10	0.70±0.06	This work[a]
...	12150±550	0.63±0.04	−7.46±0.24	−2.40	0.76[d]	Bischoff-Kim et al. 2008a[b]
...	12100	0.635	−4.5	−2.0	0.50[d]	Castanheira et al. 2009[b]
8.03±0.05	11627±390	0.609±0.012	−7.98±0.16	−1.61	0.72	Romero et al. 2012[c]

[a] Parametized static models.

[b] Parametized evolutionary models.

[c] Evolutionary models from the ZAMS.

[d] Fixed value.

Table 3.14 (Table 3.15) lists the main inferred parameters for past seismic studies of GD 165 (Ross 548) in comparison to the present effort. It should be pointed out here that the oxygen mass fraction in the core, $X({\rm O})$, corresponds to the value of the assumed *homogeneous* composition in our approach, while it corresponds to the central value in the other studies using more realistic composition profiles (except for Castanheira et al. 2009 who also assume homogeneous cores). Furthermore, we found no sensitivity of the fitted periods for GD 165 on the core composition, so this parameter is left unconstrained for that star in our study. This is not in conflict with the results of Bradley (2001) and Romero et al. (2012) because, in their cases, the core composition is not varied and is either fixed in advance (Bradley 2001) or comes from detailed calculations from the ZAMS (Romero et al. 2012). In contrast, because of the

presence of three modes probing deep into the core in Ross 548, we found a definite sensitivity of the fitted periods on the core composition. In comparison, the core composition was fixed in advance in the studies of Bischoff-Kim et al. (2008a) and Castanheira et al. (2009), or resulted from evolutionary calculations from the ZAMS (Romero et al. 2012).

Overall, we find good consistency between the three seismic models of GD 165 in Table 3.14, and a remarkably good agreement between our results for Ross 548 and the seismic model proposed by Bischoff-Kim et al. (2008a) as summarized in Table 3.15. This excellent agreement is compounded by the fact that the rate of period change of the dominant 213 s pulsation in Ross 548 was found to be equal to $2.91 \pm 0.29 \times 10^{-15}$ s/s by Bischoff-Kim et al. (2008b), which compares extremely well with our own value given in Table 3.8, $\dot{P}_{213} = 2.87 - 2.91 \times 10^{-15}$ s/s. We interpret this as an independent verification that our choice of the thin-layer solution for Ross 548 above was indeed the correct one. It is interesting to point out that these two seismic models for Ross 548 agree extremely well, even though the mode identification is at odds for three modes out of five (see Table 3.13). This situation is not new, however, and has been pointed out before by Van Grootel et al. (2008) in the context of pulsating hot B subdwarfs. The fact that an exact mode identification is not rigorously required to derive an acceptable seismic model is still considered a small "heresy" by many in the field of asteroseismology. Yet, we now have evidence that this can be the case in at least two different kinds of pulsating stars. In fact, this should not be so surprising for stars with dense period spectra.

The comparison of our seismic model for Ross 548 with those of Castanheira et al. (2009) and Romero et al. (2012) in Table 3.15 is less positive. There is conflict in terms of layering, in particular. Characterized by rather bad values of the merit function s^2 (see Table 3.13), those two models could be improved upon.

3.6 CONCLUSION

We have presented in this short series of two papers a new seismic analysis of the two classical, bright, hot ZZ Ceti stars GD 165 and Ross 548. Those were selected on the basis of the relative simplicity of their pulsation properties associated with their locations near the blue edge of the ZZ Ceti instability strip in the spectroscopic HR diagram where linear pulsation

theory – in both its adiabatic and nonadiabatic flavors – is expected to work best. Given their near spectroscopic twin nature, those two stars also present some interesting challenges from a seismic point of view because the observed periods are significantly longer in Ross 548 than in GD 165. More fundamentally, as representative of the "simpler" ZZ Ceti pulsators, those two stars were picked to test, in a white dwarf context, the parametrized asteroseismic approach that has been quite successfully developed in recent years for pulsating hot subdwarf stars. This was deemed necessary before considering the exploitation of the exquisite observations gathered by *Kepler* and *Kepler-2* on other more complicated pulsating white dwarfs.

In Paper I, we took advantage of the availability of time-series data sets of exceptional quality (by ground-based standards) to uncover, in GD 165, a total of up to 13 independent pulsation modes regrouped into six main frequency multiplets. Likewise, up to 11 independent pulsation modes, also regrouped into six multiplets, were isolated in Ross 548. For the purpose of comparing with spherically symmetric (non-rotating) models of stars, Paper I revealed the existence of two more of these "main" modes than previously known in GD 165 (f_5 and f_6 in Table 2.2), and one more in Ross 548 (f_6 in Table 2.3). Given the high-information content of such low-order modes, these constituted significant additional constraints and welcome additions to the seismic analyses to follow. Furthermore, Paper I provided updated estimates of the time-averaged atmospheric parameters of each target star in the light of recent developments on the front of atmospheric modeling for DA white dwarfs. These constitute fundamental external and independent constraints that, in our approach, seismic models must respect to be deemed acceptable.

In the present paper, we reported the results of detailed searches in parameter space for identifying an optimal model for each star that can account well and simultaneously for all the observed periods, while being consistent with the spectroscopic constraints derived in Paper I. This was done with the help of the dedicated code LUCY, which is a highly efficient optimization package that provides an objective and automatic way for identifying optimal seismic models while relying on a minimum of a priori assumptions. In the present exercises, we put no restrictions on the mode identification, except for constraining the modes to belong to the $l = 1$ or $l = 2$ families in order to exploit the fact that only dipole and quadrupole g-modes

have been formally identified in ZZ Ceti stars. The equilibrium structures that we used are full, static, spherically symmetric parametrized models of DA white dwarfs. In the spirit of keeping things as simple as possible in our seismic exercises, we varied only five basic parameters, (1) the composition of the C-O core (assumed homogeneous), (2) the surface gravity, (3) the effective temperature, (4) the mass contained in the He mantle surrounding the C-O core, and (5) the mass contained in the H layer sitting on top of that mantle. Two additional key parameters, the composition profile in the H/He transition zone and its equivalent in the He/C-O transition zone, were fixed to the shapes derived from detailed time-dependent diffusion calculations coupled to evolutionary computations carried out previously for GD 165. This "calibration" was also assumed to be valid for models of Ross 548, again for the sake of simplicity. Along with the choice of a convective efficiency fixed to the ML2/$\alpha = 1.0$ version, the adoption of the calibrated composition transition zone profiles led to the economy of three parameters that no longer needed to be optimized.

We found optimal models for each target that reproduce the six observed periods well within $\sim$0.3% on the average (see Tables 3.2 and 3.3), which is comparable to the best results achieved so far in asteroseismology. We also found that there is a sensitivity of the solution on the core composition for Ross 548, while there is practically none for GD 165. We submit that this somewhat surprising difference, along with the fact that the observed periods are significantly longer in Ross 548 than in its spectroscopic look-alike GD 165, may find a natural explanation in that the internal structures of the two stars differ in one significant aspect. Indeed, according to our seismic models, Ross 548 has a relatively thin outer envelope, while GD 165 has a rather thick one. It has been demonstrated in the past that a thinner envelope leads to a longer period for a given g-mode, all other things being the same. Furthermore, a thin envelope may allow for more efficient trapping/confinement properties. We explicitly verified that our optimal model of Ross 548 shows weight functions for three confined modes extending well into the deep core, thus explaining naturally the sensitivity of the period spectrum on the core composition in that star. In contrast, our optimal seismic model of its spectroscopic sibling, GD 165 with its thick envelope, does not trap/confine modes very efficiently, and we find weight functions for all six modes of interest that do not extend into the deep core, hence

accounting for the lack of sensitivity in that case. This discovery that confined modes must be detected in order to probe the core composition of ZZ Ceti stars has implications for future work: it means that a certain amount of luck will be needed to fall onto a "cooperative" star.

The results reported in Tables 3.6 and 3.7 represent the ultimate outcome of this series of two papers. The reliability of the properties listed in those tables rests on the credibility of the proposed seismic models. In this connection, we have strived to verify that these models are consistent with all possible indicators, including external constraints. On the first account, the optimization method we used, based on static parametrized equilibrium models, allowed us to reproduce simultaneously all of the observed periods at the highest possible accuracy, given the (small) number of free parameters that were varied and the available constitutive physics. An intrinsic part of this approach included a detailed inspection of the shape of the 5D merit function in parameter space in order to put the derived seismic models on a firm statistical basis. We verified explicitly that our static seismic models can be reproduced quite satisfactorily from full evolutionary calculations. Likewise, we verified that the seismic models and the implied mode identifications are compatible with the expectations of linear pulsation theory, particularly in terms of amplitude hierarchy and nonadiabatic considerations. We also fully exploited the observed multiplet structure to test the mode identification and to constrain the internal dynamics of the two target stars. In the case of GD 165 in particular, the mode identification was strengthened considerably through the (k,l) dependence of the observed frequency spacings within multiplets. Both GD 165 and Ross 548 were found to rotate extremely slowly by stellar standards, and very likely as solid bodies.

On the second account, as summarized in Table 3.8, we tested the compatibility of our seismic models with all of the external independent constraints that we could find in the literature. Notably, we found an excellent agreement for both stars between our seismic estimates of the surface gravity and the effective temperature and the values obtained independently through the spectroscopic method reported in Paper I. Also, again for both stars, our seismic estimates of the absolute V magnitude and of the distance turned out to be perfectly compatible with independent spectroscopic values of these quantities. Our seismic distance to GD 165 is also perfectly in line with a highly reliable parallax measurement for that star. Finally,

we found a perfect consistency between the measured rate of period change for the dominant 213 s pulsation mode in Ross 548 and the value predicted on the basis of our seismic model. We conclude from these comparisons that our proposed seismic models for GD 165 and Ross 548 are credible and reliable, and that the method that was to be assessed passes the test with flying colors.

The next step in our continuing quest for improved seismic models of pulsating white dwarfs is defined by our discovery – in Ross 548 – of the existence of deeply confined modes in white dwarfs as cool as ZZ Ceti stars. Obviously, such modes hold the potential for probing in details the composition stratification in the core. This came as a small surprise to us since we expected that, generally, the increasing degeneracy in a cooling ZZ Ceti star would have pushed the significant part of the amplitudes of g-modes (and those of their associated weight functions) to the outer envelope, thus leaving very little sensitivity of the period spectrum on the structure of the core, very much like the case of GD 165. The existence of deeply confined modes in Ross 548 implies that our seismic model for that star, contrary to that of GD 165, could be perfected by considering a more realistic description of the core than the crude one-parameter homogeneous model used here.[10] This is one important lesson that we retain for the future: since it is impossible to know in advance if a given ZZ Ceti pulsator behaves more like Ross 548 or GD 165, it is wise to include from now on a better description of the composition profile in the core. We will therefore seek to parametrize the relatively complicated composition profile expected in the core of white dwarfs in a next effort and use this improved description in future seismic analyses.

This work was supported in part by the NSERC Canada through a doctoral fellowship awarded to Noemi Giammichele, and through a research grant awarded to Gilles Fontaine. The latter also acknowledges the contribution of the Canada Research Chair Program. We are also grateful to Valérie Van Grootel who kindly carried out for us the nonadiabatic calculations reported in Figure 3.14.

[10]The inclusion of such a description, along with the relaxation of the assumption that the composition transition zone profiles calibrated for GD 165 also hold for Ross 548, would indeed likely improve our seismic model for that latter star. We suspect that solid body rotation would be better constrained in such an improved model and, furthermore, that the derived mass in the He mantle, a bit on the low side by traditional evolutionary arguments, would be revised upward.

3.7 Appendix A: SOME BACKGROUND ON PULSATIONS AND ROTATION

Within the framework of the linear theory of stellar pulsations, a mode is defined in terms of 3 "quantum numbers", k, l, and m, the first one giving the number of nodes in the radial direction of the eigenfunctions associated with that mode, and the others (l and m) being the indices of the spherical harmonic function which specifies the angular geometry of the mode.

Non-rotating (spherical) stars have eigenfrequencies that are $(2l + 1)$-fold degenerate in m. However, a slowly rotating star has en eigenmode spectrum that is not degenerate in m as a result of the destruction of the spherical symmetry. To first order, with slow rotation considered as a perturbation, one can show that,

$$\sigma_{klm} \simeq \sigma_{kl} - m(\delta\sigma_{kl}) \ , \tag{3.8}$$

where σ_{klm} is the angular frequency of mode (k, l, m), σ_{kl} is the angular frequency of the degenerate mode (k, l) in the absence of rotation, and where the frequency spacing is given by,

$$\delta\sigma_{kl} = \int_0^R \Omega_{\rm rot}(r) K_{kl}(r) dr \ . \tag{3.9}$$

This leads to a set of equally-spaced frequencies with a splitting between adjacent frequency components given by $\delta\sigma_{kl}$.

In the above expression, $\Omega_{\rm rot}(r)$ is the (assumed) spherically symmetric rotation law (expressed in units of angular frequency), and K_{kl} is the so-called first-order rotation kernel which plays the role of a weight function. It is given by,

$$K_{kl}(r) = \frac{\xi_r^2 + \{l(l+1) - 1\}\xi_h^2 - 2\xi_r\xi_h}{\int_0^R \{\xi_r^2 + l(l+1)\xi_h^2\}\rho r^2 dr} \rho r^2 \ , \tag{3.10}$$

where ξ_r and ξ_h are, respectively, the real parts of the radial and horizontal components of the displacement vector,

$$\vec{\xi} = \left[\xi_r(r), \xi_h(r)\frac{\partial}{\partial\theta}, \xi_h(r)\frac{1}{\sin\theta}\frac{\partial}{\partial\phi}\right] Y_m^l(\theta, \phi) e^{i\sigma t} \ . \tag{3.11}$$

These eigenfunctions for mode (k,l) refer to the unperturbed configuration, i.e., to a purely spherical (non-rotating) stellar model.

Hence, to first order, slow spherically symmetric ($\Omega_{\rm rot}(r)$) rotation produces a set of $2l+1$ equally-spaced frequency components out of a degenerate mode with indices (k,l). The spacing between two adjacent components of this multiplet (modes that differ by $|\Delta m| = 1$) can be computed from the unperturbed eigenfunctions as can be appreciated from equations (3.9) and (3.10). This fine structure within a multiplet is usually referred to as rotational splitting.

In the particular case of uniform rotation, $\Omega_{\rm rot}$ does not depend on the radial coordinate r, and it is easy to derive the following expression,

$$\delta\sigma_{kl} = \Omega_{\rm rot}(1 - C_{kl}) \ , \tag{3.12}$$

where C_{kl}, the first-order solid body rotation coefficient, is given by,

$$C_{kl} = \frac{\int_0^R \{\xi_h^2 + 2\xi_r\xi_h\}\rho r^2 dr}{\int_0^R \{\xi_r^2 + l(l+1)\xi_h^2\}\rho r^2 dr} \ . \tag{3.13}$$

In the asymptotic limit of high radial order ($k >> 1$) for g-modes, it is well known that the horizontal component of the displacement vector becomes much larger than the radial component ($\xi_h >> \xi_r$). Hence, from equation (3.13), the first-order solid body rotation coefficient reduces to $C_{kl} = 1/(l(l+1))$ in that limit.

Given a credible seismic model for a slowly rotating pulsating star (this implies that each frequency multiplet has been properly identified in terms of its basic indices k and l, and that the corresponding unperturbed eigenfunctions ξ_r and ξ_h are available), and given a rotation law $\Omega_{\rm rot}(r)$, it is possible to define a goodness-of-fit merit function inspired from a χ^2 approach such that,

$$S^2 = \sum_{i=1}^{N_{\rm obs}} \left(\frac{\delta\sigma_{\rm obs}^{(i)} - \delta\sigma_{\rm th}^{(i)}}{\Delta_{\rm obs}^{(i)}} \right)^2 \ , \tag{3.14}$$

where $\delta\sigma_{\rm obs}^{(i)}$ is the i^{th} observed frequency spacing between two rotationally-split frequency components within a multiplet (modes with the same values of k and l, but different values of m), $\Delta_{\rm obs}^{(i)}$ is its associated uncertainty, and $\delta\sigma_{\rm th}^{(i)}$ is the computed spacing for the same two

modes according to the previous recipe.

The merit function S^2 is minimized in parameter space to obtain the best possible fit. In the particular case of solid body rotation, parameter space reduces to a single dimension, and S^2 is optimized as a function of the uniform rotation period $P_{\rm rot}$ ($=2\pi/\Omega_{\rm rot}$).

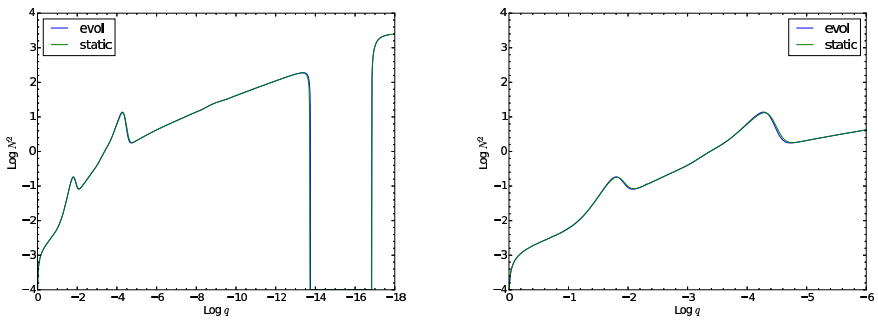

FIGURE 3.13 – Comparison of the run of the Brunt-Väisälä frequency in a representative evolutionary model of a ZZ Ceti star with that of its equivalent static model. The abcissa is the fractional mass depth. The left panel refers to the full model, while the right one provides a zoomed-in view of the inner regions. The well in the outer layers illustrated in the upper panel corresponds to that H convection zone.

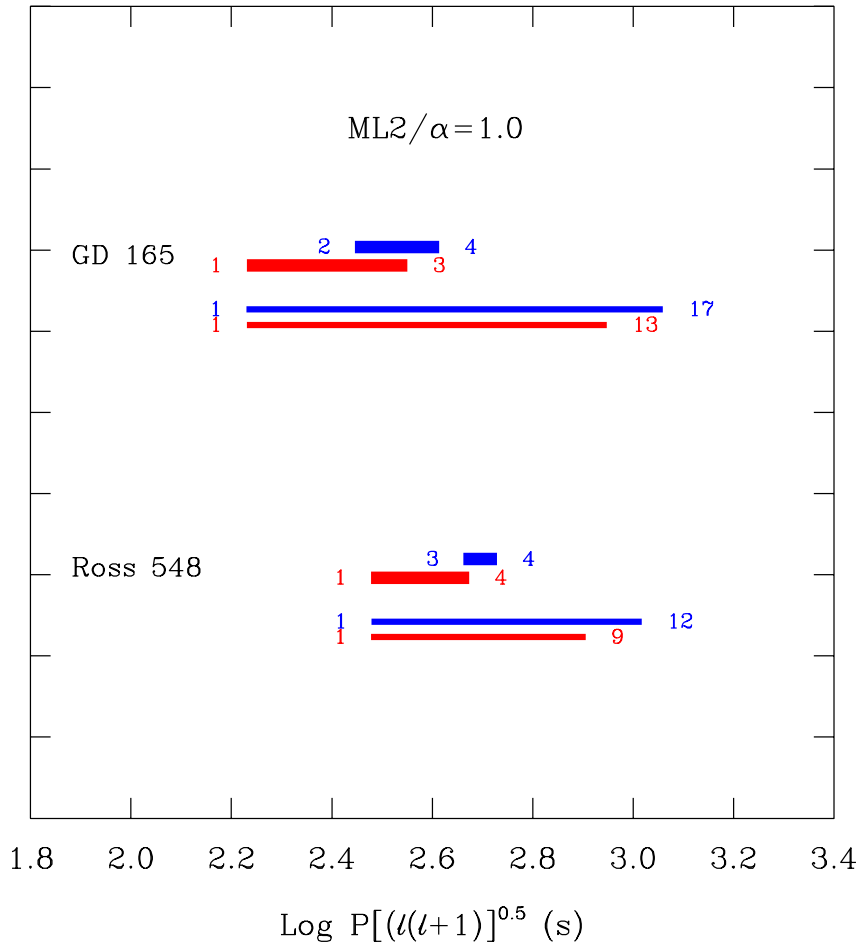

FIGURE 3.14 – Comparison of the bands of detected periods in GD 165 and Ross 548 (heavy lines) with the bands of excited periods (less heavy lines) in the seismic models of these stars as obtained from detailed nonadiabatic calculations. The reduced period is used as the abcissa in order to have comparable values for both dipole (in red) and quadrupole modes (in blue). The radial order k is indicated at both ends of each band.

3.8 REFERENCES

Bergeron, P., Saffer, R.A., & Liebert, J. 1992, ApJ, 394, 228

Bergeron, P., Wesemael, F., Lamontagne, R., et al. 1995, ApJ, 449, 258

Bischoff-Kim, A., Montgomery, M.H., & Winget, D.E. 2008a, ApJ, 675, 1505

Bischoff-Kim, A., Montgomery, M.H., & Winget, D.E. 2008b, ApJ, 675, 1512

Bradley, P.A. 1998, ApJS, 116, 307

Bradley, P.A. 2001, ApJ, 552, 326

Brassard, P., & Fontaine, G. 2005, ApJ, 622, 572

Brassard, P., & Fontaine, G. 2006, Mem. Soc. Astron. Ita., 77, 439

Brassard, P., Fontaine, G., Billères, M., Charpinet, S., Liebert, J., & Saffer, R.A. 2001, ApJ, 563, 1013

Brassard, P., Fontaine, G., Wesemael, F., & Hansen, C.J. 1992b, ApJS, 80, 369

Brassard, P., Fontaine, G., Wesemael, F., and Tassoul, M. 1992a, ApJS, 81, 747

Castanheira, B.G., & Kepler, S.O. 2009, MNRAS, 396, 1709

Charpinet, S., Fontaine, G., Brassard, P. 2009, Nature, 461, 501

Charpinet, S., Fontaine, G., Brassard, P., et al. 2005, A&A, 437, 575

Charpinet, S., Giammichele, N., Brassard, P., Van Grootel, V., & Fontaine, G. 2015, in ASP Conf. Ser. 493, 19th European Workshop on White Dwarfs, ed. P. Dufour, P. Bergeron, & G. Fontaine (San Franciso: ASP), 151

Charpinet, S., Van Grootel, V., Brassard, P., Fontaine, G., Green, E.M., & Randall, S.K. 2013, EPJ Web of Conferences, 43, 04005

Charpinet, S., Van Grootel, V., Reese, D., et al. 2008, A&A, 489, 377

Charpinet, S., Van Grootel, V., Fontaine, G., et al. 2011, A&A, 530, A3

Fontaine, G., & Brassard, P. 2002, ApJ, 581, L33

Fontaine, G., & Brassard, P. 2008, PASP, 120, 1043

Fontaine, G., Brassard, P., Bergeron, P., & Wesemael, F. 1992, ApJ, 399, L91

Fontaine, G., Brassard, P., & Charpinet, S. 2013, in ASP Conf. Ser. 469, 18th European Workshop on White Dwarfs, ed. J. Krzesinski, G. Stachowski, P. Moskalik, & K. Bajan (San Franciso: ASP), 115

Gianninas, A., Bergeron, P., & Ruiz, M.T. 2001, ApJ, 743, 138

Giammichele, N., Fontaine, G., Bergeron, P., et al. 2015a, ApJ, 815, 56, Paper I

Giammichele, N., Fontaine, G., & Brassard, P. 2013, in ASP Conf. Ser. 469, 18th European Workshop on White Dwarfs, ed. J. Krzesinski, G. Stachowski, P. Moskalik, & K. Bajan (San Franciso: ASP), 49

Giammichele, N., Fontaine, G., Charpinet, S., & Brassard, P. 2015b, in ASP Conf. Ser. 493, 19th European Workshop on White Dwarfs, ed. P. Dufour, P. Bergeron, & G. Fontaine (San Franciso: ASP), 233

Kirkpatrick, J.D. 2005, ARA&A, 43, 195

Metcalfe, T.S., Montgomery, M.H., & Kanaan, A. 2004, ApJ, 605, L133

Mukadam, A., Bischoff-Kim, A., Fraser, O., et al. 2013. ApJ, 771, 17

Romero, A.D., Córsico, A.H., Althaus, L.G., Kepler, S.O., Castanheira, B.G., & Miller Bertolami, M.M. 2012, MNRAS, 420, 1462

Tassoul, M., Fontaine, G., & Winget, D.E. 1990, ApJS, 72, 335

Tremblay, P.-E., Ludwig, H.-G., Freytag, B., et al. 2015, ApJ, 799, 142

Unno, W., Osaki, Y., Ando, H., Saio, H., & Shibahashi, H. 1989, "Non Radial Oscillations of Stars", University of Tokyo Press

Van Grootel, V., Charpinet, S., Brassard, P., Fontaine, G., and Green, E.M. 2013a, A&A, 553, A97

Van Grootel, V., Charpinet, S., Fontaine, G., et al. 2008, A&A, 488, 685

Van Grootel, V., Charpinet, S., Fontaine, G., Green, E.M., & Brassard, P. 2010a, A&A, 524, A63

Van Grootel, V., Charpinet, S., Fontaine, G., et al. 2010b, ApJ, 718, L97

Van Grootel, V., Dupret, M.-A., Fontaine, G., et al. 2012, A&A, 539, A87

Van Grootel, V., Fontaine, G., Brassard, P., & Dupret, M.-A. 2013b, ApJ, 762, 57

Chapitre 4

Seismic Studies of White Dwarfs: Parametrization of the Core

N. Giammichele[1], S. Charpinet[2], G. Fontaine[1], and P. Brassard[1]

[1] *Département de Physique, Université de Montréal, Succ. Centre-Ville, C.P. 6128, Montréal, QC H3C 3J7, Canada*

[2] *Université de Toulouse, UPS-OMP, IRAP, Toulouse F-31400, France*

CNRS, IRAP, 14 avenue Edouard Belin, F-31400 Toulouse, France

To be submitted to *The Astrophysical Journal Supplement*

4.1 ABSTRACT

We present a prescription for parametrizing the chemical profile in the core of white dwarfs in the light of the recent discovery that pulsation modes may sometimes be deeply confined in some cool pulsating white dwarfs. Such modes may be used as unique probes of the complicated chemical stratification that results from several processes that occured in previous evolutionary phases of intermediate-mass stars. This effort is part of our ongoing quest for more credible and realistic seismic models of white dwarfs using static, parametrized equilibrium structures. Inspired from successful parametrizations obtained in the aerodynamic design optimization field, we exploit Akima splines for the tracing of the chemical profile of oxygen (carbon) in the core of a white dwarf model. Our prescription includes up to seven free parameters to define properly the details of the composition profile. A series of tests are then presented to better seize the precision and the meaningfulness of the results that can be obtained in an asteroseismological context. We also show that the new parametrization passes an essential basic test, as it is used successfully to reproduce the chemical stratification of a full evolutionary model.

4.2 INTRODUCTION

In the era of space missions such as *Kepler* and *Kepler*-2 which have been providing asteroseismic data of unprecedented quality for several types of pulsating stars (including white dwarfs), we decided to revisit the problem of the seismic modeling of this latter type of pulsators using current techniques, typical of those developed quite successfully in recent years for pulsating hot B subdwarfs (see, e.g., Charpinet et al. 2013). To test these techniques in a white dwarf context, we first carried out a detailed analysis of the pulsation properties of two classical hot ZZ Ceti stars – GD 165 and Ross 548 – using the best available data from the ground. Those targets were chosen on the basis of the simplicity of their light curves (associated with their locations near the blue edge of the ZZ Ceti instability strip), their near spectroscopic twin nature, and the availability of time-series data sets of exceptional quality. The results of that analysis were presented by Giammichele et al. (2015; 2016) who found a

credible seismic model for each star able to reproduce simultaneously the six observed periods well within $\sim$0.3% on the average, which is comparable to the best results achieved so far in asteroseismology. The models provided robust mode identification and were found to be perfectly compatible with the expectations of linear pulsation theory in both its adiabatic and nonadiabatic versions. In addition, these seismic models were shown to be consistent with all the available external independent constraints such as estimates of the atmospheric parameters derived from time-averaged spectroscopy, estimates of distances provided by parallax measurements or spectrocopy, and even the measured rate of period change for one mode in Ross 548. The study of Giammichele et al. (2015; 2016) thus firmly established that our approach to quantitative seismology – based on static, parametrized models of stars – can be extended reliably to the white dwarf domain.

An unexpected result of the study of Giammichele et al. (2016) is the finding that the pulsation periods detected in GD 165 have only a weak dependence on the core composition, while those observed in Ross 548 are, on the contrary, quite sensitive to a variation of the core composition. This a priori puzzling result finds a natural explanation in that all six modes in the GD 165 model have amplitudes and weight functions that do not extend into the deep core and, consequently, their periods are not sensitive to a variation of the core composition. In comparison, three of the six modes of interest in the Ross 548 model are partly confined below its thin envelope and, therefore, have a strong sensitivity to the core composition. This discovery of the existence of deeply confined modes in Ross 548 and, potentially, in many other pulsating white dwarfs, opens up the most interesting possibility of using those modes as probes of the internal composition profile in the C-O core. In the Giammichele et al. (2016) study, to keep things as simple as possible, it was assumed that the core composition is homogeneous, which is a crude approximation in the light of the rather complicated C-O stratification expected in the cores of former AGB stars as revealed by detailed evolutionary calculations (see, e.g., Salaris et al. 2010 or Romero et al. 2012). In retrospect, such an approximation was amply sufficient in the case of GD 165, but it is now clear that for stars such as Ross 548, with deeply confined modes, our modeling could be perfected by including a parametrized description of the chemical layering in the C-O core. Presumably, this would

lead to still more realistic seismic models of pulsating white dwarfs, with theoretical periods approaching the "Holy Grail" of asteroseismology, i.e., perhaps able to reproduce the observed periods at the accuracy of the observations. Currently, as indicated above, the best one can do is to obtain average dispersions of less than ∼0.3% in periods, still a long way from the measurement uncertainties as indicated, for example, in Tables 3 and 4 of Giammichele et al. (2015). We provide, in this paper, a prescription for parametrizing the C-O core of a white dwarf, with the hope of improving future seismic models of stars of this type.

4.3 WHITE DWARFS AND SPACE-BORNE OBSERVATIONS

Ground-based observations of pulsating white dwarfs have been quite successful since Landolt (1968). However, in many instances and despite the considerable efforts invested in multi-site campaigns, the available light curves of pulsating white dwarfs still suffer more or less severely from a limited time base and large gaps in the data caused mainly by diurnal interruptions and inclement weather (Michel et al. 2008). The aliasing resulting from the daily interruptions and breaks degrades the measurements obtained from the Fourier transforms.

The advent of the space missions *MOST* (Matthews 2007), *CoRoT* (Convection, Rotation, and planetary Transit) (Baglin et al. 2009; Michel et al. 2008), and *Kepler* has revolutionized asteroseismology. While the primary aim of the latter spacecraft was the detection of Earth-size planets within the habitable zone around solar-like stars using the transit method (Borucki et al. 2010), high-quality photometric data of variable stars have been obtained, and this has constituted a true wealth for asteroseismology (Gilliland et al. 2010). The continuous monitoring by space-based telescopes of thousands of stars at a very high degree of precision has led to exquisite data sets for pulsating stars, since both resolution and signal-to-noise gain from a more complete coverage and a much longer observational baseline. The most salient features of the *Kepler* mission for asteroseismology include (1) ultra-high precision photometry measured in parts per million, (2) a nearly continuous time series over weeks to years, and (3) cadences rapid enough to sample oscillations with periods as short as a few minutes (Gilliland et al. 2010). The quarter-long (the three-month period corresponding to the time of an observation sequence, before a quarterly roll to keep the solar panels of

the satellite pointing towards the Sun), continuous, uniformly sampled time series provided by *Kepler* give the opportunity to work around aliasing ambiguity of ground-based studies (Greiss et al. 2014).

The *Kepler* mission provided ultra-high quality light curves for a handful of pulsating white dwarfs. The first one to be discovered is KIC 08626021, the only helium-atmosphere white dwarf of the sample, and believed to reside at the hot end of the V777 Her instability strip (Østensen et al. 2011). The longest-studied pulsating white dwarf by *Kepler* is KIC 4552982, a ZZ Ceti star discovered from ground-based photometry (Hermes et al. 2011). It presents considerable frequency modulation in the long-period modes (Bell et al. 2015). Greiss et al. (2014) and Greiss et al. (2015) uncovered some 42 DA white dwarfs and ZZ Ceti candidates in the *Kepler* field, including five pulsators being followed up before the failure of the second reaction wheel in May 2013.

The resulting mission using only the two remaining wheels, $K2$, is planned to observe fields uninterruptedly in the direction of the ecliptic for approximately 75 days. As part of the initial test of the twowheel-controlled pointing, short-cadence photometry was collected on the cool ZZ Ceti GD 1212 during a run in January and February 2014 (Hermes et al. 2014). In upcoming $K2$ mission fields, *Kepler* is bound to observe additional pulsating white dwarfs (Howell et al. 2014). Thus, there are exceptionally high-quality data available from *Kepler* for a handful of pulsating white dwarfs, and those are stars that we are planning to model using our proven seismic approach.

In the light of our discovery of deeply confined modes in Ross 548, and with the aim of fully exploiting the seismic information contained in the *Kepler* light curves, we felt that it would be most useful to upgrade our modeling technique by including a detailed parametrization of the composition profile in the core. Given that evolutionary calculations predict a rather complicated composition profile, this requires some work in order to have a flexible enough procedure to reproduce the salient features of the core, while having the lowest possible number of free parameters to adjust. In this way, we hope that at least some of the *Kepler* pulsating white dwarfs will feature confined modes that will be useful probes of that core.

4.4 PARAMETRIZATION OF THE CORE OF A WHITE DWARF

In our seismic studies, the problem revolves around a merit function defined by the sum of the squared differences between the observed and theoretical periods obtained for a specific star (see, e.g., Giammichele et al. 2016). In our previous efforts on GD 165 and Ross 548, we fixed the convective efficiency to a standard version, we also imposed fixed composition profiles at the H-He and He-core interfaces as obtained from detailed evolutionary calculations of GD 165 taking into account diffusion between the atomic species. We were thus left with five parameters to define a full, static model of a ZZ Ceti star, (1) the surface gravity, (2) the effective temperature, (3) the mass contained in the He mantle, (4) the mass contained in the H outermost layer, and (5) the core composition. Given the small number of modes available (six for both GD 165 and Ross 548), we strove to keep the number of free parameters to a minimum value, so we assumed crudely that the composition in the core would be homogeneous and specified by a single quantity, the oxygen mass fraction $X(\mathrm{O})$. We now consider a more realistic depth-dependent core composition as obtained from detailed evolutionary calculations.

The problem of inferring the most realistic composition profile given an ensemble of observed periods sensitive to the details of the core can be defined as a shape optimization problem. As generally stated, shape optimization, or optimal design, is the set of methods that gives the best possible form in order to fulfill the desired requirements. The typical problem is to find the shape which is optimal in that it minimizes a certain cost, or merit, function while satisfying given constraints. These methods are widely encountered in numerous domains such as aerodynamics, hydrodynamics, acoustics, electromagnetism, and many more. Our situation, the ”drawing” of the chemical profile to best match what is occuring in stars, quantified by the minimization of our merit function, is, in all particulars, analogous to airfoil shape optimization, just to name one.

In general, the ideal airfoil shape, entirely defined by a set of parameters, is determined by minimizing a simple merit function. In the case of aerodynamic problems, the merit function to minimize is usually defined to be the inverse of the lift-to-drag ratio. Here the number of

parameters used to define the airfoil shape has nothing to do with the number of quantities in the merit function. Every single airfoil shape will give a lift-to-drag ratio, independently of the number of parameters that are needed to define the shape of the airfoil. We will adopt the exact same approach for parametrizing the chemical profile of the core. Every single shape of chemical profile will lead to a single merit function, no matter how many periods are observed.

If the parametrization technique is not flexible enough, which translates into not being able to represent all possible shapes, then a true optimal shape cannot be attained. On the other hand, if the number of parameters is too large, the optimization problem becomes unfeasible in term of excessive computational time. Different shape parametrizations have been used in the aerodynamic field, among others: analytical, discrete, polynomial and spline representations (Gallart 2002). Every method has its advantages and drawbacks. In the analytic representation, given an original shape, a set of functions deform the original shape. The design variables represent the deformations added to the original shape in order to create the new shape. This method has the advantages of reducing the necessary number of design variables to a small set, while obtaining a smooth surface. On the other hand, it is only applicable to simple geometries and the deformations are dependent on the shape functions used. The discrete representation is easy to implement and can be used with any geometry. However, it requires a large number of design variables and the final shape can have high frequency oscillations. For the polynomial method, the design variables used are the coefficients of a polynomial. The main advantage in this method is that a small set of design variables can be used, but as for the analytical method, if a low order polynomial is used, some shapes become impossible to represent. The most commonly used representations in areas of expertise such as aerodynamics or automobile design are the spline representations, being the sum of weighted polynomials. In this case, the set of the weighting parameters, called control points, are used as the design variables. There exist several types of splines: Bezier curves, B-splines and non-uniform rational B-spline (NURBS), just to name a few. There are several reasons for using splines: it allows for a reduction in the number of design variables required because the control points of the B-spline can be used as the design variables; the perturbation of one control point has only local effects on the design shape; it results in a curve with C^2

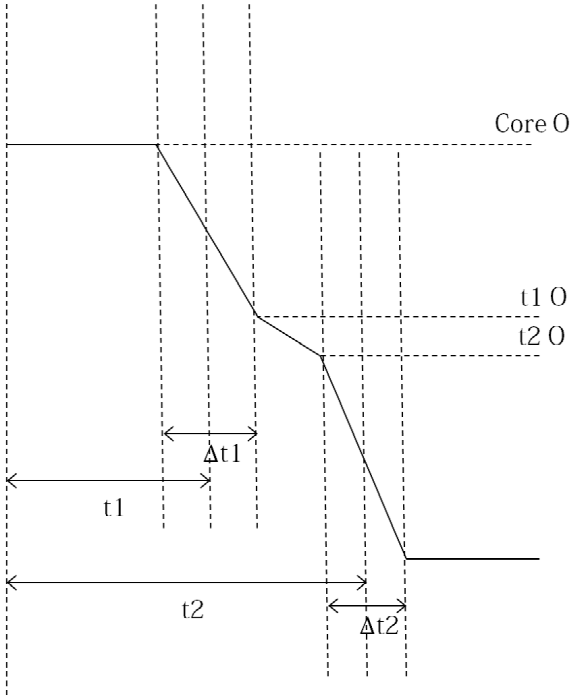

FIGURE 4.1 – Proposed parametrization of $X(\mathrm{O})$ using a two-transition model white dwarf core. All the parameters are labeled in this schematic view.

continuity, therefore it guarantees a shape that is smooth enough for our purposes without any high frequency oscillations.

In the present case, we opt for Akima splines (Akima 1970). The Akima interpolation is a continuously differentiable sub-spline interpolation. It is built from piecewise third order polynomials. Only data from the next neighbor points is used to determine the coefficients of the interpolation polynomial. The disadvantage of cubic splines is that they could oscillate in the neighborhood of an outlier. The Akima spline is a special spline which is stable against such points. Figure 4.1 presents the different shape parameters defining the new parametrization. These shape parameters control the Akima spline and are specifically chosen in order to best imitate an evolved white dwarf chemical profile. Seven control points are necessary to fully define a two-transition chemical profile in the core: core O (the central oxygen value), t1(log q of the first transition), Δt1(the width of the first transition), t1(O) (the oxygen value at the end of the first transition), t2(log q of the second transition), Δt2(the width of the second transition) and t2(O) (the oxygen value at the end of the second transition). The

parametrization is flexible enough that it is allowing us to define a simpler one-transition profile by only using a subset of three shape parameters, core O, t1 and Δt1. In that case and by construction, in order to have a smooth profile, t1(O) and t2(O) are set to zero, while the value of t2 is far enough not to interfere and Δt2 is set to a non-zero value.

We have in hands a new parametrization that can imitate smoothly enough one or two steep "drops" in the oxygen profile (and complementarily the carbon profile) in the core. Now, we have to validate the capacities of our method and new parametrization in an asteroseismic context.

4.5 TESTS ON THE ACHIEVABLE PRECISION OBTAINED WITH ASTEROSEISMOLOGY

The measurements of the stellar parameters of white dwarfs using asteroseismology are quite precise if we refer to the earlier analysis of Ross 548 and GD 165. However, periods are still not fitted at the precision of the observations. In this section, we are interested in testing the degree of precision we can expect from the results of a seismic analysis if the uncertainties were only coming from observations either ground- or space-based.

We start by assuming that the pulsating white dwarf model is perfect, with known global and shape parameters. The model and pulsation properties of the reference star are thus entirely known. Let us pick a subset of 10 periods out of the pulsation spectrum to simulate what we have from a campaign of observations. Artificial observations are then built by adding to each "picked" period a random number following a Gaussian distribution. The mean value of the distribution does not vary, while its standard deviation shows random fluctuations at the desired value. Three cases of different levels of precision are investigated. The first situation is comparable to current period fit precision with a standard deviation of $\sigma = 10$ μHz. The second test case happens if the precision is limited by the accuracy of ground-based data, which is approximately taken to be of the order of 0.1 μHz. The third and last test case represents the situation where the precision is only limited by the accuracy of *Kepler* data, approximatively of the order of 0.001 μHz.

From these modified subsets of periods, we will try to retrieve the global and shape parameters with our optimization tools, performed in the same configuration as for the analysis of Ross 548 et GD 165 (see Giammichele et al. 2016). Three parametrizations are also tested. The first set of tests is performed with a simple variable homogeneous core, while the second set uses the new one-transition parametrization, and the third set the two-transition parametrization.

4.5.1 Parametrization with a Varying Homogeneous Core

The subset of modified periods are initially computed from the reference model with the stellar parameters presented in Table 4.1. It is the model of a standard ZZ Ceti star, with a rather thick hydrogen envelope. As mentioned before, once the periods are calculated from the reference model, a subset of these periods is picked, and these periods are modified to show random fluctuations along a gaussian distribution to the order of the chosen precision. This process is detailed in Table 4.2, where we have the values of the periods at all stages. The first column shows the periods of the reference star, while the following columns list the modified periods for each degree of precision: current fit, ground-based data, *Kepler* data precision. The search range for the optimization, for each parameter, is also presented in Table 4.1. The search range is vast and satisfies almost any conditions to retrieve a ZZ Ceti star.

TABLE 4.1 – Parameters of the reference star as well as the search range for the optimization with a variable homogeneous core.

Parameter	Value	Search range
$T_{\rm eff}$ (K)	12,000	11,000 - 13,000
Log g	8.00	7.80 - 8.20
D(H)	-5.0	-9.0 - -4.0
D(He)	-3.0	-4.0 - -1.5
Total mass ($M_\odot$)	$5.9479\text{x}10^{-1}$	...
Radius ($R_\odot$)	$1.2765\text{x}10^{-2}$	...
Core oxygen fraction (%)	50	0 - 100

Table 4.3 presents the results obtained for the three optimizations with the modified subsets of periods with various degree of precision. Each entry is statistically calculated from the likelihood function from our χ^2-type merit function S^2 that was sampled by the optimization

TABLE 4.2 – Selected and modified periods for the reference star with a variable homogeneous core.

l	k	Period (s)	$\sigma = 10$ μHz	$\sigma = 0.1$ μHz	$\sigma = 0.001$ μHz
1	1	151.53791917	...	...	...
1	**2**	**227.016706244**	**226.98946604**	**227.01643381**	**227.01670352**
1	**3**	**313.807911837**	**313.66203636**	**313.80645241**	**313.80789724**
1	**4**	**325.278884448**	**325.58422098**	**325.28193498**	**325.27891495**
1	**5**	**379.026095735**	**380.55088833**	**379.04128317**	**379.02624760**
1	**6**	**436.100785261**	**433.16916032**	**436.07127260**	**436.10049011**
1	7	459.45372755	...	...	...
2	2	131.65045899	...	...	...
2	**3**	**181.920837778**	**181.85326019**	**181.92016175**	**181.92083102**
2	**4**	**212.206268924**	**212.35274848**	**212.20773272**	**212.20628356**
2	**5**	**224.636765373**	**224.25083274**	**224.63289947**	**224.63672671**
2	**6**	**260.460240785**	**259.40908188**	**260.44968703**	**260.46013524**
2	**7**	**282.114308484**	**283.05460137**	**282.12368049**	**282.11440220**
2	8	306.14572754	...	...	...
2	9	336.77469004	...	...	...
2	10	357.86963676	...	...	...
2	11	387.57588290	...	...	...
2	12	414.11284901	...	...	...
2	13	437.72710109	...	...	...
2	14	467.36842954	...	...	...
2	15	491.40529857	...	...	...

code during the search for the best-fit models (Giammichele et al. 2016). In test case 1 (current fit precision), all parameters are retrieved to a precision of generally slightly less than 1%, for a rather poor value of S^2 of 9.1. The optimization is less sensitive to chemical profiles deeper than the envelope, in particular the central homogeneous oxygen value which gives 6% difference from the reference model. For ground-based data precision, the S^2 reaches four order of magnitude less, for a general improvement of a factor of the order of 100 in precision for most of global stellar parameters. Another four orders of magnitude are gained by switching to *Kepler* data precision. Stellar parameters are retrieved to an impressive precision of ~ 0.0002 %. The homogeneous core is still less precise by one order of magnitude compared to the other stellar parameters.

Figures 4.2, 4.3 and 4.4 depict the maps of the projected merit function S^2, on a log scale, onto the $T_{\rm eff}$-log g and D(He)-D(H) planes, as well as the probability density functions for all

the retrieved stellar parameters for the current fit precision ($\sim$ 10 μHz), the typical ground-based data ($\sim$ 0.1 μHz) and for *Kepler* precision ($\sim$ 0.001 μHz), respectively. White contours show regions where the period fits have S^2 values within the 1-σ, 2-σ,and 3-σ confidence levels relative to the best-fit solution. The gain in precision from current fit precision to *Kepler* data precision is clearly visible from the inspection of the 2-D maps. For current fit precision (Fig. 4.2), the best-fit solution within 1-σ is partly diluted in the background noise. With increasing observational precision, we get much narrower confidence level regions in the 2-D maps from Figures 4.3 and 4.4, as well as much narrower probability distributions for all stellar parameters.

TABLE 4.3 – Results from the three optimizations from the reference star with a variable homogeneous core and with different levels of precision: current fit precision, ground-based data and *Kepler* data precision.

	Test case 1	Test case 2	Test case 3
	$\mu = 0$ $\sigma = 10$ μHz	$\mu = 0$ $\sigma = 0.1$ μHz	$\mu = 0$ $\sigma = 0.001$ μHz
S^2	9.1	9.1 x 10^{-4}	9.2 x 10^{-8}
$T_{\rm eff}$ (K)	11,970 $\pm$ 140 (0.3 %)	12,000.5 $\pm$ 4.0 (0.0042 %)	11,999.99 $\pm$ 0.06 (0.0001 %)
Log g	8.008 $\pm$ 0.030 (0.1 %)	7.9999 $\pm$ 0.0008 (0.0012 %)	8.00000 $\pm$ 0.00001 (0.0001 %)
D(H)	-5.03 ± 0.15 (0.6 %)	-5.000 ± 0.002 (0.02 %)	-5.00000 ± 0.00004 (0.0002 %)
D(He)	-3.07 ± 0.10 (2.3 %)	-3.000 ± 0.003 (0.03 %)	-3.00001 ± 0.00004 (0.0003 %)
Total mass ($M_\odot$)	0.60 $\pm$ 0.02 (0.9 %)	0.5948 $\pm$ 0.0005 (0.002 %)	0.594791 $\pm$ 0.000006 (0.0002 %)
Radius ($R_\odot$)	0.0127 $\pm$ 0.0003 (0.5 %)	0.01277 $\pm$ 0.00001 (0.04 %)	0.01276541 $\pm$ 0.00000008 (0.003 %)
Core oxygen fraction (%)	53 $\pm$ 8 (6 %)	50.0 $\pm$ 0.3 (0.2 %)	50.001 $\pm$ 0.003 (0.002 %)

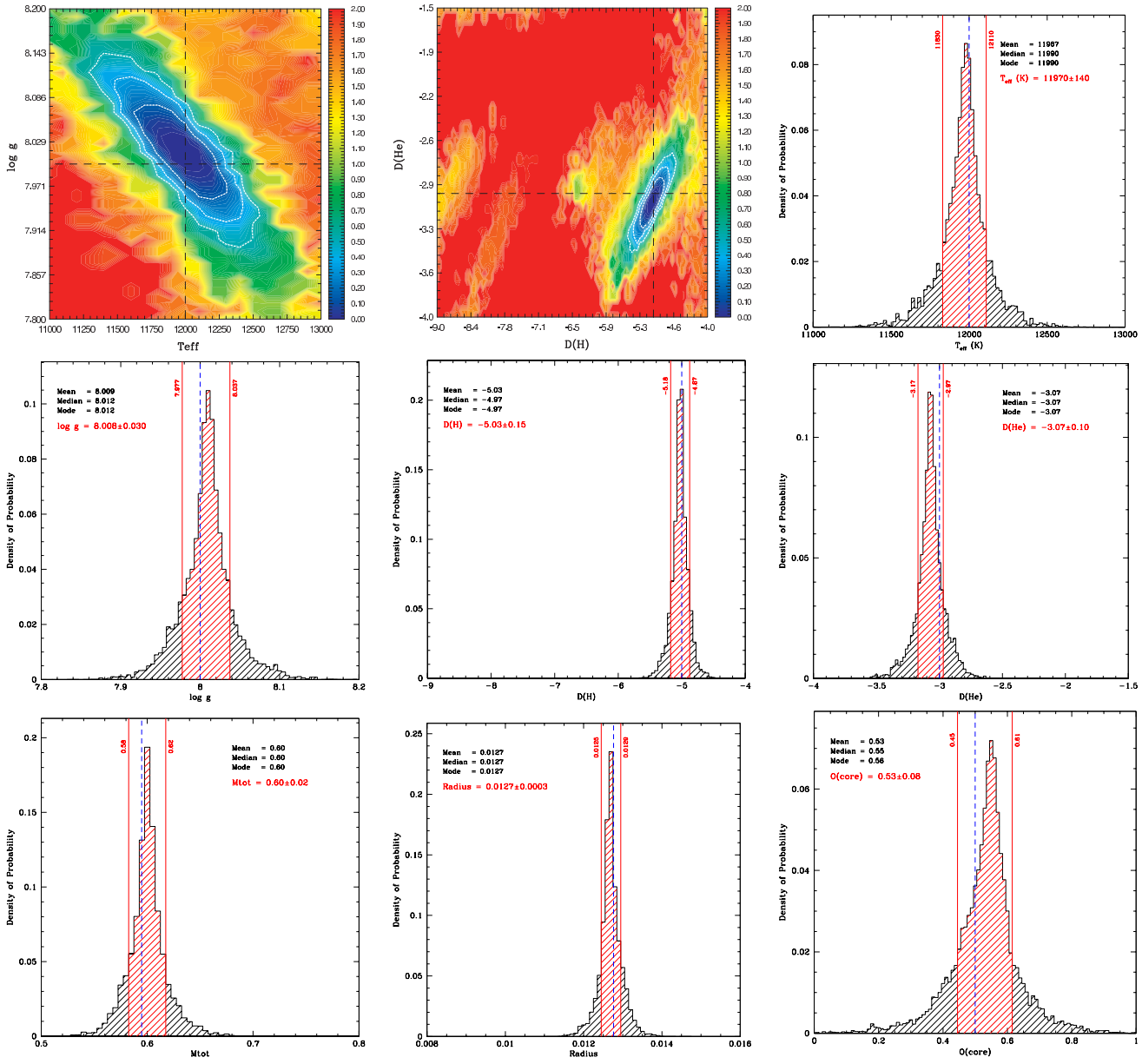

FIGURE 4.2 – Map of the projected merit function S^2 (on a log scale) onto the $T_{\rm eff}$-log g and D(He)-D(H) plane as well as the probability density functions for all the retrieved stellar parameters from the reference star with a variable homogeneous core. The degree of precision of the "observations" is set to the current fit precision level. The red-hatched region between two vertical solid red lines defines the 1σ range, containing 68.3% of the distribution. The blue vertical dashed line indicates the value from the reference model.

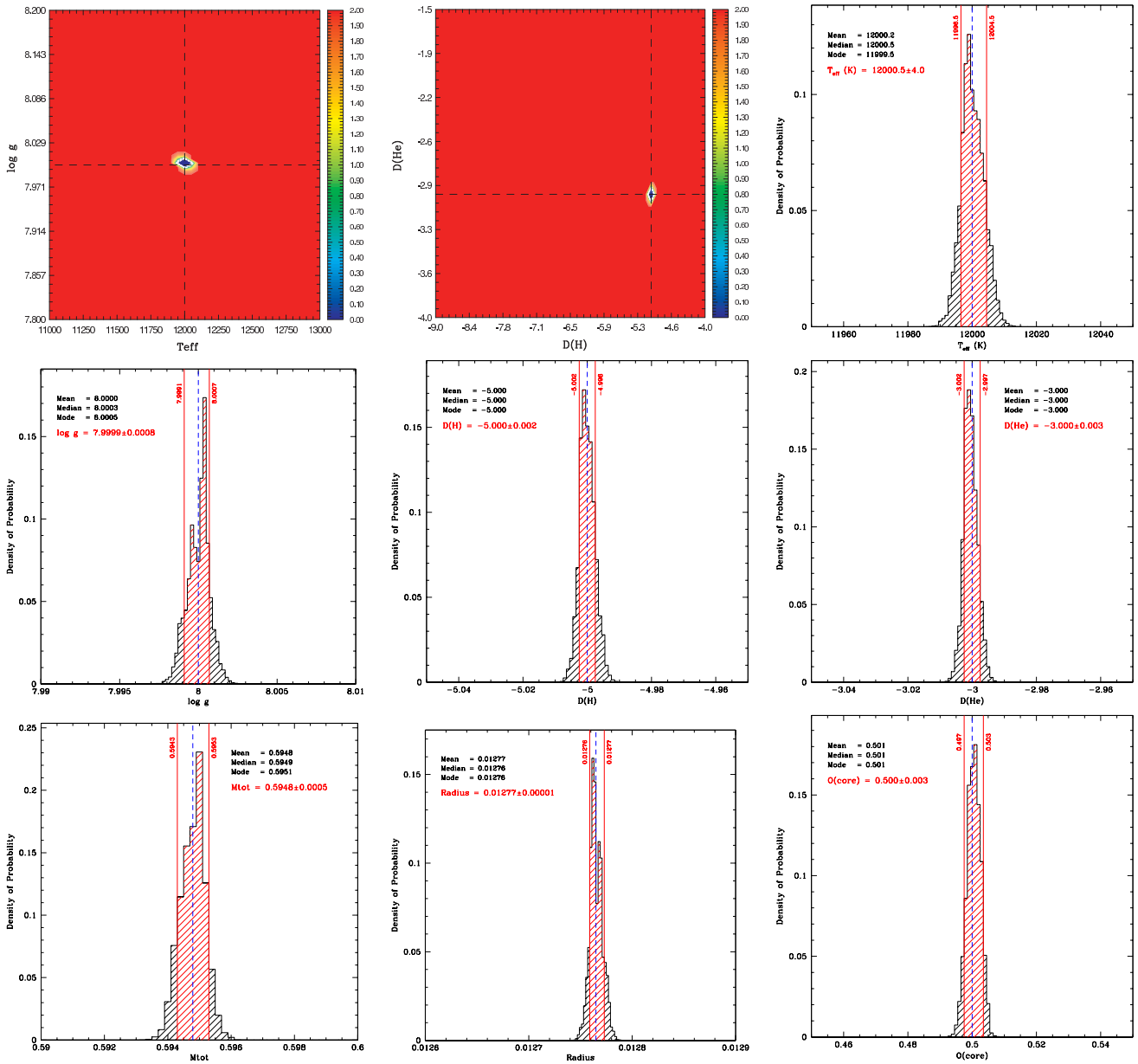

FIGURE 4.3 – Map of the projected merit function S^2 (on a log scale) onto the $T_{\rm eff}$-log g and D(He)-D(H) plane as well as the probability density functions for all the retrieved stellar parameters from the reference star with a variable homogeneous core. The degree of precision of the "observations" is set to the ground-based data level. The red-hatched region between two vertical solid red lines defines the 1σ range, containing 68.3% of the distribution. The blue vertical dashed line indicates the value from the reference model.

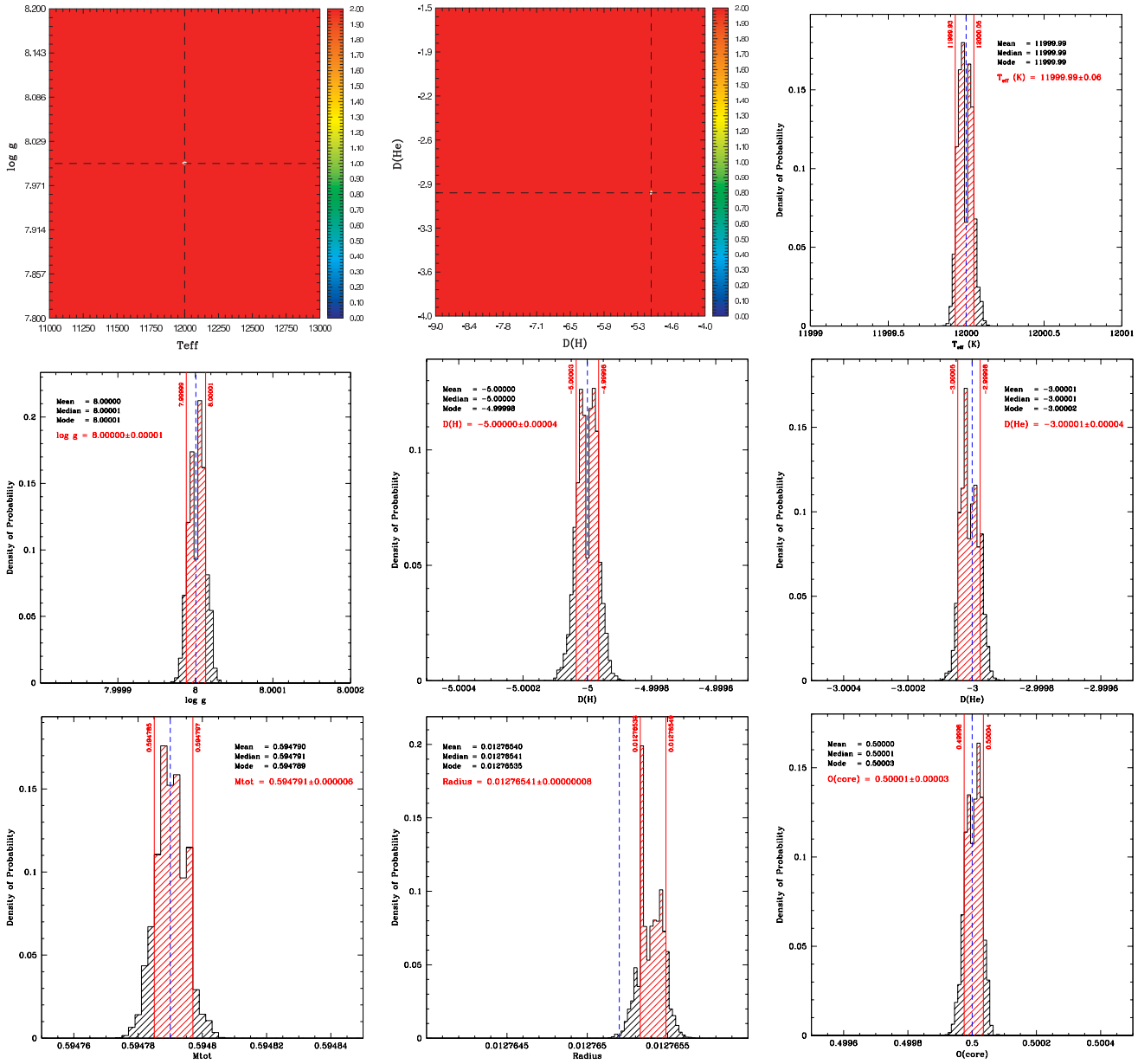

FIGURE 4.4 – Map of the projected merit function S^2 (on a log scale) onto the $T_{\rm eff}$-log g and D(He)-D(H) plane as well as the probability density functions for all the retrieved stellar parameters from the reference star with a variable homogeneous core. The degree of precision of the "observations" is set to the *Kepler* data level. The red-hatched region between two vertical solid red lines defines the 1σ range, containing 68.3% of the distribution. The blue vertical dashed line indicates the value from the reference model.

4.5.2 Core Parametrization with One Transition Zone

The same exercise is conducted bearing in mind the use of the new parametrization. The reference star is this time computed with the adjustable core composition with one transition with the global and shape parameters defined in Table 4.4. Periods are computed from this reference star, and then modified using the same technique as described in the prior section. The modified subset of periods used for the three test cases with different degree of precision is shown in Table 4.5 for reference.

TABLE 4.4 – Parameters of the reference star as well as the search range for the optimization with a one-transition core.

Parameter	Value	Search range
$T_{\rm eff}$ (K)	12,000	11,000 - 13,000
Log g	8.00	7.80 - 8.20
D(H)	-5.0	-9.0 - -4.0
D(He)	-3.0	-4.0 - -1.5
Total mass ($M_\odot$)	$5.9593\text{x}10^{-1}$	...
Radius ($R_\odot$)	$1.2778\text{x}10^{-2}$	...
Core oxygen fraction (%)	70	0 - 100
t_1	-0.3	-0.50 - -0.15
Δt_1	0.06	0.010 - 0.10

In test case 1, where we lean toward the precision of current fits, we obtain after the optimization procedure a best fit solution with a S^2 of 3.1, the same order of magnitude as previously found from the seismic analysis with the homogeneous core. The errors on the retrieved global and shape parameters presented in Table 4.6 (in the first column for the test case 1) are slightly larger than the previous parametrization with the homogeneous core but approximately of the same order of magnitude. The optimization is less sensitive to the shape parameter Δt_1, the error on the value of this specific parameter reaching 20 %. As we move to better precision for the test case 2, with a deviation from the original periods of $\sigma = 0.1$ μHz, the increase in precision is remarkable. The best-fit solution with an S^2 of 3.0 x 10^{-4} gives error on stellar parameters approximately of the order of 0.01%. If seismic analyses were only limited by the precision of the observations from ground-based data we would reach an impressive accuracy of 0.05 % for the determination of the mass for example. Shape parameters are slightly less accurate, with errors of the order of 0.1-1%. By using *Kepler* data, we gain

TABLE 4.5 – Selected and modified periods for the reference star with the one-transition core.

l	k	Period (s)	$\sigma = 10$ μHz	$\sigma = 0.1$ μHz	$\sigma = 0.001$ μHz
1	1	151.75446102	...	...	...
1	**2**	**216.81536572**	**216.79051854**	**216.81511722**	**216.81536323**
1	**3**	**233.92848154**	**233.08021901**	**233.91996835**	**233.92839640**
1	**4**	**315.62545841**	**315.91293268**	**315.62833057**	**315.62548713**
1	**5**	**372.35739163**	**373.82889673**	**372.37204934**	**372.35753820**
1	**6**	**407.89150141**	**405.32576007**	**407.86568322**	**407.89124321**
1	7	456.09585372	...	...	...
2	2	133.59921893	...	...	...
2	**3**	**151.31237295**	**151.26561948**	**151.31190527**	**151.31236828**
2	**4**	**182.34310127**	**182.45124394**	**182.34418206**	**182.34311208**
2	**5**	**216.56591828**	**216.20719723**	**216.56232518**	**216.56588235**
2	**6**	**241.19856963**	**241.88556292**	**241.20542025**	**241.19863814**
2	**7**	**264.34846623**	**264.24494250**	**264.34743059**	**264.34845587**
2	8	299.27669790	...	...	...
2	9	328.49590688	...	...	...
2	10	350.35377602	...	...	...
2	11	385.35347602	...	...	...
2	12	407.54276181	...	...	...
2	13	422.40023701	...	...	...
2	14	447.50516837	...	...	...
2	15	475.14880300	...	...	...

a factor of a hundred with reference to the precision of ground-based data. The S^2 obtained in that particular test case 3, is of 6.1 x 10^{-7} and the errors on the global parameters are $\sim$ 0.0002 %, like for the seismic mass measurement. As before the shape parameters, the core oxygen central value and Δt_1, are defined less precisely than the global parameters, while the transition t_1 is well retrieved.

Figures 4.5, 4.6 and 4.7 show as before the maps of the projected merit function S^2 onto the $T_{\rm eff}$-log g and D(He)-D(H) plane as well as the probability density functions for all the retrieved stellar parameters for the current fit precision ($\sim$ 10 μHz), the typical ground-based data ($\sim$ 0.1 μHz) and for *Kepler* precision ($\sim$ 0.001 μHz) respectively. The 2-D maps of Figure 4.5 show a slightly shifted solution, if we only consider the 1-σ region, but fall well within the 2-σ region. The slight bias is probably generated by the random numbers applied to the selected periods, which tip the balance towards a specific region. If we consider only

the precision of the current fits, we can see that the solution is obscured in the background noise. Based on the histograms, the seismic optimization is clearly not sensitive enough to the parameter Δt_1 at this level of precision. With increasing observational precision, from ground-based data to *Kepler* data precision, we get much narrower confidence level regions in the 2-D maps from figures 4.6 and 4.7, as well as much narrower probability distributions for all stellar parameters, including the shape parameters of the core. The new adjustable core parametrization behave well under the seismic analysis and allow to retrieve with a remarkable precision the stellar and shape parameters of the reference star.

TABLE 4.6 – Results from the three optimizations from the reference star with a one-transition core and with different levels of precision: current fit precision, ground-based data and *Kepler* data precision.

	Test case 1 $\mu = 0$ $\sigma = 10$ μHz	Test case 2 $\mu = 0$ $\sigma = 0.1$ μHz	Test case 3 $\mu = 0$ $\sigma = 0.001$ μHz
S^2	3.1	3.0×10^{-4}	6.1×10^{-7}
$T_{\rm eff}$ (K)	11,770 ± 120 (1.9 %)	11,998.5 ± 3.0 (0.01%)	11999.96 ± 0.05 (0.0003%)
Log g	8.045 ± 0.022 (0.6 %)	8.0006 ± 0.0005 (0.008%)	8.000005 ± 0.000008 (0.0001%)
D(H)	−5.17 ± 0.10 (3.4 %)	−5.002 ± 0.02 (0.04%)	−5.00002 ± 0.0000025 (0.0004%)
D(He)	−3.15 ± 0.06 (5.0 %)	−3.002 ± 0.0012 (0.07%)	−3.00002 ± 0.00002 (0.0007%)
Total mass ($M_\odot$)	0.62 ± 0.01 (4.0 %)	0.5962 ± 0.0003 (0.05%)	0.595930 ± 0.000003 (0.0002%)
Radius ($R_\odot$)	0.0124 ± 0.0002 (3.0 %)	0.012772 ± 0.000004 (0.05%)	0.0127775 ± 0.0000001 (0.004%)
Core oxygen fraction (%)	66 ± 3 (5.7 %)	0.6998 ± 0.0015 (0.03%)	0.70000 ± 0.00002 (0.001%)
t_1	−0.300 ± 0.018 (0.3 %)	−0.3003 ± 0.0006 (0.1 %)	−3.00000 ± 0.000008 (0.0003%)
Δt_1	0.072 ± 0.015 (20 %)	0.0607 ± 0.0015 (1.2 %)	0.060015 ± 0.000013(0.03%)

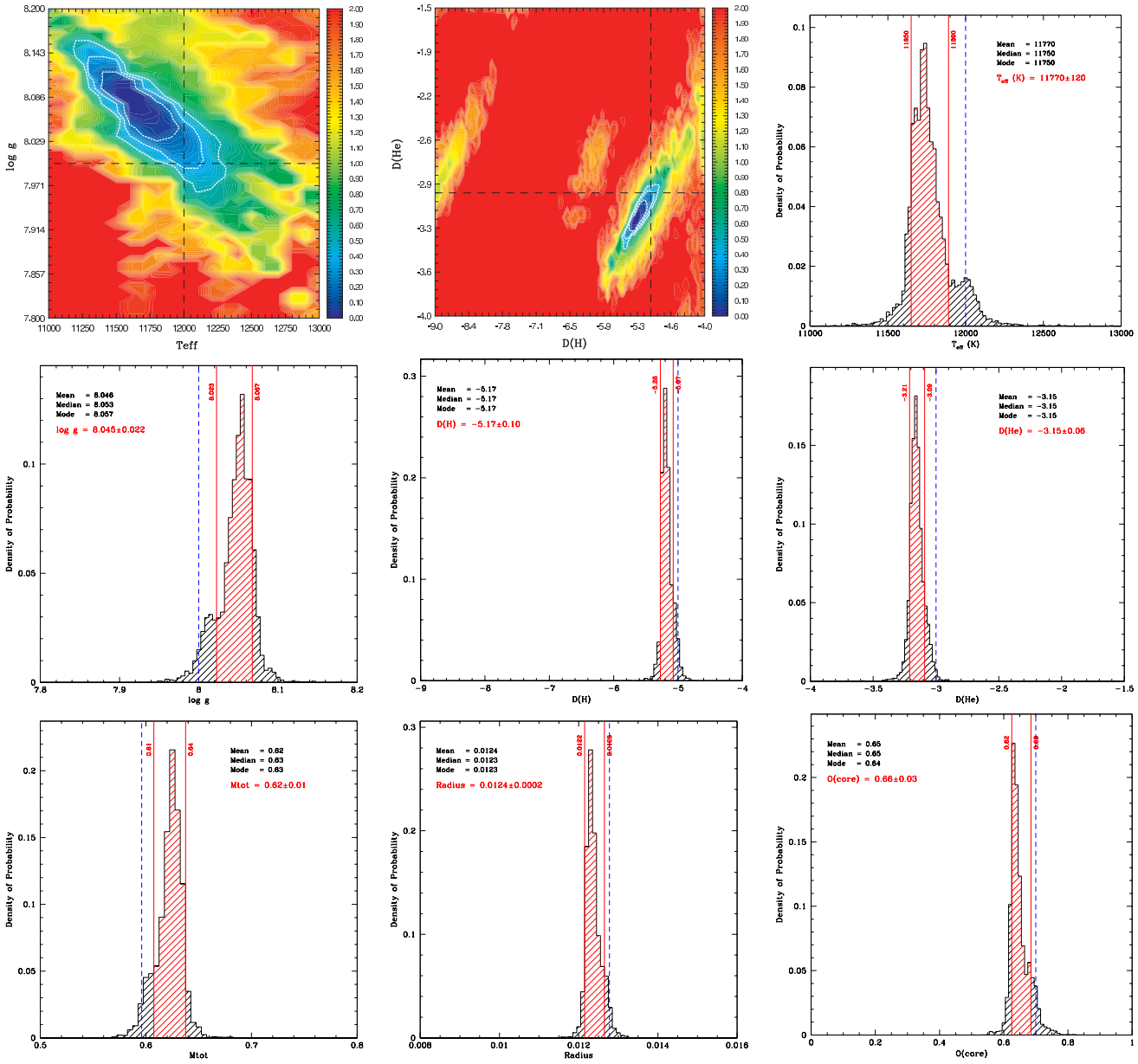

FIGURE 4.5 – Map of the projected merit function S^2 (on a log scale) onto the $T_{\rm eff}$-log g and D(He)-D(H) plane as well as the probability density functions for all the retrieved stellar parameters from the reference star with one-transition core. The degree of precision of the "observations" is set to the current fit precision level. The red-hatched region between two vertical solid red lines defines the 1σ range, containing 68.3% of the distribution. The blue vertical dashed line indicates the value from the reference model.

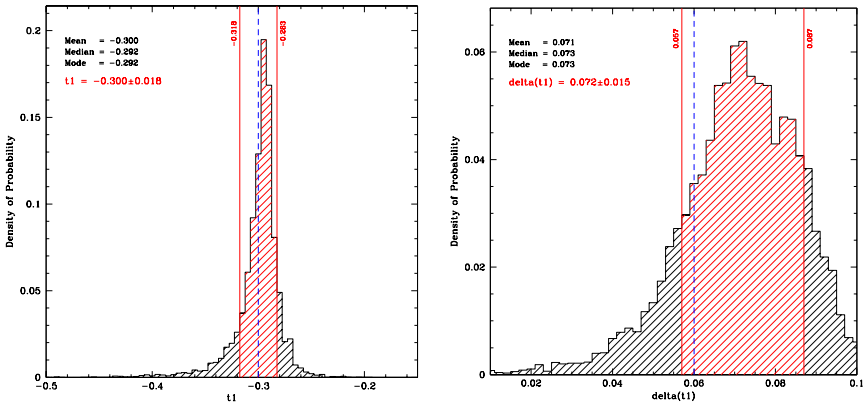

FIGURE 4.5 – Continued.

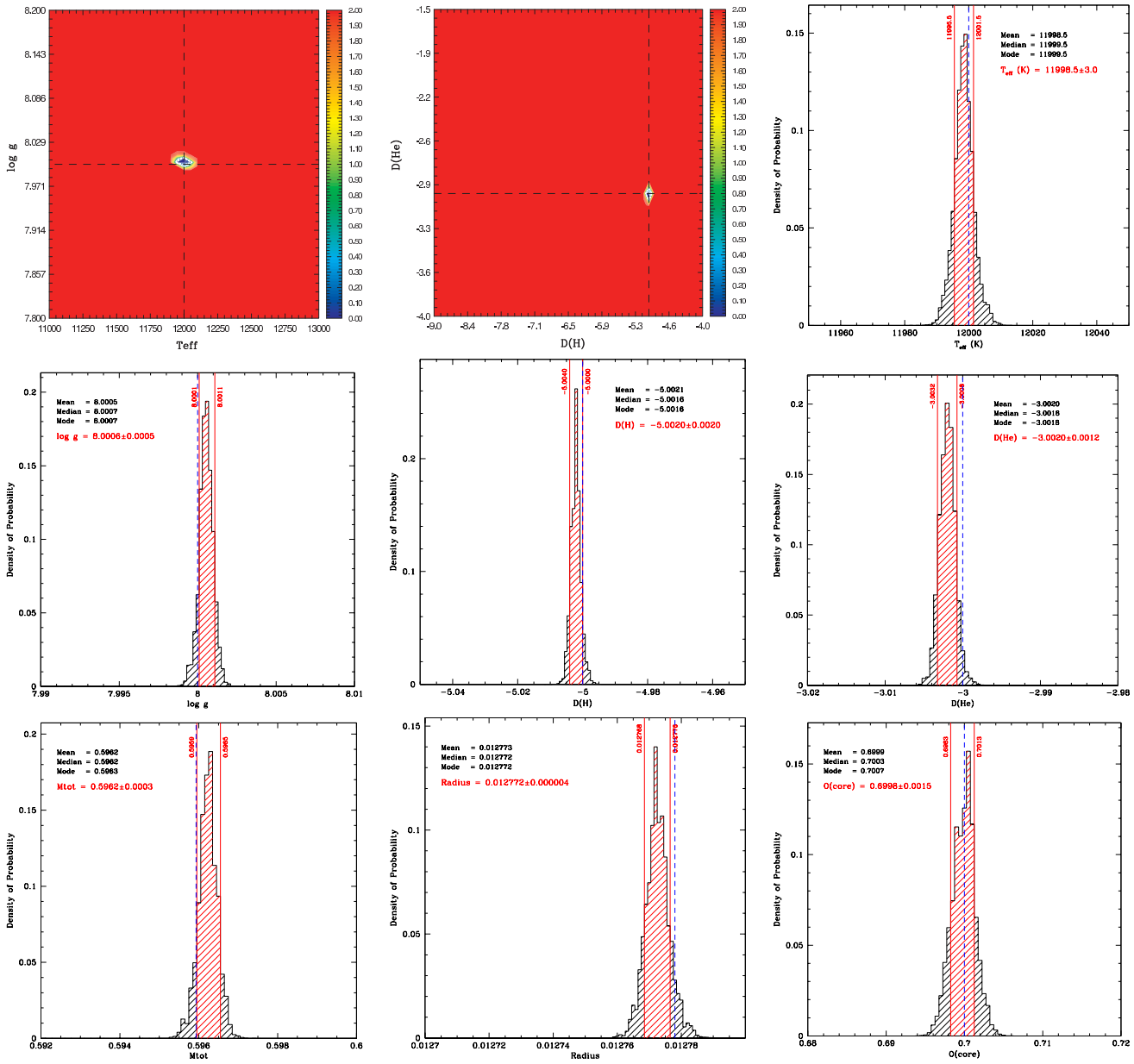

FIGURE 4.6 – Map of the projected merit function S^2 (on a log scale) onto the $T_{\rm eff}$-log g and D(He)-D(H) plane as well as the probability density functions for all the retrieved stellar parameters from the reference star with one-transition core. The degree of precision of the "observations" is set to the ground-based data precision level. The red-hatched region between two vertical solid red lines defines the 1σ range, containing 68.3% of the distribution. The blue vertical dashed line indicates the value from the reference model.

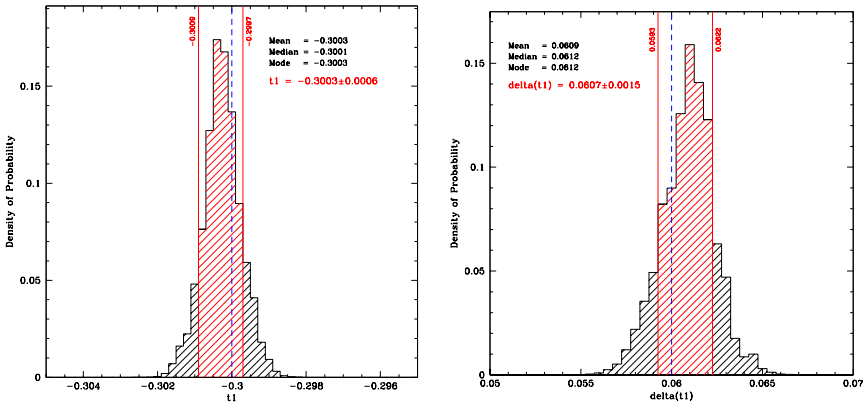

FIGURE 4.6 – Continued.

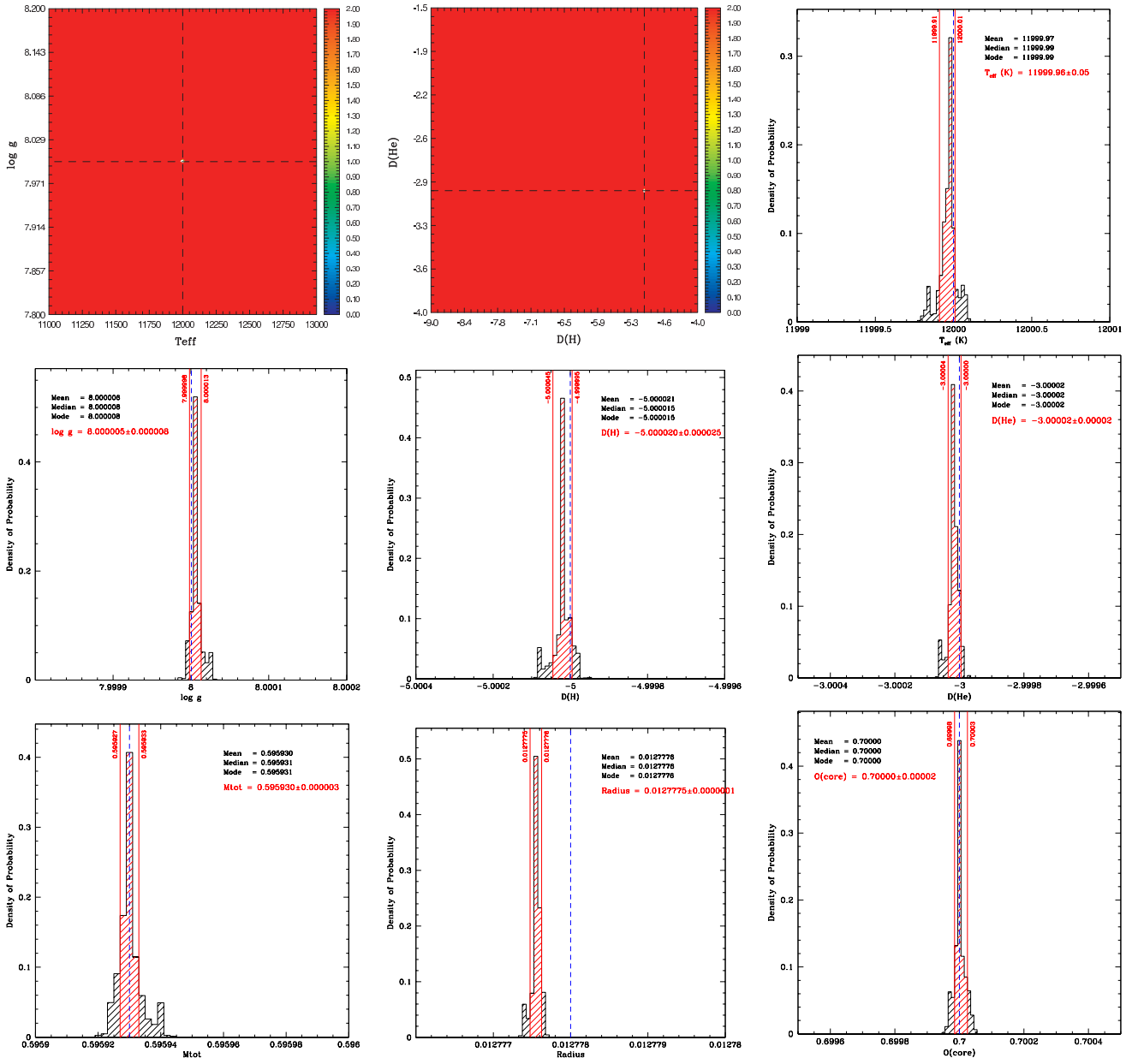

FIGURE 4.7 – Map of the projected merit function S^2 (on a log scale) onto the $T_{\rm eff}$-log g and D(He)-D(H) plane as well as the probability density functions for all the retrieved stellar parameters from the reference star with one-transition core. The degree of precision of the "observations" is set to the *Kepler* data precision level. The red-hatched region between two vertical solid red lines defines the 1σ range, containing 68.3% of the distribution. The blue vertical dashed line indicates the value from the reference model.

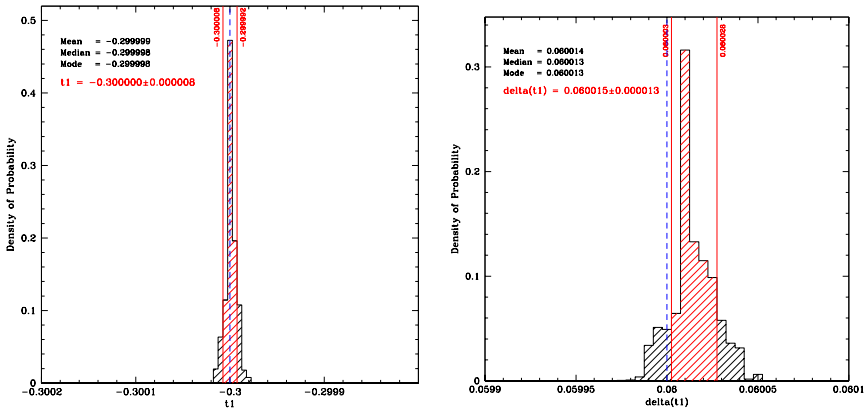

FIGURE 4.7 – Continued.

4.5.3 Core Parametrization with Two Transition Zones

For the last test, we use the full potential and flexibility of the new core parametrization using the two transitions, for the reference star, and for the optimization. The parameters of the standard reference star are presented in Table 4.7 as well as the search range for each stellar and shape parameter. Periods are computed again from this reference star, and then modified using the same technique as already described. The modified subset of periods used for the three test cases with different degree of precision is shown in Table 4.8.

TABLE 4.7 – Parameters of the reference star as well as the search range for the optimization with a two-transition core.

Parameter	Value	Search range
$T_{\rm eff}$ (K)	12,000	11,000 - 13,000
Log g	8.00	7.80 - 8.20
D(H)	-5.0	-9.0 - -4.0
D(He)	-3.0	-4.0 - -1.5
Total mass ($M_\odot$)	$5.9521\text{x}10^{-1}$	...
Radius ($R_\odot$)	$1.2770\text{x}10^{-2}$	...
Core oxygen fraction (%)	70	0 - 100
t_1	-0.3	-0.50 - -0.15
Δt_1	0.06	0.010 - 0.10
t_1 oxygen (%)	40	0 - 100
t_2	-1.5	-2.00 - -0.60
Δt_2	0.08	0.010 - 0.10
t_2 oxygen (%)	20	0 - 100

The same pattern can be observed for the recovered parameters from the two-transition parametrization as the variable homogeneous core and the one-transition parametrization for the core. The increase in precision on the retrieved stellar parameters gained during the transition from current fit precision to ground-based data to *Kepler* data is quite remarkable, a factor of 100 at each transition. If we examine Table 4.9 into more details, we notice that shape parameters are slightly less accurate, especially Δt_1 and Δt_2 for which the error on the obtained value reaches $\sim 30\%$, for the example with current fit precision. This situation is corrected as we increase the precision on the observations from either ground-based or *Kepler* data precision. To precisely identify the shape parameters defining the core, the precision of our current seismic fits must reach at least the precision of 0.1 μHz.

TABLE 4.8 – Selected and modified periods for the reference star with the two-transition core.

l	k	Period (s)	$\sigma = 10$ μHz	$\sigma = 0.1$ μHz	$\sigma = 0.001$ μHz
1	1	151.653409370	...	...	...
1	**2**	**228.787742059**	**228.76007521**	**228.78746536**	**228.78773929**
1	**3**	**264.030696374**	**263.92742134**	**264.02966322**	**264.03068604**
1	**4**	**315.524781925**	**315.81207274**	**315.52765225**	**315.52481063**
1	**5**	**369.012046557**	**370.45717843**	**369.02644206**	**369.01219051**
1	**6**	**399.888135738**	**397.42178861**	**399.86332075**	**399.88788757**
1	7	455.034684809	...	...	...
2	2	133.361713913	...	...	...
2	**3**	**178.011613603**	**177.94690859**	**178.01096632**	**178.01160713**
2	**4**	**183.545746313**	**183.65532062**	**183.54684141**	**183.54575726**
2	**5**	**216.944553720**	**216.58457827**	**216.94094804**	**216.94451766**
2	**6**	**238.597497023**	**237.71509923**	**238.58864062**	**238.59740846**
2	**7**	**263.710718836**	**264.53215547**	**263.71890795**	**263.71080072**
2	8	298.974939191	...	...	...
2	9	327.792644523	...	...	...
2	10	348.111904002	...	...	...
2	11	380.831879546	...	...	...
2	12	405.577093095	...	...	...
2	13	427.351916311	...	...	...
2	14	445.672564712	...	...	...
2	15	473.357290231	...	...	...

Figures 4.8, 4.9 and 4.10 show again the maps of the projected merit function S^2 onto the $T_{\rm eff}$-log g and D(He)-D(H) plane as well as the probability density functions for all the retrieved stellar parameters for the current fit precision ($\sim$ 10 μHz), the typical ground-based data ($\sim$ 0.1 μHz) and for *Kepler* precision ($\sim$ 0.001 μHz) respectively. The 2-D maps of Figure 4.8 present again a slightly shifted solution, if we only consider the 1-σ region, but fall well within the 2-σ region. If we consider only the precision of the current fits, we can see that the solution is polluted by the background noise. Based on the histograms, the seismic optimization is clearly not sensitive enough to the parameter Δt_1 and Δt_2 at this level of precision. With increasing precision, from ground-based data to *Kepler* data precision, we get much narrower confidence level regions in the 2-D maps from Figures 4.9 and 4.10, as well as much narrower probability distributions for all stellar parameters. The values of the majority of the shape parameters of the reference star do not fall within the 1-σ probability distribution

of the recovered parameters. This is mainly caused by the deficiency in the sampling during the optimization, since the colossal increase in the parameter space with the addition of six new parameters was not balanced out by an additional initial population of the genetic algorithm during the optimization. The initial population was kept constant at a thousand of individuals for the three parametrizations.

In summary, our seismic optimization is perfectly capable of retrieving stellar and shape parameters from a reference star with different degree of precision in the "observational" data. If the limiting factor is purely observational, stellar and shape parameters are recovered to a remarkable precision. Although our asteroseismic method gives robust, precise and accurate constraints on either stellar or shape parameters, the limiting factor is not the precision of the observations but the constitutive physics behind our models that need to be adressed in order to go beyond current achievements. Moreover, if we want better constraints on the core chemical profiles, we need to improve the quality of the current fits.

TABLE 4.9 – Results from the three optimizations from the reference star with a two-transition core and with different levels of precision: current fit precision, ground-based data and *Kepler* data precision.

	Test case 1	Test case 2	Test case 3
	$\mu = 0$ $\sigma = 10$ μHz	$\mu = 0$ $\sigma = 0.1$ μHz	$\mu = 0$ $\sigma = 0.001$ μHz
S^2	2.8	2.7 x 10^{-4}	2.9 x 10^{-8}
$T_{\rm eff}$ (K)	11880 ± 90 (1 %)	11999.0 ± 1.5 (0.008 %)	11999.98 ± 0.05 (0.0002%)
Log g	8.037 ± 0.020 (0.5 %)	8.00052 ± 0.00015 (0.007 %)	8.000005 ± 0.000013 (0.001%)
D(H)	−5.15 ± 0.08 (3 %)	−5.002 ± 0.0012 (0.04 %)	−5.00002 ± 0.00004 (0.0004%)
D(He)	−3.15 ± 0.06 (5 %)	−3.002 ± 0.001 (0.07 %)	−3.00005 ± 0.00003 (0.002 %)
Total mass ($M_\odot$)	0.62 ± 0.01 (4 %)	0.5955 ± 0.0002 (0.05 %)	0.595209 ± 0.000006 (0.0002 %)
Radius ($R_\odot$)	0.0124 ± 0.0002 (3 %)	0.012765 ± 0.000002 (0.04 %)	0.0127698 ± 0.0000001 (0.002%)
Core oxygen fraction (%)	70 ± 5 (1 %)	70.0 ± 0.1 (0.1 %)	70.005 ± 0.002 (0.007 %)
t_1	−0.310 ± 0.013 (3 %)	−0.3004 ± 0.0003 (0.1 %)	−0.29989 ± 0.00001 (0.04 %)
Δt_1	0.044 ± 0.023 (27 %)	0.0607 ± 0.0010 (1.2 %)	0.05956 ± 0.00004 (0.07 %)
t_1 oxygen (%)	45 ± 5 (13 %)	40 ± 0.2 (0.3 %)	40.038 ± 0.003 (0.1 %)
t_2	−1.61 ± 0.10 (7 %)	−1.502 ± 0.002 (0.1 %)	−1.5009 ± 0.0001 (0.06 %)
Δt_2	0.057 ± 0.028 (29 %)	0.0803 ± 0.0015 (0.4 %)	0.08008 ± 0.00047 (0.1 %)
t_2 oxygen (%)	15 ± 4 (25 %)	20.1 ± 0.1 (0.5 %)	19.96 ± 0.01 (0.2 %)

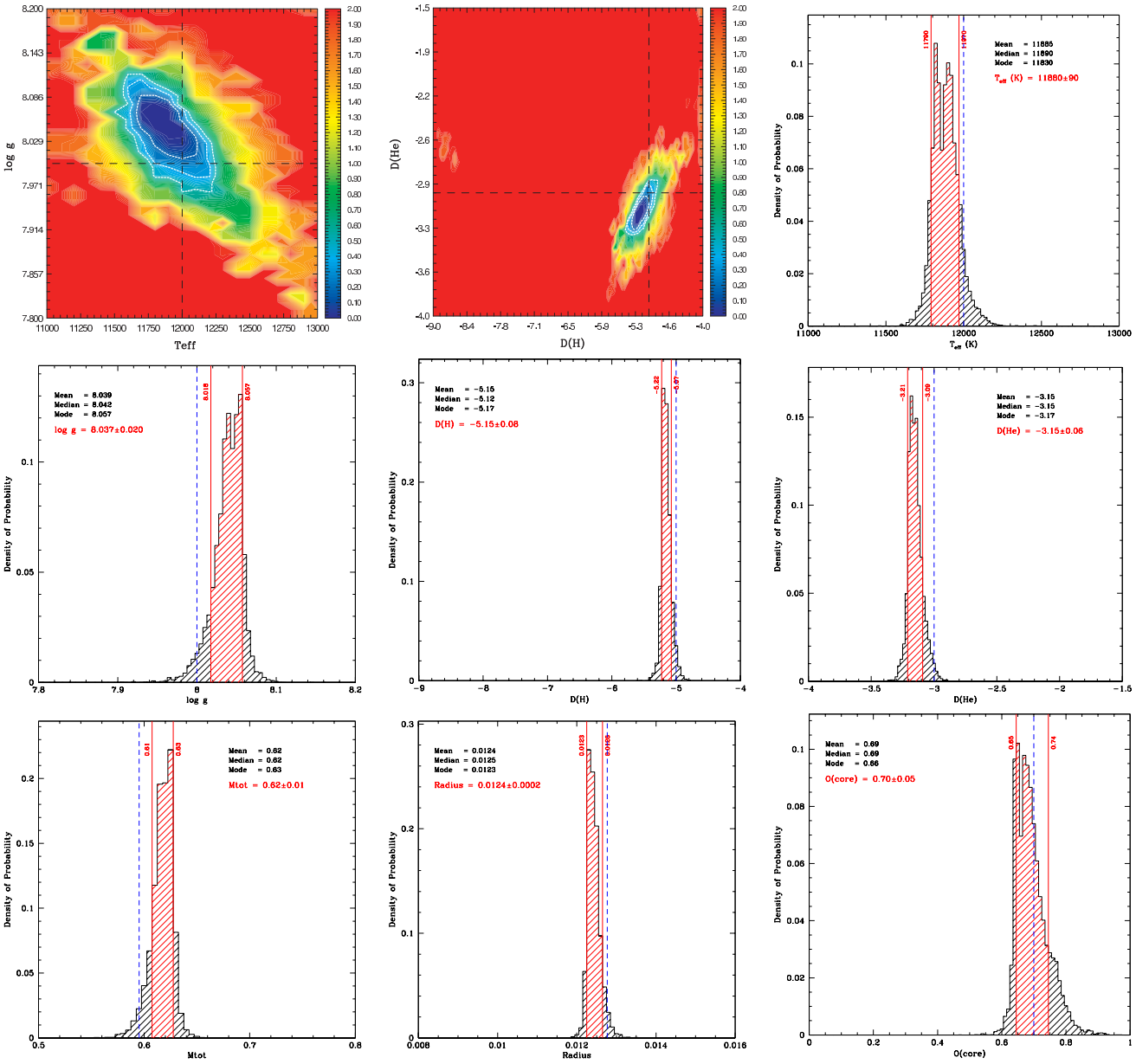

FIGURE 4.8 – Map of the projected merit function S^2 (on a log scale) onto the $T_{\rm eff}$-log g and D(He)-D(H) plane as well as the probability density functions for all the retrieved stellar parameters from the reference star with two-transition core. The degree of precision of the "observations" is set to the current fit precision level. The red-hatched region between two vertical solid red lines defines the 1σ range, containing 68.3% of the distribution. The blue vertical dashed line indicates the value from the reference model.

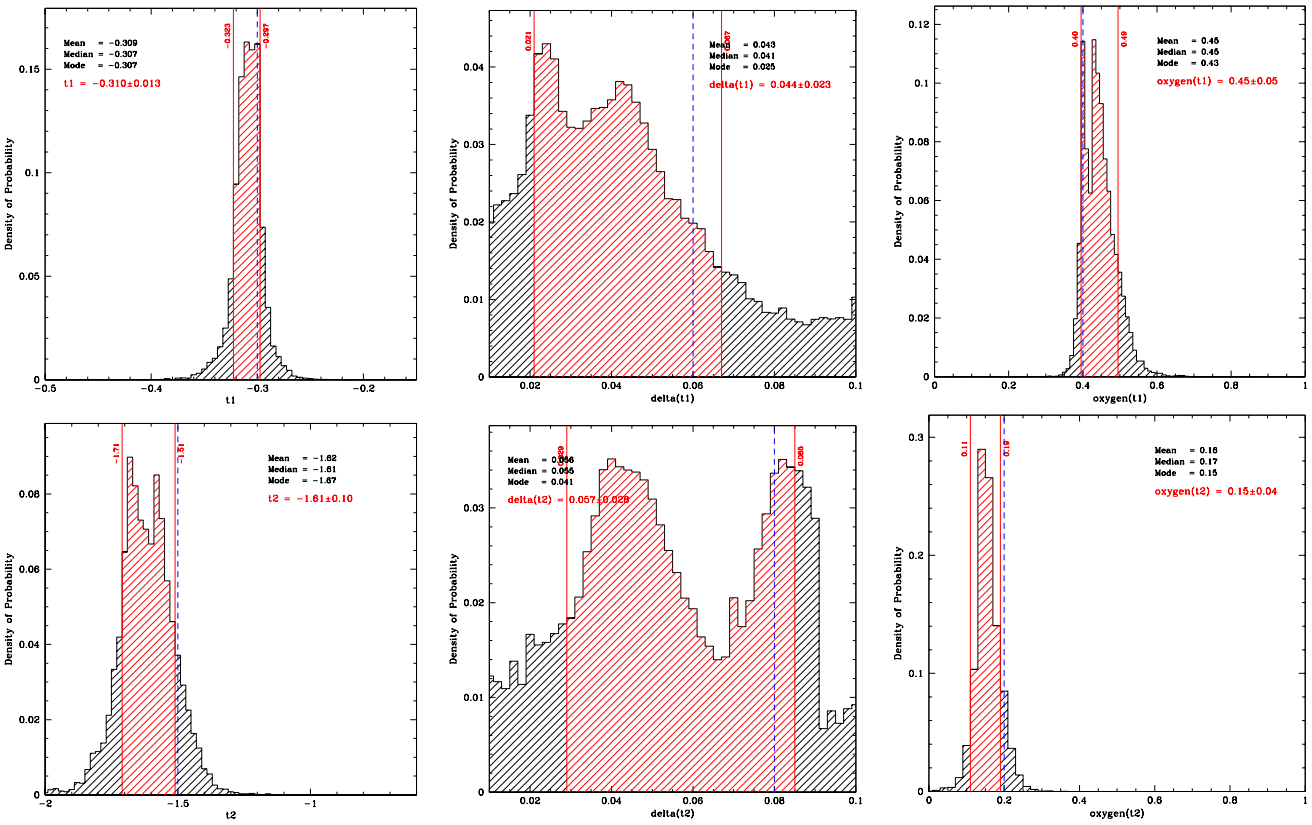

FIGURE 4.8 – Continued.

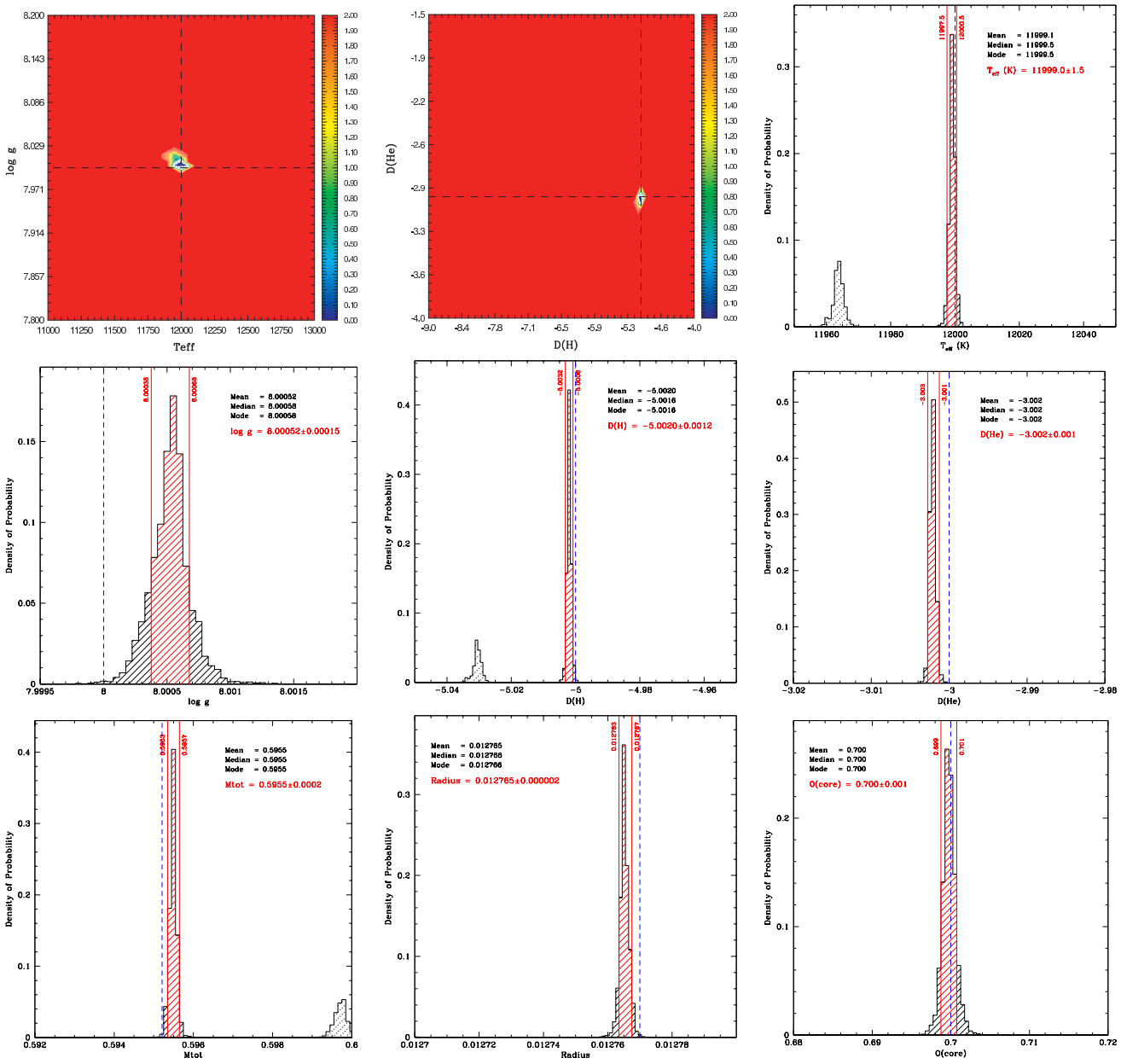

FIGURE 4.9 – Map of the projected merit function S^2 (on a log scale) onto the $T_{\rm eff}$-log g and D(He)-D(H) plane as well as the probability density functions for all the retrieved stellar parameters from the reference star with two-transition core. The degree of precision of the "observations" is set to the ground-based data precision level. The red-hatched region between two vertical solid red lines defines the 1σ range, containing 68.3% of the distribution. The blue vertical dashed line indicates the value from the reference model.

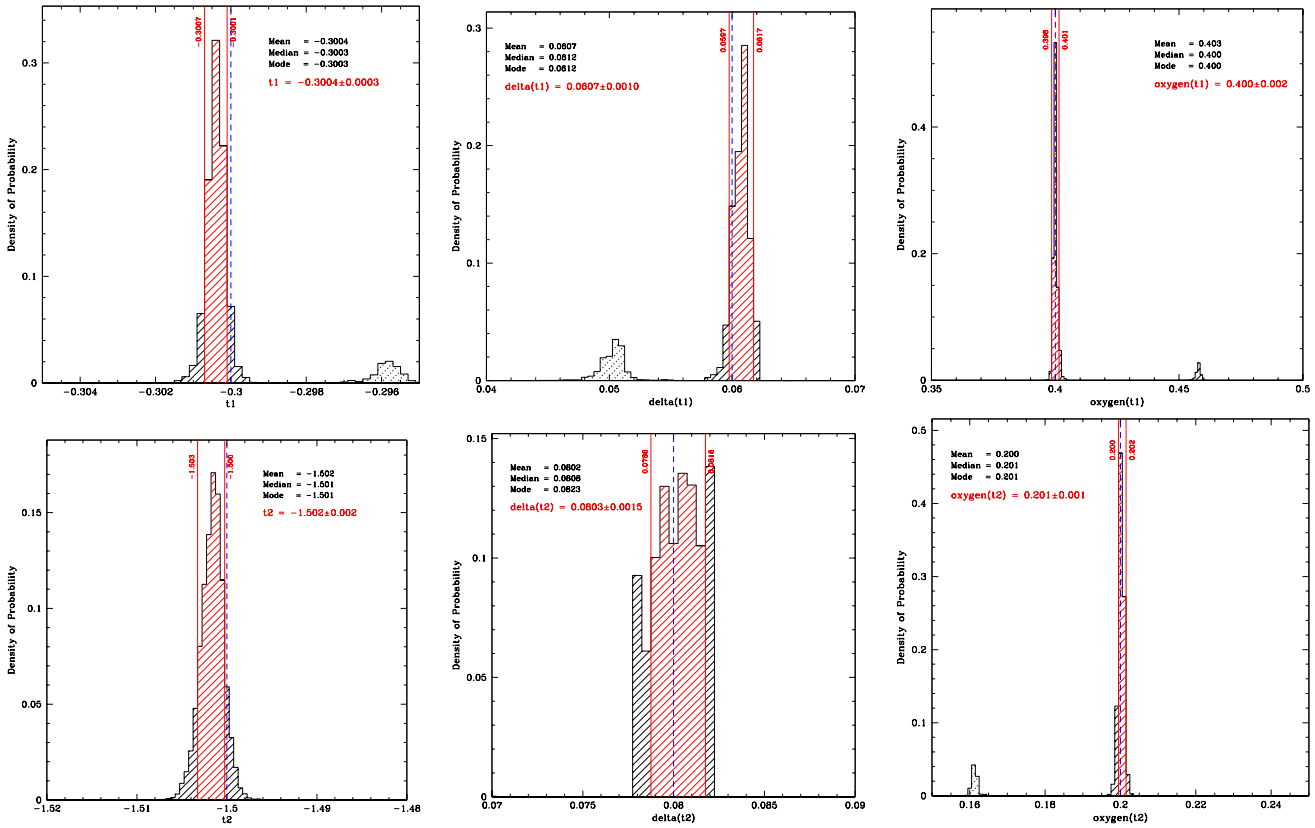

FIGURE 4.9 – Continued.

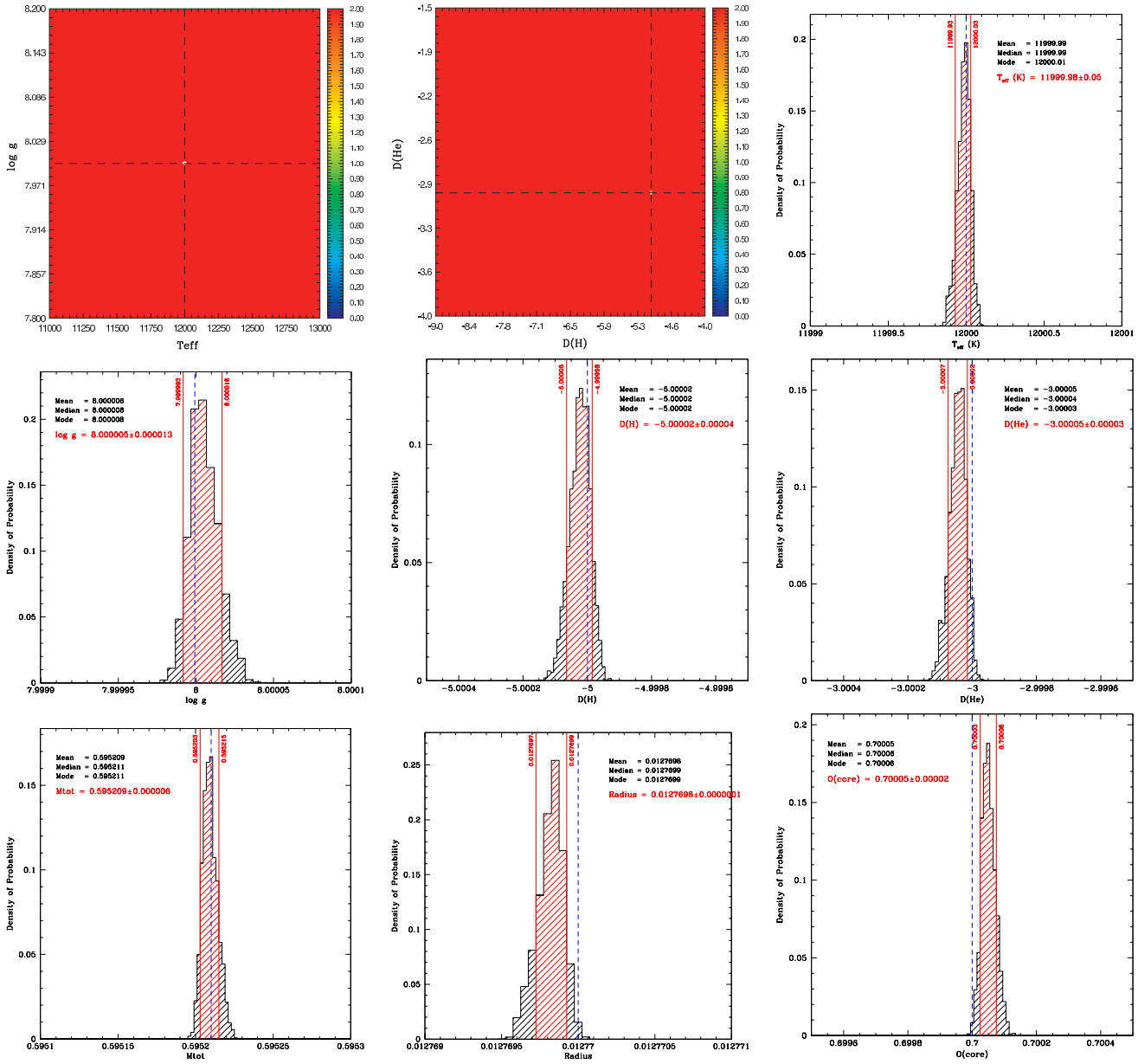

FIGURE 4.10 – Map of the projected merit function S^2 (on a log scale) onto the $T_{\rm eff}$-log g and D(He)-D(H) plane as well as the probability density functions for all the retrieved stellar parameters from the reference star with two-transition core. The degree of precision of the "observations" is set to the *Kepler* data precision level. The red-hatched region between two vertical solid red lines defines the 1σ range, containing 68.3% of the distribution. The blue vertical dashed line indicates the value from the reference model.

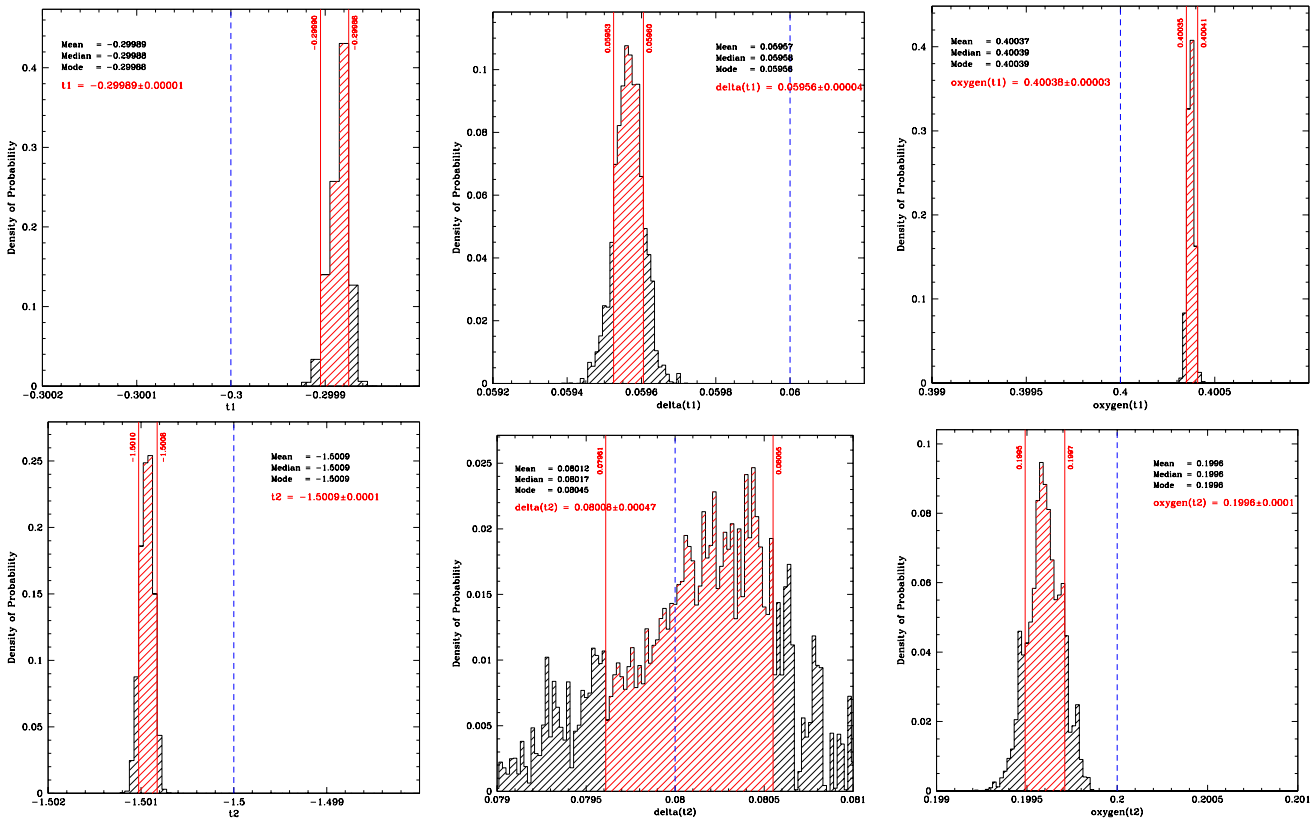

FIGURE 4.10 – Continued.

4.6 TESTS WITH RANDOM PERIOD SEQUENCES

In this section, we perform tests with randomly generated period sets. When we perform a seismic analysis, the optimization process is governed by the minimization of the merit function. During the optimization, the merit function will take on different values as we search in parameter space. The point here is that there will always be a minimum value found at the end of the process. But this minimum value is not necessarily statistically significant. This test will allow to estimate an average value for the best-fit solution of the optimization process over which any random set of periods can be fitted. This average value will define the threshold for credible seismic analyses. Obviously, this test should be performed a large number of times in order to get significant statistics, but because of calculating power limits and time constraints, we only performed this test five times for each core parametrization presented earlier. This will still give a rough idea of what to expect when the merit function is calculated.

Periods are randomly computed with the only restriction that they have to be between 100 and 500 seconds, in order to remain in the same range as the previous tests and calculations. Five random tests are performed, and the pulsation spectra used in each case are presented in Table 4.10.

TABLE 4.10 – Pulsation spectra for the five test cases.

Case 1	Case 2	Case 3	Case 4	Case 5
109 s	128 s	111 s	118 s	113 s
125 s	173 s	113 s	148 s	143 s
148 s	179 s	136 s	199 s	193 s
228 s	183 s	146 s	207 s	234 s
282 s	196 s	281 s	362 s	247 s
285 s	209 s	283 s	363 s	301 s
329 s	236 s	323 s	367 s	326 s
374 s	377 s	338 s	389 s	367 s
400 s	388 s	399 s	430 s	450 s
423 s	486 s	490 s	455 s	460 s

Results for the five test cases for the three differents core definitions are presented in Table 4.11. The merit function S^2, an unweighted χ^2, as well as the $< \Delta\nu >$ and the $< \Delta P >$ are

disclosed. The first observation that can be made out of this test, is that when we go through the columns, the values of either the S^2 or the $< \Delta\nu >$ and $< \Delta P >$ are greatly varying. Since we are just interested in an estimation of the threshold for a credible seismic analysis, these five test cases are sufficient for having a rough idea of the value of S^2 above which the fit must be considered as not statistically significant. The second observation is that the increase in flexibility of the core definition from the varying homogeneous core to the one- and two-transition parametrization leads to a decrease of the "passing" values of the merit function and the average frequency and period differences. The threshold is obviously not the same if we are using an homogeneous core or a more complex core chemical profile parametrization, being more stringent in the latter case.

For the case of the varying homogeneous core, we have to realize that the merit function went to as low as about fifteen or so, even if the median value and the mean are quite higher. The corresponding average period dispersion is around 2 s. For the one- and the two-transition parametrization, the dispersion between the values is less important. The mean and median values for S^2 are of the order of ten. In these cases the average period difference is less than 1 s. Depending on the parametrization used, we can define a conservative threshold of about 10 for the unweighted χ^2 for a subset of 10 periods, but, more significatively, of about 1 s for the average period dispersion.

TABLE 4.11 – Results from the five random cases.

	Case 1	Case 2	Case 3	Case 4	Case 5	Mean	Median
Hom. core:	$S^2 = 23.9$	$S^2 = 209.0$	$S^2 = 212.0$	$S^2 = 57.6$	$S^2 = 15.2$	103.5	57.6
	$< \Delta\nu > = 35.1$ μHz	$< \Delta\nu > = 90.6$ μHz	$< \Delta\nu > = 159.1$ μHz	$< \Delta\nu > = 41.6$ μHz	$< \Delta\nu > = 16.1$ μHz	68.5	41.6
	$< \Delta P > = 1.6$ s	$< \Delta P > = 3.8$ s	$< \Delta P > = 3.9$ s	$< \Delta P > = 2.0$ s	$< \Delta P > = 0.9$ s	2.44	2.0
1 transition:	$S^2 = 11.3$	$S^2 = 22.0$	$S^2 = 4.0$	$S^2 = 31.1$	$S^2 = 6.6$	15.0	11.3
	$< \Delta\nu > = 10.5$ μHz	$< \Delta\nu > = 34.2$ μHz	$< \Delta\nu > = 12.7$ μHz	$< \Delta\nu > = 17.8$ μHz	$< \Delta\nu > = 7.6$ μHz	16.6	12.7
	$< \Delta P > = 0.7$ s	$< \Delta P > = 1.2$ s	$< \Delta P > = 0.5$s	$< \Delta P > = 1.3$ s	$< \Delta P > = 0.6$ s	0.9	0.7
2 transitions:	$S^2 = 6.6$	$S^2 = 9.0$	$S^2 = 1.9$	$S^2 = 10.3$	$S^2 = 3.7$	6.3	6.6
	$< \Delta\nu > = 21.6$ μHz	$< \Delta\nu > = 18.0$ μHz	$< \Delta\nu > = 12.0$ μHz	$< \Delta\nu > = 10.9$ μHz	$< \Delta\nu > = 13.0$ μHz	15.1	13.0
	$< \Delta P > = 0.5$ s	$< \Delta P > = 0.7$ s	$< \Delta P > = 0.3$ s	$< \Delta P > = 0.9$ s	$< \Delta P > = 0.5$ s	0.6	0.5

4.7 TESTING THE REPRODUCIBILITY OF THE CHEMICAL STRATIFICATION RESULTING FROM EVOLUTIONARY PROCESSES

In this section, we investigate the flexibility of the new parametrization and its capability to reproduce the chemical stratification derived from evolutionary models. For this test, we start with a static model with the definition of the core chemical profiles coming from Maurizio Salaris' evolutionary models. The core profile is obtained by interpolating between the available profiles derived for different masses by Salaris et al. (2008). The resulting core profile is then smoothed out to remove as much as possible the numerical noise still unfortunately present in the resulting curve. The retained static model has the following standard global parameters listed in Table 4.12. The search range used in the optimization process for every parameter of interest is also indicated.

TABLE 4.12 – Parameters of the reference model.

Parameter	Value	Search range
$T_{\rm eff}$ (K)	12,000	11,000 - 13,000
Log g	8.00	7.80 - 8.20
q(H)	-4.04	$[D(\mathrm{H})]$ -9.0 - -4.0
q(He)	-2.10	$[D(\mathrm{He})]$ -4.0 - -1.5

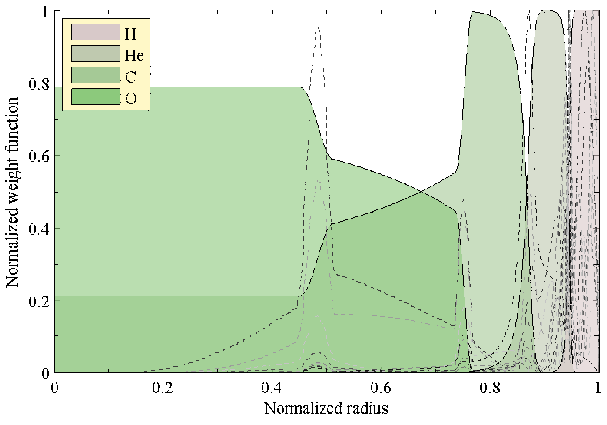

FIGURE 4.11 – Weight functions of the selected modes from the reference model.

The resulting chemical profiles as well as the Brunt-Väisälä and Lamb frequencies for $l = 1$

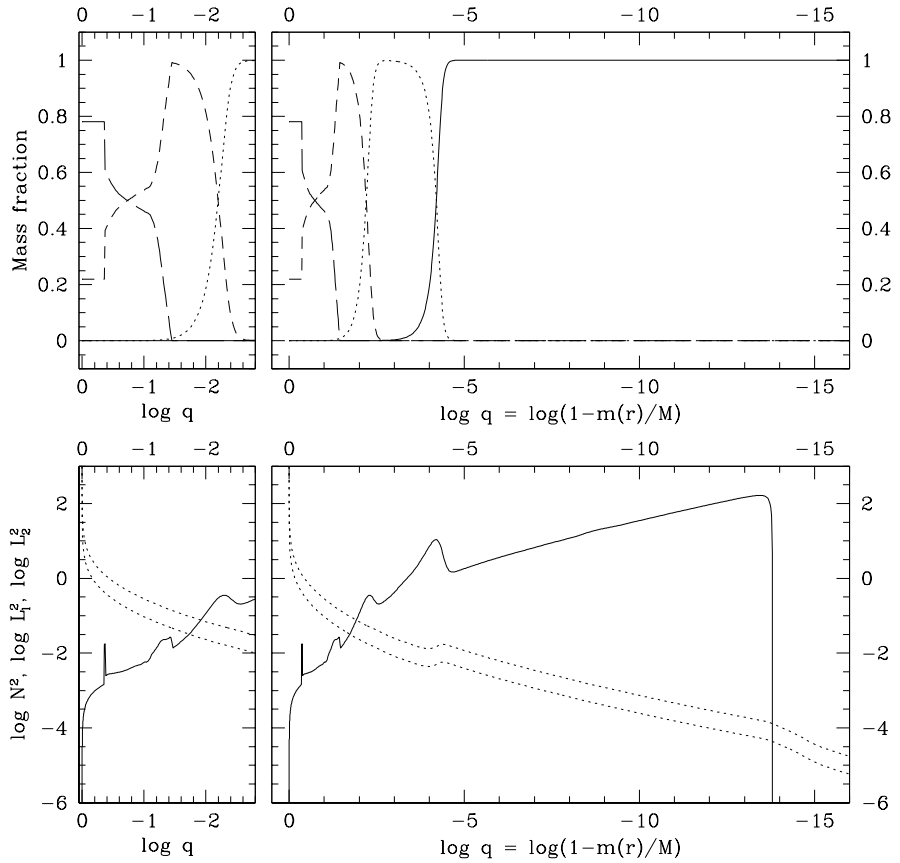

FIGURE 4.12 – Top panel: Chemical abundance profiles of the reference model, oxygen (long-dashed curve), carbon (dashed curve), helium (dotted curve), and hydrogen (solid curve). The abscissa shows the fractional mass depth (with $\log q = 0$ corresponding to the center of the star). Bottom panel: run of the square of the Brunt-Väisälä frequency (solid curves) and of the Lamb frequency for $l = 1$ (lower dotted curve) and $l = 2$ (upper dotted curve). The left part of both panels emphasizes a zoomed-in view of the deep interior of the star.

and $l = 2$ are illustrated in Figure 4.12. We can still observe some noisy features in the Brunt-Väisälä frequency which are most probably due to the numerical noise that was propagated from the evolutionary process during the pre-white dwarf phases. Table 4.13 presents the periods and mode identification chosen from the reference model. A set of ten periods were picked: five dipole modes with consecutive values of the radial order k from 2 to 6, and a similar group of five quadrupole modes with k from 3 to 7. These were picked in order to best represent ZZ Ceti stars close to the blue edge of the instability strip. Also, we made sure that our choice would include modes that probe the deep interior as illustrated in Figure 4.11. Those modes are the equivalent of the deeply confined modes discovered in Ross 548

(Giammichele et al. 2016), and their presence in the "observational" data considered here is of course necessary for testing our different core parametrizations. The ultimate test is then to try to recover the global parameters of the "observed" reference model (the white dwarf defined by an evolutionary profile) with chemical profiles defined by the different levels of sophistication of our parametrization. The first test consists in using the simplest parametrized static model we have, the varying homogeneous core.

The resulting global parameters for this first test are given in Table 4.14, and the associated chemical profiles are illustrated in Figure 4.13. The S^2 value of 17.5 obtained for the best solution is somewhat high and has to be considered carefully as it reaches some of the values obtained in the randomness tests described in the previous section. A close examination of Table 4.13 reveals, however, that a substantial part of this large value of S^2 is due to the particularly poor mismatch between the theoretical and "observed" period for the mode with $l = 1$ and $k = 6$. Otherwise, the period fits for the nine other modes are not bad at all. We do point out that four out of the ten modes of interest have not been identified correctly in terms of their defining indices l and k. And, of course, the detailed composition profile of our reference model cannot be reproduced in the context of this first test with homogeneous cores. This is well illustrated in Figure 4.13. Despite these shortcomings, and perhaps somewhat surprisingly, the hypothesis of an homogeneous core still leads to quite reasonable estimates of the global structural parameters of the reference model as can be observed in Table 4.14. We attribute this behavior to partial compensation associated with the variations of the defining parameters. We recall in this context that the hypothesis of homogeneous cores has proven itself a good approximation in the cases of GD 165 – in particular – and Ross 548 for which the six observed periods were well fitted for each star (Giammichele et al. 2016). We remind the reader here that the current set of ten periods was specifically chosen to probe deep into the reference star, since we were mainly concerned in showing the improvement brought up by the new parametrization.

A substantial gain on all fronts is obtained by using parametrized cores defined by three free parameters and corresponding to a chemical profile with a single transition zone. This parametrization, a particular case of the complete two-transition model, is obtained by setting

TABLE 4.13 – Periods from the reference model and from the resulting optimizations.

l	k	Chosen periods (s)	l	k	Var. hom. core (s)	l	k	1-transition (s)	l	k	2-transition (s)
1	2	206.429533263	2	5	207.80387574	1	2	205.91667143	1	2	206.30355349
1	3	259.558241480	1	3	261.26271139	1	3	260.35665876	1	3	259.72976629
1	4	285.787098098	2	9	285.94654263	1	4	285.73410324	1	4	285.88885831
1	5	316.227894252	2	10	315.89655226	1	5	314.83482318	1	5	316.31323695
1	6	375.973051700	1	6	373.22825616	1	6	375.51411398	2	12	376.01101225
2	3	150.725138295	2	3	151.01496289	2	3	150.89406262	2	3	150.78465417
2	4	177.098921306	2	4	178.19931882	2	4	178.35162669	2	4	177.05147091
2	5	195.326732918	1	2	196.91534658	2	5	195.37498858	2	5	195.34102115
2	6	218.924655751	2	6	217.81162674	2	6	217.73166428	2	6	218.75794933
2	7	245.287135903	2	7	245.41225685	2	7	247.37133055	2	7	245.34295988

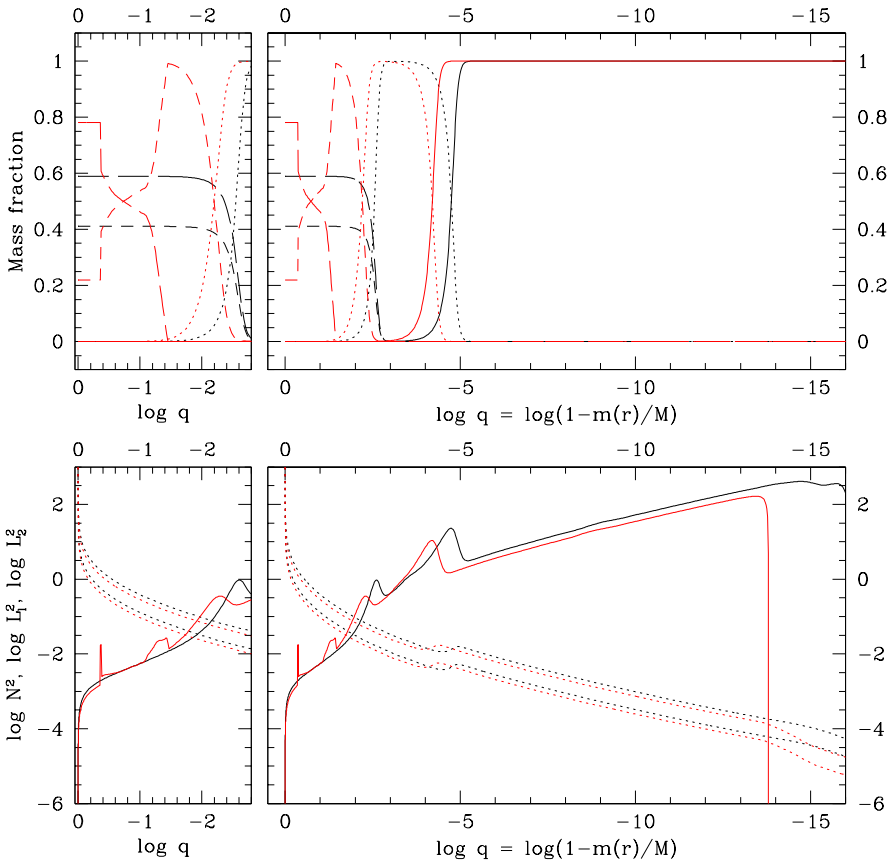

FIGURE 4.13 – Similar to Fig. 4.12, but showing the stratifications of the optimal model calculated with an homogeneous core (black curves) compared to those of the reference model (red curves).

TABLE 4.14 – Retrieved stellar parameters from the three optimizations.

Parameter	Var. hom. core	1-transition	2-transition
S^2	17.5	10.4	1.0 x 10^{-1}
$<\Delta\nu>$ (μHz)	19.6	15.0	1.7
$<\Delta P>$ (s)	1.1	0.8	0.09
$T_{\rm eff}$ (K)	12,820 (6.8%)	12,540 (4.5%)	11,770 (1.9%)
Log g	8.11 (1.4%)	8.04 (0.5%)	8.02 (0.3%)
q(H)	-4.60 (13.9%)	-4.35 (7.7%)	-4.15 (2.7%)
q(He)	-2.53 (20.5%)	-2.25 (7.1%)	-2.35 (11.9%)

$t1_o$ and $t2_o$ to zero, $\Delta t2$ to a non-zero value and $t2$ fixed at -2.00, far enough that it does not interfere within the range of $t1$. Table 4.14 now reveals a significant improvement of the merit function, from $S^2 = 17.5$ to 10.4, and the average dispersion in period, $<\Delta P>$, has dropped below 1 s. In both cases, much of the deviation is dominated by a particularly poor mismatch, this time associated with the $l = 2$ and $k = 7$ mode (see Table 4.13). The period fits are quite acceptable for the nine other modes. In addition, the mode identification is perfectly recovered. Moreover, the global parameters are noticeably closer to the ones from the reference model. A look at Figure 4.14 also reveals a net improvement of the ressemblance of the Brunt-Väisälä frequency with the one of the reference model. The first core feature is almost perfectly positioned at the first transition, along with the two chemical transitions between the core and the helium-rich mantle, and between the helium layers and the hydrogen envelope. The central values of carbon and oxygen are somehow inverted, a rather striking result, but since this inversion does not reflect on the Brunt-Väisälä frequency, this constraint is relatively weak on the period-fitting optimization process. The relatively poor S^2 fit is almost entirely due to the absence of the second feature in the core corresponding to the second drop in the oxygen profile, but the chemical stratification is overall quite well reproduced with the one-transition parametrization.

At this stage, the need for a two-transition parametrization should be clear. The Salaris profile presents two major drops in the oxygen stratification, so it is most natural to try to recover the reference model with a two-transition core parametrization. The advantage of a more flexible parametrization at this level is expected to be visible through an improved value

of S^2 and, therefore, a better match between the "observed" periods of the reference model and the computed theoretical periods. The question remaining is how accurately the periods and the chemical profiles in the core can be reproduced.

As above, the results of this third test are presented in Table 4.14. The S^2 value of 0.1 and the average $< \Delta P >$ of 0.09 s obtained for the best-fit model are, respectively, two and one orders of magnitude smaller than previously achieved with the variable homogeneous core and the one-transition parametrization. This is quite an impressive result, which demonstrates that our prescription can indeed mimic quite well the complex chemical stratification expected in the cores of white dwarfs. By inspecting the theoretical periods matched to the periods of the reference model in Table 4.13, we can notice that the period 376.01101225 s is wrongly identified, but this is a minor detail as the correct identification would have only very slightly increased the merit function S^2 as the value of the $l = 1, k = 6$ mode period is almost identical to the $l = 2, k = 12$ mode period. Beside this slight error, the global atmospheric parameters of the calculated model are significantly better constrained than before, save for the helium layer mass.

Looking at Fig. 4.15, we can observe that the two-transition prescription for the oxygen profile matches rather well the Salaris oxygen profile. The central homogeneous values of the oxygen and carbon mass fractions are correctly recovered, and the two transitions are perfectly placed. The layering of the helium and the hydrogen envelope is well superimposed on the chemical profiles of the reference model. The exact shapes of the first and, mostly, the second feature of the Brunt-Väisälä frequency corresponding to the reference model are not so well matched, but this does not seem a major problem as the periods and the overall model are finely reproduced.

The flexibility of the new two-transition core parametrization was explored and proven to be sufficient, as well as necessary, to recover sufficiently accurately the details of the complex chemical stratification expected from evolutionary calculations. Global parameters can be estimated fairly reliably from the approximation of homogeneous cores, but this has to be handled with some care, especially in cases where weight functions probe deeper than the enveloppe of the star. To best reproduce the core chemical profile, the two-transition parametrization is

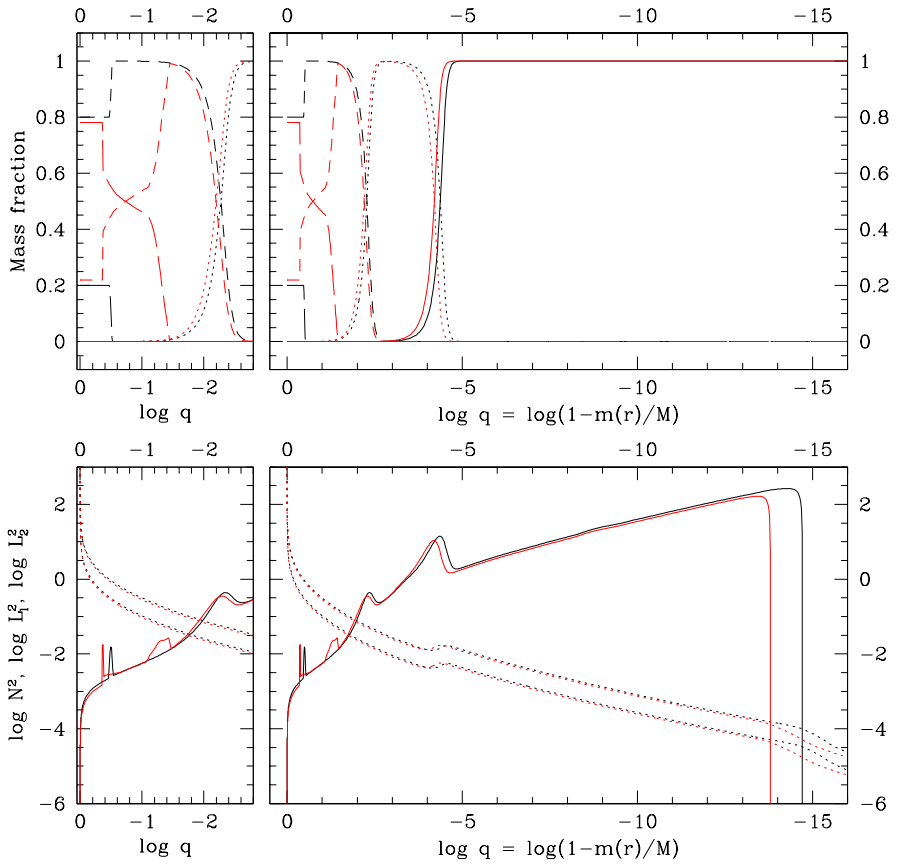

FIGURE 4.14 – Similar to Fig. 4.12, but showing the stratifications of the optimal model calculated with the adjustable core parametrization with one transition (black curves) compared to those of the reference model (red curves).

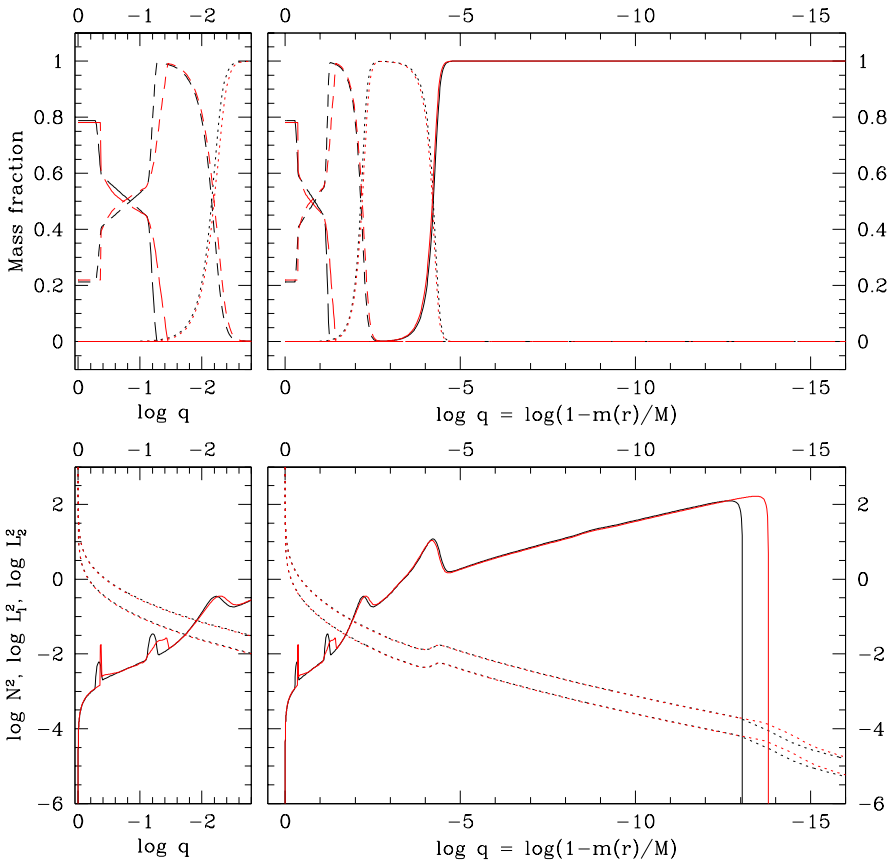

FIGURE 4.15 – Similar to Fig. 4.12, but showing the stratifications of the optimal model calculated with the adjustable core parametrization with two transitions (black curves) compared to those of the reference model (red curves).

necessary and cannot be replaced by the simpler one-transition particular case.

4.8 CONCLUSION

We presented a new parametrization that can replicate smoothly one or two steep "drops" in the chemical profile of oxygen in the core of a white dwarf model in order to better reproduce the features of an evolutionary model. The flexibility of the new two-transition core parametrization was explored and proven to be sufficient and necessary for recovering the structure expected from evolutionary calculations. We plan to use this parametrization in upcoming seismic studies of pulsating white dwarfs, particularly those with available *Kepler* data.

For the future, we retain the following lessons from the current work. Based on tests generated with random sequences of periods, we can define a conservative threshold of about 10 for the unweighted χ^2 of a 10 period fit, and about 1 s for the average period dispersion. Results from seismic analyses exceeding those values should not be considered as statistically significant. Moreover, we showed that our seismic method is perfectly capable of retrieving stellar and shape parameters from a reference star with different degree of precision in the "observational" data. If the limiting factor was purely observational, stellar and shape parameters would be recovered to a remarkable precision. Although our asteroseismic method gives robust, precise and accurate constraints on either stellar or shape parameters, the limiting factor is not the precision of the observations, but the constitutive physics behind our models that need to be adressed in order to go beyond current achievements.

This work was supported in part by the NSERC Canada through a doctoral fellowship awarded to Noemi Giammichele, and through a research grant awarded to Gilles Fontaine. The latter also acknowledges the contribution of the Canada Research Chair Program. Stéphane Charpinet acknowledges financial support from "Programme National de Physique Stellaire" (PNPS) of CNRS/INSU, France, and from the Centre National d'Études Spatiales (CNES, France). This work was granted access to the HPC resources of CALMIP under allocation number 2015-p0205.

4.9 REFERENCES

Akima, H. 1970, JACM, Vol. 17, No. 4, 589

Baglin, A., Auvergne, M., Barge, P., et al. 2009, IAU Symposium, 253, 71

Bell, K.J., Hermes, J.J., Bischoff-Kim, A., et al. 2015, ApJ, 809, 14

Gallart, M.S. 2002, M.Sc. thesis, École Polytechnique

Charpinet, S., Van Grootel, V., Brassard, P. et al. 2013, in EPJ Web of Conf., Aging Low Mass Stars: From Red Giants to White Dwarfs, ed., A. Noels & V. Van Grootel, 43, 04005

Giammichele, N., Fontaine, G., Brassard, P., & Charpinet, S. 2015, ApJ, 815, 56

Giammichele, N., Fontaine, G., Brassard, P., & Charpinet, S. 2016, submitted to ApJS

Gilliland, R.L., Brown, T.M., Christensen-Dalsgaard, J., et al. 2010, PASP, 122, 131

Greiss, S., Gänsicke, B.T., Hermes, J.J., et al. 2014, MNRAS, 438, 3086

Greiss, S., Gänsicke, B.T., Hermes, J.J., et al. 2015, 19th European Workshop on White Dwarfs, 493, 169

Hermes, J.J., Mullally, F., Østensen, R.H., et al. 2011, ApJ, 741, L16

Hermes, J.J., Charpinet, S., Barclay, T., et al. 2014, ApJ, 789, 85

Landolt, A.U. 1968, ApJ, 153, 151

Matthews, J.M. 2007, Communications in Asteroseismology, 150, 333

Michel, E., Baglin, A., Auvergne, M., et al. 2008, Science, 322, 558

Østensen, R.H., Silvotti, R., Charpinet, S., et al. 2011, MNRAS, 414, 2860

Østensen, R.H., Bloemen, S., Vučković, M., et al. 2011, ApJ, 736, L39

Romero, A.D., Córsico, A.H., Althaus, L., et al. 2012, MNRAS, 420, 1462

Salaris, M., Cassisi, S., Pietrinferni, A. et al. 2010, ApJ, 716, 1241

Van Grootel, V., Charpinet, S., Brassard, P., Fontaine, G., & Green, E.M. 2013, A&A, 553, A97

Chapitre 5

Ultra-High Precision Asteroseismological Analysis of KIC 08626021

N. Giammichele[1], S. Charpinet[2], G. Fontaine[1], P. Brassard[1], and W. Zong[2]

[1] *Département de Physique, Université de Montréal, Succ. Centre-Ville, C.P. 6128, Montréal, QC H3C 3J7, Canada*

[2] *Université de Toulouse, UPS-OMP, IRAP, Toulouse F-31400, France*

CNRS, IRAP, 14 avenue Edouard Belin, F-31400 Toulouse, France

To be submitted to *The Astrophysical Journal*

5.1 ABSTRACT

We present a detailed seismic analysis of the *Kepler* target KIC 08626021, a pulsating white dwarf of the V777 Her type. This analysis is based on a frequency extraction exercise that has revealed the presence of at least 13 independent pulsation modes regrouped into eight main frequency multiplets. We use our recently-developed parametrization scheme for white dwarfs to search for an optimal seismic model in parameter space. For the first time ever, we are able to reproduce the periods detected in a pulsating star at the accuracy of the observations. Our seismic model of KIC 08626021 indicates that it is the hottest star of its class, and places it at the blue edge of the V777 Her instability strip. This is consistent with the empirical period-luminosity relationship, and with the independent spectroscopic estimates of the atmospheric parameters of this star that we also provide in this paper. On the basis of our seismic modeling, we present a number of inferences on KIC 08626021, including an interesting view of its complex internal chemical stratification. We also analyze the available multiplet structure under the hypothesis that it is due to rotation. We find that the internal rotation profile of this ∼30,000 K DB white dwarf can be mapped over the outer 70% of its radius, which contains some 80% of its mass. KIC 08626021 rotates rigidly and extremely slowly, having a total angular momentum some 291 times smaller than that of the actual Sun.

5.2 INTRODUCTION

In the era of space missions such as *Kepler* and *Kepler*-2 which have been providing asteroseismic data of unprecedented quality for several types of pulsating stars (including white dwarfs), we decided to revisit the problem of the seismic modeling of this latter type of pulsators using current techniques, typical of those developed quite successfully in recent years for pulsating hot B subdwarfs (see, e.g., Charpinet et al. 2013). We first tested these techniques in a white dwarf context by carrying out a detailed analysis of the pulsation properties of two classical hot ZZ Ceti stars – GD 165 and Ross 548 – using the best available data from the ground. This study, reported in Giammichele et al. (2015; 2016a), established firmly that our approach to quantitative seismology – based on static, parametrized models of stars – can

indeed be extended reliably to the white dwarf domain. At the same time, it revealed that g-modes can sometimes be confined in the deep core of cool white dwarfs, thus offering the potential of probing the complex chemical stratification at such depths. We thus decided to upgrade our modeling capabilities of white dwarfs by introducing a parametrized description of the chemical layering in the C-O core. The results of this work were reported in Giammichele et al. (2016b). We use this improved modeling tool in the present paper to exploit the set of pulsation periods extracted by Zong et al. (2016) from an exquisite and unique time-series data set obtained with the *Kepler* satellite on the pulsating DB (V777 Her) white dwarf KIC 08626021.

White dwarf stars with helium-dominated atmospheres represent about 20% of the total white dwarf population. Of those, the so-called DB stars are found in a range of effective temperature from about 12,000 K to upward of 35,000 K, and thus feature strong lines of neutral helium in their spectra. They are believed to descend from hotter He-atmosphere counterparts of the DO and PG1159 spectral types, themselves the products of a born-again episode during which the post-AGB ancestor loses its thin remaining hydrogen envelope in a late final flash (Iben et al. 1983). The chemical stratification in the core of a white dwarf is not only determined by the nuclear reaction rate $^{12}\mathrm{C}(\alpha,\gamma)^{16}\mathrm{O}$ that synthesizes the oxygen content from the ashes of the core helium burning phase, but also on the scheme of convective mixing used in the models (Straniero et al. 2003). Two distinct composition transition zones are found in the envelope surrounding the core of a DB white dwarf, if we rely on detailed evolutionary models of DB white dwarfs which include time-dependent diffusion (see, e.g., Figure 1 of Fontaine & Brassard 2002). Around the carbon-oxygen core, there exists a first transition zone composed of a mixture of helium, carbon, and oxygen, while surrounding it there exists a pure helium envelope formed by the settling of the heavier elements carbon and oxygen, a process that is still ongoing during the DB phase. Asteroseismology is the only tool capable of unveiling the interior of pulsating stars. By comparing the pulsation properties to those of theoretical models, it is possible to match the appropriate model of the star to the actual state of the targeted pulsating star.

KIC 08626021 (a.k.a, WD J1929+4447 or GALEX J192904.6+444708), the only known

pulsating DB white dwarf in the Kepler field, was first discovered by Østensen et al. (2011) and then analyzed successively by Bischoff-Kim & Østensen (2011), Córsico et al. (2012), and Brassard & Fontaine (2013) on the basis of the five extracted periods from the first month of short cadence *Kepler* data. Their results only concurred on the fact that the effective temperature had to be significantly hotter than the spectroscopic value given by Østensen et al. (2011). The mass found by Córsico et al. (2012) differed, however, quite dramatically from the two other studies. With nine further months of *Kepler* observations, Ostensen (2013) uncovered two more periods, to reach a total of seven independent modes for that star. Using the reported modes, Bischoff-Kim et al. (2014) performed an updated asteroseismic analysis. However, the detailed reanalysis of the nearly two years of *Kepler* photometry for that star by Zong et al. (2016) uncovered a new independent frequency that was previously incorrectly identified as a component of a rotationnally-split triplet by Bischoff-Kim et al. (2014). This addition is significant as there is quite a bit of seismic information in low-order modes (as they must be as indicated by their short periods). Hence, there are, in fact, eight modes (excluding fine structure due presumably to rotation in three of them) that have been revealed by *Kepler* on KIC 08626021.

We present in Section 5.3 a recapitulation of the pulsation properties as well as a discussion of the time-averaged spectroscopic properties of KIC 08626021. Our forward modeling approach is described briefly in Section 5.4, including our new improvement on the front of parametrized modeling. Section 5.5 is dedicated to the asteroseismic analysis of the eight-period spectrum of KIC 08626021, while Section 5.6 is devoted to an investigation of the internal rotation profile.

5.3 SPECTROSCOPIC CONSTRAINTS AND PULSATION PROPERTIES

5.3.1 Spectroscopic Analysis

The first analysis of the time-averaged optical spectrum of KIC 08626021 was presented by Østensen et al. (2011). They used a low signal-to-noise ratio (S/N) spectrum gathered

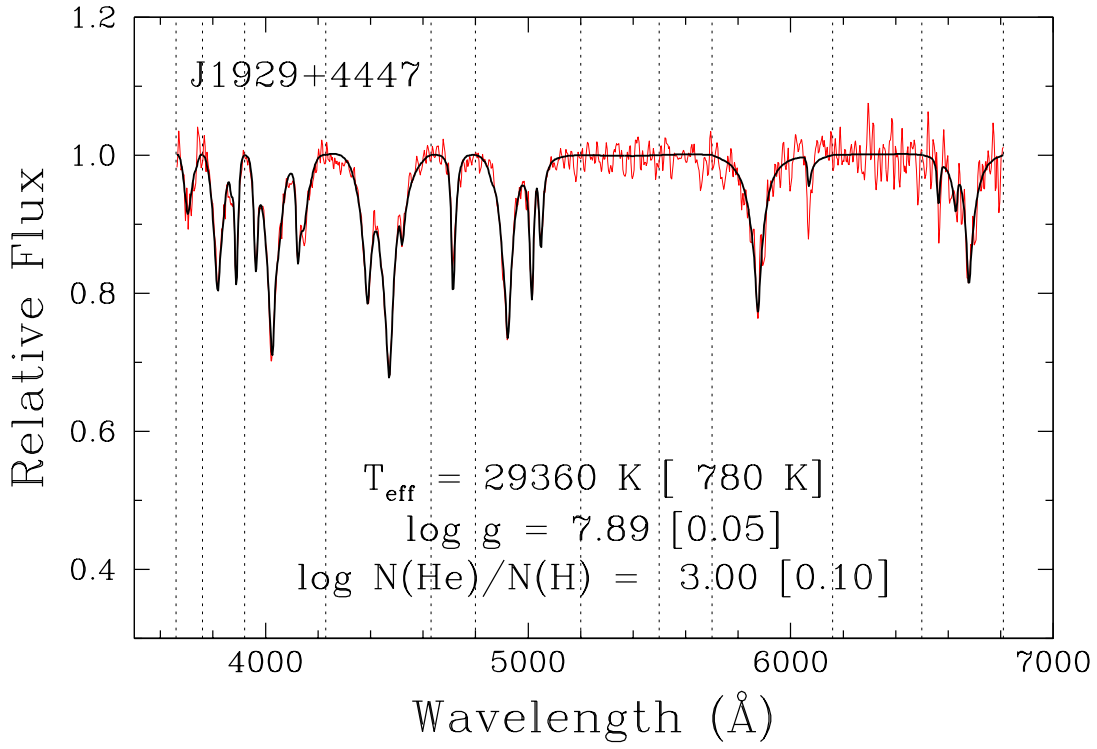

FIGURE 5.1 – Model fit to the Bok spectrum of KIC 08626021. The vertical dotted lines correspond to the adopted points for the continuum. The presence of the Hα line of hydrogen is obvious, making this star the hottest known DBA white dwarf. At the same time, our estimates indicate that KIC 08626021 is also the hottest of the known pulsators of the V777 Her type.

with the ISIS spectrograph on the William Herschel Telescope combined with spectroscopic model grids from Koester (2010). The mixing length prescription of ML2/α = 1.25 for DB models calibrated by the Montréal group was adopted. The standard fitting procedure gave $T_{\rm eff} = 24,900 \pm 750$ K and $\log g = 7.91 \pm 0.07$. Their fit shows a depression around 3900 Å, and the strengh of the lines are not well fitted. Without doing any further modeling, the derived effective temperature was immediately suspect in the eyes of many, given that KIC 08626021 shows the shortest observed pulsation periods of all of the known V777 Her stars and, therefore, *has* to be among the hottest of the class according to the well-known period-effective temperature relation depicted, for example, in Figure 25 of Fontaine & Brassard (2008). Hence, the true effective temperature of KIC 08626021 has to be significantly higher than the estimate provided by Østensen et al. (2011).

We are fortunate, in that respect, to dispose of a better spectrum kindly obtained for us

by our collaborator Betsy Green of Steward Observatory. This is a low-resolution spectrum (∼8.7 Å at 4500 Å), but with a value of S/N∼50, which is excellent for a faint star such as KIC 08626021 with $K_p = 18.46$ and $r = 18.41$. It took our collaborator some 3.5 h of exposure on the B&C spectrograph attached to the 2.3 m Bok Telescope of the Steward Observatory at Kitt Peak. A preliminary analysis of that time-averaged spectrum was presented by two of us in the recent past (Brassard & Fontaine 2013). Our updated fit is presented in Figure 5.1. The fit to the available lines is quite good, and leads to the following atmospheric parameters: $T_{\rm eff} = 29,360 \pm 780$K, $\log g = 7.89 \pm 0.05$, and $\log$ H/He $= -3.0 \pm 0.1$. Interestingly, we detect a nonnegligible trace of H, making KIC 08626021 the hottest known DBA white dwarf. At the same time, and more importantly in the present context, our revised estimate of the effective temperature also makes KIC 08626021 the hottest of the known V777 Her pulsators (as it should on the basis of its short observed periods). In the seismic analysis that follows below, our estimates of $T_{\rm eff}$ and $\log g$ will be used as important independent constraints. Any seismic model to be found must be compatible with these constraints in order to be credible.

5.3.2 Pulsation properties

We exploit here the thorough analysis of Zong et al. (2016) to carry out this new seismic study. That analysis has shed new light on the 23 months of photometric data of KIC 08626021. In particular, even if the 13 retained frequencies are consistent with those of Bischoff-Kim et al. (2014), the interpretation of one of the structures leads to an important correction. The structure in the 3677-3686 μHz range identified as a triplet by Bischoff-Kim et al. (2014), is actually a doublet, f_3, with an independant mode, f_7, close by. The seismic modeling is going to be largely influenced by the addition of this eighth frequency as it probes a different part of the star and helps to better lock a unique solution. The list of extracted periods is provided in Table 1 of Zong et al. (2016), with all their specifications, and we refer the reader to their work for inquiries on the extraction process and on the frequencies detected. We will use the same convention as Zong et al. (2016) for the sake of simplicity.

This present seismic analysis is thus based on the following list of frequencies: f_1, f_2, f_3, f_4, f_5, f_6, f_7, and f_9. f_8 and f_{10} are linear combination frequencies, and as such are excluded

from the analysis. We also do not consider f_{11} and f_{12} since they do not reach the secure threshold of 5.6σ established by Zong et al. (2016). It is safer to be more conservative in our case, as a single wrong period can falsify the entire result, as will be shown later. f_1 and f_2 are two clearly identified and nearly symmetric rotational triplets corresponding to a rotation timescale of about 42 h if the two modes are assumed to be dipole modes and if the asymptotic expression for the first-order rotation coefficient is used, i.e., $C_{kl} = 1/(l^2 + l)$. The structure defined as f_3 is interpreted as a doublet with a frequency separation similar to the two triplets.

5.4 METHODOLOGY

The method and tools used in this work are the same as those employed in the recent successful test presented by Giammichele et al. (2016a) in the case of the pulsating ZZ Ceti stars GD 165 and Ross 548. The approach is inspired from the work on sdB pulsators carried out by Charpinet et al. (2005) (and references therein). For more technical details on the tools used, the reader is referred to Charpinet et al. (2005) and Charpinet et al. (2008). The forward approach used here consists in comparing the pulsational properties of large numbers of theoretical stellar models to the observed periods of the pulsating star in question. By optimizing this process, it is then possible to infer the structural parameters of the appropriate stellar model via the best fit to the observed pulsational properties. Since we have no preconceived idea of the mode identification, the optimization process has to be two-fold. The technique relies on a double-optimization scheme that, first, best matches the observed periods with the periods calculated from a theoretical stellar model, using a chi-squared-type formalism viewed as a combinatorial optimization problem. The process outputs from the best fit the identification of the modes. The second optimization uses a multimodal optimizer based on a massively parallel hybrid genetic algorithm to find the best fit model in the N-dimensional parameter space, the quality of the fit being quantified by a merit function, S^2 (an unweigthed χ^2):

$$S^2(a_1, a_2, ..., a_N) = \sum_{i=1}^{N_{obs}} (P_{obs}^{(i)} - P_{th}^{(i)})^2, \tag{5.1}$$

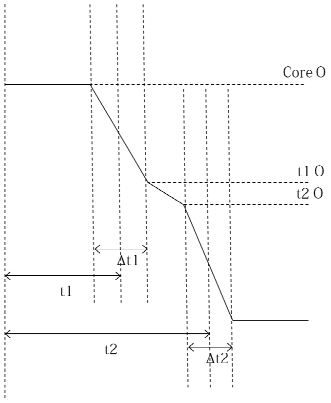

FIGURE 5.2 – New parameterization using a two-transitions model in the DB white dwarf core. All the parameters are labeled on this schematic view.

where N_{obs} is the number of observed periods, $\{a_1, a_2, ..., a_N\}$ are the parameters of the model, and each $\{P_{obs}^{(i)}, P_{th}^{(i)}\}$ is a pair of theoretical/observed periods for this model. The code used is briefly described in Charpinet et al. (2008) and fulfils two fundamentals guarantees: first, a complete and exhaustive exploration of the entire model parameter space and second, feedback on the uniqueness (or not) of the solution.

In order to compare the quality of our fit to Bischoff-Kim et al. (2014), we also use the same formalism for the Bayes Information Criterion (BIC;Koen & Laney (2000)):

$$\mathrm{BIC} = \mathrm{N}(\frac{\log \mathrm{N_{obs}}}{\mathrm{N_{obs}}}) + \log \sigma^2, \tag{5.2}$$

where σ^2 is given by weighting our merit function S^2. Note that there seems to be a mistake in the expression reported by Bischoff-Kim et al. (2014) in that the last term on the right is multipled by N_{obs}, and it should not be. Furthermore, we must point out that the BIC indicator is formally significant in the limit when $N_{obs} >> N$, which is not the case in this application. Hence, we are not certain of the statistical validity of the BIC indicator in the present context, and we do not use it in our study, except uniquely for comparison purposes.

The evaluation of S^2 requires the computation of large batch of theoretical stellar models from which we obtain the spectrum of pulsation. Our stellar models are parametrized to best represent the real structure of the star. The use of chemical profile originating from evolutionary sequences as used in Romero et al. (2012) for example is quite risky, as compa-

ring results from different investigators yields significant differences with the addition of the numerical noise coming from the accumulated uncertainties through all the various stages of pre-white dwarf evolution. This is a real killer in term of asteroseismology. The best compromise is to use parameterized models, based on evolutionary calculations, which are smooth enough and devoided of the uncertainties and numerical noise carried on and amplified during the evolutionary calculations carried out from the ZAMS. The previous seismic analysis of KIC 08626021 by some of the coauthors (Brassard & Fontaine 2013) was intended toward a better understanding of the evolution of the double-layered structure of the envelope of the DB star. This was carried out using a parametrized model including a homogeneous C/O core. Our present efforts include a full treatment of the core according to the detailed discussion presented in Giammichele et al. (2016b). Figure 5.2 presents the different parameters added to the parameterization in order to add flexibility to best imitate an evolved white dwarf chemical profile. Seven control points defining an Akima spline are necessary to fully define a two-transition chemical profile in the core: core O, t1, Δt1, t1(O), t2, Δt2 and t2(O). The Akima spline is a continuously differentiable sub-spline interpolation, built from piecewise third order polynomials, which is stable to the outliers contrary to cubic splines that tend to oscillate in the neighborhood of such points. To fully define the double-layered structure of the white dwarf, we need seven more parameters: the effective temperature $T_{\rm eff}$, the surface gravity $\log g$, the position in $\log q$ of the double-layered envelope transition D(He) and D(envelope), the amount of helium in the envelope Envelope(He), the steepness of the slope at the first and second transition Profac(He) and Profac(envelope). Once the structure is fully defined the following step is to evaluate the adiabatic pulsation properties of the model, assumed purely spherical, using an efficient and robust code based on finite element techniques ((Brassard et al. 1992); (Brassard & Charpinet 2008)).

TABLE 5.1 – Defining parameters for the optimal seismic model found for KIC 08626021

Quantity	Optimum Value	Test with a wrong period
$T_{\rm eff}$ (K)	30219	3 %
$\log g$	7.913	0.1%
D(He)	−6.043	17 %
D(envelope)	−2.944	41 %
Envelope(He)	0.137	389 %
Profac(He)	1.424	10 %
Profac(envelope)	11.97	1%
Core(O)	0.816	5 %
t1	−0.735	61%
Δt1	0.137	48 %
t1(O)	0.265	48 %
t2	−1.762	22 %
Δt2	0.040	7 %
t2(O)	0.130	62 %

5.5 ASTEROSEISMIC ANALYSIS

5.5.1 Search for an Optimal Model

The search for best-fit solutions starts with the largest possible parameter space for DBV stars. Constraints on $T_{\rm eff}$ and $\log g$ rely on typical spectroscopic values found for DBV stars, being as inclusive as possible. Evolutionary tracks from Salaris et al. (2010) influenced the range on the seven parameters defining the C/O core: core O, t1, Δt1, t1(O), t2, Δt2 and t2(O). We consider all modes of degree $l = 1$ and 2 in the period range from 100 to 500 s, which encompasses the range of the eight main observed modes in KIC 08626021. Modes with higher degree are excluded, as they are hardly visible due to cancellation effects of their surface geometry. Since the periods of low radial order modes are quite insensitive to the prescribed convective efficiency, we fixed the latter to the so-called ML2/α=1.0 prescription and did not vary it in parameter space. We thus searched parameter space in fourteen dimensions in order to best fit eight periods. A priori, this seems like an underconstrained problem, but this point of view is naive in the context of the present optimization exercise as discussed by Giammichele et al. (2016a) and further commented on below.

Keeping this in mind, we singled out an essentially “perfect” model in parameter space,

able to match the observed periods at an unprecedented level of precision defined by a merit function of $S^2 = 4.9 \times 10^{-10}$. The defining parameters for this unique solution are listed in Table 5.1. Figure 5.3 shows the projection map of the merit function onto the $T_{\rm eff} - \log g$ and D(He)-D(envelope) plane. The merit function is normalized in a way that the global miminum is equal to one, on a logarithmic scale. As can be seen, the seismic effective temperature is slightly higher than the spectroscopic 1σ box, but falls well into the 2σ interval. The seismic $\log g$ is in excellent agreement with the spectroscopic determination within 1σ. With an effective temperature of 30,219 K, this is indeed the hottest DBA and the hottest V777 Her star discovered so far. This effective temperature is slightly higher than what Bischoff-Kim et al. (2014) predict ($T_{\rm eff}$ = 29,650 K), but still in very good agreement. The region of interest in the D(He)-D(envelope) plane is as sharply defined as the one in the $T_{\rm eff} - \log g$ plane, there is no ambiguity on the solution found. The pure helium layer is rather thin with a value of D(He) = -6.043, representing the position of the transition between the envelope and the pure helium layer in the $\log q$ coordinate. The envelope composed of a mixture of carbon and helium, with a global mass fraction of 13.7% of helium, is defined by D(envelope) = -2.944, which corresponds to a $\log(M({\rm He})/M) = -3.622$.

Information on the best-fit model, including the details of the period spectrum and mode identification, are presented in Table 5.2. The relative average dispersion for this best-fit model reaches a very impressive value of $\overline{\Delta X/X}$ = 0.00000301%, where X is either the period P or the frequency ν. This corresponds to an average dispersion of $\overline{\Delta P}$ = 0.00000690 s and $\overline{\Delta \nu}$ = 0.00014229 μHz. These very precise seismic results reach, for the first time ever, the actual observational limits. In the present case, those observational limits are $\overline{\Delta P} = 0.000038$ s and $\overline{\Delta \nu} = 0.00060$ μHz, as derived from some two years of *Kepler* data on KIC 08626021.

Now if we wish to compare to the other studies of KIC 08626021, we obtain a BIC of -8.63, orders of magnitude better than the best-fit result obtained by Bischoff-Kim et al. (2014) with seven free parameters and seven periods and giving BIC = -0.16 (calculated from their σ_{RMS} = 0.362 s after correcting for the suspected mistake in their equation as mentioned above). Since the BIC is a statistical tool that penalizes the merit function by taking into account the number of free parameters and the number of constraints, our much lower value

TABLE 5.2 – Mode identification, details of the period fit obtained for the optimal solution characterized by $S^2 = 4.96 \times 10^{-10}$ ($s^2 = 6.20 \times 10^{-11}$), and some relevant model quantities. The mean relative dispersion of the fit is $\overline{\Delta X/X} = 0.00000301\%$ (or $\overline{\Delta P} = 0.00000690$ s and $\overline{\Delta \nu} = 0.00014229$ μHz.

l	k	$\nu_{\rm obs}$ (μHz)	$\nu_{\rm th}$ (μHz)	$P_{\rm obs}$ (s)	$P_{\rm th}$ (s)	log $E_{\rm kin}$ (erg)	$A_{\rm obs}$ (%)	ID	
1	−1	...	8177.819	...	122.28	48.91346	0.2891235	...	
1	−2	...	6088.221	...	164.25	47.78023	0.3993251	...	
1	−3	5073.234	5073.234	197.11	197.11	47.24692	0.4259222	0.705	f_2
1	−4	4309.915	4309.915	232.02	232.02	46.69799	0.4562645	0.804	f_1
1	−5	3681.803	3681.803	271.61	271.61	46.20367	0.4694429	0.397	f_3
1	−6	3294.369	3294.369	303.55	303.55	46.14357	0.4673883	0.139	f_6
1	−7	...	2935.405	...	340.67	45.79077	0.4798999	...	
1	−8	...	2628.105	...	380.50	45.53807	0.4832558	...	
1	−9	...	2401.713	...	416.37	45.47883	0.4817043	...	
1	−10	...	2203.315	...	453.86	45.00331	0.4889313	...	
1	−11	...	2021.103	...	494.78	44.67657	0.4894387	...	
2	−2	...	9854.447	...	101.48	47.49831	0.0956968	...	
2	−3	...	8068.125	...	123.94	46.94580	0.1098051	...	
2	−4	6981.261	6981.261	143.24	143.24	46.57756	0.1214170	0.079	f_9
2	−5	...	6129.698	...	163.14	46.09420	0.1417694	...	
2	−6	...	5347.435	...	187.01	45.95478	0.1413396	...	
2	−7	...	4842.700	...	206.50	45.74782	0.1448797	...	
2	−8	4398.372	4398.372	227.36	227.36	45.46756	0.1519110	0.161	f_5
2	−9	...	3953.364	...	252.95	45.20157	0.1529942	...	
2	−10	3677.994	3677.994	271.89	271.89	44.95758	0.1538404	0.125	f_7
2	−11	...	3407.589	...	293.46	44.51306	0.1583018	...	
2	−12	...	3163.115	...	316.14	44.24635	0.1581152	...	
2	−13	...	2991.592	...	334.27	43.97262	0.1593393	...	
2	−14	...	2825.862	...	353.87	43.85995	0.1603264	...	
2	−15	2658.777	2658.777	376.11	376.11	43.72671	0.1611361	0.233	f_4
2	−16	...	2521.944	...	396.52	43.68157	0.1607207	...	
2	−17	...	2394.613	...	417.60	43.37381	0.1623213	...	
2	−18	...	2279.078	...	438.77	43.24629	0.1621960	...	
2	−19	...	2179.753	...	458.77	42.98349	0.1630733	...	
2	−20	...	2088.497	...	478.81	42.94041	0.1629144	...	
2	−21	...	2005.547	...	498.62	42.83683	0.1634942	...	

of BIC indicates that the increase in free parameters to fourteen is not excessive compared to the increase in the quality of the fit. We show in Figure 5.4 the position and identification of the optimized frequencies obtained during this analysis (red) with observations in the background, contrasted with the best results found in the literature (blue), by Bischoff-Kim et al. (2014).

Figure 5.5 shows the histograms obtained for the probability distribution of three primary and three secondary parameters used during the present optimization. The technique used relies on the likelihood function calculated from the sampling of the merit function S^2 during the search for the best fit model. This method developed by Van Grootel et al. (2013) allows to make more quantitative statements on the value of each parameter by statistically estimating the value of each parameter and its associate error from the seismic fit. In a nutshell, all the histograms show very narrow peaks, with the mean and median values of the distribution nearly equal. The derived errors are listed in Table 5.3.

Figure 5.6 illustrates on the upper panel the internal chemical profile, with a zoomed-in-view of the core of the star, while the lower panel presents the distribution of the square of the Brunt-Väisälä and Lamb frequencies with $l = 1$ (lower dotted curve) and $l = 2$ (upper dotted curve). The first transition in the double-layered helium zone leaves almost no imprint on the Brunt-Väisälä frequency. It is not the case as we go deeper into the core, and we can see that the two new transitions affect the Brunt-Väisälä frequency quite obviously. We can also notice the well in the profile due to the superficial He convection zone. Figure 5.7 illustrates in better details the zoom-in view of the core chemical profile of oxygen, with the 1- and 3-σ region, contrasted with standard evolutionary profiles from Salaris et al. (2010) and Romero et al. (2012). The two comparison profiles come from standard DA (hydrogen-rich atmosphere) white dwarf evolutionary tracks of similar mass, but are still representative of DB white dwarfs because the internal structures, from an evolutionary point of view, derive from the same processes. The amount of oxygen in the innermost part of the carbon-oxygen core where the local composition is homogeneous reaches 81.6%, equivalent to evolutionary calculations proposed by Salaris et al. (2010), but higher than results from Romero et al. (2012). The region of the homogeneous carbon-oxygen core is also extended to twice the mass according to our calculations compared to what evolutionary calculations suggest. Another

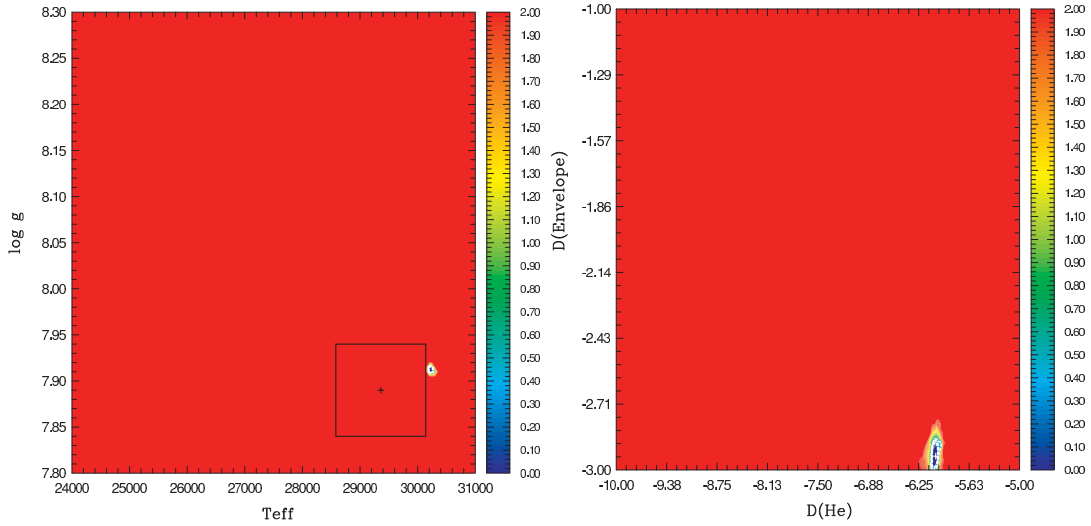

FIGURE 5.3 – Map of the projected merit function S^2 (on a log scale) along the $T_{\rm eff}$-log g (left) and D(He)-D(envelope) (right) plane. White contours show regions where the frequency fit have S^2 values within the 1σ, 2σ, and 3σ confidence levels relative to the best-fit solution. The spectroscopic solution given within 1σ is illustrated with a black box.

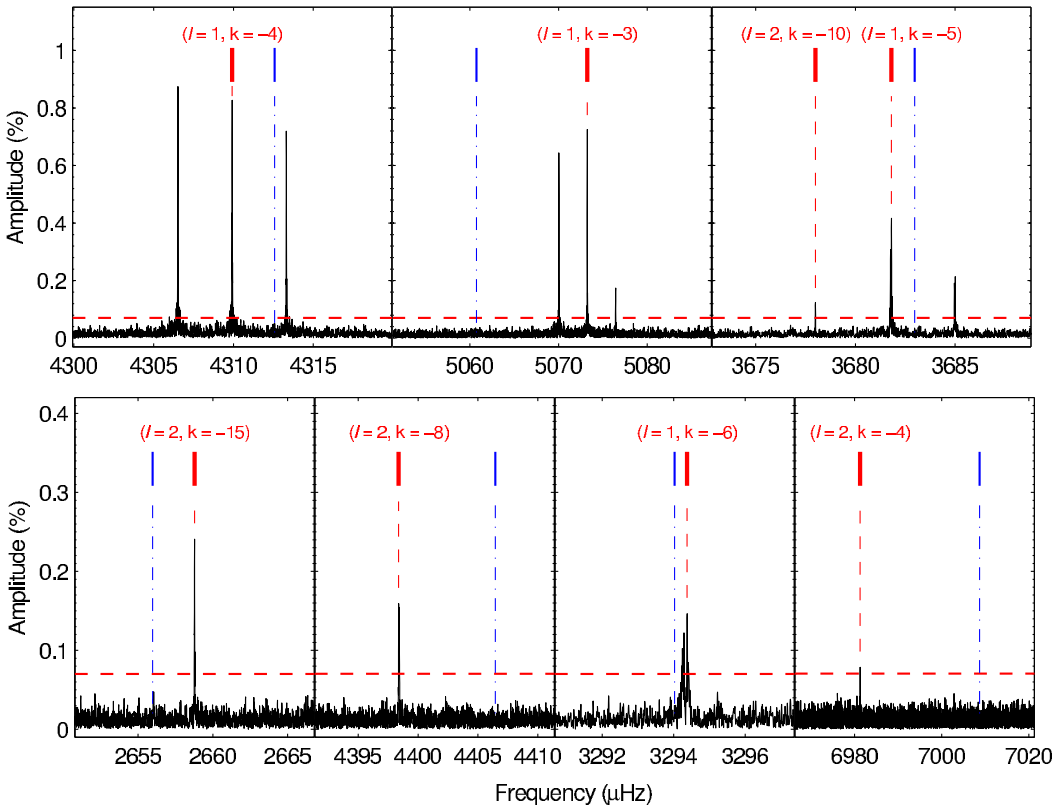

FIGURE 5.4 – Lomb-Scargle Periodogram (amplitude in % of the mean brigthness vs frequency in μHz) of the features of the DBAV star KIC08626021, superimposed with the identified theoretical frequencies for this work (red) compared to the results of Bischoff-Kim et al. (2014) (blue).)

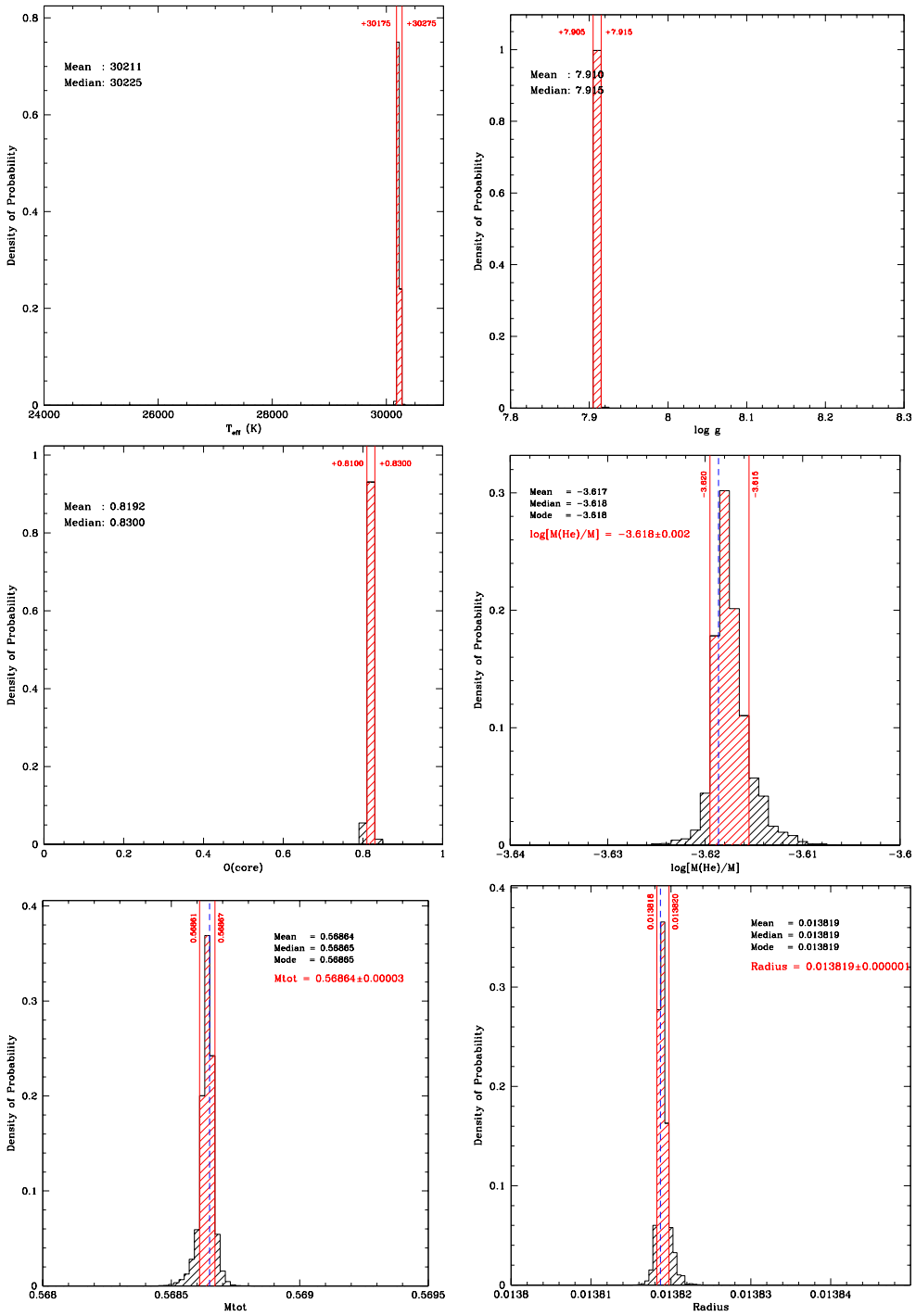

FIGURE 5.5 – Probability density function for the most interesting primary and secondary parameters inferred from our seismic study. The red-hatched region between the two vertical solid red lines defines the 1σ range.

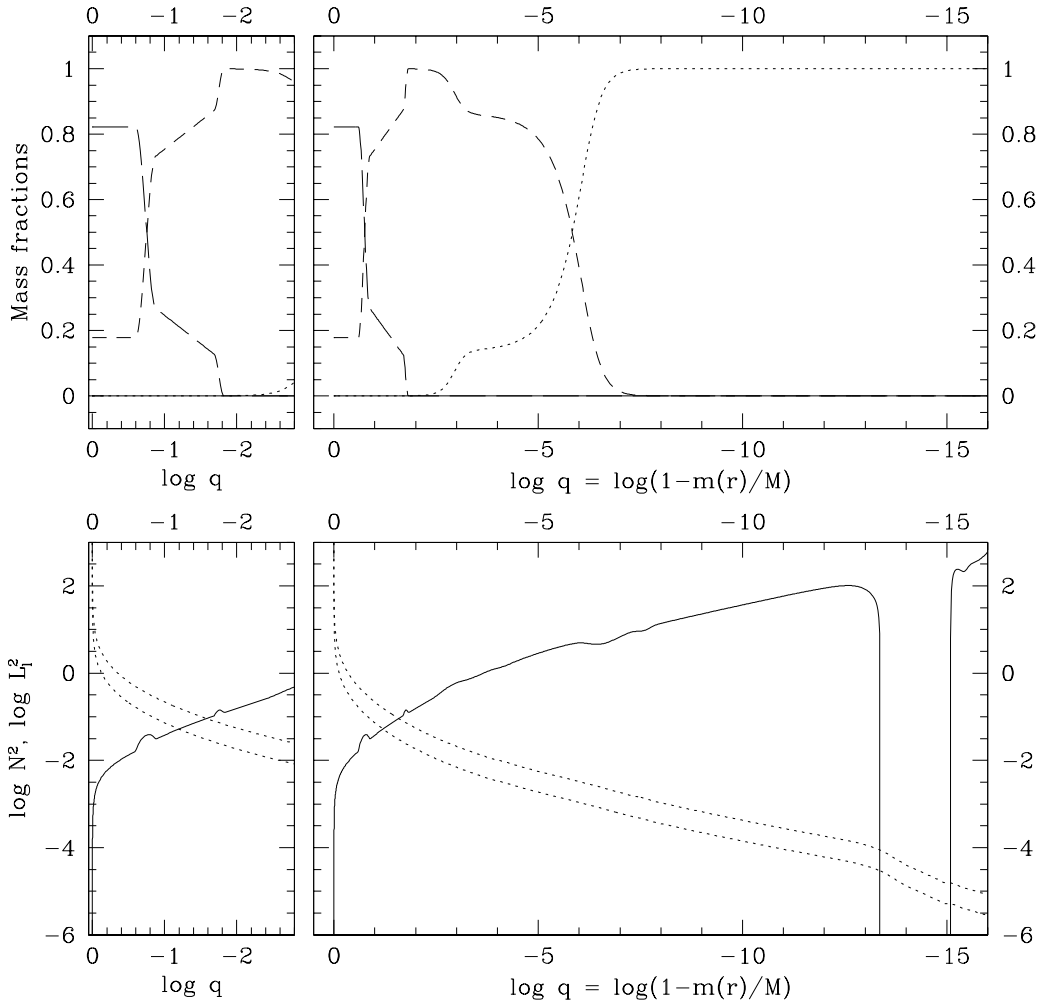

FIGURE 5.6 – Top panel: Chemical abundance profiles of the optimal model calculated, oxygen (long-dashed line), carbon (dashed line), and helium (dotted line). The abscissa shows the fractional mass depth (with $\log q = 0$ corresponding to the center of the star) The left part of both panels emphasizes a zoom-in-view of the deep interior of the star. Bottom panel: run of the square of the Brunt-Väisälä (solid line) and Lamb frequencies (dashed lines).

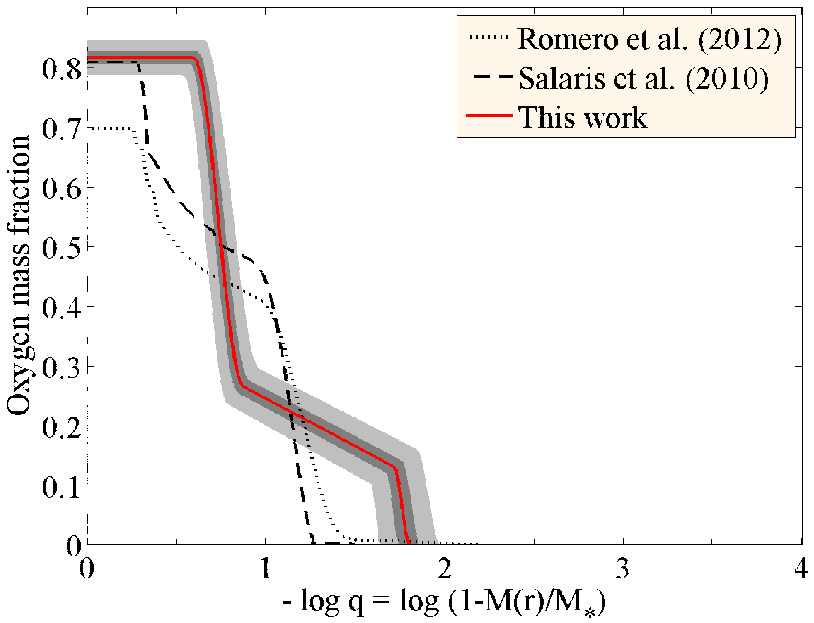

FIGURE 5.7 – Zoomed-in-view of the obtained core oxygen mass fraction (red), emphasizing the two-transitions parameterization, with the 1- and 3-σ contour (dark and light grey respectively). In contrast, available evolutionary profiles from Salaris et al. (2010) and Romero et al. (2012).

major difference between our result and available evolutionary profiles is the height of the oxygen profile in the first and the second transition zones. Our oxygen profile tends to drop much faster than what theory predicts, reaching 26.5 % at a $\log q \sim -0.9$, and 13 % at a $\log q \sim -1.7$.

TABLE 5.3 – Inferred properties of KIC 08626021 on the basis of asteroseismology

Quantity	Estimated value
$\log g$ (cm s^{-2})	7.910±0.005
$T_{\rm eff}$ (K)	30225±50
$\log M({\rm He})/M_*$	−3.618±0.002
$X({\rm He})_{\rm env}$	0.14±0.01
$\log q$ [X(He)=0.5×$X({\rm He})_{\rm env}$]	−2.93±0.02
$\log q$ [X(He)=X(C)=0.5]	−5.84±0.10
$X({\rm O})_{\rm center}$	0.820±0.010
$\log q$ [X(C)=X(O)=0.5]	−0.75±0.05
$M_*/M_\odot$	0.56864±0.00003
$R_*/R_\odot$	0.013819±0.000001
$L_*/L_\odot$	0.14304±0.00097
$P_{\rm rot}$ (h)	46.4±2.6
$V_{\rm eq}$ (km s^{-1})	0.36±0.02
J (kg m^2 s^{-1})[a]	6.61±0.38×10^{38}
$J/J_\odot$	1/291
M_r[b]	10.262±0.001
d (pc)	425±39

[a] Assuming solid body rotation throughout the star.

[b] Based on a model atmosphere with the seismic values of $\log g$, $T_{\rm eff}$, and M_*, coupled to the uncertain value of r = 18.40±0.20 for KIC 08626021.

5.5.2 Fourteen Parameters and Eight Periods: An Unconstrained Problem?

A legitimate question that may come to the mind of the reader is the following: does the fact that fourteen defining parameters have been used in the present search exercise compared to only eight periods necessarily imply that the problem is underconstrained? Giammichele et al. (2016b) have presented some tests geared to answer that question, and they found that this is not the case. We provide here further quantitative arguments, starting with the simplest test that we can imagine to address the simplistic point of view that fourteen free parameters should be plenty enough to fit perfectly eight periods. If this is true, then a set a eight randomly generated periods should be perfectly fitted in our approach. In this Subsection, we thus present the results of another search exercise aimed at fitting a "fake" stellar spectrum entirely composed of random periods. We decided to opt for a spectrum of eight periods, all of them randomly picked to have their values between 100 to 400 s, the exact same situation for our DBAV KIC 08626021. The list of the periods randomly selected used in the example presented in this section is: 125, 161, 164, 166, 187, 223, 231, and 271 s. The parameter space used for the fit of our "fake" star is rigorously the same as the one used to find our best fit of KIC 08626021, to guarantee consistency in our comparison process.

We find, in fact, that the quality of the fit is quite poor as we obtain a value of the merit function $S^2 = 9.2$, with a period dispersion $\langle \Delta P \rangle$ of 0.7 s. The degradation of the merit function is spectacular, as we lose some ten orders of magnitude in precision compared to the fit of KIC 08626021. This sets the limit for proper seismic fitting precision, as we can easily find a model that will fit any random distribution with a S^2 of the order of ten in the present case with eight periods. Clearly then, it is not true that a number of free parameters larger than the number of fitted periods will necessarily imply a perfect fit in this type of seismic exercise.

5.5.3 Another Test: Inserting a Single Wrong Period

Another test that can be made is to insert a false period, randomly determined at 325 s, in the spectrum to better illustrate the need for ultra-high precision asteroseismology. In order to keep the total number of periods constant, the closest period to the false period,

303.5 s, was removed. This test is designed to assess the effects of making a single mistake in the choice of observed retained periods. The simplistic view would have it that, even with a wrong period, the play of fourteen free parameters would compensate and still produce a perfect fit to a set of only eight periods. As before the parameter space used for this test is exactly the same as the one used for our best fit of KIC 08626021.

The merit function is here again spectacularly degraded, as we reach a minimum of S^2 of 2.7, with a period dispersion $\langle \Delta P \rangle$ of 0.4 s. The best fit for this example is about as poor as the fit for the "fake" star example. The deviation from the global parameters of the best fit of KIC086 is presented in the third column of table 5.1. Beside the two main atmospheric parameters $T_{\rm eff}$ and $\log g$, the global structure is significantly different, with percentages varying up to 389 %. The definition of the core is also noticeably altered from the one obtained for our best fit of KIC 08626021, with difference percentages ranging between 5 to 62 %. This is a proof that inserting a wrong period in the spectrum is fatal as the result can be entirely undermined. The relatively large number of free parameters, compared to the number of fitted periods, clearly is not an argument for guaranteed perfection.

5.5.4 How Many Parameters Are Sufficient to Properly Determine the Core Chemical Profile?

The question remaining is how many parameters are necessary and sufficient to best model the core chemical profile. Is fourteen parameters an overkill? We conducted an experiment by comparing different parametrizations with different numbers of control points in the core. Mainly, we identified three test cases: homogeneous C/O core with only one parameter defining the core composition, one transition in the core with three control points (core O, t1, Δt1, while t1(O), t2 and Δt2 are set to zero and t2 far enough so that it does not conflict with t1), and the full treatment of the core with the two transitions and the seven parameters defining the core. We performed the test using the eight independent modes of KIC 08626021, as well as the case of the "fake" star and the wrong period in the spectrum to better compare if there is an improvement of the merit function by the increase of the number of parameters, or if we reach a stagnation point. Results are illustrated in Figure 5.8, with four different

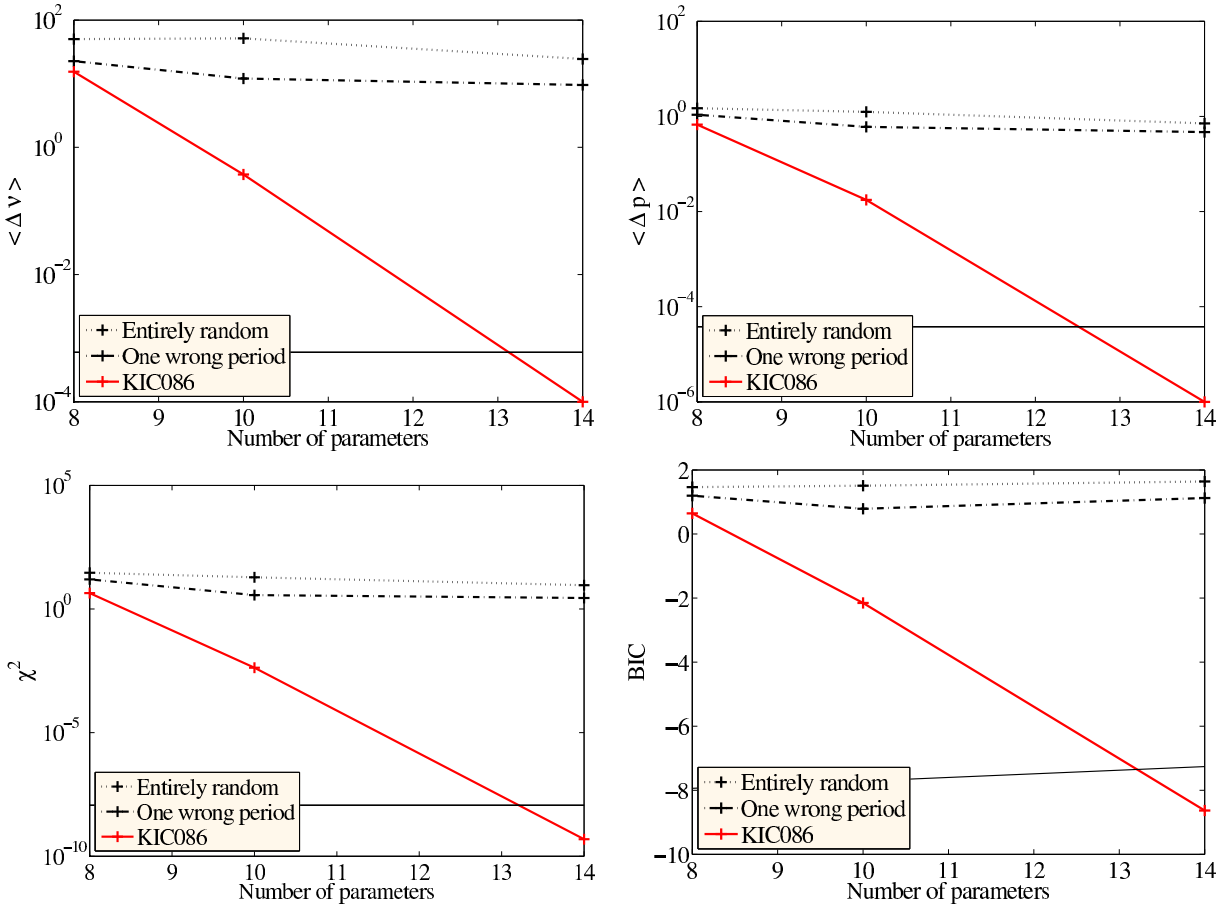

FIGURE 5.8 – Measurement of the average frequency and period dispersion, as well as the S^2 and the BIC, as a function of the number of parameters, for three distinct test cases: homogeneous, one transition and two transition core chemical profile. The measurement of this four parameters was performed for the three cases described: enterely random frequency spectrum (dotted line), one wrong period in the frequency spectrum (dashed and dotted line) and the frequency spectrum of KIC 08626021 (red solid line). Comparison can be made with the observational precision calculated from this set of *Kepler* data (black solid line).

criterions: S^2, BIC, $\langle \Delta P \rangle$, $\langle \Delta \nu \rangle$ investigated. The results are unequivocal for all of the the four criteria: We only reach ultra-high precision matching the precision of the observational *Kepler* data (delimited by the black continuous line) with the two-transition core model. For all four criteria, the increase in precision follows the increase in the number of control points for KIC 08626021 in contrast with the trend for the "fake" star and the wrong period in the spectrum cases being steady with an increasing number of parameters. Parameterization with a two-transition chemical profile in the core is necessary for ultra-high precision seismic analysis for DBV white dwarfs stars.

5.6 INTERNAL ROTATION PROFILE

The method employed here rely on the analysis of the frequency spacing between modes of adjacent values of azimuthal order m. Two assumptions have to be made in order to proceed any further. The first one is to assume the slow rotation of the star, and by slow rotation we mean that the rotation period must be very large compared to the pulsation periods of the star. The second assumption implies that the star rotates as a solid body. The test used here corresponds to the third method to test the solid body rotation as described in Giammichele et al. (2016a). A rotation law with a variable step is employed. The star is considered to be composed of two sections rotating as solid body, independently from one another, an internal region encircled by an external region at an arbitrary depth. By varying this delimitation, it is possible to map the depth where the deviation from the solid body rotation becomes apparent, if there is such a deviation.

If we consider the optimal model of KIC 08626021, the internal rotation profile determined by inversion using the test of the rotation law with a variable step, is given in Figure 5.9. Evolution has started to push the g-modes toward external zones of the star caused by the increased in degeneracy along the cooling sequence. We cannot probe as deep as in the case of GW Vir stars as demonstrated by Charpinet et al. (2009), but still obtained a satisfactory result of probing 70% of the star depth. Within this 70 %, corresponding to some 80% of the mass, we can assert that the star is rotating as a solid body. The relatively slow period of rotation of 46.4 $\pm$ 2.6 h is in agreement with the suggestion of Charpinet et al. (2009) that

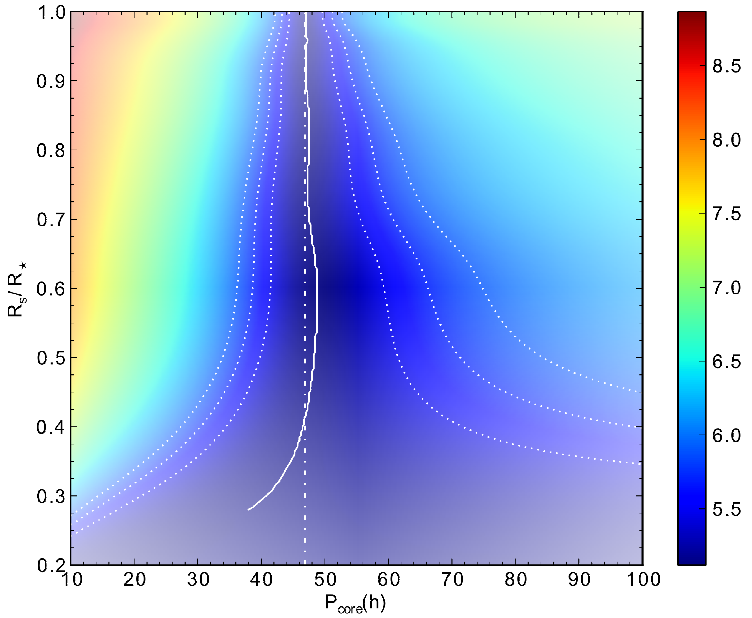

FIGURE 5.9 – Contour map showing the behaviour of the normalized merit function S^2 in terms of the radius and in terms of the rotation period of the inner region for solid body rotation in a two-zone approach defined by Charpinet et al. (2009). Horizontal dot-dashed curves give an indication on the encompassed mass. The solution is illustrated by the nearly vertical white curve and the dotted white curves depict the 1, 2 and 3σ contours. In comparison, the vertical dot-dashed white curve gives the exact solution for solid-body rotation. At larger depths, the gravity modes lose their ability to measure local rotation, giving the divergence in the 1, 2 and 3σ contours.

an isolated white dwarf must have lost most of its angular momentum during pre-white dwarf phases.

5.7 CONCLUSION

In this paper we have carried out a new asteroseismic analysis of KIC 08626021 based on a set of eight periods unveiled in the recent study of Zong et al. (2016). Spectroscopic and asteroseismic determinations of the atmospheric parameters indicate clearly that KIC 08626021 is a blue edge DBA pulsator, the hottest of its class.

We presented a new parametrization including a double layered atmosphere as well as a flexible two-transition core modelization aimed at performing detailed seismic analyses of hydrogen-deficient white dwarf pulsators. These new static structures are flexible enough to allow a quasi-perfect fit of the match of observed/theoretical periods, pushing back the limit of precision and reaching the observational precision of this set of *Kepler* data.

We unraveled the core chemical composition and contrasted with evolutionary chemical profiles of similar masses. A high amount of central oxygen of 81.6% is found. Significant differences are to be noted, especially on the size of the inner homogeneous carbon-oxygen core, which appears to be twice the size on a mass scale. The two "drops" in the oxygen abundances are also deeper than what are predicted by evolutionary models.

Several tests were made to demonstrate that an optimization with fourteen parameters and eight periods does not guarantee a perfect fit of any random frequency spectrum. Moreover, proof has been made that inserting a false period in the period spectrum can be fatal to the seismic analysis.

The essential results of the present analysis are summarized in Table 5.3, where we present a number of interesting inferences on KIC 08626021 coming from seismology. We point out that the very small uncertainties on the derived parameters only reflect the errors of the fit, not systematic effects likely associated with our specific model parametrization and the input constitutive physics that we used.

This work was supported in part by the NSERC Canada through a doctoral fellowship awarded to Noemi Giammichele, and through a research grant awarded to Gilles Fontaine. The

latter also acknowledges the contribution of the Canada Research Chair Program. Stéphane Charpinet acknowledges financial support from "Programme National de Physique Stellaire" (PNPS) of CNRS/INSU, France, and from the Centre National d'Études Spatiales (CNES, France). This work was granted access to the HPC resources of CALMIP under allocation number 2015-p0205. The authors are most grateful to Betsy Green for gathering for us a spectrum of KIC 08626021 as well as Pierre Bergeron for permission to use his grids of model atmospheres and synthetic spectra of DB white darfs.

5.8 REFERENCES

Bischoff-Kim, A., & Østensen, R. H. 2011, ApJ, 742, LL16

Bischoff-Kim, A., Østensen, R. H., Hermes, J. J., & Provencal, J. L. 2014, ApJ, 794, 39

Brassard, P., Pelletier, C., Fontaine, G., & Wesemael, F. 1992, ApJS, 80, 725

Brassard, P., & Charpinet, S. 2008, Ap&SS, 316, 107

Brassard, P., & Fontaine, G. 2013, European Physical Journal Web of Conferences, 43, 05010

Charpinet, S., Fontaine, G., Brassard, P., Green, E. M., & Chayer, P. 2005, A&A, 437, 575

Charpinet, S., Van Grootel, V., Reese, D., et al. 2008, A&A, 489, 377

Charpinet, S., Fontaine, G., & Brassard, P. 2009, Nature, 461, 501

Charpinet, S., Van Grootel, V., Brassard, P. et al. 2013, in EPJ Web of Conf., Aging Low Mass Stars: From Red Giants to White Dwarfs, ed., A. Noels & V. Van Grootel, 43, 04005

Córsico, A. H., Althaus, L. G., Miller Bertolami, M. M., & Bischoff-Kim, A. 2012, A&A, 541, AA42

Fontaine, G., & Brassard, P. 2002, ApJ, 581, L33

Fontaine, G., & Brassard, P. 2008, PASP, 120, 1043

Giammichele, N., Fontaine, G., Brassard, P., & Charpinet, S. 2015, ApJ, 815, 56

Giammichele, N., Fontaine, G., Brassard, P., & Charpinet, S. 2016a, submitted to ApJS

Giammichele, N., Charpinet, S., Fontaine, G., & Brassard, P. 2016b, submitted to ApJS

Iben, I., Jr., Kaler, J. B., Truran, J. W., & Renzini, A. 1983, ApJ, 264, 605

Koen, C., & Laney, D. 2000, MNRAS, 311, 636

Koester, D. 2010, Mem. Soc. Astron. Italiana, 81, 921

Østensen, R. H., Bloemen, S., Vučković, M., et al. 2011, ApJ, 736, LL39

Ostensen, R. H. 2013, 18th European White Dwarf Workshop., 469, 3

Romero, A. D., Córsico, A. H., Althaus, L. G., et al. 2012, MNRAS, 420, 1462

Salaris, M., Cassisi, S., Pietrinferni, A., Kowalski, P. M., & Isern, J. 2010, ApJ, 716, 1241

Straniero, O., Domínguez, I., Imbriani, G., & Piersanti, L. 2003, ApJ, 583, 878

Van Grootel, V., Charpinet, S., Brassard, P., Fontaine, G., & Green, E. M. 2013, A&A, 553, A97

Zong, W., Charpinet, S., Vauclair, G., Giammichele, N., & Van Grootel, V. 2016, A&A, 585, 22

Chapitre 6

GD 1212: probing deep into the heart of ZZ Ceti stars

N. Giammichele[1], S. Charpinet[2], G. Fontaine[1], and P. Brassard[1]

[1] *Département de Physique, Université de Montréal, Succ. Centre-Ville, C.P. 6128, Montréal, QC H3C 3J7, Canada*

[2] *Université de Toulouse, UPS-OMP, IRAP, Toulouse F-31400, France*

CNRS, IRAP, 14 avenue Edouard Belin, F-31400 Toulouse, France

To be submitted to *The Astrophysical Journal*

6.1 ABSTRACT

We present a detailed seismic analysis of the first ZZ Ceti star observed with *Kepler*2. We investigate the case of GD 1212, observed for a total of 11.5 days during the preliminary engineering run in January and February 2014. We report the results of the frequency extraction exercise that lead to the seismic analysis of this cold ZZ Ceti pulsator. We uncovered 25 independent pulsation modes in GD 1212, for which we can identify 11 multiplets useful for the seismic exercise. We infer several global and structural parameters for this star using the forward method based on physically sound models. We unravel the internal structure as well as the rotation profile of GD 1212 deeper than in any other white dwarf stars studied so far. This opens up interesting prospects for future analyses of the white dwarf pulsators monitored in the *Kepler* and *Kepler*2 fields.

6.2 INTRODUCTION

ZZ Ceti stars or DAVs, from the prototype star Ross 548, are pulsating hydrogen-dominated atmosphere white dwarfs. They represent a transiting phase of about 80% of all the entire population of white dwarf, which when cooling down, go through an instability strip around an effective temperature of $\sim$ 12,000 K and start to pulsate. Pulsations are non-radial g-modes generated by the rise of the opacity due to the partial ionisation in the thin hydrogen layer enveloping the helium mantle, surrounding the carbon-oxygen core.

There is a very wide and rich variety of light curves from pulsating white dwarfs (Fontaine & Brassard 2008). The blue edge of the pulsating strip is usually characterized by stars with rather "simple" pulsation spectra, where the amplitudes tend to remain low. For asteroseismological purposes, the mode identification, the connection between the theoretical models and the observed periods, is fairly easy, but the number of frequencies available, and therefore the information available to decrypt the star structure, tends to be low. As we move along into the instability strip, pulsation spectra tend to become more complicated, varying dramatically with time, with numerous harmonics and linear combinations. The task of finding the proper mode identification become arduous, complicating greatly any asteroseismic analysis of the

involved stars. As we reach toward the red edge of the instability strip, light curves tend to become simpler again, with the amplitude going down, as if the pulsations were simply dying out. The red edge of this white dwarf pulsating narrow band is thus a good working platform to perform seismic analyses, as the number of involved observed periods is quite larger than at the corresponding blue edge.

The cool ZZ Ceti star GD 1212 (a.k.a WD 2336−079, GJ 4355) was first discovered to pulsate by Gianninas et al. (2006). GD 1212 was observed during a preliminary engineering run of *Kepler*2 (K2) in January and February 2014. The NASA *Kepler* mission launched in 2009 has revolutionized the study of exoplanets and astrophysics by providing high-precision, high-cadence, continuous light curves of tens of thousands of stars (Howell et al. 2014). The loss of the second reaction wheel of the *Kepler* spacecraft forced the initial mission that was monitoring the same portion of the sky for four continuous years to reorientate the field of view near the ecliptic plane. However, all *Kepler* assets are kept the same, the high cadence and the high-precision photometry that made the first mission a success. GD 1212 was observed for a total of 264.5 hr. A frequency extraction from the K2 light curve and a preliminary analysis of this cool pulsating white dwarf was performed by Hermes et al. (2014). We felt that it would be timely to exploit this data set in the light of our recent efforts to improve and renew the seismic modeling of white dwarf stars.

The first section will present the pulsational and spectroscopic properties of GD 1212 based on the frequency extraction of the K2 light curve. A different extraction procedure is performed, unveilling 6 more frequencies than the 19 independent modes presented by Hermes et al. (2014). We will also present in that section how the identification of the independent modes necessary for the seismic exercise is performed. In section 2, we present the asteroseismological analysis per se, unravelling the internal structure of the pulsator. The last section will present the study of the internal rotation based on the identified rotationaly split multiplets.

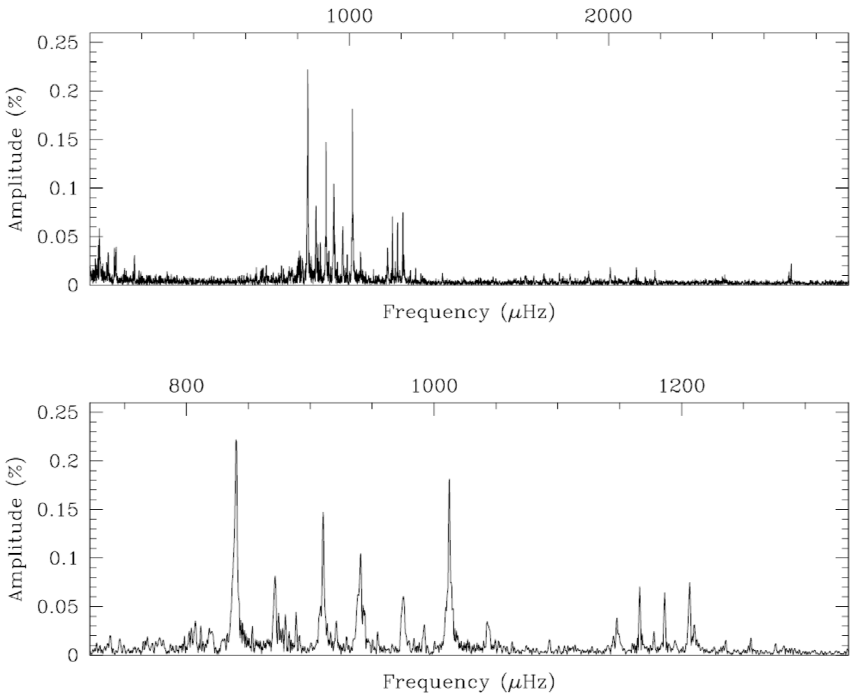

FIGURE 6.1 – Lomb Scargle periodogram of the 9-day lightcurve of GD 1212 showing the signal recorded by K2 (top panel), with a zoom-in-view of the central region of interest (bottom panel).

6.3 PULSATIONAL AND SPECTROSCOPIC PROPERTIES

6.3.1 Prewhitening Procedure

Observation and reduction procedures for the treatment of the light curve from the raw data are described in great details in Hermes et al. (2014) and are in all points similar here.

The data obtained on GD 1212 during the *Kepler* 2 test run come in two pieces of continuous data separated by roughly 15 days. The first set is a short lightcurve of $\sim$ 2.5 days. The second set is a lightcurve covering 9 days. It is best to examine each set separately as the 15 day interruption strongly degrades the window function and introduces strong aliases in the Fourier Transform if we combine the data.

The total length of the second set of lightcurve is 8.98942 days with a nearly 100 % duty cycle, giving a formal resolution of 1.29 μHz. Median noise level near 500 and 1500 μHz is down to $\sim$0.0036 % (36 ppm). Figure 6.1 shows the corresponding amplitude spectrum.

One difficulty is the unstable nature of most of the peaks whose amplitude, frequency,

and possibly phase vary with time during the observation. These peaks cannot be smoothly prewhitened in the standard way because fitting a pure sine wave does not completely remove the pulse shape. However, one can always get rid of the broadened signal with a linear combination of sinewaves (because sinewaves form a basis of functions and any function form can in principle be projected on such a basis).

An example is given with the main peak, as can be seen in Fig. 6.2. It is possible to remove completely and cleanly the signal associated to the dominant peak with the superposition of five sinewaves having close frequencies. The main peak is then deconstructed with f1 of 840.2108 μHz and four other signals of 836.8270, 837.9999, 839.1828, and 842.0158 μHz. Of course this set of frequencies correspond to only one real mode and should not be interpreted as five independent frequencies. The dominant frequency can then be selected as an estimate of the true frequency of the mode (this is the simplest option used here; although the uncertainties given by the fit are then underestimated for that mode) or one could compute the "average" properties of the mode (frequency, amplitude and their uncertainties) by taking the averages of the values given by the five sinewaves and their dispersion. Doing it this way for all the peaks, one can dig out all the frequencies with the prewhitening technique.

Based on all frequencies above 4σ, including multi-frequencies associated to broaden peaks as discussed previously, we can reconstruct the Lomb-Scargle periodogram and contrast it with the observed one in Fig. 6.3 and reconstruct the lightcurve and compared it to the observed one in Fig.6.4.

Table 6.1 provides the final list of significant frequencies after removing the side frequencies of the broad peaks. For the latter, the values of the dominant peaks have been kept as the reference but no error is given as the value obtained from prewhithening certainly underestimates the uncertainties because of the broadening.

Based on the results presented in Table 6.1, we can extract 48 "cleaned" frequencies. Out of these 48 independant signals, we can deduct 16 frequencies that are most certainly nonlinear combinations of parent modes that are listed in the comments of Table 6.1. They are located in the $1700 - 2200$ μHz range (sums involving the main peaks) and at frequencies below 200 μHz (differences involving the main peaks). This leaves us with 31 main modes to work with,

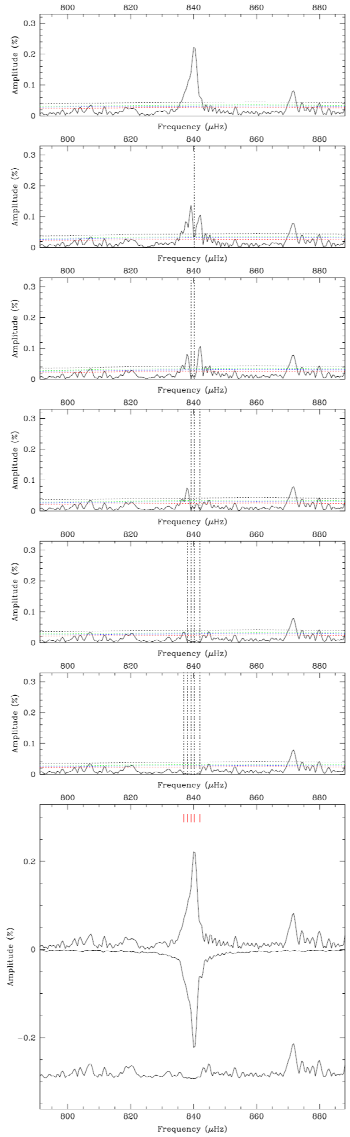

FIGURE 6.2 – Prewhithenning sequence (top panels) and reconstructed shape (bottom panel) of the broadened main peak. Five sinewaves above 4x the noise are sufficient here to reproduce the waveshape and remove the peak without affecting the neighborhood. Of course, this series of prewhitenned peaks corrresponds in fact to only one physical mode.

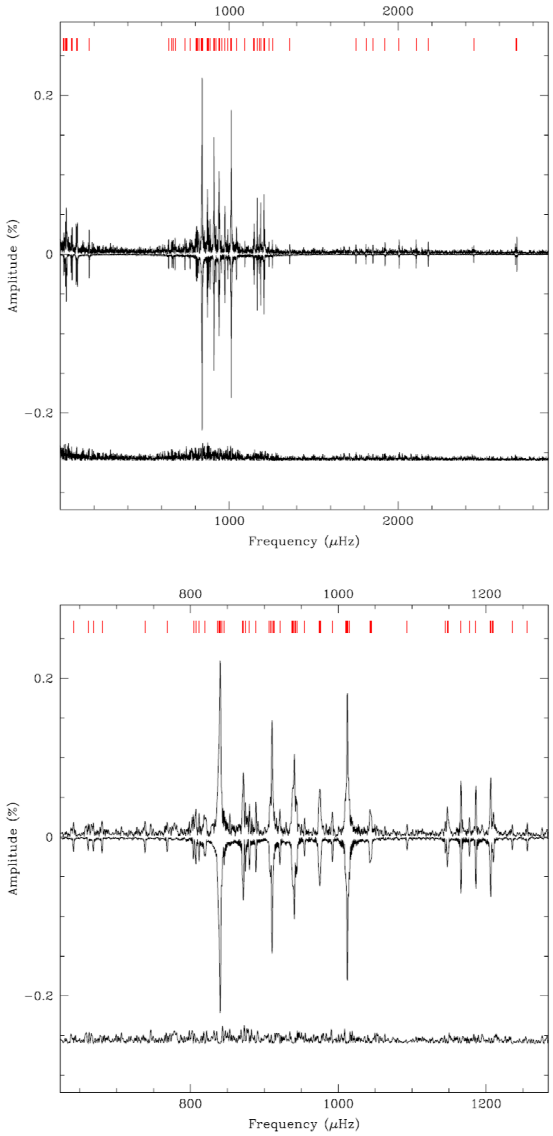

FIGURE 6.3 – Reconstructed Lomb Scargle periodogram (plotted upside down) of the 9 day lightcurve of GD 1212 compared to the observed one. The bottom curve shows the residual. The lower panel is a close up view of the region between 700 and 1300 μHz.

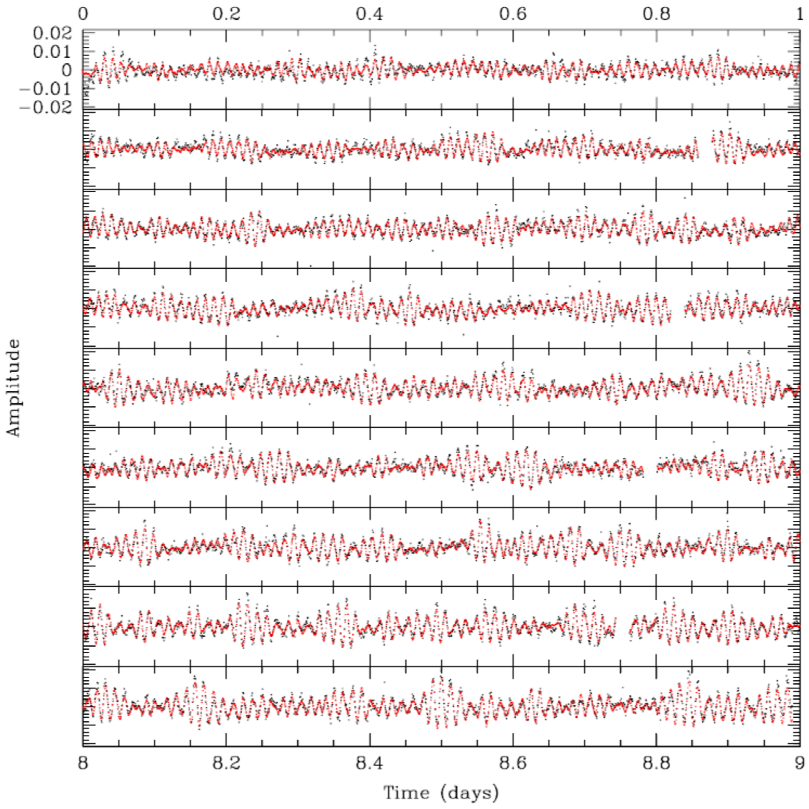

FIGURE 6.4 – Lightcurve reconstructed from all the frequencies, compared to the observed light curve.

TABLE 6.1 – Final list of significant frequencies above 4σ for the 9d run. Bracketted frequencies may be unsure.

Id.	Frequency (μHz)	σ_f (μHz)	Period (s)	σ_P (s)	Amplitude (%)	σ_A (%)	Phase (s)	$\sigma_{\rm Ph}$ (s)	S/N	Comments
f_{048}	20.6931	0.1402	48325.2773	327.3270	0.0301	0.0059	0.2202	0.0270	5.1	f1-f21
f_{054}	25.1616	0.1624	39743.1002	256.5863	0.0259	0.0059	0.5367	0.0313	4.4	f42-f21
f_{032}	32.4511	0.1046	30815.5820	99.2811	0.0402	0.0059	0.5069	0.0200	6.8	f7-f3
f_{015}	36.4081	0.0654	27466.4281	49.3249	0.0641	0.0059	0.5414	0.0063	10.9	
$[f_{027}]$	[38.1695]	[0.0965]	[26198.9033]	[66.2164]	[0.0433]	[0.0059]	[0.9670]	[0.0095]	[7.4]	f2-f10?; blend with f15
$[f_{046}]$	[40.1084]	[0.1342]	[24932.4336]	[83.4495]	[0.0310]	[0.0059]	[0.1985]	[0.0259]	[5.3]	f4-f7?; blend with f15
f_{057}	64.7091	0.1666	15453.7724	39.7892	0.0238	0.0056	0.4011	0.0335	4.3	f4-f6 ?
f_{049}	69.8447	0.1361	14317.4751	27.8906	0.0292	0.0056	0.6677	0.0139	5.2	f2-f5 ?
f_{053}	71.4853	0.1494	13988.8825	29.2276	0.0265	0.0056	0.6006	0.0152	4.8	f4-f1 ?
f_{036}	94.5555	0.1028	10575.8013	11.5015	0.0371	0.0054	0.5161	0.0213	6.9	f2-f31 ?
$[f_{047}]$	[100.2178]	[0.1265]	[9978.2649]	[12.5987]	[0.0303]	[0.0054]	[0.4270]	[0.0130]	[5.6]	f5-f1?; blend with f33
f_{033}	101.6019	0.1006	9842.3383	9.7465	0.0382	0.0054	0.5418	0.0103	7.1	f31-f21 ?
f_{044}	171.8924	0.1091	5817.5941	3.6936	0.0325	0.0050	0.7269	0.0241	6.5	f2-f1 ?
f_{069}	641.6091	0.1575	1558.5814	0.3826	0.0181	0.0040	0.0048	0.0433	4.5	
$[f_{073}]$	[661.4700]	[0.1769]	[1511.7843]	[0.4043]	[0.0172]	[0.0043]	[0.4423]	[0.0460]	[4.0]	several weak peaks around
$[f_{072}]$	[668.5275]	[0.1724]	[1495.8247]	[0.3858]	[0.0179]	[0.0043]	[0.3825]	[0.0442]	[4.1]	*; several weak peaks around
f_{065}	680.2633	0.1554	1470.0190	0.3358	0.0199	0.0044	0.0097	0.0395	4.6	
f_{064}	738.4715	0.1696	1354.1484	0.3110	0.0202	0.0048	0.8138	0.0390	4.2	
f_{061}	768.4389	0.1692	1301.3396	0.2866	0.0222	0.0053	0.9265	0.0354	4.2	*
f_{051}	803.9796	0.1447	1243.8127	0.2239	0.0272	0.0055	0.8632	0.0311	4.9	*
f_{035}	807.1185	0.1049	1238.9754	0.1611	0.0375	0.0055	0.1074	0.0233	6.8	*
f_{062}	811.5749	0.1788	1232.1722	0.2714	0.0220	0.0055	0.9186	0.0373	4.0	*
f_{021}	819.9788	...	1219.5437	...	0.0536	...	0.6406	...	9.6	
f_{001}	840.2108	...	1190.1774	...	0.2477	...	0.9957	...	43.4	
$[f_{042}]$	[844.8180]	[0.1201]	[1183.6868]	[0.1683]	[0.0333]	[0.0056]	[0.1009]	[0.0243]	[5.9]	*; may be linked to f1
f_{007}	871.6296	...	1147.2763	...	0.0866	...	0.7558	...	15.3	
f_{030}	874.0884	0.0992	1144.0491	0.1298	0.0406	0.0057	0.8393	0.0209	7.2	*
f_{023}	879.8627	0.0827	1136.5410	0.1068	0.0486	0.0057	0.0691	0.0166	8.6	
f_{029}	888.5756	0.0946	1125.3967	0.1198	0.0416	0.0055	0.7081	0.0191	7.5	
f_{004}	910.4287	...	1098.3837	...	0.1513	...	0.2721	...	28.7	
f_{031}	921.1198	0.0936	1085.6351	0.1103	0.0402	0.0053	0.6656	0.0197	7.6	
f_{005}	940.7330	...	1063.0009	...	0.1099	...	0.1926	...	21.1	
f_{060}	954.4381	0.1667	1047.7369	0.1829	0.0223	0.0052	0.4139	0.0354	4.3	*
f_{010}	975.3833	...	1025.2379	...	0.0740	...	0.5623	...	14.1	
f_{039}	992.3267	0.1021	1007.7326	0.1037	0.0358	0.0052	0.1987	0.0220	7.0	
f_{002}	1012.3867	...	987.7648	...	0.1846	...	0.5738	...	37.0	
f_{040}	1043.7635	...	958.0714	...	0.0348	...	0.6009	...	7.1	*
f_{076}	*1093.3840*	*0.1962*	*914.5918*	*0.1641*	*0.0162*	*0.0045*	*0.2470*	*0.0485*	*3.6*	probably higher S/N
$[f_{071}]$	[1145.0845]	[0.1522]	[873.2980]	[0.1161]	[0.0180]	[0.0039]	[0.9228]	[0.0453]	[4.7]	*; may be linked to f34
f_{034}	1147.7071	...	871.3025	...	0.0380	...	0.1785	...	9.9	
f_{011}	1166.2026	0.0367	857.4839	0.0270	0.0722	0.0037	0.7412	0.0109	19.3	
f_{059}	1177.7694	0.1146	849.0626	0.0826	0.0226	0.0036	0.2073	0.0350	6.2	*
f_{014}	1186.3756	0.0394	842.9034	0.0280	0.0643	0.0036	0.9827	0.0123	18.0	
f_{012}	1206.6583	...	828.7351	...	0.0715	...	0.7307	...	21.5	
f_{043}	1210.3198	...	826.2279	...	0.0329	...	0.4581	...	9.9	
f_{077}	1235.7486	0.1525	809.2261	0.0999	0.0148	0.0032	0.0759	0.0533	4.7	*
f_{070}	1256.0633	0.1229	796.1382	0.0779	0.0180	0.0031	0.7257	0.0436	5.8	*
f_{081}	1358.7756	0.1703	735.9567	0.0922	0.0118	0.0028	0.4088	0.0663	4.2	*
f_{082}	1750.5275	0.1703	571.2564	0.0556	0.0118	0.0028	0.5140	0.0666	4.2	f7+f23 ?
f_{080}	1810.0618	0.1754	552.4673	0.0535	0.0119	0.0029	0.1206	0.0659	4.0	f7+f5 ?
f_{083}	1850.9599	0.1796	540.2602	0.0524	0.0117	0.0030	0.7794	0.0672	4.0	f4+f5 ?
f_{078}	1923.0760	0.1429	520.0002	0.0386	0.0143	0.0029	0.9558	0.0550	5.0	f4+f2 ?
f_{067}	2006.4317	0.1067	498.3972	0.0265	0.0185	0.0028	0.5714	0.0424	6.7	f1+f11
f_{068}	2107.0454	0.0989	474.5982	0.0223	0.0185	0.0026	0.6984	0.0425	7.2	f5+f11
f_{075}	2178.6038	0.1052	459.0096	0.0222	0.0167	0.0025	0.0820	0.0472	6.7	f2+f11
f_{084}	2447.9299	0.1386	408.5084	0.0231	0.0111	0.0022	0.1256	0.0706	5.1	
f_{079}	2695.3338	0.1034	371.0116	0.0142	0.0136	0.0020	0.0507	0.0577	6.9	
f_{063}	2703.8441	0.0647	369.8438	0.0089	0.0217	0.0020	0.9544	0.0363	11.0	

with frequencies ranging from $\sim$ 35 μHz to 2700 μHz, over the 4σ threshold. The remaining frequency is slightly below the 4σ, but might have a higher signal-to-noise ratio (S/N).

Hermes et al. (2014) decided to use Lorentzian profiles to prewhiten the signal, and more specifically the central peak, half-width-half-maximum, and intensity of this Lorentzian to define the adopted periods, period uncertainties, and amplitudes of the broad peaks of the Fourier Transform. The traditional method of fitting Lorentzian profiles to the power spectrum of photometric data is intended for deriving frequencies, amplitudes, and mode lifetimes from stochastically driven pulsation. This is not the case here, and there is a priori no reason to use Lorentzian profiles to fit pulsations in standard cool ZZ Ceti stars, which tends to largely overestimate the uncertainties of the broadened peaks.

6.3.2 Secure Detection Threshold

Following the procedure of the false alarm probability defined by Zong et al. (2016), we need to define a secure detection threshold method to base our seismic analysis on other than simply assume the usual rule of the thumb limit of 4-5σ. The method is as follow: 10 000 artificial light curves of white gaussian noise are generated, using the same time sampling as the observation (in our case nine days). For each artificial light curve, the Lomb-Scargle Periodogram and the median value of the noise are calculated. The number of time that at least one peak in the LSP is above a chosen thresold is then calculated, for any given S/N threshold. The false alarm probability P_1 of having at least one peak above a given S/N threshold due to noise is given by dividing by the number of tests.

Fig. 6.5 illustrates the result obtained for the false alarm probability P_1 as a function of the S/N threshold. We are mainly interested in the limit corresponding to 1 chance out of 10 000 that a single peak due to noise has been found among the 10 000 randomly generated lightcurves, which correspond to a S/N = 4.9. We also see that the probability of having a false detection reaches 10% for S/N slightly below 4σ, which show the danger of using any arbitrary value of detection limit to observations, especially with space observations from *Kepler*, even if the run test of the *Kepler*2 mission is not a standard observation in our case.

Based on the result of these calculations, we will use the threshold of 4.9σ as conservative

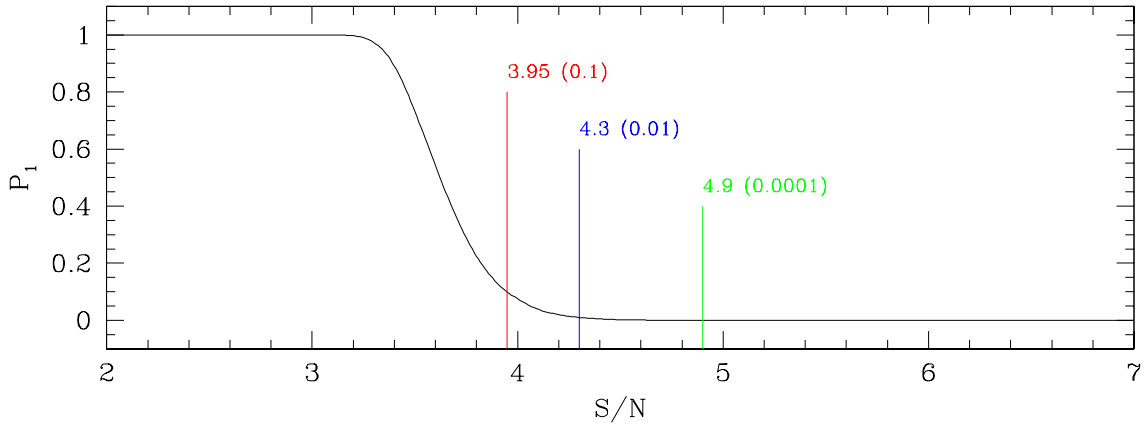

FIGURE 6.5 – False alarm probability P_1 of having one peak cause by noise above a given S/N threshold in the Lomb-Scargle periodogram of GD 1212. The three vertical lines indicate from left to right, the S/N value corresponding to $P_1 = 0.1, 0.01, 0.0001$, respectively. The limit that concern us, $P_1 = 0.0001$, meaning that the risk of having a false detection above that threshold is reduced to less than one chance over 10,000, defines the adopted criterion. It corresponds in our case to the limit of 4.9σ.

limit of detection of the observation of GD 1212. If we go back to Table 6.1, out of the 31 independent peaks over the 4 σ limit, we can cut away 6 modes that are under our threshold. We are left with 25 independent modes to work with.

6.3.3 Mode Pre-Identification

One major difficulty by looking at this spectrum is the complexity of the identification of the modes. Modes seem to form an intricate pattern composed of various multiplets, interlaced into each other. Mode identification is crucial in our case, as one single misidentified mode can ruin the whole seismic analysis. If we concentrate on the central part of the Fourier transform of the signal, we can divide the central part into two main sections, one ranging from 800 to 1100 μHz (region 1), while the second region ranges from 1100 to 1300 μHz (region 2). Region 2 has the interesting perspective that it presents three narrow peaks, f11-f14-f12 with a nearly perfect constant spacing of 20.2 μHz between them. Moreover this spacing is also found (in region 2 as well) between two peaks f77-f70 (even if the signal-to-noise ratio of the mode f77 of 4.7 σ is slightly under the conservative threshold of 4.9 σ, we can still get a clue of the mode identification by observing the same difference between these two peaks). If we assume that this spacing in frequency corresponds to rotation splitting of $l = 1$ g-modes, we can estimate

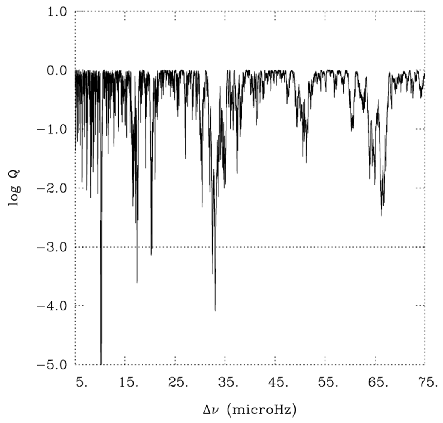

FIGURE 6.6 – Statistical Kolmogorov-Smirnov test perfomed on all the periodicities.

the expected rotation splitting of quadrupole modes by using first order solid body rotation in the asymptotic limit of high radial order:

$$\Delta\sigma = \Omega(1 - \frac{1}{l(l+1)}), \tag{6.1}$$

where Ω corresponds to the assumed uniformed angular rotation frequency. For $l = 2$, we would thus obtain a frequency spacing of 33.6 μHz. Always focusing on region 2, this spacing is found between peaks f71-f59-f43, suggesting that mode f59 could be the central component of a rotationnally split triplet of $l = 2$.

Furthermore, if we perform a statistical Kolmogorov-Smirnov test to find the recurrent spacing in frequency among the list of all periodicities of region 1 and region 2, two frequency spacings 20.225 μHz and 33.035 μHz (and their multiples) stand out as can be seen in Fig.6.6. This is quite conforting as we get the idea of a correct interpretation of all the various splitting of region 2.

At this stage, we have identified three independant modes coherently with each other, but we need to disentangled a few more modes in order to perform a solid seismic analysis. Focusing on the high frequency region from 1700-2800 μHz (region 3), we notice three peaks f84, f79, and f63 that are not linear combinations of other modes. Their spacing does not show presence of the rotational splitting previously identified of 20.2 μHz and 33.6 μHz for $l = 1$ and $l = 2$, and these three modes are above the estimated threshold of 4.9 σ. We can quite

safely interpret these three peaks as independant modes.

We have now six secured identified independent modes: f59, f14, f70, f84, f79, and f63 to continue the mode identification of the various regions, and especially region 1 where the majority of the high amplitude peaks are. We need to be extremely careful about the selection in region 1, and we repeat ourselves here, we only want to secure independent modes for the seismic analysis as the whole exercise can be easily ruined by one wrong period (Giammichele et al. in prep. 2016). To better detangled the various modes in region 1, we have to use an alternate method to better inspect and determine the independent modes, a tool that is capable of identifying the rotationally split multiplets. In this case, we are using as preliminary analysis to tag the different peaks the algorithm LUCY with the inclusion of stellar rotation, algorithm included in the Toulouse package. The complete description can be found in Charpinet et al. (2008). In a nutshell, LUCY is the genetic algorithm that performs the double-scheme optimisation that finds the various theoretical models corresponding to minima of the process during which observed pulsation periods are matched to theoretical calculated periods. Several steps are required in order to do so, the first one being the computation of the static white dwarf model using a set of identified parameters. Once this step is completed, the code evaluate the adiabatic pulsation properties of the model assumed purely spherical at this stage. The third step is to incorporate the effect of stellar rotation into the pulsation spectrum. By computing for each mode the first-order perturbations of the pulsation frequencies caused by rotation, we obtain a complete rotationally-split theoretical period spectrum. This step neglects higher-order perturbation effects and assume solid body rotation, since we have a priori no available rotation law to apply. We will discuss later the implication of these assumptions. Once these steps are performed, LUCY will perform the double optimisation providing a mapping of the χ^2 obtained from the matching of the periods of the large batches of models calculated, but more importantly in the present case will give for each model the best identification of the periods matched and the complete rotationally-split pulsation spectrum. Using LUCY with the inclusion of stellar rotation is only used in this context to obtain the best pre-identification of the modes present in the spectrum, and the complete analysis to follow will be based on the adiabatic pulsation properties of purely spherical models by only

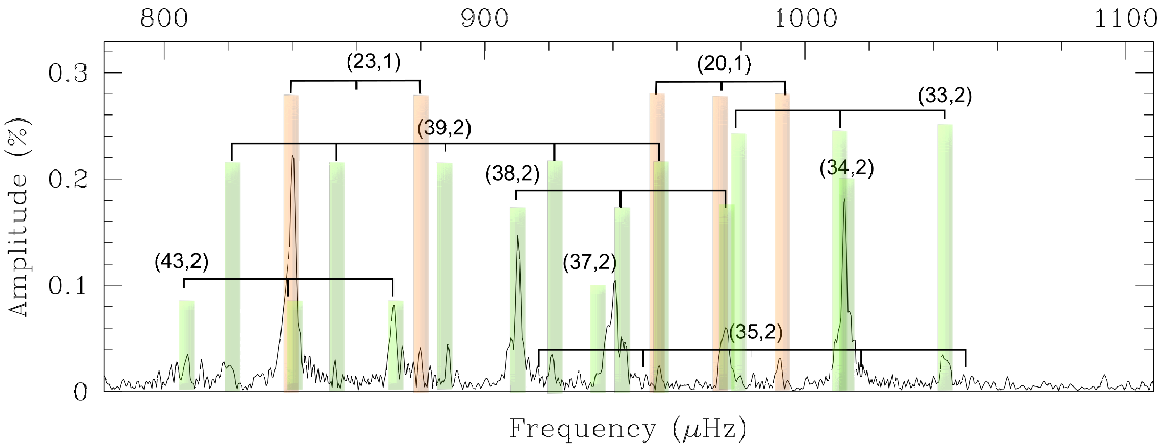

FIGURE 6.7 – All identified multiplets from the test with LUCY with the inclusion of stellar rotation for region 1.

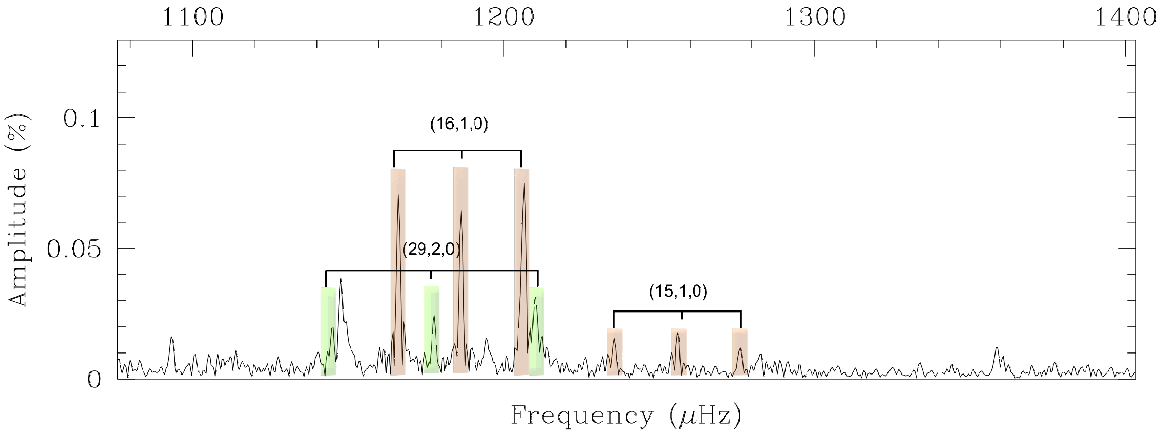

FIGURE 6.8 – Same as before, for region 2.

selecting the appropriate identified $m = 0$ modes, in order not to assume any a priori rotation law, matter that will be inspected afterward.

After performing a complete double-optimisation run, we obtain the following identification showed in Fig. 6.7 and 6.8. Three of the six previously identified independant modes f59, f14, f70, were fixed to their appropriate value of identified mode degree and radial order, all of the others were left to vary. We repeat here that this exercise was done in the unique purpose to pre-identified which modes to use in the case of purely spherical models for the asteroseismological analysis to come. To the six previously identified independant modes, we can add f40, f2, f4, f29, and f35, leaving us with eleven independant modes over the 4.9 σ detection limit to work with. The rest of the peak identified are shown in Fig. 6.7, a particular

attention to the fact that the peaks with the highest amplitudes: f1 and f2 are not central components of multiplets but rather $m = +1$ components, and will not be taken into account for the seismi analysis to come.

6.3.4 Independent Spectroscopic and Photometric Determinations

The most recent estimate of spectroscopic determination of effective temperature and surface gravity determined by P. Bergeron (private communication) of $T_{\rm eff} = 11,121 \pm 40$K and $\log g = 8.211 \pm 0.021$ have to be corrected with the 3D model corrections of Tremblay et al. (2013), as the determination of the effective temperature places this star right in the "high $\log g$ problem" region. This gives the following corrected effective temperature and surface gravity of: $T_{\rm eff} = 11,035 \pm 194$K and $\log g = 8.084 \pm 0.049$. The parallax of 62.72 mas determined by Subasavage et al. (2009) puts GD 1212 at a distance of 15.9 ± 0.4 pc. With this parallax measurement, photometry fits to energy distribution yeld a measurement of the $\log g$ value of 8.25 ± 0.3 and of $T_{\rm eff} = 10,938 \pm 198$K (Giammichele et al. (2012). The explanation put forward by the authors for the discrepancy between spectroscopic and photometric determination of the surface gravity might be the presence of an unresolved DC (featurless spectrum) companion white dwarf, diluting the signal of GD 1212, which would also explain the shallower Hα line profile than predicted and the drop in amplitude variations. The latter phenomenon is also plausible with the observed tendancy that pulsations are dying out as stars draw closer to the red edge of the ZZ Ceti instability strip.

6.4 ASTEROSEISMIC ANALYSIS

6.4.1 Technique

The procedure for deriving the structural parameters of GD 1212 are the same as the one described in Giammichele et al. in prep. (2016)(and references therein) for the pulsating DB star KIC 08626021. We use the so-called forward approach which consists in comparing large batches of pulsational properties of theoretical models to the observed ones. It necessitates the use of a double scheme optimization, which in the first step find the best match between the

observed visible pulsating spectrum (with 11 independent frequencies) and a complete theoretical spectrum. It is a combinatorial optimization problem that gives the mode identification. The second step performs the search in the parameter space of the best fitting theoretical model, once the identification of the modes is done. This is done by minimizing a χ^2-type merit function, using a multimodal optimizer based on a massively parallel hybrid genetic algorithm to find the best fit model in the N-dimension parameter space:

$$S^2(a_1, a_2, ..., a_N) = \sum_{i=1}^{N_{obs}} (P_{obs}^{(i)} - P_{th}^{(i)})^2, \tag{6.2}$$

where N_{obs} is the number of observed periods, $\{a_1, a_2, ..., a_N\}$ are the parameters of the model, and each $\{P_{obs}^{(i)}, P_{th}^{(i)}\}$ is a pair of theoretical/observed periods for this model.

It is worth reminding the reader that since we are looking for the best match of theoretical and observed periods, we are always strictly comparing the same number of periods. The problem is uniquely determined, since it is not an inversion problem, we can allow to have more parameters during the optimisation than the number of periods. The only drawback is the increase in size of the parameter space, which can slow down substantially the calculation time.

The description of the theoretical model in the case of a ZZ Ceti star is based on entirely parameterized static models, similarly to the analysis of the DBV in Giammichele et al. in prep. (2016). Four fundamental parameters are required to best represent the white dwarf global structure: the effective temperature $T_{\rm eff}$, the surface gravity $\log g$, the transition point of the helium layer D(He) and of the hydrogen layer D(H). To add some flexibility at the transition zones to the parameterization, we add two additional parameters to this description: Profac(H) and Profac(He), which caracterize the steepness of the transitions at the H/He and He/C-O interface respectively. For the core description we have the option of using a homogeneous core, a parameterized core with one or two transitions, imitating at best evolutionary profiles from Salaris et al. (2010). The positionning and definition of the different control points of the Akima spline for the two transition core is shown in details in Giammichele et al. in prep. (2016). Seven additional are required to fully describe the oxygen profile in the core: core O,

t1, Δt1, t1(O), t2, Δt2 and t2(O). Core O, t1(O), and t2(O) define the amount of oxygen at the star center, and in between the two transitions. T1 and t2 locate the position of the two transitions, while Δt1 and Δt2 quantify the slope at these positions. By using a subset of these control points: Core O, t1, Δt1, and t1(O), we can define the one transition-core. For the homogeneous core, only one parameter: core O is necessary.

Once the structure is fully defined the following step is to evaluate the adiabatic pulsation properties of the model, assumed purely spherical, using an efficient and robust code based on finite element techniques (Brassard et al. (1992); Brassard & Charpinet (2008)).

6.4.2 Period Fit and Determination of Global Parameters

The search for best-fit solutions starts with the largest possible parameter space for GD 1212 based on spectroscopic constraints. The limits used are shown in Table 6.3. Constraints on $T_{\rm eff}$ and $\log g$ rely on the spectroscopic values found for GD 1212. Evolutionary tracks from Salaris et al. (2010) influenced the range on the seven parameters defining the C/O core: core O, t1, Δt1, t1(O), t2, Δt2 and t2(O).

In the 300 to 1500 s range, we consider all modes of degree $l = 1$ and 2. Modes with higher degree are excluded, as we can expected them to be hardly visible due to cancellation effects of their surface geometry. Since low radial order modes are quite insensitive to the prescribed convective efficiency, we fixed the latter to the so-called ML2/α=1.0 prescription and did not vary it in parameter space.

One clear family of models is singled out during the multimodal optimization search in the specified domain, around an absolute and very deep minimum of $S^2 = 5.10^{-4}$, reaching and going beyond the precision of the observations, estimated to be around $S^2 = 10^{-1}$ in the case of this *Kepler*2 run. The relative average dispersion achieved for this best fit model is $\overline{\Delta X/X} = 0.001\%$, where X is either the period P or the frequency ν, giving $\overline{\Delta P} = 0.01$ s or $\overline{\Delta\nu} = 0.015$ μHz. More information on the best-fit model including the details of the period spectrum and mode identification are presented in Table 6.2. This kind of unprecedented precision was also achieved in Giammichele et al. in prep. (2016) using the same parameterized core for the pulsating helium-rich white dwarf KIC 08626021.

TABLE 6.2 – Mode identification and details of the frequency fit obtained for the optimal solution. The mean relative dispersion of the fit is $\overline{\Delta X/X} = 0.001\%$ (or $\overline{\Delta P} = 0.01$ s and $\overline{\Delta\nu} = 0.015$ μHz; $S^2 = 5.9x10^{-4}$).

l	k	$\nu_{\rm obs}$ (μHz)	$\nu_{\rm th}$ (μHz)	$P_{\rm obs}$ (s)	$P_{\rm th}$ (s)	$\log E$ (erg)	C_{kl}	$\Delta X/X$ (%)	ΔP (s)	$\Delta\nu$ (μHz)	Amplitude (%)	Id.
1	−5	2695.334	2695.352	371.01	371.01	44.639	0.4197	+0.00	+0.00	−0.018	0.0136	f_{79}
1	−6	2447.930	2447.948	408.51	408.51	44.156	0.4755	+0.00	+0.00	−0.018	0.0111	f_{84}
1	−7	...	2310.919	...	432.73	43.677	0.4967	...	...	...	...	
1	−8	...	1997.319	...	500.67	44.003	0.4566	...	...	...	...	
1	−9	...	1885.446	...	530.38	43.563	0.4819	...	...	...	...	
1	−10	...	1728.915	...	578.40	43.606	0.4718	...	...	...	...	
1	−11	...	1626.635	...	614.77	43.412	0.4879	...	...	...	...	
1	−12	...	1535.336	...	651.32	43.307	0.4896	...	...	...	...	
1	−13	...	1407.578	...	710.44	43.378	0.4853	...	...	...	...	
1	−14	...	1340.255	...	746.13	43.233	0.4915	...	...	...	...	
1	−15	1256.063	1256.073	796.14	796.13	43.138	0.4916	+0.00	+0.01	−0.010	0.0180	f_{70}
1	−16	1186.376	1186.382	842.90	842.90	43.121	0.4917	+0.00	+0.00	−0.006	0.0643	f_{14}
1	−17	...	1126.674	...	887.57	43.080	0.4895	...	...	...	...	
1	−18	...	1066.865	...	937.33	43.051	0.4894	...	...	...	...	
1	−19	...	1028.013	...	972.75	42.927	0.4936	...	...	...	...	
1	−20	...	979.775	...	1020.64	42.784	0.4941	...	...	...	...	
1	−21	...	935.939	...	1068.45	42.596	0.4947	...	...	...	...	
1	−22	...	896.880	...	1114.98	42.303	0.4948	...	...	...	...	
1	−22	...	858.844	...	1164.36	41.634	0.4960	...	...	...	...	
1	−23	...	825.638	...	1211.18	31.817	0.4999	...	...	...	...	
1	−24	...	796.935	...	1254.81	40.304	0.4958	...	...	...	...	
1	−25	...	791.416	...	1263.56	41.982	0.4938	...	...	...	...	
1	−26	...	763.714	...	1309.39	42.443	0.4947	...	...	...	...	
1	−27	...	740.466	...	1350.50	42.782	0.4961	...	...	...	...	
1	−28	...	715.901	...	1396.84	42.996	0.4969	...	...	...	...	
1	−29	...	691.308	...	1446.53	43.242	0.4966	...	...	...	...	
1	−30	...	668.768	...	1495.29	43.888	0.1416	...	...	...	...	
2	−9	...	3130.035	...	319.49	43.487	0.1528	...	...	...	...	
2	−10	...	2926.265	...	341.73	43.372	0.1560	...	...	...	...	
2	−11	2703.844	2703.774	369.84	369.85	43.676	0.1394	−0.00	−0.01	+0.070	0.0217	f_{63}
2	−12	...	2531.307	...	395.05	43.222	0.1568	...	...	...	...	
2	−13	...	2392.309	...	418.01	43.396	0.1519	...	...	...	...	
2	−14	...	2244.926	...	445.45	43.233	0.1551	...	...	...	...	
2	−15	...	2131.030	...	469.26	43.123	0.1583	...	...	...	...	
2	−16	...	2021.144	...	494.77	43.141	0.1592	...	...	...	...	
2	−17	...	1920.565	...	520.68	42.928	0.1622	...	...	...	...	
2	−18	...	1817.143	...	550.31	42.991	0.1598	...	...	...	...	
2	−19	...	1726.007	...	579.37	42.881	0.1592	...	...	...	...	
2	−20	...	1652.026	...	605.32	42.704	0.1599	...	...	...	...	
2	−21	...	1584.472	...	631.12	42.523	0.1601	...	...	...	...	
2	−21	...	1522.267	...	656.92	42.071	0.1610	...	...	...	...	
2	−22	...	1461.290	...	684.33	41.312	0.1615	...	...	...	...	
2	−23	...	1410.877	...	708.78	31.817	0.1666	...	...	...	...	
2	−24	...	1380.332	...	724.46	41.100	0.1634	...	...	...	...	
2	−25	...	1356.311	...	737.29	42.154	0.1637	...	...	...	...	
2	−26	...	1302.715	...	767.63	42.649	0.1632	...	...	...	...	
2	−27	...	1256.036	...	796.16	42.961	0.1626	...	...	...	...	
2	−28	...	1213.635	...	823.97	43.155	0.1628	...	...	...	...	
2	−29	1177.769	1177.778	849.06	849.06	43.305	0.1634	+0.00	+0.01	−0.009	0.0226	f_{59}
2	−30	...	1140.689	...	876.66	43.478	0.1630	...	...	...	...	
2	−31	...	1106.903	...	903.42	43.536	0.1639	...	...	...	...	
2	−32	...	1076.410	...	929.01	43.610	0.1646	...	...	...	...	
2	−33	1043.764	1043.747	958.07	958.09	43.672	0.1648	−0.00	−0.02	+0.016	0.0348	f_{40}
2	−34	1012.387	1012.398	987.76	987.75	43.766	0.1645	+0.00	+0.01	−0.011	0.1846	f_2
2	−35	...	983.101	...	1017.19	43.868	0.1640	...	...	...	...	
2	−36	...	957.929	...	1043.92	43.865	0.1644	...	...	...	...	
2	−37	...	934.459	...	1070.14	43.911	0.1646	...	...	...	...	
2	−38	910.429	910.427	1098.38	1098.39	43.969	0.1644	−0.00	−0.00	+0.002	0.1513	f_4
2	−39	888.576	888.578	1125.40	1125.39	43.977	0.1648	+0.00	+0.00	−0.003	0.0416	f_{29}
2	−40	...	868.257	...	1151.73	43.963	0.1652	...	...	...	...	
2	−41	...	847.200	...	1180.36	43.974	0.1653	...	...	...	...	
2	−42	...	826.078	...	1210.54	44.031	0.1650	...	...	...	...	
2	−43	807.119	807.116	1238.98	1238.98	44.046	0.1649	−0.00	−0.00	+0.002	0.0375	f_{35}
2	−44	...	790.287	...	1265.36	44.020	0.1652	...	...	...	...	
2	−45	...	773.452	...	1292.90	44.033	0.1652	...	...	...	...	
2	−46	...	756.713	...	1321.50	44.072	0.1651	...	...	...	...	
2	−47	...	741.471	...	1348.67	44.049	0.1653	...	...	...	...	
2	−48	...	727.245	...	1375.05	44.014	0.1656	...	...	...	...	
2	−49	...	712.293	...	1403.92	44.018	0.1656	...	...	...	...	
2	−50	...	697.642	...	1433.40	44.034	0.1654	...	...	...	...	
2	−51	...	684.373	...	1461.19	44.012	0.1655	...	...	...	...	
2	−52	...	671.926	...	1488.26	0.000	0.0000	...	...	...	...	

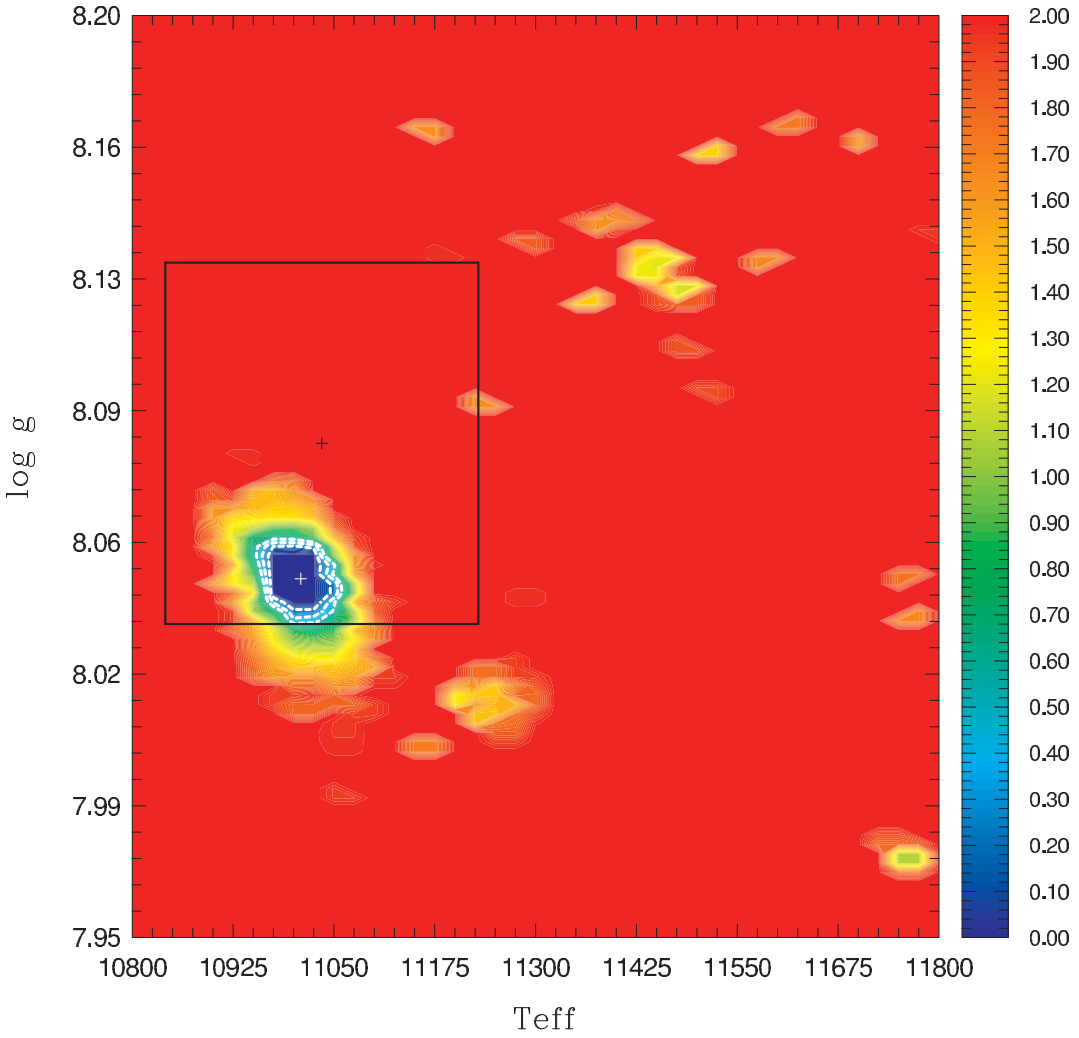

FIGURE 6.9 – Map of the projected merit function S^2 (on a log scale) along the $T_{\rm eff}$-log g plane. White contours show regions where the frequency fit have S^2 values within the 1σ, 2σ, and 3σ confidence levels relative to the best-fit solution. The spectroscopic solution given within 1σ is illustrated with a black box.

TABLE 6.3 – Defining parameters for the optimal seismic model found for GD 1212.

Quantity	Minimum	Maximum	Optimum Value
$T_{\rm eff}$ (K)	10,800	11,800	11,009
$\log g$	7.95	8.20	8.047
D(H)	-9.0	-4.0	-4.52
D(He)	-4.0	-1.5	-3.345
Profac(H)	1	3	1.441
Profac(He)	1	5	3.57
Core(O)	0.5	1.0	0.703
t1	-0.50	-0.15	-0.333
Δt1	0.01	0.10	0.063
t1(O)	0	0.8	0.608
t2	-2.0	-0.6	-1.328
Δt2	0.01	0.10	0.086
t2(O)	0	0.6	0.087

The main stellar parameters found are $T_{\rm eff} = 11{,}009$ K and $\log g = 8.047$, with a rather thick hydrogen envelope of $log(m(H)/M) = -4.34$, and a thin helium layer of $log(m(He)/M) = -3.25$. The rest of the parameters defining the white dwarf core and the stellar global parameters are presented in Table 6.3. As can be seen in Fig. 6.9, the map of the projection of the merit function on the 2-dimensional plane of $T_{\rm eff}$-$\log g$ (where at any given point on the map, the S^2 value corresponds to the minimum of all the values when the others parameters are varied independently), the well-defined seismic effective temperature and surface gravity are in perfect agreement with the corrected spectroscopic determination of $T_{\rm eff}$ and $\log g$ within 1σ, a reassuring condition on the validity of the calculated seismic solution. Fig. 6.10 presents the map of the projection of the merit function on the 2-dimensional plane of D(H)-D(He) (the natural input variable to our code for the definition of the hydrogen and helium layers, linked to the $log(m(HorHe)/M)$ by a simple linear relation). We can observe that one unique solution stands out, there is no degeneracy in the determination of either the hydrogen or the helium layer. The rather thick hydrogen and thin helium layer observed in our seismic solution are well within the canonical values of hydrogen and helium concentration defined by evolutionary calculation of white dwarfs. The determinations of the thickness of the hydrogen and helium layer are closely related to the values of the steepness of the chemical profiles

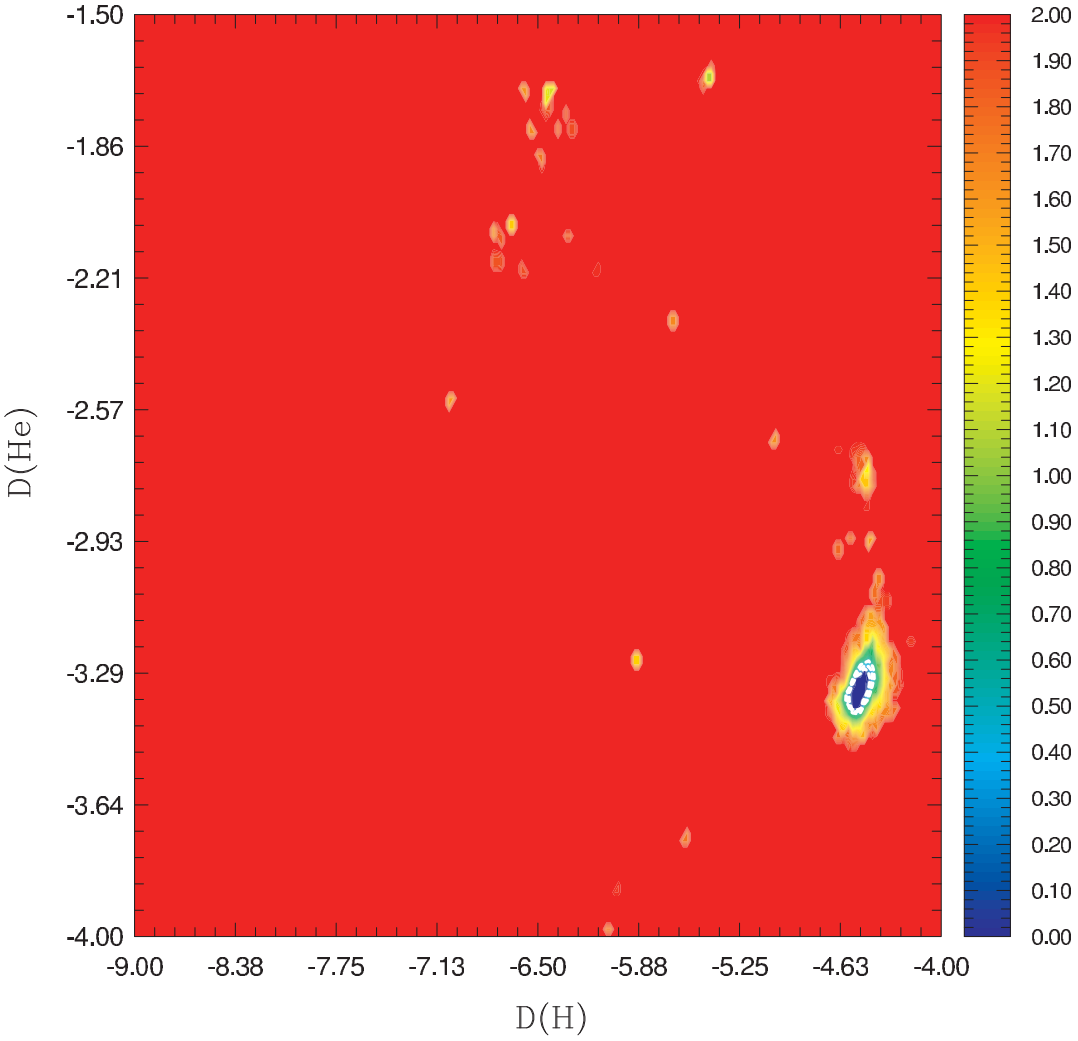

FIGURE 6.10 – Map of the projected merit function S^2 along the D(H)-D(He) plane.

at the two interfaces H/He and He/C-O. The latter values of profac(H) and profac(He) are uniquely and precisely determined as can be seen in Fig. 6.11.

Fig. 6.12 illustrates on the upper panel the internal chemical profiles of the differents elements present in the white dwarf, with a zoom-in-view of the core of the star, while the lower panel presents the distribution of the square of the Brunt-Väisälä and Lamb frequencies. At first glance, the central oxygen distribution seems to follow a linear descent, as if the second transition was removed. With a careful examination of the corresponding distribution of the square of the Brunt-Väisälä frequency, the second inflexion point is clearly present and influence sufficiently the Brunt-Väisälä frequency to form a plateau along the slope ended by

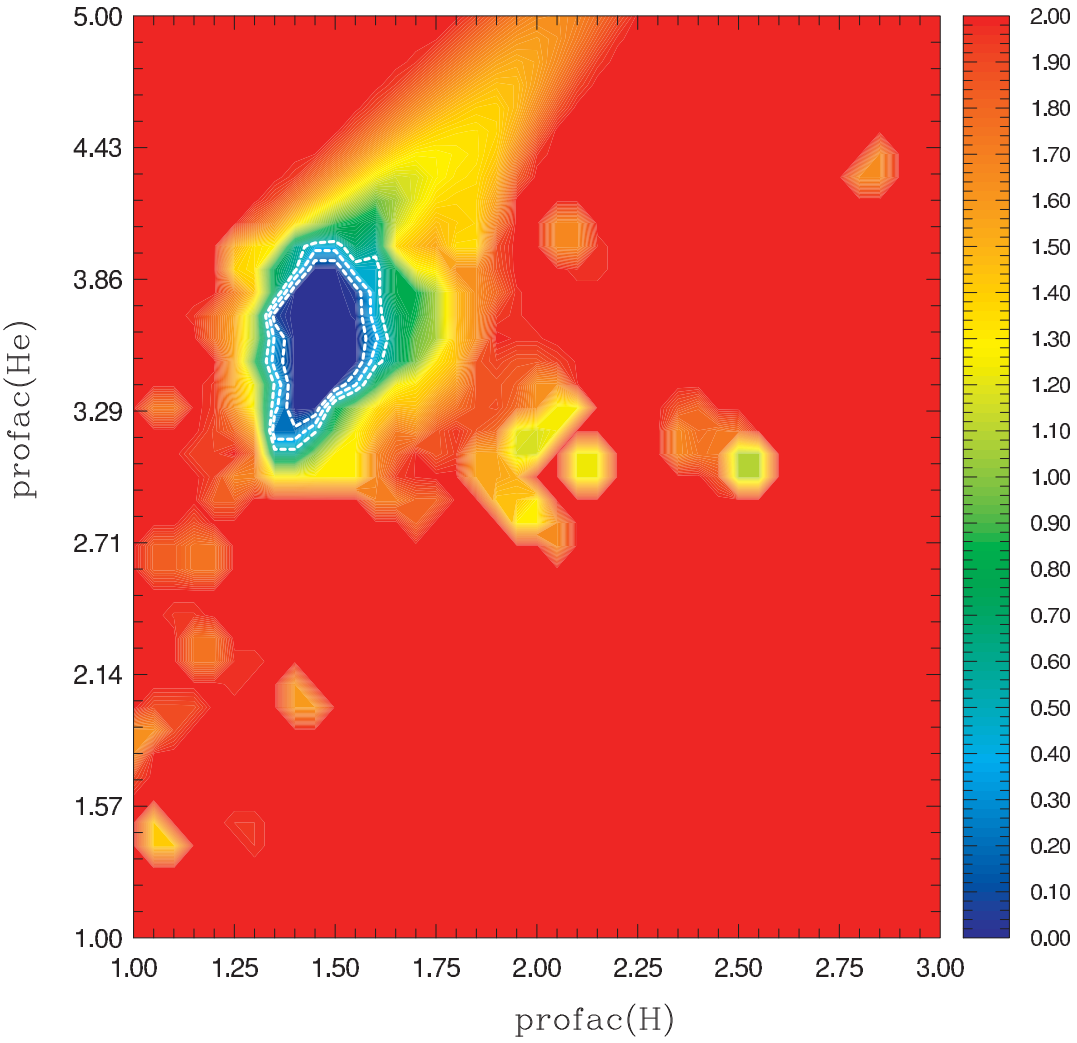

FIGURE 6.11 – Map of the projected merit function S^2 along the profac(H)-profac(He) plane.

a small bump. This unique signature is necessary to get the precision reached, as a similar analysis with only one transition was performed and the S^2 was noticeably degraded by more than four orders of magnitude. As expected, the two chemical interfaces are responsible for the two other bumps along the Brunt-Väisälä frequency. The well in the profile is due to the presence of the superficial convective zone engendered by the partial ionization of hydrogen in the model. All those structures are significant as they pinch the eigenfunctions and can ultimately trap or confine modes, leading to a unique non-uniform distribution of the periods.

The central oxygen concentration is found to be at 70.3%. In Fig. 6.13, we can notice that within 3 σ, the central homogeneous composition reaches the higher oxygen rate found to be with evolutionary calculations either by Salaris et al. (2010) or Romero et al. (2012) for white dwarfs of similar mass. The size of the central homogeneous core is exactly as predicted by Salaris et al. (2010) and slightly larger than what is anticipated by Romero et al. (2012). The oxygen profile is then slowly decreasing with what appears to be a linear slope, reaching the zero point at $\log q \sim -1.5$. If we compare our profile to what is predicted by Salaris et al. (2010), the first steep descent corresponds in the two curves until the two profiles crosses again at $\log q \sim -0.7$. Then they join at $\log q \sim -1.5$, where the oxygen die out. The profile is significantly different than the one obtained from Romero et al. (2012).

Fig. 6.14 shows the histograms obtained for the probability distribution of the various parameters used during this optimization. The technique used relies on the likelihood function calculated from the sampling of the merit function S^2 during the search for the best fit model. This method developed by Van Grootel et al. (2013) allows to make more quantitative statements on the value of each parameter by statistically estimating the value of each parameter and its associate error from the seismic fit. In a nutshell, the histograms tends to show narrow gaussian-alike peaks, the derived errors defined by the 1σ standard deviation are in consequences quite small. Errors presented in Table 6.3 are only internal errors to the fit, and should be interpreted as such. By examining more carefully Fig. 6.14, we can notice that a second solution seems to appear very close to the best-fit solution, almost as if the most probable solution was splitting up, with a density of probability as large as the best-fit solution. This splitting has repercussions on the determination of the derived errors, which

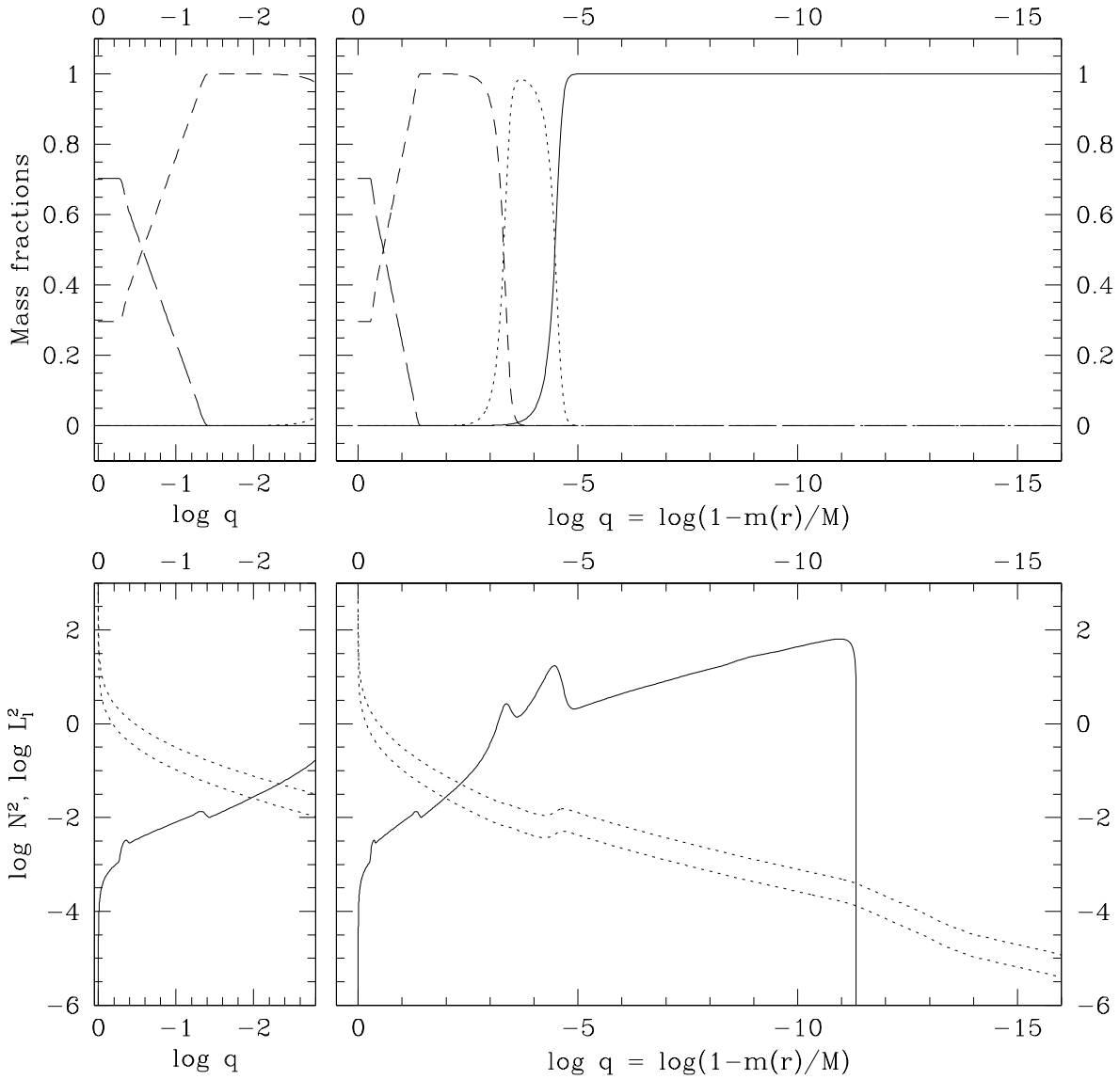

FIGURE 6.12 – Top panel: Chemical abundance profiles of the optimal model calculated, oxygen (long-dashed line), carbon (dashed line), and helium (dotted line). The abscissa shows the fractional mass depth (with $\log q = 0$ corresponding to the center of the star) The left part of both panels emphasizes a zoom-in-view of the deep interior of the star. Bottom panel: run of the square of the Brunt-Väisälä (solid line) and Lamb frequencies (dashed lines).

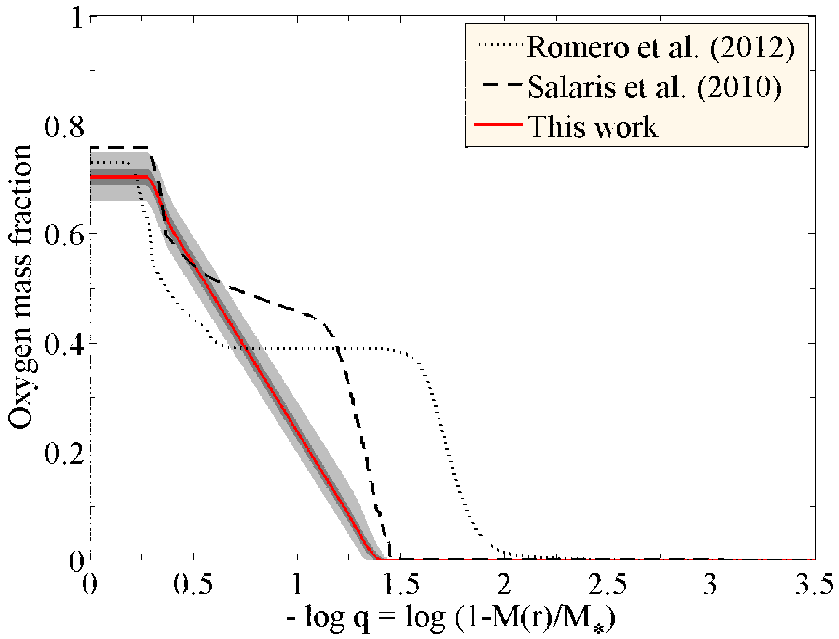

FIGURE 6.13 – Zoomed-in-view of the obtained core oxygen mass fraction (red), emphasizing the two-transitions parameterization, with the 1- and 3-σ contour (dark and light grey respectively). In contrast, available evolutionary profiles from Salaris et al. (2010) and Romero et al. (2012).

tends to slightly overestimate them.

6.4.3 Internal Rotation Profile

The method employed here rely on the analysis of the frequency spacing between modes of adjacent values of azimuthal order m. Two assumptions have to be made in order to proceed any further. The first one is to assume the slow rotation of the star, and by slow rotation we intend that the rotation period must be very large compared to the pulsation periods of the star. The second assumption implies that the star rotate as a solid body object. The test used here correspond to the third method to test the solid body rotation of Charpinet et al. (2009). A rotation law with a variable step is employed. The star is considered to be composed of two sections rotating as solid body, independantly from one another, an internal region encircled by an external region at an arbitrary depth. By varying this delimitation, it is possible to map the depth where the deviation from the solid body rotation becomes apparent, if there is such a deviation.

First, let us have a look at the distribution of the rotational kernels of the modes showing frequency splitting, that indicate the internal regions that contribute the most to the rotational splitting. Figure 6.15 shows the different shapes of the rotational kernels of the identified modes in GD 1212. We can immediately notice that evolution and the increase in degeneracy along the cooling sequence has mainly relegate the influence of the g-modes to the external zones of the star. But a few modes have rotational kernels going back all the way to the center of the star. And not only they are reaching the core, they are also presenting different shapes, a must for testing and mapping the rotation inside the star.

Figure 6.16 exposes the internal rotation profile determined by inversion using the test of the rotation law with a variable step based on the optimal model of GD 1212. The striking result is double: first, we observe a perfect straight vertical line implying that the test for solid body rotation has led to positive results, secondly we can probe for more than 80 % of the star, deep into the core of the pulsator, a first for a ZZ Ceti star. The value of the 1-,2- and 3-σ delimitations are very tightly surrounding the line of interest. The use of the only two modes f14 and f70 (the two rotationaly split multiplets of $l = 1$) are the cause to the limited error. By

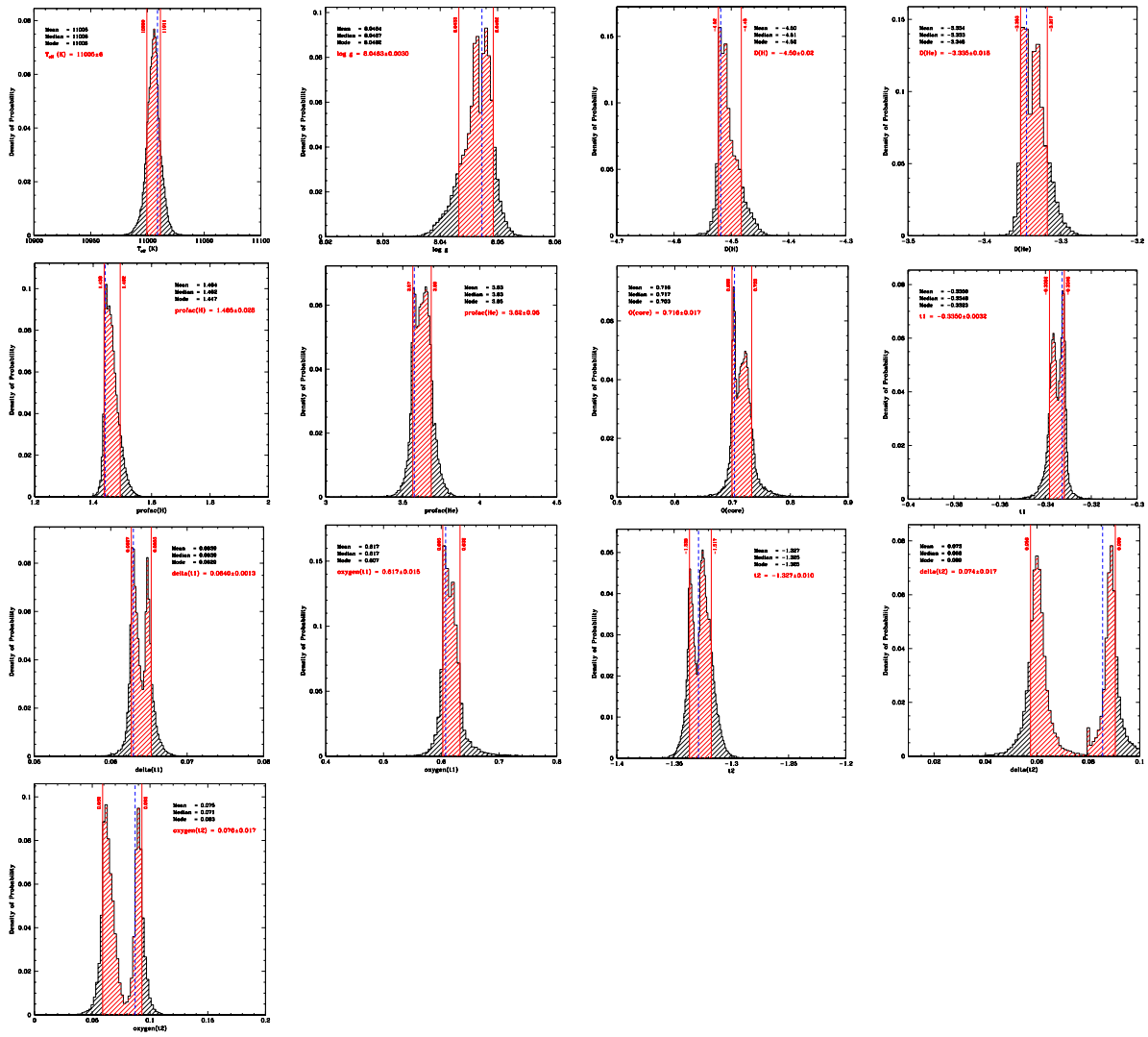

FIGURE 6.14 – Probability density function for every stellar parameter used in the asteroseismological fit. The red-hatched region between the two vertical solid red lines defines the 1σ range.

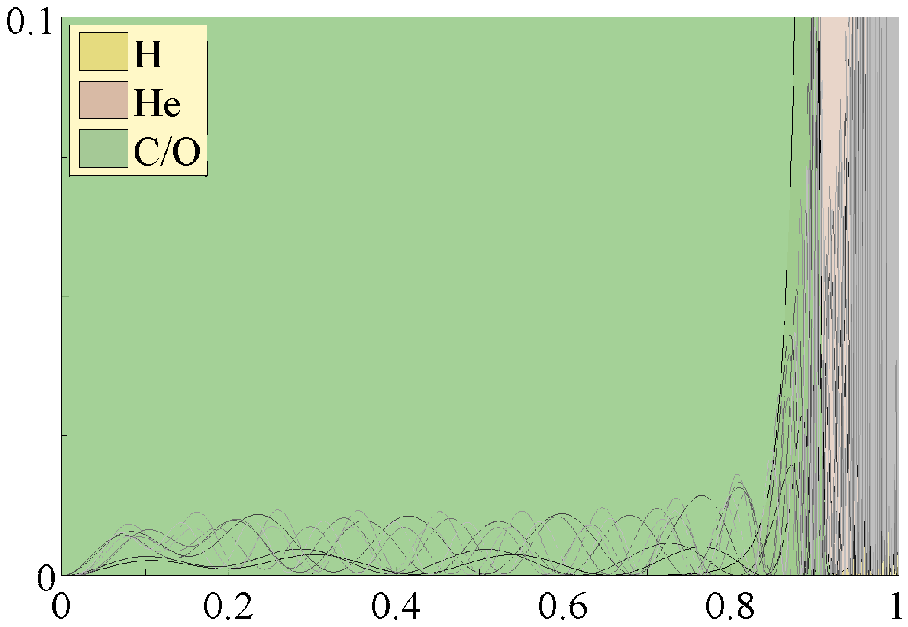

FIGURE 6.15 – Rotation kernels of the modes showing rotational splitting.

using the smallest subset of modes which rotational kernels probe deep into the interior of the star, we are able to constrain the uncertainties to their minimal value. Results using all the possible rotationaly split multiplets is in all point similar, straight vertical line over 80 % of the radius of the star, but with increased uncertainties. Since we have in hands the possibility of naturally narrowing these values, we will use them to present the more constraining results. The period of rotation of 6.98 h $\pm$ 0.02 is consistent with the assumption of slow rotation of the star and with the conclusion that this pulsator has lost most of its angular momentum prior to the white dwarf cooling sequence.

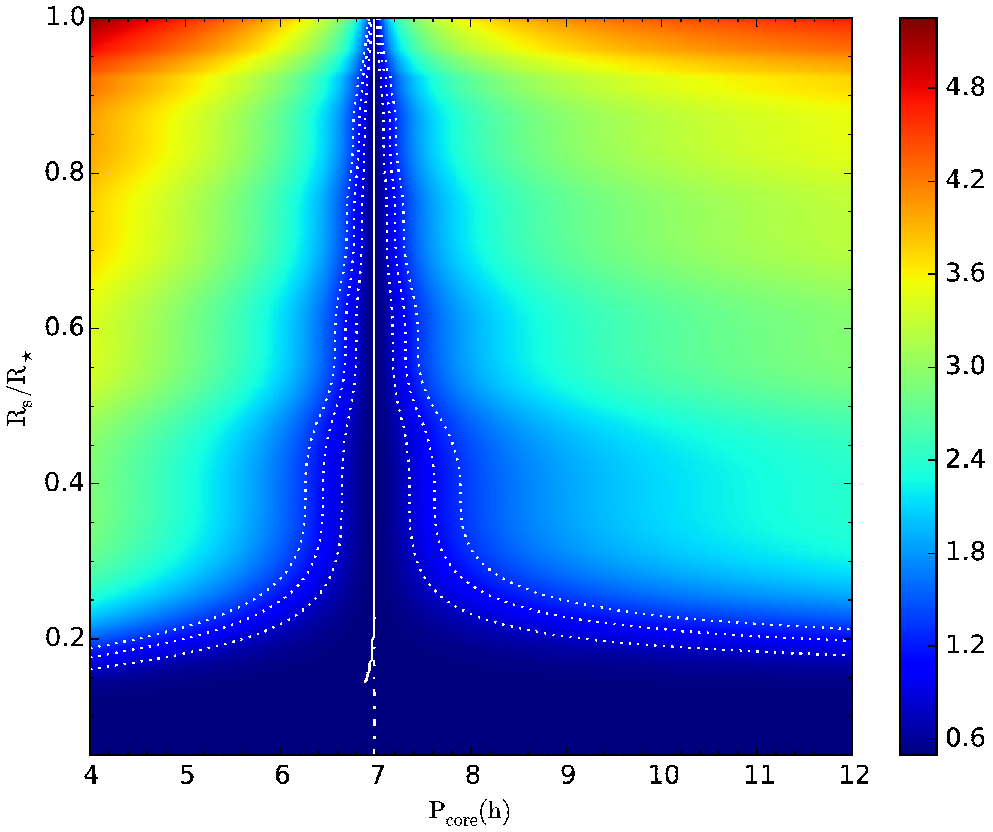

FIGURE 6.16 – Contour map showing the behaviour of the normalized merit function S^2 in terms of the radius and in terms of the rotation period of the inner region for solid body rotation in a two-zone approach defined by Charpinet et al. (2009). Horizontal dot-dashed curves give an indication on the encompassed mass. The solution is illustrated by the nearly vertical white curve and the dotted white curves depict the 1, 2 and 3σ contours. In comparison, the vertical dot-dashed white curve gives the exact solution for solid-body rotation. At larger depths, the gravity modes lose their ability to measure local rotation, giving the divergence in the 1, 2 and 3σ contours.

TABLE 6.4 – Inferred properties of GD 1212 on the basis of asteroseismology

Quantity	Estimated value
$\log g$ (cm s^{-2})	8.0463±0.0030
$T_{\rm eff}$ (K)	11005±6
$\log M(\mathrm{H})/M_*$	−4.360±0.013
$\log M(\mathrm{He})/M_*$	−3.270±0.018
$\log q$ [X(He)=X(H)=0.5]	−4.48
$\log q$ [X(C)=X(He)=0.5]	−3.31
$X(\mathrm{O})_{\rm center}$	0.716±0.017
$\log q$ [X(O)=X(C)=0.5]	−0.58
$M_*/M_\odot$	0.6260±0.0012
$R_*/R_\odot$	0.01237±0.00002
$L_*/L_\odot$	0.002014±0.000011
$P_{\rm rot}$ (h)	6.98±0.02
$V_{\rm eq}$ (km s^{-1})	2.15±0.01
J (kg m^2 s^{-1})[a]	3.98±0.02×10^{39}
$J/J_\odot$	1/48
M_V[b]	11.96±0.01
d (pc)	18.19±0.34

[a] Assuming solid body rotation throughout the star.

[b] Based on a model atmosphere with the seismic values of $\log g$, $T_{\rm eff}$, and M_*.

6.5 CONCLUSION

In this paper we presented the complete asteroseismological analysis of the pulsating ZZ Ceti GD 1212. The nearly ten days of photometric observations by Kepler-2 allowed the extraction of 25 independent modes and the identification of 11 multiplets over 4.9 σ, the calculated significative threshold. The main stellar parameters found for GD 1212 are summarized in Table 6.4. The effective temperature and surface gravity are in excellent agreement within 1σ of the corrected spectroscopic determination.

We also capitalized on the content from the observed frequencies of the 11 identified multiplets to probe deep into the heart of GD 1212. By taking advantage of the full potential that can be delivered by asteroseismology, we can unravel the inner structure of the star. The central oxygen and carbon content is, within the uncertainties, in agreement with available evolutionary calculations. The size of the central homogeneous core and the position where the oxygen dies out found through seismic means is consistent with the evolutionary profile derived by Salaris et al. (2010), while the almost linear descent contrasts with evolutionary calculations. Another striking result emerging from the observed and identified multiplets is the precise confirmation of solid-body rotation over 80% of the radius of the star, a first for a ZZ Ceti star.

This work was supported in part by the NSERC Canada through a doctoral fellowship awarded to Noemi Giammichele, and through a research grant awarded to Gilles Fontaine. The latter also acknowledges the contribution of the Canada Research Chair Program. This work made extensive use of the computing facilities offered by the Calcul en Midi-Pyrénées (CALMIP) project.

6.6 REFERENCES

Brassard, P., Pelletier, C., Fontaine, G., & Wesemael, F. 1992, ApJS, 80, 725

Brassard, P., & Charpinet, S. 2008, Ap&SS, 316, 107

Charpinet, S., Van Grootel, V., Reese, D., et al. 2008, A&A, 489, 377

Charpinet, S., Fontaine, G., & Brassard, P. 2009, Nature, 461, 501

Fontaine, G., & Brassard, P. 2008, PASP, 120, 1043

Giammichele, N., Bergeron, P., & Dufour, P. 2012, ApJS, 199, 29

Giammichele, N., et al., 2016 in preparation

Gianninas, A., Bergeron, P., & Fontaine, G. 2006, AJ, 132, 831

Hermes, J. J., Charpinet, S., Barclay, T., et al. 2014, ApJ, 789, 85

Howell, S. B., Sobeck, C., Haas, M., et al. 2014, PASP, 126, 398

Romero, A. D., Córsico, A. H., Althaus, L. G., et al. 2012, MNRAS, 420, 1462

Salaris, M., Cassisi, S., Pietrinferni, A., Kowalski, P. M., & Isern, J. 2010, ApJ, 716, 1241

Subasavage, J. P., Jao, W.-C., Henry, T. J., et al. 2009, AJ, 137, 4547

Tremblay, P.-E., Ludwig, H.-G., Steffen, M., & Freytag, B. 2013, A&A, 559, A104

Van Grootel, V., Charpinet, S., Brassard, P., Fontaine, G., & Green, E. M. 2013, A&A, 553, A97

Zong, W., Charpinet, S.,Vauclair, G., Giammichele, N., & Van Grootel, V. 2015, arXiv:1510.06884

Chapitre 7

Conclusions

7.1 L'analyse sismique de GD 165 et Ross 548, étoiles du bord chaud de la bande d'instabilité

La principale motivation de l'analyse sismique de GD 165 et Ross 548, le duo de naines blanches pulsantes spectroscopiquement jumelles, provient principalement de la qualité exceptionnelle des données photométriques obtenues au CFHT avec l'instrument LAPOUNE en 1995 et 1991, respectivement, qui n'avaient à ce jour pas été exploitées. L'approche en parallèle mise de l'avant pour l'étude de ces deux pulsateurs provient du problème non résolu que malgré le fait qu'elles soient jumelles spectroscopiques, elles ne possèdent pas les mêmes propriétés de pulsation. De plus ce sont des pulsateurs "simples" avec lesquels nous pouvons mettre à l'épreuve notre méthode d'analyse sismologique.

L'analyse astérosismique débute par l'extraction des fréquences de pulsations. Les résultats des séquences de "prewhitening" exposent 13 modes indépendants de pulsations, regroupés en 6 multiplets pour GD 165, ainsi que 11 modes indépendants de pulsations pour Ross 548, également regroupés en 6 multiplets. La qualité sans précédent des observations permet de rajouter aux analyses précédentes deux modes supplémentaires dans le cas de GD 165, et d'un mode supplémentaire pour Ross 548. L'explication la plus plausible pour la présence des multiplets dans les deux étoiles est la rotation qui détruit la symétrie sphérique de l'étoile et lève la dégénérescence qui existe pour les fréquences propres d'un mode. Par ailleurs, le

chapitre 2 fait également une révision des paramètres atmosphériques des deux étoiles en tenant compte des dernières corrections et calibrations.

Au chapitre 3, on présente les résultats des deux analyses sismiques avec l'identification de solutions en accord avec les paramètres atmosphériques déterminés indépendamment. La recherche d'un modèle optimal a été réalisée avec l'aide du code LUCY, sans restrictions aucunes sur l'identification des modes, exceptées sur la contrainte qu'un mode doit appartenir à la famille $l = 1$ ou $l = 2$, ceux-ci ayant été les seuls formellement identifiés dans les étoiles ZZ Ceti. Les structures utilisées sont des modèles statiques, entièrement paramétrisés de naines blanches de type DA. Pour l'étude de cas présentée dans ce chapitre, la simplicité du modèle est de mise, en n'utilisant que cinq paramètres: la composition supposée homogène du cœur C-O, la gravité de surface, la température effective, la masse du manteau d'hélium, ainsi que la masse de la couche superficielle d'hydrogène.

Les modèles optimaux trouvés, reproduisent simultanément les six périodes de pulsations à $\sim$0.3% en moyenne, ce qui est comparable aux meilleurs résultats obtenus à date dans le domaine de l'astérosismologie. On dévoile la présence d'une sensibilité de la solution sur la composition du noyau de Ross 548, alors qu'il n'y en pratiquement pas pour GD 165. Ceci ajouté au fait que la couche d'hydrogène de Ross 548 est relativement mince comparée à celle de GD 165, permet de donner une explication naturelle à la différence entre le spectre de pulsation de Ross 548 et GD 165. Il avait déjà été démontré qu'une enveloppe plus fine, à modèle égal, génère des périodes plus longues et permet un piégeage/confinement plus efficace des modes. On a explicitement vérifié que trois des fonctions poids des modes confinés du modèle optimal de Ross 548 creusent profondément dans le cœur, expliquant naturellement la sensibilité du spectre de pulsation sur la composition du cœur. Sa jumelle spectroscopique, GD 165, avec son enveloppe épaisse qui ne permet pas un piégeage/confinement efficace des modes, ne présente pas au contraire de modes dont les fonctions poids sondent profondément dans le coœur. La découverte que les modes confinés doivent être détectés afin de sonder la composition du cœur a des implications sur de futurs travaux.

La fiabilité des paramètres primaires et secondaires obtenus pour Ross 548 et GD 165 a été démontrée par tous les moyens possibles. Les modèles sismiques ont été reproduits à l'aide

de calculs évolutifs, la compatibilité des modèles sismiques et de l'identification des modes a été testée avec les résultats de la théorie linéaire des pulsations et en particulier avec la théorie non-adiabatique, et la forme de la fonction mérite a été minutieusement inspectée avec notre approche statistique. Par ailleurs, les paramètres primaires et secondaires ont été comparés et trouvés compatibles avec toutes les contraintes externes disponibles dans la littérature. En particulier, les paramètres atmosphériques des deux étoiles, obtenus par la méthode spectroscopique, sont en parfait accord avec les résultats sismiques, et le taux de changement de période pour le mode de pulsation dominant de Ross 548 prédit par notre modèle est en excellent accord avec la valeur mesurée.

Les derniers tests réalisés exploitent la structure présentant du splitting rotationnel de GD 165 et Ross 548. On démontre que les deux étoiles tournent extrêmement lentement, et que la rotation est probablement solide.

7.2 Validation de la méthode et d'une nouvelle paramétrisation

Après les résultats obtenus lors du chapitre 2 et de l'exercice sismique des étoiles GD 165 et Ross 548 au chapitre 3, et en particulier de la dépendance de certains modes de pulsations à la composition centrale du noyau de la naine blanche, la prochaine étape était de se pencher sur une nouvelle paramétrisation des profils de carbone et d'oxygène présents dans le cœur. Dans le but d'améliorer la qualité de la comparaison entre les données observationnelles et les modèles paramétrisés, surtout en ces temps d'observations spatiales avec les missions MOST, CoRoT et surtout ce qui nous intéresse dans le cadre de cette thèse, les missions *Kepler* et *Kepler*-2. L'augmentation sans précédent de la précision des données *Kepler* nous force la main pour essayer de mieux reproduire à l'aide de nos modèles statiques l'état actuel de la naine blanche observée.

La nouvelle paramétrisation prend ses racines dans les domaines tels que l'aérodynamique, où on optimise une forme globale caractérisée par une fonction mérite. La paramétrisation se doit d'être assez flexible pour reproduire au mieux la géométrie attendue, tout en ayant un

minimum de paramètres afin de minimiser le temps de calcul qui peut être très coûteux, et également d'obtenir une géométrie lisse, facteur très important pour l'exercice astérosismologique. La représentation à l'aide de splines a été choisie, et en particulier la spline Akima, qui à l'avantage d'être beaucoup plus stable aux alentours des points hors norme, en évitant les oscillations présentes lors de l'utilisation, par exemple, de splines cubiques. Dans notre cas, la nouvelle définition d'un profil d'oxygène (et conséquemment du profil de carbone) se fait au moyen des points de contrôle régissant la spline Akima. Afin de reproduire le plus spécifiquement possible les profils obtenus par moyens de calculs évolutifs, il est nécessaire d'utiliser 7 points de contrôle, ou paramètres de forme, stratégiquement placés afin de définir la paramétrisation à deux transitions. Il est également possible d'obtenir une paramétrisation intermédiaire à l'aide de seulement 3 paramètres de forme, la paramétrisation à une transition.

Maintenant que nous disposons de nouveaux outils afin de mieux modéliser le profil d'oxygène dans le noyau des naines blanches, il est possible de tester la capacité et la précision de notre méthode dans un contexte astérosismologique. Le premier test présenté au chapitre 3, montre la précision que l'on peut obtenir si les incertitudes proviennent uniquement des données observationnelles, en faisant l'hypothèse que les modèles sont parfaits. Que ce soit avec un cœur homogène variable, la nouvelle paramétrisation avec une ou deux transitions, on retrouve les paramètres globaux de l'étoile de référence avec une précision dépendante de la perturbation appliquée sur le sous-ensemble de périodes qui sert de données "d'observation". On a utilisé trois ordres de grandeur pour la perturbation appliquée au sous-ensemble de périodes dans chaque cas de paramétrisation du cœur: la précision des fits actuels, $\sigma = 10$ μHz, la précision des données du sol, $\sigma = 0.1$ μHz, et la précision des données spatiales, $\sigma = 0.001$ μHz. L'augmentation de la précision des paramètres stellaires retrouvés à partir des données "d'observation" se répercute et passe d'un facteur 100 à chaque transition entre la précision des fits actuels, des données du sol ainsi que des données de l'espace. Par ailleurs, afin de bien déterminer les paramètres de forme définissant le noyau de l'étoile, il faut augmenter la précision des fits actuels d'au moins 2 ordres de grandeur. Ces tests démontrent que si le facteur limitant est purement observationnel, les paramètres stellaires et de forme sont récupérés avec une précision remarquable. Malgré le fait que notre méthode sismique donne des contraintes

robustes et précises sur les paramètres stellaires ou de forme, le facteur limitant provient bien de la modélisation et de la physique constitutive qu'il faut parfaire afin d'améliorer la précision des fits actuels.

La deuxième série de tests présentée au chapitre 3 permet d'estimer la limite de validité au dessus de laquelle un fit n'a plus de signification statistique. On a effectué 5 tests à partir de spectres de pulsation aléatoirement choisis, et complété dans chaque cas une analyse sismique standard en utilisant les trois différentes paramétrisations. Idéalement, il aurait fallu effectuer bien plus de tests pour que le résultat soit statistiquement significatif, mais le calcul étant coûteux et le temps de calcul limité, il a fallu se contenter de 5 tests. C'est toutefois suffisant pour donner une idée de l'ordre de grandeur attendu. Les valeurs minimales obtenues de S^2 pour un fit à 10 périodes aléatoires sont de l'ordre de la dizaine, et donne une dispersion moyenne en périodes de l'ordre de la seconde. Il est donc difficile d'accorder une grande crédibilité à des résultats obtenus au dessus de cette limite de validité.

Le troisième et dernier test du chapitre 3 permet d'évaluer la capacité des 3 paramétrisations du cœur à reproduire des profils issus de séquences évolutives à l'aide d'un exercice astérosismologique. Le sous-ensemble de 10 périodes à analyser provient d'une étoile référence construite avec un cœur à la Salaris, simulant une étoile "réelle". Les résultats obtenus à la suite d'exercices sismiques complets tendent bien à montrer que la modélisation avec cœur homogène peut être déficiente quand les modes excités sont ceux qui sondent profondément dans le cœur. Il y a une nette amélioration lorsque l'on utilise la paramétrisation à une ou deux transitions en ce qui a trait à l'identification des modes. En ce qui a trait à la capacité de l'algorithme de retrouver avec précision les paramètres globaux de l'étoiles, la paramétrisation à deux transitions est nécessaire.

7.3 L'analyse sismique de KIC 08626021, DBV du champ *Kepler*

Maintenant armé d'une nouvelle paramétrisation qui permet de retracer le profil du noyau d'une naine blanche pulsante et d'augmenter la précision des fits obtenus, il faut trouver une étoile qui posséderait les caractéristiques requises pour une analyse sismique en profondeur, avec des données d'observation d'une précision remarquable. Le choix s'est arrêté sur KIC

08626021, la seule DBV du champ du satellite *Kepler*, observée pendant presque 2 ans. Plusieurs analyses sismiques se sont succédées, mais aucun consensus n'a été trouvé ne serait-ce que sur les paramètres globaux de l'étoile, que ce soit la température effective ou la masse. Qui plus est, la température effective et gravité de surface initialement spectroscopiquement déterminées par Østensen et al. (2011) ne semblent pas correspondre ni aux analyses sismiques présentées ni à la relation luminosité-période empirique de la bande d'instabilité des DBs. La ré-analyse en détails des presque 2 ans de données photométriques de *Kepler* et en particulier de la nouvelle identification des modes par Zong et al. (2016), permet l'addition d'un nouveau mode de pulsation indépendant à rajouter aux 7 précédemment identifiés par Bischoff-Kim et al. (2014). Nous voici donc en possession de 8 modes de pulsations indépendants identifiés, ainsi que 2 triplets et 1 doublet pour tester l'hypothèse de rotation solide au travers de l'étoile.

En premier lieu, il convient de clore le débat sur la détermination spectroscopique des paramètres atmosphériques de cette étoile. Le spectre de KIC 08626021, étoile dont la luminosité est assez faible ($K_p = 18.46$) a été mis à notre disposition par Elisabeth Green. L'analyse du spectre avec les dernières versions de modèles par Pierre Bergeron donne bien une température effective beaucoup plus chaude que celle déterminée par Østensen et al. (2011), en accord avec la totalité des analyses sismiques de cet étoile, mais surtout rétabli sa position sur le bord chaud de la bande d'instabilité en accord avec la relation luminosité-période empirique des DBs, vu les courtes périodes que l'étoile nous présente. De plus l'analyse spectroscopique détaillée révèle la présence de trace d'hydrogène, faisant formellement de KIC 08626021 une DBA, la plus chaude de sa catégorie.

La structure d'une étoile DB est déterminée par un canal évolutif différent comparé à des étoiles DA, telles que GD165 et Ross 548, présentée au chapitre 2 et 3. Dans le scénario le plus probable, l'étoile se débarrasse de sa fine couche superficielle d'hydrogène après un épisode "born again". Si l'on se base sur des calculs évolutifs détaillés de DB incluant la diffusion dépendante du temps, on peut définir deux transitions de compositions différentes dans l'enveloppe de la DB. Entourant le noyau de carbone-oxygène, il existe une couche comportant de l'oxygène, du carbone ainsi que de l'hélium, alors que la couche superficielle ne contient que de l'hélium, déterminée par le coulage des éléments plus lourds. Cette structure

particulière a été prise en compte dans la réalisation des modèles statiques avec un cœur paramétrisé, ce qui monte le nombre de paramètres à 14.

La solution obtenue pour le modèle sismique de KIC 08626021 atteint un impressionnant S^2 de 4.9 $.10^{-10}$. Les paramètres globaux de l'étoile sont: $T_{\rm eff} = 30{,}219.5$ K and $\log g = 7.913$, en bon accord à deux sigma près de la température effective et un sigma près de la gravité de surface spectroscopique. La dispersion moyenne en période, $\overline{\Delta P} = 0.00000690$ s, dépasse pour la première fois la précision des mesures. On est en position de se poser la question de savoir si le nombre de paramètres de 14 est trop grand pour le problème sismique défini par les 8 périodes observées de KIC 08626021. Deux tests ont été réalisés afin de valider la qualité de la solution obtenue et de se défaire des idées préconçues. Le premier test permet de démontrer que 14 paramètres ne donnent pas nécessairement un fit parfait pour 8 périodes, à l'aide d'un spectre de périodes complètement aléatoire. Le deuxième test réalisé, insérer une fausse période dans le spectre des périodes observées, montre qu'une période faussement identifiée est aussi dangereux et compromet le résultat autant que d'avoir toutes les périodes aléatoirement choisies. On peut également se demander si le gain apporté par le fait d'avoir 14 paramètres peut se comparer à un résultat obtenu avec moins de paramètres. Donc à savoir si le nombre de paramètres est nécessaire dans notre cas, pour la précision atteinte. Le résultat de ce dernier test montre qu'il est nécessaire d'avoir un cœur paramétrisé à deux transitions afin d'égaler et même dépasser la précision des observations, ce qu'un cœur homogène variable et à une transition ne sont capable d'égaler.

Le dernier résultat présenté au chapitre 4 se sert du splitting rotationnel observés dans les trois structures du spectre de pulsation de KIC 08626021, les deux triplets et le doublet, pour analyser la rotation à l'intérieur de la DBV. En utilisant la technique présentée au chapitre 3, et en utilisant le modèle optimal de KIC 08626021, on découvre que la rotation est solide sur plus de 70 % du rayon de l'étoile, avec une période de rotation de 46.8 h.

7.4 GD 1212: l'analyse sismique d'une étoile du bord froid de la bande d'instabilité

L'analyse préliminaire de GD 1212 de Hermes et al. (2014), en dévoilant quelques 19 modes de pulsations indépendants, présente tout un défi. Cette ZZ Ceti froide a été observée durant une période de test d'environ 11.5 jours par le satellite *Kepler* dans la deuxième mission, K2, après l'arrêt de deux des gyroscopes du télescope spatial. Contrairement aux étoiles ZZ Ceti situées proche du bord chaud de la bande d'instabilité telles que celles présentées et analysées aux chapitre 2 et 3, les étoiles plus froides présentent un spectre de pulsation qui est beaucoup plus compliqué, variant dramatiquement dans le temps, avec de nombreuses harmoniques et des combinaisons linéaires. La tâche de trouver la bonne identification des modes devient extrêmement difficile, et comme on l'a vu au chapitre 5, une seule mauvaise fréquence peut ruiner toute l'analyse.

Il convient en premier lieu de refaire l'extraction de fréquences car la méthode employée par Hermes et al. (2014) d'utiliser des profils lorentziens, surestime grandement les incertitudes associées et certains pics n'ont pas été pris en compte. La difficulté rencontrée dans le cas de GD 1212, est la nature instable des amplitudes et des fréquences, ce qui rend impossible tout prewhitening standard. à la place, on utilise une combinaison linéaire de sinusoïdes. Des 48 fréquences extraites, en excluant les combinaisons linéaires, 25 se retrouvent au dessus la limite de 4.9σ. Cette limite a été calculée en faisant la probabilité de fausse alerte en fonction du S/N, qui donne la probabilité d'avoir un pic au dessus d'un certain niveau de bruit. L'utilisation de l'algorithme LUCY avec l'inclusion de la rotation stellaire ainsi que d'un test statistique de Kolmogorov-Smirnov a permis de déduire l'identification de 11 fréquences indépendantes, qui serviront à l'analyse sismique, basés sur des modèles stellaires sphériques.

La solution obtenue pour le modèle sismique de GD 1212 atteint un $S^2 = 5.10^{-4}$, surpassant la précision des mesures estimée dans notre cas à un $S^2 = 10^{-1}$. Les paramètres atmosphériques de l'étoile $T_{\rm eff} = 11{,}009$ K and $\log g = 8.047$ sont en très bon accord avec ceux déterminés par la méthode spectroscopique, corrigés pour les effets du problème du $\log g$ élevé de $T_{\rm eff} = 11,035 \pm 194$K and $\log g = 8.084 \pm 0.049$. La dispersion moyenne des périodes

$\overline{\Delta P} = 0.01$s est bien en dessous de la limite de crédibilité établie lors du chapitre 3. La définition du profil d'oxygène du noyau obtenue à la suite de l'exercice sismique est comparée à celles obtenues lors de calculs évolutifs par d'autres auteurs. On a remarqué que la quantité centrale d'oxygène rejoint celle calculée par des calculs évolutifs à 3σ près. Le rayon de la partie centrale homogène est également comparable à celui trouvé lors de calculs évolutifs. La descente d'oxygène est toutefois différente et ne présente pas les deux transitions attendues, bien que le point où l'oxygène disparaît soit comparable à celui trouvé par Salaris et al. (2010).

Le dernier résultat vient en bonus avec l'analyse sismique de toute étoile pulsante présentant du splitting rotationnel, comme c'est le cas de GD 1212. Nous avons en notre possession 9 multiplets qui ont été identifiés sur les 25 modes indépendants extraits de la transformée de Fourier. La présence de modes présentant du splitting rotationnel ayant des kernels de rotation creusant profondément dans le cœur de l'étoile permet pour la première fois de sonder et infirmer la rotation solide sur plus de 80 % du rayon d'une ZZ Ceti, avec la détermination de la période de rotation "lente" de 6.98 h $\pm$ 0.02 pour GD 1212.

En conclusion finale, nous avons développé et établi la crédibilité d'une méthode permettant de reproduire les périodes observées dans les naines blanches, à la précision. Cette méthode permet d'extraire le maximum possible d'informations de nature sismique de ces étoiles. Il s'agira maintenant de l'appliquer de façon systématique aux nombreuses étoiles pour lesquelles des données photométriques fiables sont disponibles. Quelles seront la stratification et la dynamique interne de ces étoiles et existent-ils des comportements semblables?

Bibliographie

Bischoff-Kim, A., Montgomery, M. H., & Winget, D. E. 2008, ApJ, 675, 1505

Bischoff-Kim, A., Østensen, R. H., Hermes, J. J., & Provencal, J. L. 2014, ApJ, 794, 39

Bradley, P. A. 1998, ApJs, 116, 307

Brassard, P., Pelletier, C., Fontaine, G., & Wesemael, F. 1992, ApJs, 80, 725

Castanheira, B. G., & Kepler, S. O. 2008, mnras, 385, 430

Castanheira, B. G., & Kepler, S. O. 2009, mnras, 396, 1709

Charpinet, S., Van Grootel, V., Reese, D., et al. 2008, A&A, 489, 377

Charpinet, S., Brassard, P., Fontaine, G., et al. 2009, American Institute of Physics Conference Series, 1170, 585

Charpinet, S., Fontaine, G., & Brassard, P. 2009, Nature, 461, 501

Fontaine, G., & Brassard, P. 2008, PASP, 120, 1043

Fontaine, G., & Brassard, P. 2008, Communications in Asteroseismology, 157, 177

Fontaine, G., Brassard, P., Charpinet, S., Quirion, P.-O., Randall, S.K., Van Grootel, V., & Giammichele, N. (en préparation), chapitre de livre "The White Dwarf Stars".

Hermes, J. J., Charpinet, S., Barclay, T., et al. 2014, ApJ, 789, 85

Christensen-Dalsgaard, J., 2007. `http://astro.phys.au.dk/~jcd/HELAS/puls_HR/`

Lynden-Bell, D., & Ostriker, J. P. 1967, MNRAS, 136, 293

Montgomery, M. H., & O'donoghue, D. 1999, Delta Scuti Star Newsletter, 13, 28

Mukadam, A. S., Bischoff-Kim, A., Fraser, O., et al. 2013, ApJ, 771, 17

Østensen, R. H., Bloemen, S., Vučković, M., et al. 2011, ApJ, 736, LL39

Romero, A. D., Córsico, A. H., Althaus, L. G., et al. 2012, MNRAS, 420, 1462

Salaris, M., Cassisi, S., Pietrinferni, A., Kowalski, P. M., & Isern, J. 2010, ApJ, 716, 1241

Schmidt, G. D., & Grauer, A. D. 1997, ApJ, 488, 827

Van Grootel, V., Charpinet, S., Brassard, P., Fontaine, G., & Green, E. M. 2013, A&A, 553, AA97

Yeates, C. M., Clemens, J. C., Thompson, S. E., & Mullally, F. 2005, ApJ, 635, 1239

Zong, W., Charpinet, S., Vauclair, G., Giammichele, N., & Van Grootel, V. 2016, A&A, 585, A22

Annexe A

40^{th} Liège International Astrophysical Colloquium. Ageing Low Mass Stars: From Red Giants to White Dwarfs

EPJ Web of Conferences **43**, 05007 (2013)
DOI: 10.1051/epjconf/20134305007

Quantitative asteroseismology: Determination of the core composition and layering of the ZZ Ceti star R548. Part I

N. Giammichele[a], G. Fontaine and P. Brassard

Département de Physique, Université de Montréal, CP. 6128, Succursale Centre-Ville, Montréal, QC H3C 3J7, Canada

Abstract. We present a detailed asteroseismological study of the pulsating white dwarf R548 based on fits to newly detected periods and the use of the forward method. In this first part, we concentrate on the frequency extraction analysis. Based on an unexploited CFHT/LAPOUNE broadband photometric campaign of high S/N, we are able to obtain a finer frequency spectrum and uncover two triplets, two doublets, and two singlets. The low-amplitude and "simple" pulsator R548 is an ideal candidate for carrying on a complete asteroseismological analysis within the framework of the adiabatic approximation to obtain optimized structural parameters, including the envelope layering and the bulk composition of the core.

1. INTRODUCTION

Asteroseismology is a unique tool that allows to probe the internal structure and the evolutionary state of a pulsating star. By comparing the pulsation properties with those predicted by refined theoretical models of stars, it is possible to independently unveil unique features of the stars such as the onion-like chemical structure in pulsating white dwarfs, for example. This method has been applied and slowly perfected over the past two decades on the study of many compact pulsators, and in particular very successfully realised upon the class of hot pulsating B subdwarf stars (see, e.g., the review of [1] for more details).

Despite valiant attempts (see [2] for a historical account), reliable and convincing seismic models of pulsating white dwarfs, particularly those with an hydrogen dominated atmosphere, the ZZ Ceti stars, have remained far and few. Unfortunately enough, cool ZZ Ceti stars tend to show rather complicated pulsation spectra composed of numerous harmonics, frequency sum and difference peaks due to strongly nonlinear pulse features. Their mode identification can even be further complicated by dramatic variations of the pulsation spectra with time. Without the exact pulsation spectrum, it is impossible to pinpoint the corresponding internal structure as the resulting theoretical spectrum is very sensitive to any changes in the parameters of the model. On the other hand, ZZ Ceti variables closer to the blue edge tend to present too few pulsation frequencies, limiting greatly any possible analysis due to the degeneracy of the possible solutions in parameter space. This is the main reason for focusing our efforts on pulsators closer to the blue edge of the instability strip, with the condition of having a reasonable minimal number of pulsation modes.

R548, the prototype star of the ZZ Ceti class, is one of the low-amplitude pulsator found in the hotter region of the instability strip, showing a quite stable and rather uncomplicated light curve with several independent modes. While it is also one of the most well observed ZZ Ceti star, the few asteroseismological studies realised so far gave mitigated results. Best fits using evolutionnary models

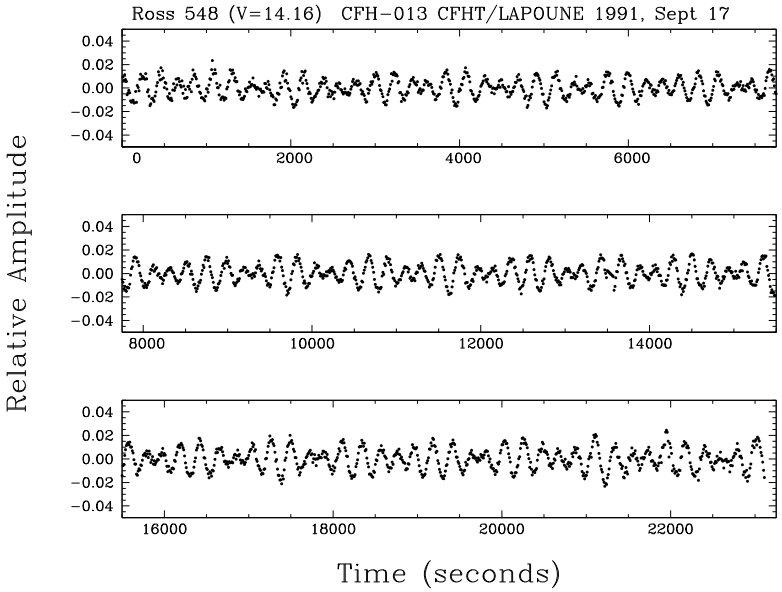

Figure 1. Representative broadband optical light curve obtained in one night for R548. Other nights are similar in length and quality. Each plotted point represents a time sampling of 10 s. The amplitude is expressed in term of residual intensity relative to the mean brightness of the star.

found by [3] and [4], do not seem to precisely narrow down the thickness of the hydrogen layer and give non-negligeable discrepancies between the observed and theoretical period spectrum, of the order of a few seconds per mode.

We have developed at Universit de Montr al an approach for quantitative seismic analyses of compact pulsators based on large scale computations relying on a cluster of dedicated computers and the use of parametrized static models. The latter allow us the needed flexibility to explore in great details parameter space, a task that cannot be performed with evolutionary models. We apply this approach to R548 in the present work, a star for which a very high quality photometric data set has been obtained at the CFHT in the past, but has remained largely unexploited. In this report, we present the results of a frequency extraction analysis that we carried out on this data set. The subsequent search for a suitable seismic model in parameter space will be presented elsewhere in the second and final part of our work ([5]).

2. LIGHT CURVE PROCESSING

The photometric data processed in this study was taken from the campaign carried out in September 1991, using the CFHT run with the LAPOUNE instrument, a 3-channel portable photometer. The broadband "white light" photometric data extracted was sampled for a total of 19 h over four nights. Figure 1 shows a typical light curve obtained for one of the observing night. Each plotted point represents a sampling time of 10 s, whereas the amplitude is expressed relatively to the mean brightness of the star. As can be seen, the light curve expectedly shows a rather low-amplitude variation.

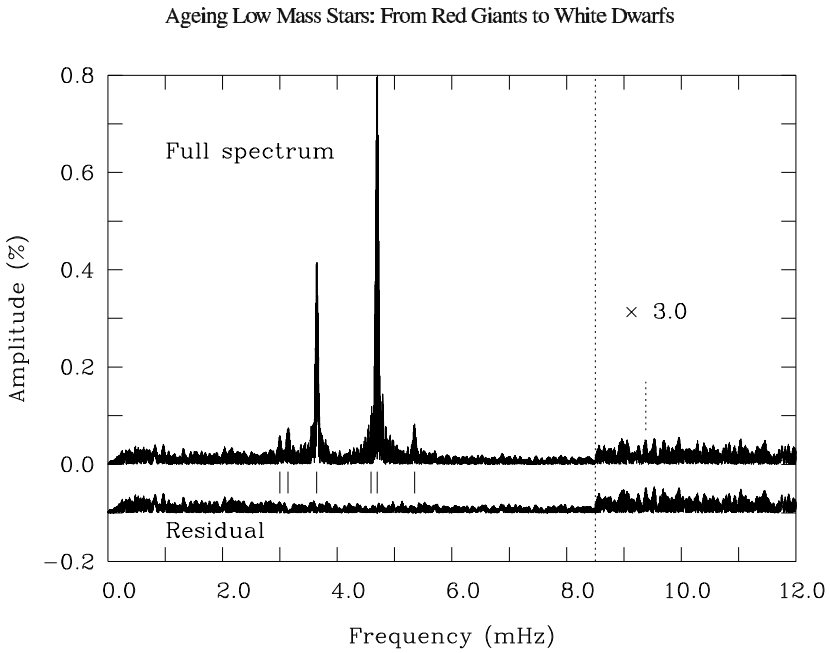

Figure 2. Fourier amplitude spectrum of the R548 light curve. A total of 12 independent periodicities were uncovered out of 6 main peaks, which include 2 triplets, 2 doublets, and 2 singlets. The only nonlinear frequency peak observed — the first harmonic of the dominant peak — is identified and magnified on the right.

The frequency resolution obtained during this run was 2.76 μHz and the duty cycle of 18.8%. Despite the low value of the duty cycle, the signal-to-noise ratio of the obtained spectrum is quite remarkable, one of the best ever obtained on a ZZ Ceti star.

Standard Fourier transform techniques followed by least-square fits and prewhitening sequences were performed on the light curve. The resulting Fourier spectrum and its residual after extracting all apparently significant signals are illustrated in Fig. 2. Out of the six main frequency peaks, we uncovered a total of 12 modes, including two triplets, two doublets, and two singlets. We can notice though that the Fourier spectrum is mainly dominated by the 2 triplets complexes at 213 s and 274 s. The only nonlinear feature of the light curve of R548, the first harmonic of the dominant mode of the main complex at 213 s is magnified on the right part of Fig. 2. The residual intensity from the prewhitened curve is shown at the bottom of figure. It is the first check that every feature above the noise level was correctly identified in our analysis.

Table 1 summarizes the details of the extracted periodicities : the periods P, amplitudes A, frequencies ν, and the frequency spacing inside a complex $\Delta\nu$. Uncertainties on the period, amplitude and frequency are drawn from the formalism proposed by [6]. Except for the 217.8362 s mode and the 318.7672 period, the S/N reached in amplitude is above 5σ.

Figure 3 shows the prewhitening sequences for each of the six main frequency peaks detected in the Fourier transform of the CFHT light curve on R548. The segments of the Fourier transform are vertically and horizontally shifted for a better vizualization. Each column illustrates from top to bottom, the prewhitening sequence obtained for a given peak indentified by its approximate central period (in s). Here we can distinguish the two triplets, two doublets, and the two singlets presented before. It is likely

Table 1. Observed pulsation properties of R548.

P(s)	A(%)	S/N	ν(μHz)	$\Delta\nu$(μHz)	
186.4882 (0.0068)	0.0411 (0.0053)	5.8	5362.27 (0.196)	22.618	f_1
187.2781 (0.0047)	0.0597 (0.0053)	9.4	5339.65 (0.135)		...
212.7684 (0.0009)	0.4201 (0.0056)	59.7	4699.94 (0.020)	3.972	...
212.9484 (0.0028)	0.1394 (0.0056)	19.7	4695.97 (0.062)	<4.015>	f_2
213.1326 (0.0006)	0.6658 (0.0056)	95.1	4691.91 (0.013)	4.058	...
217.8362 (0.0131)	0.0312 (0.0057)	4.5	4590.61 (0.275)		f_3
274.2508 (0.0017)	0.4346 (0.0063)	55.0	3646.30 (0.022)	3.647	...
274.5254 (0.0063)	0.1144 (0.0063)	14.7	3642.65 (0.084)	<3.475>	f_4
274.7745 (0.0023)	0.3140 (0.0063)	39.8	3639.35 (0.030)	3.302	...
318.0671 (0.0144)	0.0734 (0.0069)	8.4	3143.99 (0.142)	6.905	f_5
318.7672 (0.0356)	0.0299 (0.0069)	3.6	3137.09 (0.350)		...
333.6421 (0.0196)	0.0622 (0.0072)	6.9	2997.22 (0.176)		f_6

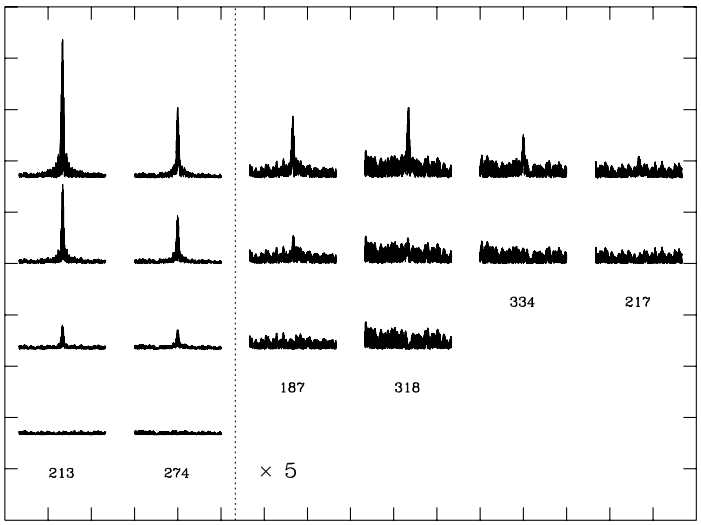

Figure 3. Prewhitening sequences of the R548 light curve. The various prewhitened sequences, are shifted vertically for better clarity (from top to bottom) and are identified by their central period (s). One tick mark in abscissa corresponds to 1 mHz, and one in ordinate to 0.2%.

that there are multiplet components in the doublet and the singlet features that have not been detected because their amplitude are smaller than the detection level.

Figure 4 and Fig. 5 provide a zoomed-in view of the two triplet complexes. The reconstructed Fourier transform is superimposed on the actual "observed" Fourier transform at the top of the figure.

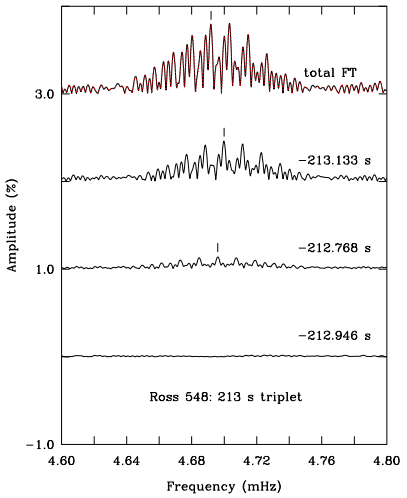

Figure 4. Prewhitening sequence for the 213 s feature.

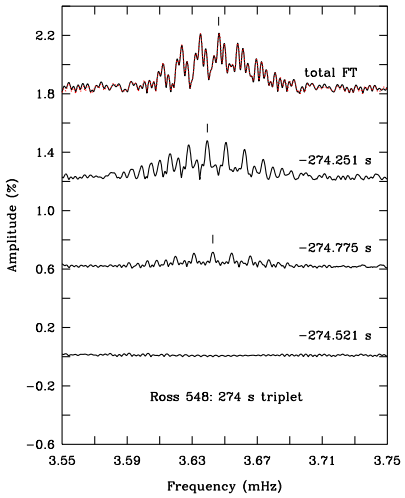

Figure 5. Prewhitening sequence for the 274 s feature.

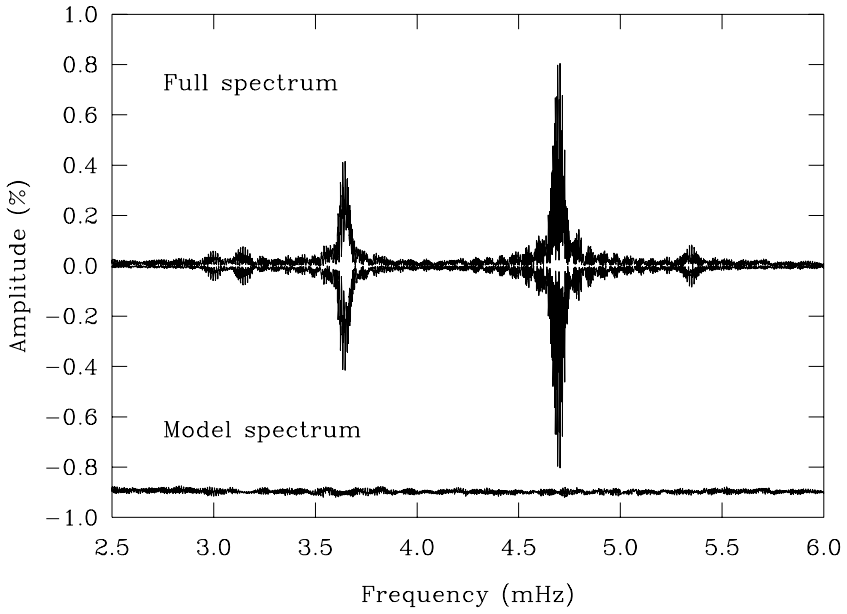

Figure 6. Modeled and observed Fourier transform. The point-by-point subtraction from the two curves is also shown at the bottom of the figure.

The absence of any noticeable differences between the reconstructed and the "observed" Fourier transforms emphasizes the righteous choice of extracted periods within the two multiplets. The resulting noise level after the two complete prewhitening sequences is very low, which is also a good indication that the extracted frequencies are appropriate. The observed spacings between the frequency components within these multiplets most likely indicate rotational splitting due to the slow rotation of the star. We note that, for over more than two decades, the central components of the 213 s and 274 s structures had not been detected, leading to the speculation that magnetic splitting, instead of rotation, was responsible for the existence of the two "doublets". This is clearly not the case, as demonstrated by our CFHT observations.

Figure 6 contrasts the full frequency spectrum with the modeled frequency spectrum based on the extracted periods. On the lower part of the graph, we illustrate the point-by-point subtraction of the two curves. The smoothness of this curve is the last check that the obtained periods are quite consistent with the CFHT light curve of R548, and that no false detection has been introduced in the extraction process.

We will refer the reader to [5] for a detailed description of the methodology and the presentation of the results obtained from the asteroseismological optimization exercise carried out on the basis of the frequencies derived here for R548.

References

[1] Charpinet, S., Brassard, P., Fontaine, G., et al. 2009, American Institute of Physics Conference Series, **1170**, 585
[2] Fontaine, G., & Brassard, P. 2008, PASP, **120**, 1043
[3] Bischoff-Kim, A., Montgomery, M.H., & Winget, D.E. 2008, ApJ, **675**, 1505
[4] Romero, A.D., C rsico, A.H., Althaus, L.G., et al. 2012, MNRAS, **420**, 1462
[5] Giammichele, N., Fontaine, G., & Brassard, P. 2012, in Proc. 18th European Workshop on White Dwarfs, ASP Conference Series, in press
[6] Montgomery, M.H., & O'donoghue, D. 1999, Delta Scuti Star Newsletter, **13**, 28

Annexe B

18^{th} European White Dwarf Workshop

18th EUROPEAN WHITE DWARF WORKSHOP
ASP Conference Series, Vol. 469
Krzesiński, Stachowski, Moskalik, and Bajan, eds.

Quantitative Asteroseismology: Determination of the Core Composition and Layering of the ZZ Ceti Star R 548. Part II

N. Giammichele,[1] G. Fontaine,[1] and P. Brassard[1]

[1]*Département de physique, Université de Montréal, C.P. 6128, Succursale Centre-Ville, Montréal, QC H3C3J7, Canada*

Abstract. We present a preview of a detailed asteroseismological study of the pulsating white dwarf R548 based on fits to newly detected periods and the use of the forward method. We first exploited a very high S/N photometric data set gathered with the CFHT/LAPOUNE combination, and isolated five secure independent periods for seismic modeling with spherical models. The details of this frequency extraction analysis having been summarized elsewhere, we now turn to a brief description of the seismic analysis *per se*. Using a method that has been developed and refined over more than a decade for applications to pulsating hot subdwarf stars mostly, we computed several million models during the course of an automatic and objective search in parameter space for the optimal model. Combining our results with independent spectroscopic constraints, we find that the global structural parameters of R548 can be well determined, including the envelope layering and the bulk composition of the core.

1. Introduction

Asteroseismology is a unique tool that allows to probe the internal structure and the evolutionary state of a pulsating star. By comparing the pulsation properties with those predicted by refined theoretical models of stars, it is possible to independently unveil unique features of the star such as its compositional stratification. Until recently, however, applications of the method to pulsating white dwarfs have been far and few, and have often suffered from an insufficient exploration of parameter space. To remedy this situation, we have begun to apply to white dwarfs the same double-optimization technique that has been used quite successfully in the context of pulsating hot B subdwarfs (see, e.g., the review of Charpinet et al. (2009) for more details).

In the present work, we focussed on the "simple" pulsator R548, ZZ Ceti itself and the prototype of the class. We took advantage of a previously unexploited data set of high S/N obtained with the CFHT/LAPOUNE combination to extract pulsation periods in the first part of this venture (Giammichele et al. 2012). We were able to isolate 6 frequency peaks, made of 2 triplets, 2 doublets, and 2 singlets. The multiplet structure is very likely due to rotational splitting, and not magnetic splitting as has been often suggested in the past. For comparison with spherical models, however, only 6 values of the pulsation periods were retained. In addition, to be conservative, we retained only those pulsations with amplitudes with a S/N higher than 5. We thus carried out our seismic analysis on the basis of 5 very secure periods observed in R548. We present some details and our main results in this paper.

2. The search for the optimal model

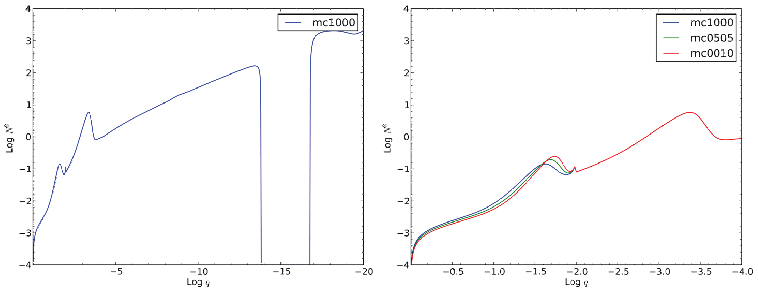

Figure 1. Entire and zoomed-in profile of the logarithm of the square of the Brunt-Väisälä frequency as a function of the fractional mass depth for a model with $T_{\rm eff}$ = 12 000 K and $\log g$ = 8.0 (left and right figure respectively). The value of $\log q = 0$ corresponds to the center of the star. We can notice the well in the profile due to the superficial H convection zone, as well as the two bumps associated with the H/He and He/C transition zones. On the right-hand side, we see the systematic differences between the three *uniform* core compositions from pure C, C-O mixed, and pure O (blue, green, and red curve respectively). Further out in the star, profiles are identical and are perfectly superimposed.

Given the high quality of the data presented in Giammichele et al. (2012), our goal is now to apply the same forward approach that has been successfully performed on hot pulsating subdwarfs. The technique relies on a first optimization leading to the best possible fit between the 5 observed periods (in the present case) with five periods out of the theoretical spectrum of a given (spherical) stellar model. The second optimization step next leads to the best model in parameter space. The quality of the match is quantified by a merit function S^2 (an unweighted χ^2), which is minimized as a function of $T_{\rm eff}$, $\log g$, $\log (M_{\rm H}/M_*)$, and $\log (M_{\rm He}/M_*)$; necessary parameters to fully define a static, but complete white dwarf model. It is also essential to finely calibrate the composition profiles, representing the steepness of the composition variation at the transition zones (H/He and He/C interfaces). In our models, we used the calibrated values of the composition profiles determined for the ZZ Ceti star GD!165 based on full evolutionary tracks including diffusion, since these two stars are quite comparable in mass and evolutionary status. The last sensitive parameter is the composition of the stellar core. In the present work, we considered only the bulk composition (assumed to be uniform). As can be seen in Fig.1, the distribution of the Brunt-Väisälä frequency in the deepest layers is slightly but sufficiently perturbed by the different chemical core compositions. The whole optimal model search exercise is here repeated for three different core composition scenarios. Lastly, tests have shown that low radial order modes are quite insensitive to the choice of the convective efficiency as prescribed by the mixing-length theory. In our calculations, the value of ML2/α=1.0 is fixed, and does not belong to our parameter space. The forward procedure as a whole necessitates the computation of many million models and their respective period spectra in a reasonable amount of time, and the use of our dedicated cluster of 320 nodes is a necessity. It is worth mentioning that there

is no *a priori* guaranty to find an optimal model that could match the spectroscopic determination of atmospheric parameters.

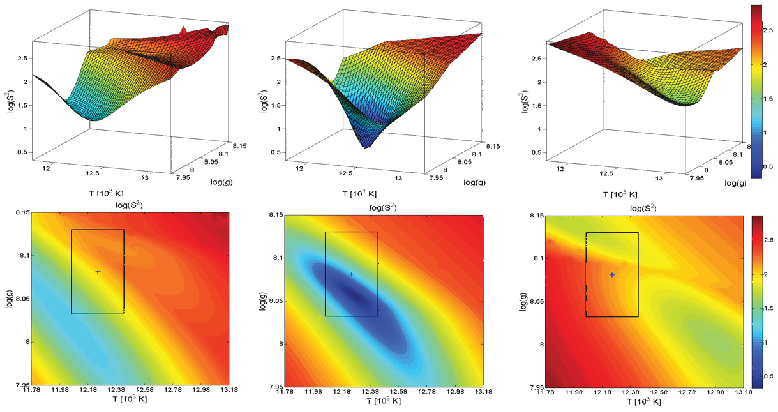

Figure 2. 3D and contour maps of the merit function S^2 in the log g-$T_{\rm eff}$ plane for 3 different core compositions from pure C, C-O mixture (50-50, proportions by mass), and pure O. 3D maps are presented to better visualize the relative depth of the three optimal models planes. Each grid point shows the optimized log g-$T_{\rm eff}$ model with respect to the other two dimensions, log ($M_{\rm H}/M_*$) and log ($M_{\rm He}/M_*$). The enhanced top view of the contour maps better indicates the optimum values and the morphology of the parameter space. The most recent and reliable spectroscopic solution given within 1σ from P. Bergeron (private communication) is illustrated with a black box.

Based on known mode identification in white dwarfs, the expected values for l can be restricted to 1 and 2, as a time-saving measure. Results are presented in Fig.2, Table 1, and Table 2. The first general remark that can be made is that optimal models are found for each of the three assumed core compositions. These models unambiguously suggest that R548 is composed of a thick hydrogen and helium layer, close to the the upper limits defined by evolutionary calculations. Moreover, the solution gives automatically the mode identification, with consecutive values of the radial order k for the $l = 1$ modes, perfectly consistent with the prediction from nonadiabatic theory that pulsation modes are excited in consecutive modes. More detailed results show that within a same valley of S^2, all solutions possess the same characteristics in terms of mode identification.

If we consider the newest spectroscopic determination of $T_{\rm eff}$ and log g for R548 kindly provided to us by P. Bergeron (private communication), the mixed C-O core best matches the optimum seismic solution found. We see here how the use of a precise spectroscopic determination can be used as a calibration tool to probe the unknown core composition of white dwarf stars. By varying the core composition, we also observe a better quality fit in term of the S^2 value leaning towards a mixed C-O core composition. This consistency between the optimum fit and the independent spectroscopic determination contributes in giving credibility to the process and the determination of the asteroseismological solution found.

Table 1. Parameters of the optimal models with the three core compositions

Parameters	C pure	C-O	O pure
S^2	14.69	2.14	42.36
$T_{\rm eff}$	12 905 K	12 270 K	13 005 K
$\log g$	8.015	8.055	8.000
$\log (M_{\rm H}/M_*)$	-4.36	-4.49	-4.30
$\log (M_{\rm He}/M_*)$	-2.16	-2.45	-2.56

Table 2. Mode identification for the best-fitting model with a mixed C-O core composition

Observed Periods	Fitted Periods	l	k
212.96	212.14	1	2
274.53	274.02	1	3
318.43	318.36	1	4
334.12	334.89	1	5
186.89	187.67	2	4

3. Conclusion

We presented a new seismic study of the pulsating white dwarf R548. This asteroseismological exercise has unravelled in a robust way the unique onion-like stratification of the star. In addition, by combining the seismic solutions with independent spectroscopic constraints, we were able to exploit a sensitivity of the results on the core composition in bulk. We found that, as expected from theoretical considerations, the core composition of R548 is a mixture of C and O. The fact that the spectroscopic values of the atmospheric parameters agree best with the C-O solution, while the latter also displays the best (lowest) value of the merit function S^2 boosts our confidence in the reliability of the proposed seismic model.

References

Charpinet, S., Brassard, P., Fontaine, G., Green, E. M., van Grootel, V., Randall, S. K., & Chayer, P. 2009, in American Institute of Physics Conference Series, edited by J. A. Guzik, & P. A. Bradley, vol. 1170 of American Institute of Physics Conference Series, 585

Giammichele, N., Fontaine, G., & Brassard, P. 2012, in The European Physical Journal, edited by J. Montalban, & V. Van Grootel, vol. 9999 of EPJ Web of Conferences, in press

Annexe C

6th Meeting on Hot Subdwarf Stars and Related Objects

6th Conference on Hot Subdwarf Stars and Related Objects
ASP Conference Series, Vol. 481
V. Van Grootel, E. M. Green, G. Fontaine, and S. Charpinet, eds.

Updates on the Asteroseismological Study of the ZZ Ceti Star R548: Determination of the Bulk Core Composition

N. Giammichele, G. Fontaine, and P. Brassard

[1]*Université de Montréal, Pavillon Roger-Gaudry, Département de physique, CP 6128, Succursale Centre-Ville, Montréal QC, H3C 3J7, Canada*

Abstract. We present a progress report on the detailed asteroseismological analysis of the pulsating white dwarf R548 with the use of the forward method. ZZ Ceti variables are nonradially g-mode pulsating white dwarfs with a hydrogen-dominated atmosphere. The low-amplitude and "simple" pulsator R548 is an ideal candidate for carrying on a complete asteroseismological analysis as five independent frequencies are unequivocally singled out. Using the successful double-optimization technique that has been applied and refined on pulsating hot B subdwarfs for more than a decade, we are capable of unraveling global structural parameters. Taking advantage of independent measurements of spectroscopic temperature and surface gravity, we investigate the constraints on the envelope layering and the bulk composition of the core of R548.

1. Introduction

Asteroseismology is a unique tool that allows us to probe the internal structure and the evolutionary state of a pulsating star. By comparing the observed pulsation properties with those predicted by theoretical models of stars, it is possible to unveil unique features of the star such as its compositional stratification. Until recently however, applications of the method to pulsating white dwarfs were few, and suffered from an insufficient exploration of the parameter space. To remedy this situation, we have begun to apply to white dwarfs the same double-optimization technique that has been successfully used in the context of pulsating hot B subdwarfs (see, e.g., the review of Charpinet et al. 2009).

In the present work, we focussed on the pulsating white dwarf R548, ZZ Ceti itself and the prototype of the class. R548 is one of the low-amplitude pulsators found in the hotter region of the instability strip. It shows a stable and uncomplicated curve, compared to cooler ZZ Ceti stars that present strongly non-linear pulse features. We took advantage of a previously unexploited data set of high S/N obtained with the CFHT/LAPOUNE combination to extract pulsation periods. We were able to isolate 6 frequency peaks, made of 2 triplets, 2 doublets, and 2 singlets. The multiplet structures are very likely due to rotational splitting, and not magnetic splitting as has been often suggested in the past. For comparison with spherical models, however, only 6 values of the pulsation periods were retained. In addition, to be conservative, we retained only those pulsations with amplitudes with a S/N higher than 5. We thus carried out our seismic analysis on the basis of 5 very secure periods observed in R548. We present the first part of this venture in Giammichele et al. (2013b), while details and preliminary results on the optimization process are shown in Giammichele et al. (2013a). We

present here complete results of the sensitivity of the bulk composition of the core on the theoretical period spectrum.

2. The Resulting Parameter Space

We applied the same forward approach that has been successfully performed on hot pulsating subdwarfs. The technique relies on a first optimization leading to the best possible fit between the five observed periods with five periods out of the theoretical spectrum of a given (spherical) stellar model. The second optimization step next leads to the best model in the parameter space. The quality of the match is quantified by a merit function S^2 (an unweighted χ^2), which is minimized as a function of $T_{\rm eff}$, $\log g$, $\log (M_{\rm H}/M_*)$, and $\log (M_{\rm He}/M_*)$; necessary parameters to fully define a static, but complete white dwarf model. The calculated period spectrum is also quite sensitive to the composition profiles, representing the steepness of the composition variation at the transition zones (H/He and He/C interfaces). In our models, we used the calibrated values of the composition profiles from full evolutionary calculations including diffusion, determined for the ZZ Ceti star GD165, since these two stars are comparable in mass and evolutionary status. Tests have shown that low radial order modes are quite insensitive to the choice of the convective efficiency as prescribed by the mixing-length theory. In our calculations, the value of ML2/α=1.0 is fixed, and does not belong furthermore to our parameter space. The last sensitive parameter is the composition of the stellar core. In the present work, we consider only the bulk composition, assumed to be uniform. As can be seen in Fig. 1 of Giammichele et al. (2013b), the distribution of the Brunt-Väisälä frequency in the deepest layers is sufficiently perturbed by the different chemical core compositions. The whole optimal model search exercise is here repeated for different core composition scenarios, ranging from pure carbon to pure oxygen with steps of 10% in proportion of mass.

Table 1.: Parameters of the optimal models with three core compositions.

Parameters	C pure	C-O (60-40)	O pure
S^2	14.69	0.86	42.36
$T_{\rm eff}$	12,905 K	12,165 K	13,005 K
$\log g$	8.015	8.060	8.000
$\log (M_{\rm H}/M_*)$	-4.36	-4.51	-4.30
$\log (M_{\rm He}/M_*)$	-2.16	-2.42	-2.56

The first general remark that can be made is the nice agreement between the spectroscopic and seismic determination of atmospheric parameters presented. Table 1 exposes results from the two extreme and the optimal cases. Resulting models unambiguously suggest that R548 is composed of a thick hydrogen and helium layer, the upper limit defined by evolutionary calculations. The solution gives automatically the mode identification, with consecutive values of the radial order k, perfectly consistent with the prediction from nonadiabatic theory that pulsation modes are excited in consecutive modes. More detailed results show that within a same valley, all solutions possess the same characteristics in term of mode identification. The best quality fit in term of minimal S^2 corresponds to a chemical composition of the core of a mixture of C-O of

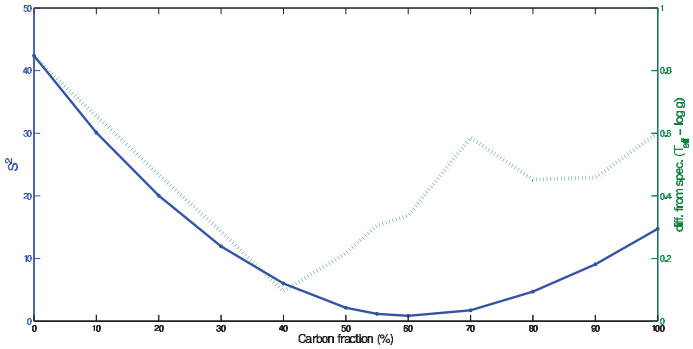

Figure 1.: Variation of the merit function S^2 (left-hand axis) and a weighted measure of the difference from the seismic values and the spectroscopic estimations of $T_{\rm eff}$ and $\log g$ (right-hand axis) as a function of the core composition. A pure O (C) core is shown on the extreme left (right).

60/40 as can be seen in Fig. 1. Cores composed of pure carbon and oxygen can be unambiguously ruled out from the poor matches of frequency spectrum. If we consider the newest spectroscopic determination of $T_{\rm eff}$ and $\log g$ for R548 kindly provided to us by P. Bergeron (private communication), the mixed C-O core (60/40) best matches the optimum seismic solution found. We see here how the use of a precise spectroscopic determination can be used as a calibration tool to probe the unknown core composition of white dwarf stars. If we consider both independent measures, a mix C-O core composition (around 50/50) gives a nice fit and boosts our confidence in the reliability of the proposed seismic model.

3. Conclusion

We presented updates on the seismic study of the pulsating white dwarf R548. This asteroseismological exercise has unravelled in a robust way the unique onion-like stratification of the star. In addition, by combining the seismic solutions with independent spectroscopic constraints, we were able to exploit the sensitivity of the results on the core composition in bulk. We found that, as expected from theoretical considerations, we can exclude a core entirely composed of either carbon or oxygen and lean forward a mixture composed of C-O (60/40). The fact that the spectroscopic values of the atmospheric parameters agree best with the C-O solution, while the latter also displays the best (lowest) value of the merit function S^2 contributes in giving credibility to the proposed method and seismic model found.

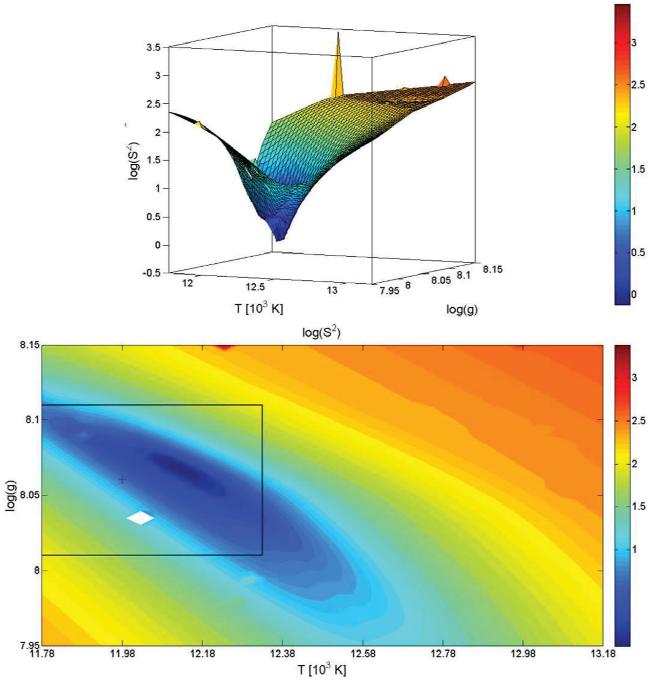

Figure 2.: 3D and contour maps of the merit function S^2 in the log g-$T_{\rm eff}$ plane for the optimal core composition: C-O mixture (60-40, proportions by mass). Each grid point shows the optimized log g-$T_{\rm eff}$ model with respect to the other two dimensions, log $(M_{\rm H}/M_*)$ and log $(M_{\rm He}/M_*)$. The enhanced top view of the contour maps better indicates the optimum values and the morphology of the parameter space. The most recent and reliable spectroscopic solution given within 1σ from P. Bergeron (private communication) is illustrated with a black box.

References

Charpinet, S., Brassard, P., Fontaine, G., Green, E. M., Van Grootel, V., Randall, S. K., & Chayer, P. 2009, in American Institute of Physics Conference Series, edited by J. A. Guzik, & P. A. Bradley, vol. 1170 of American Institute of Physics Conference Series, 585

Giammichele, N., Fontaine, G., & Brassard, P. 2013a, in 18th European White Dwarf Workshop., edited by Krzesiń, J. ski, G. Stachowski, P. Moskalik, & K. Bajan, vol. 469 of Astronomical Society of the Pacific Conference Series, 49

— 2013b, in European Physical Journal Web of Conferences, edited by J. Montalban, A. Noels & V. Van Grootel, vol. 43 of European Physical Journal Web of Conferences, 5007

Annexe D

Precision Asteroseismology, Proceedings of the International Astronomical Union, IAU Symposium

Precision Asteroseismology
Proceedings IAU Symposium No. 301, 2013
J. A. Guzik, W. J. Chaplin, G. Handler & A. Pigulski, eds.

doi:10.1017/S1743921313014464

The internal structure of ZZ Cet stars using quantitative asteroseismology: The case of R548

N. Giammichele[1], G. Fontaine[1], P. Brassard[1], and S. Charpinet[2]

[1]Département de physique, Université de Montréal,
C.P. 6128, Succursale Centre-Ville, Montréal, QC H3C3J7, Canada

[2]Université de Toulouse, UPS-OMP, IRAP, Toulouse, France;
CNRS, IRAP, 14 avenue Edouard Belin, 31400, Toulouse, France

Abstract. We explore quantitatively the low but sufficient sensitivity of oscillation modes to probe both the core composition and the details of the chemical stratification of pulsating white dwarfs. Until recently, applications of asteroseismic methods to pulsating white dwarfs have been far and few, and have generally suffered from an insufficient exploration of parameter space. To remedy this situation, we apply to white dwarfs the same double-optimization technique that has been used quite successfully in the context of pulsating hot B subdwarfs. Based on the frequency spectrum of the pulsating white dwarf R548, we are able to unravel in a robust way the unique onion-like stratification and the chemical composition of the star. Independent confirmations from both spectroscopic analyses and detailed evolutionary calculations including diffusion provide crucial consistency checks and add to the credibility of the inferred seismic model. More importantly, these results boost our confidence in the reliability of the forward method for sounding white dwarf internal structure with asteroseismology.

Keywords. stars: oscillations, white dwarfs

1. Introduction

Asteroseismology is a unique tool that allows us to probe the internal structure of a pulsating star. Until recently however, applications of the method to pulsating white dwarfs were few, and greatly suffered from an insufficient exploration of parameter space. The use of fully evolutionary models tend to propagate errors, and by the end of the calculation, uncertainties are greatly boosted. Moreover, such calculations are lenghty and it is impossible to thoroughly explore parameter space. To remedy this situation, we have begun to apply to white dwarfs the same double-optimization technique based on the forward approach that has been successfully used in the context of pulsating hot B subdwarfs (see, e.g., the review of Charpinet *et al.* 2009a). Targeted white dwarfs were chosen lying close to the blue edge, where the simplest pulsators are found. Even if only a few modes are excited in such stars, they still contain individually quite a bit of complementary information since they are low-order modes, far away from the asymptotic regime. We took advantage of a previously unexploited data set of very high S/N, obtained with the CFHT/LAPOUNE combination to extract pulsation periods in the first part of this venture (Giammichele *et al.* 2013a). We carried out our seismic analysis on the basis of five very certain periods observed in R548 (an improved extraction exercise was performed since Giammichele *et al.* 2013a and slightly different pulsation periods were obtained and used hereinafter). Results are presented in Giammichele *et al.* (2013b). This work contains the final validations of this asteroseismic exercise.

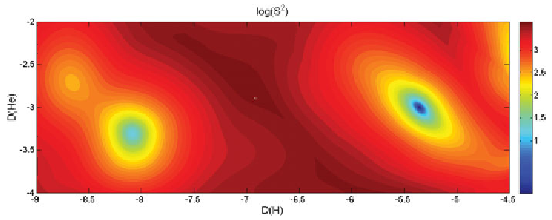

Figure 1. Contour map of the merit function as a function of the top of the transition zones $D(\mathrm{H})$ and $D(\mathrm{He})$, while the remaining parameters are fixed at their optimized values. $D(\mathrm{H})$ and $D(\mathrm{He})$, natural parameters of the optimization exercise, are directly related to the more familiar parameters $\log(M_{\mathrm{H}}/M_*)$ and $\log(M_{\mathrm{He}}/M_*)$ through: $\log(M_{\mathrm{H}}/M_*) = D(\mathrm{H}) + C$ (similar for the helium layer) where C is a small positive term, slightly dependent on the model parameters, determined by the mass of hydrogen or helium present inside the transition zones.

2. Internal structure

2.1. *Optimization procedure*

Given the high quality of our data, our goal is now to apply the same forward approach that has been successfully performed on hot pulsating subdwarfs. The technique relies on a first optimization leading to the best possible fit between the five observed periods (in the present case) with five periods out of the theoretical spectrum of a given stellar model. The second optimization step next leads to the best model in parameter space. To fully define a static white dwarf model, we have to specify the surface gravity (alternatively, the mass), the effective temperature, the chemical stratification in the envelope, and the core composition. Since low radial-order modes are quite insensitive to the prescribed convective efficiency, we fixed the latter to the so-called ML2/$\alpha = 1.0$ prescription and did not vary it in parameter space. The quality of the match is then quantified through a second optimization by a merit function S^2 (an unweighted χ^2), which is minimized as a function of T_{eff}, $\log g$, $\log(M_{\mathrm{H}}/M_*)$, and $\log(M_{\mathrm{He}}/M_*)$, given a core composition. Thus, for every set of T_{eff}, $\log g$, $\log(M_{\mathrm{H}}/M_*)$, and $\log(M_{\mathrm{He}}/M_*)$, we get a unique period spectrum to compare with the observed frequencies.

The forward procedure as implemented in Montréal (a full grid approach) necessitates the computation of many millions of models and their respective period spectra in a reasonable amount of time, and the use of our dedicated cluster of 320 nodes is a necessity. The same exercise with fully evolutionary sequences, including diffusion would be impracticable. It is worth repeating that there is no a priori guarantee to find an optimal model and, moreover, to find an optimal model that would be consistent with independent spectroscopic determinations of the atmospheric parameters.

The resulting optimum asteroseismic model presents a very low $S^2 = 0.83$, with $T_{\mathrm{eff}} = 12\,095$ K, $\log g = 8.070$, $\log(M_{\mathrm{H}}/M_*) = -4.54$, and $\log(M_{\mathrm{He}}/M_*) = -2.42$. Details on the mode identification, given automatically by the solution, are presented in Table 1. Consecutive values of the radial order k, are perfectly consistent with the prediction from nonadiabatic theory that pulsation modes are excited in consecutive modes. Moreover, the nice agreement between the newest spectroscopic determination of $T_{\mathrm{eff}} = 11\,980$ K, $\log g = 8.06$ (kindly provided to us by P. Bergeron) and our seismic determination of atmospheric parameters boosts our confidence in the validity of the solution found.

2.2. *Chemical stratification*

Figure 1 unambiguously suggests that R548 is composed of a thick hydrogen and thick helium layer as indicated by the deeper minimum. A much less convincing "thin" envelope

Table 1. Mode identification for the best-fitting model with a mixed C-O core composition (mass fraction: 60-40).

Observed periods	Fitted periods	l	k
212.96	212.98	1	2
274.53	274.60	1	3
318.43	318.18	1	4
334.12	334.96	1	5
186.89	187.14	2	4

possibility also appears in the figure, but can readily be ruled out on the grounds of its significantly degraded merit function. There is no degeneracy in the optimized grid of seismic solutions. The chemical stratification with thick hydrogen and helium layers found for R548 ought to be reliable.

A first validation of the use of the forward method in this context is illustrated in Figure 2. We explore the importance of the imposed steepness of the chemical profile at the interface between the H/He and He/C-O layers in our static models. While the transition between the H/He layers leaves a stronger signature on the period spectrum than the deeper He/C-O interface, we still find a very narrow and well-defined minimum for a(H/He) = 1.3 and a(He/C-O) = 3.3, the parameters defining steepness. Here again, these two parameters do not lead to any degeneracy in the asteroseismic solution. More importantly, evolutionary calculations, including diffusion, confirm transition steepness values of a(H/He) = 1.31 and a(He/C-O) = 3.20, in almost perfect agreement with our asteroseismic values.

2.3. *Core composition*

The distribution of the Brunt-Väisälä frequency in the deepest layers is slightly but sufficiently perturbed by the different possible core compositions to allow us to probe the bulk composition. The best quality fit in terms of minimal $S^2 = 0.83$ corresponds to a chemical composition of the core made of a mixture of C-O of mass fraction 60/40 as can be seen in Fig. 1 of Giammichele *et al.* (2014, in press). Cores composed of pure carbon and oxygen can be unambiguously ruled out from the poor matches of the observed frequency spectrum. If we consider the newest spectroscopic determination of $T_{\rm eff}$ and $\log g$ for R548, the mixed C-O core is the solution that agrees best with spectroscopic

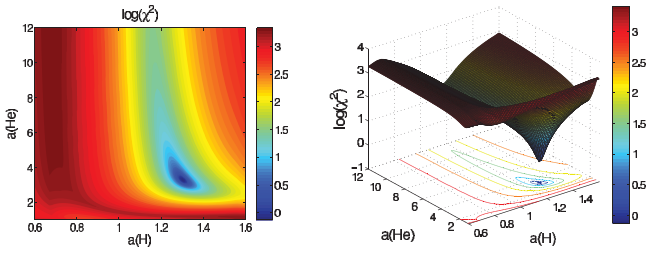

Figure 2. Contour and 3-D map of the merit function S^2 as a function of the values of the chemical profile steepness at the interface between the H/He and He/C-O layers, for the optimal effective temperature and surface gravity.

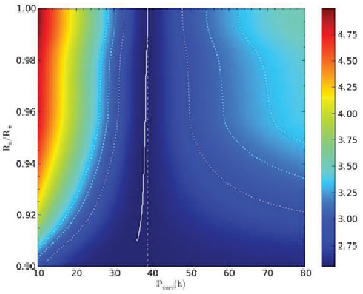

Figure 3. Contour map showing the behaviour of the normalized merit function S^2 in terms of the radius and in terms of the rotation period of the inner region for solid body rotation in a two-zone approach defined by Charpinet *et al.* (2009b). The solution is illustrated by the nearly vertical white curve and the dotted white curves depict the 1, 2 and 3σ contours. In comparison, the vertical dot-dashed white curve gives the exact solution for solid-body rotation.

parameters while displaying the best (lowest) value of the merit function S^2 of the seismic solution. This contributes in giving credibility to the proposed method.

It must be pointed out that it is the imposed smoothness of the core profile (assumed homogeneously mixed) that has allowed us to carry out successfully our asteroseismic exercise. Indeed, through numerous tests, we found that detailed post-AGB models contain too much noise in the core for pursuing quantitative seismology. For example, we implemented in some of our test models the detailed core chemical profiles computed by Salaris *et al.* (2010). Even if the grid of optimized parameters is showing the same global geometry, the surface turns out to be too noisy to identify a global minimum. We believe that current post-AGB models leave core structures that are most probably not physical, rendering the seismic exercise difficult if not impossible.

2.4. *Rotation profile structure*

Based on the rotational splitting (Giammichele *et al.* 2013a) shown in four out of the five modes listed in Table 1 and on the optimal model of R548, we determined whether or not its internal rotation profile corresponds to solid-body rotation, as seen in Figure 3. Unfortunately, evolution has pushed the g-modes to the outer part of the star because of the increase of degeneracy along the cooling track. Unlike the case of GW Vir stars (see Charpinet *et al.* 2009b), rotation kernels have large amplitudes in the outermost layers only. Therefore, we can only probe about 10% of the radius, and less than 1% of the total mass. But within the outer 10% radius, we can assert that R548 is rotating as a solid body. The relatively low period of 39 h is consistent with the suggestion of Charpinet *et al.* (2009b) to the effect that isolated white dwarfs must have lost essentially all of their angular momentum during evolutionary phases prior to the white dwarf stage.

References

Charpinet, S., Fontaine, G., & Brassard, P. 2009a, *A&A*, 493, 595
Charpinet, S., Fontaine, G., & Brassard, P. 2009b, *Nature*, 461, 501
Giammichele, N., Fontaine, G., & Brassard, P. 2013a, *European Physical Journal Web of Conferences*, 43, 5007
Giammichele, N., Fontaine, G., & Brassard, P. 2013b, *ASP-CS*, 469, 49
Salaris, M., Cassisi, S., Pietrinferni, A., Kowalski, P. M., & Isern, J. 2010, *ApJ*, 716, 1241

Annexe E

The space photometry revolution. CoRoT Symposium 3, Kepler KASC-7 joint meeting.

EPJ Web of Conferences **101**, 01012 (2015)
DOI: 10.1051/epjconf/201510101012

GD1212: Probing deep into the interior of a pulsating white dwarf star

N. Giammichele[1,a], G. Fontaine[1], S. Charpinet[2], P. Brassard[1], and S. Greiss[3]

[1] Université de Montréal, Montréal, Québec, Canada
[2] Institut de Recherche en Astrophysique et Planétologie (IRAP), Observatoire Midi-Pyrénées, Université Paul Sabatier / CNRS, Toulouse, France
[3] The University of Warwick, Coventry CV4 7AL, UK

Abstract. We present the first self-consistent seismic analysis of a white dwarf star, GD 1212, in the *Kepler*2 field. We precisely establish the fundamental parameters of the star using the forward method based on physically sound models. We unravel the internal structure as well as the rotation profile of GD1212 deeper than in any other ZZCeti stars studied so far. This opens up interesting prospects for future analyses of the white dwarf pulsators monitored in the *Kepler* and *Kepler*2 fields.

1 Introduction

Efforts made on the search for pulsating white dwarfs in the *Kepler* field have proven to be quite successful with the discovery of several new ZZ Ceti stars. The analysis presented here focus on the ZZ Ceti star: GD 1212, which was observed by *Kepler*-2 in the test run field (see [4] for more details). GD 1212 was specifically picked as it represents the boundary of the pure ZZ Ceti instability strip. Spectroscopic determination of $\log g$ and $T_{\rm eff}$ places GD 1212 near the red edge. This is further confirmed by the comparison between their mean excited period and their position in the $\log g - T_{\rm eff}$ diagram as presented in Figure 1.

The light curve of GD 1212 is composed of 9 consecutive days of data. It reveals a quite complicated structure, standard for stars further away from the blue edge, where the simple pulsators are usually located. As we move along the cooling track of WDs, cooler ZZ Ceti stars have pulsation spectra with numerous harmonics, frequency sums and differences associate with nonlinear pulse shapes. Pulsation spectra can furthermore vary importantly with time, which tends to make the mode identification exercise quite challenging. Standard reduction techniques were used on GD 1212 light curve; details can be found in [4]. The spectrum of GD 1212 is quite rich as we can use thirteen independent modes for the internal structure of the star, and nineteen components of rotationally-split multiplets for the internal rotation profile.

2 Internal structure

The technique relies on a double-optimization scheme that, first, best matches the observed periods with the periods calculated from a theoretical, parameterized model, using a χ^2 formalism. The second optimization uses a multimodal optimizer based on a genetic algorithm to find the best-fit model in parameter space, the quality of the fit being quantified by a merit function. We search around a very large domain around the spectroscopic values to guide us. It is important to point out that there is no a priori guaranty to find an optimal model that could match the spectroscopic solution. The onion-like

Article available at http://www.epj-conferences.org or http://dx.doi.org/10.1051/epjconf/201510101012

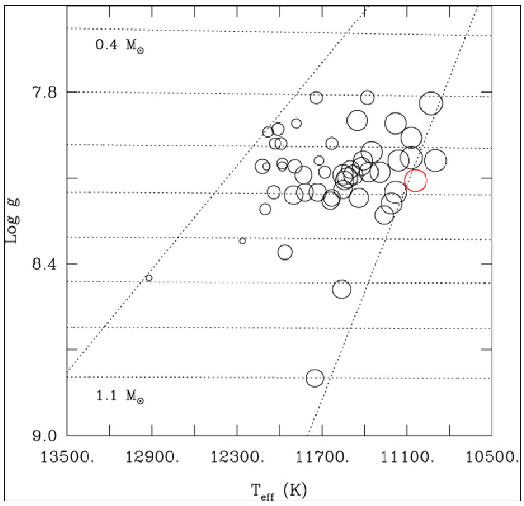

Fig. 1. Correlation between excited period and effective temperature or surface gravity for ZZ Ceti stars. The size of the open circles gives a measure of the representative period on a logarithmic scale for each star. The two diagonal dotted lines are the empirical blue and red edge of the instability strip. Figure originating from [2].

structure of the white dwarf is best described by a parameterized model with eight parameters: $T_{\rm eff}$, log g, $D(H)$, $D(He)$, Pf_1, Pf_2, (uniform) core composition and convective efficiency. Pf_1 and Pf_2 are inherent to the chemical layering of the two outermost layers, and represent the steepness of the chemical transition between the H/He layers and the He/CO core, respectively. Tests have shown that for low radial order, models are quite insensitive to the choice of the mixing length theory. Standard value of ML2/α=1.0 is then fixed in our case. The pulsation periods detected in ZZ Ceti pulsators are mostly sensitive to the first four parameters: surface gravity, effective temperature, and envelope layering, particularly the thickness of the outermost hydrogen envelope. But there is also some sensitivity of the pulsation periods to the core composition, more difficult to exploit since we must rely on the detection of modes that have relatively large amplitudes in the core.

Figure 2a shows the projection on the $T_{\rm eff}$-log g plane of the merit function for GD 1212. The logarithmic scale emphasizes the great contrast in S^2 between the minimum solution (blue) and maxima located elsewhere in parameter space (red). In both cases, we converge toward a particular solution that fits nicely within the spectroscopic solution bounding box. Resulting parameters are presented in the following table:

	$T_{\rm eff}$	Spect. $T_{\rm eff}$	log g	Spect. log g	D(H)	D(He)
GD 1212	11,244	11,035	8.10	8.08	-6.04	-2.82

The case of the use of non-parameterized C/O core descriptions coming from evolutionary sequences, has to be dealt with great precaution. White dwarf models derived from main sequence evolution suffer from many uncertainties and are numerically too noisy to use for quantitative adiabatic asteroseismology. We can see an example of such an experiment in the case of GD1212 in Figure 2b. Not only the best S^2 is noticeably degraded from 28 to 252, the mapping of the solution on the $T_{\rm eff}$-log g plane is scattered with local minima due to the numerical noise from the evolutionary profile. The best fit does not even lie within the spectroscopic limits anymore. Similar experiment with other ZZ Ceti stars yelds similar results. Parameterized models are much better suited for this purpose.

If we look at Figure 3a, we can see the weight functions of the different modes present in the pulsation spectrum. Evolution has pushed the g-modes to the outside because of the increase of de-

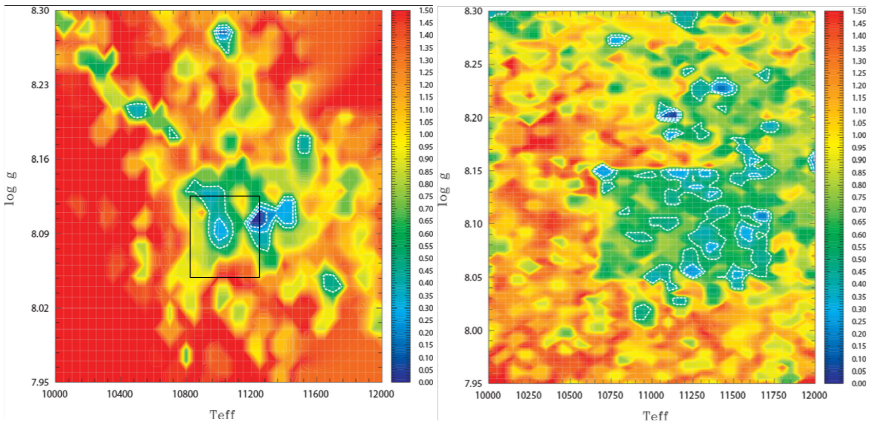

Fig. 2. Projection on the $T_{\rm eff}$-log g plane of the merit function S^2 for GD 1212. The spectroscopic solution given within 1σ is illustrated with a black box.*Left:* Homogeneous C/O core. *Right:* Non-homogeneous core with chemical profiles coming from evolutionary models.

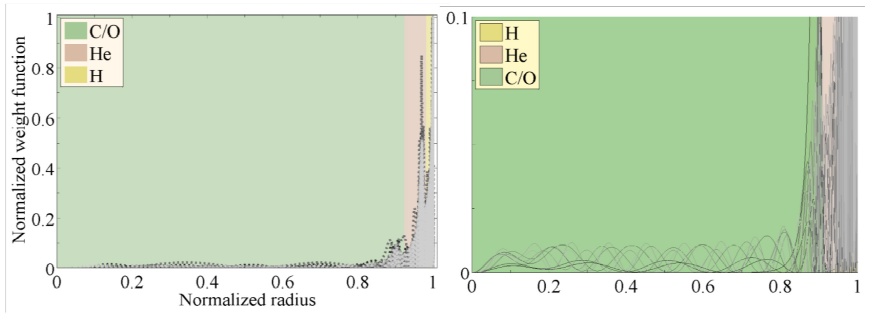

Fig. 3. *Left:* Normalized weight functions of the modes present in GD 1212 as a function of the radius of the star. The area under the each curve is the same. *Right:* Zoom-in view of the normalized rotation kernels as a function of radius for each mode identified in the optimal model of GD 1212.

generacy along the cooling track. This implies as we see in Figure 3a that weight functions have large amplitude in the outermost layers. But we can also notice that the core is almost entirely sampled by low-amplitude weight functions. Taking advantage of this behavior, we can properly assess the bulk C/O core composition to be 47-53 %. Since the interior of the star is not entirely sampled, it is important in order to infer the proper bulk composition of the star to have some kind of normalization. If we consider a profile coming from evolutionary sequences at the same effective temperature and similar surface gravity, by normalizing with the weight functions we can compare directly the two compositions. By doing so, we find quite a nice agreement between the two C/O core compositions found, the latter coming from evolutionary model being 43-57 %. We find slightly more carbon in our homogeneous composition, but, all in all, it agrees nicely and boost our confidence in the proper sampling of the core.

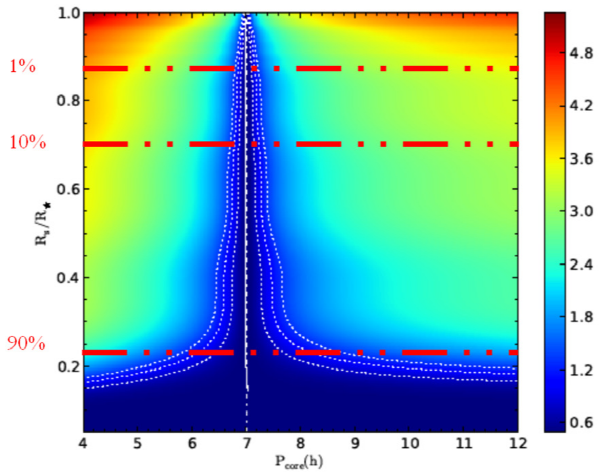

Fig. 4. Contour map showing the behaviour of the normalized merit function S^2 in terms of the radius and in terms of the rotation period of the inner region for solid body rotation in a two-zone approach defined by [1]. Horizontal dot-dashed curves give an indication on the encompassed mass. The solution is illustrated by the nearly vertical white curve and the dotted white curves depict the 1, 2 and 3σ contours. In comparison, the vertical dot-dashed white curve gives the exact solution for solid-body rotation. At larger depths, the gravity modes lose their ability to measure local rotation, giving the divergence in the 1, 2 and 3σ contours.

3 Internal rotation profile

Figure 3b emphasizes the low-amplitude, but still present, rotational kernels in the interior of the star. Many rotationally-split structures sound the deep interior. Based on the optimal model of GD 1212, we determined its internal rotation profile as seen in Figure 4. Probing more than 85% of the radius, and more than 90% of the total mass, we can assert that GD 1212 is rotating as a solid body. Unlike other ZZ Ceti stars analysed, it is the first time that such a depth into the interior of a star of the kind is probed. Indeed, and unfortunately, "simple" blue edge pulsators analysed so far do not exhibit rotational splitting on modes present in the core of the star, and we can only sound a few percent of the radius into the interior.

4 Conclusion

These results boost our confidence in the reliability of the forward method with parameterized models for sounding white dwarf internal structure with asteroseismology. For the first time, we explore to great depths the internal composition and rotation profile of a ZZ Ceti star.

References

1. Charpinet, S.,Fontaine, G., & Brassard, P., Nat **461**, 501 (2009)
2. Fontaine, G., & Brassard, P., PASP **120**, 1043 (2008)
3. Greiss, S., Gänsicke, B. T., Hermes, J. J., et al., MNRAS **438**, 3086 (2014)
4. Hermes, J. J., Charpinet, S., Barclay, T., et al., ApJ **789**, 85 (2014)

Annexe **F**

19^{th} European Workshop on White Dwarfs

19th European Workshop on White Dwarfs
ASP Conference Series, Vol. 493
Dufour, Bergeron, and Fontaine, eds.

Parametric Modeling in Action: High Accuracy Seismology of Kepler DAV Stars

N. Giammichele,[1] G. Fontaine,[1] S. Charpinet,[2] P. Brassard,[1] and S. Greiss[3]

[1]*Université de Montréal, Montréal, Québec, Canada;* [redacted]

[2]*Institut de Recherche en Astrophysique et Planétologie (IRAP), Observatoire Midi-Pyrénées, Université Paul Sabatier / CNRS, Toulouse, France*

[3]*The University of Warwick, Coventry CV4 7AL, UK*

Abstract. We summarize here the efforts made on the quantitative seismic analyses performed on two ZZ Ceti stars observed with the Kepler satellite. One of them, KIC 11911480, is located close to the blue edge of the instability strip, while the other, GD 1212, is found at the red edge. We emphasize the need for parameterized modeling and the forward approach to uniquely establish the fundamental parameters of the stars. We show how the internal structures as well as rotation profiles are unravelled to surprisingly large depths for degenerates such as ZZ Ceti stars, which further confirms the loss of stellar angular momentum before the white dwarf stage detected previously in GW Vir pulsating white dwarfs. This opens up interesting prospects for the new mission to come, Kepler-2, in the field of white dwarf asteroseismology.

1. Introduction

Efforts made on the search for pulsating white dwarfs in the Kepler field have proven to be quite successful with the discovery of several new ZZ Ceti stars. The analyses presented here focus on two opposite extreme ZZ Ceti stars: KIC 11911480 (KIC 119, for short) discovered by Greiss et al. (2014) during the Kepler-1 mission, while the second pulsating white dwarf GD 1212 was observed by Kepler-2 in the test run field (see Hermes et al. 2014 for more details). KIC 119 and GD 1212 were specifically picked as they represent both boundaries of the pure ZZ Ceti instability strip. Spectroscopic determination of $\log g$ and $T_{\rm eff}$ places KIC 119 at the blue edge, while GD 1212 is located near the red edge. This is further confirmed by the comparison between their mean excited period and their position in the $\log g - T_{\rm eff}$ diagram as presented in Figure 1.

The light curve of KIC 119 gathered during Quarters 12 and 16, over 85 days each, presents three main structures showing what is most probably rotational splitting. The light curve of GD 1212 is, on the other hand, a lot shorter, composed of 9 consecutive days of data. It reveals a much complicated structure, standard for stars further away from the blue edge, where the simple pulsators are usually located. As we move along the cooling track of WDs, cooler ZZ Ceti stars have pulsation spectra with numerous harmonics, frequency sums and differences associate with nonlinear pulse shapes. Pulsation spectra can furthermore vary importantly with time, which tends to

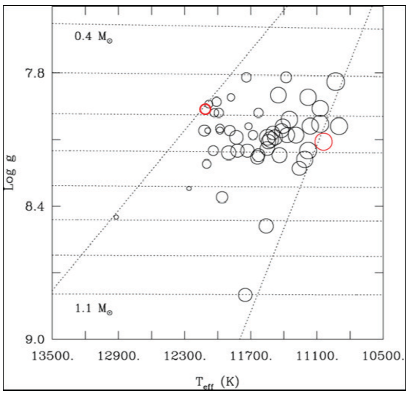

Figure 1. Correlation between excited period and effective temperature or surface gravity for ZZ Ceti stars. The size of the open circles gives a measure of the representative period on a logarithmic scale for each star. The two diagonal dotted lines are the empirical blue and red edge of the instability strip. Figure originating from Fontaine & Brassard (2008).

make the mode identification exercise quite challenging. Standard reduction techniques were used on KIC 119 and GD 1212 light curves; details can be found in Greiss et al. (2014) and in Hermes et al. (2014) for each star, respectively. A total of five independent modes were recovered for the seismic exercise of the structure of KIC 119, and another five components of rotationally-split multiplets can be used to probe the internal rotation profile of the star. The spectrum of GD 1212 is much richer as we can use thirteen independent modes for the internal structure of the star, and nineteen components of rotationally-split multiplets for the internal rotation profile.

2. Internal Structure

The technique relies on a double-optimization scheme that, first, best matches the observed periods with the periods calculated from a theoretical, parameterized model, using a χ^2 formalism. The second optimization uses a multimodal optimizer based on a genetic algorithm to find the best-fit model in parameter space, the quality of the fit being quantified by a merit function. We search around a very large domain around the spectroscopic values to guide us. It is important to point out that there is no a priori guaranty to find an optimal model that could match the spectroscopic solution. The onion-like structure of the white dwarf is best described by a parameterized model with eight parameters: $T_{\rm eff}$, log g, $D(H)$, $D(He)$, Pf_1, Pf_2, (uniform) core composition and convective efficiency. Pf_1 and Pf_2 are inherent to the chemical layering of the two outermost layers, and represent the steepness of the chemical transition between the H/He layers and the He/CO core, respectively. Tests have shown that for low radial order, models are quite insensitive to the choice of the mixing length theory. Standard value of ML2/α=1.0 is then fixed in our case. The pulsation periods detected in ZZ Ceti pulsators are mostly sensitive to the first four parameters: surface gravity, effective

temperature, and envelope layering, particularly the thickness of the outermost hydrogen envelope. But there is also some sensitivity of the pulsation periods to the core composition, more difficult to exploit since we must rely on the detection of modes that have relatively large amplitudes in the core.

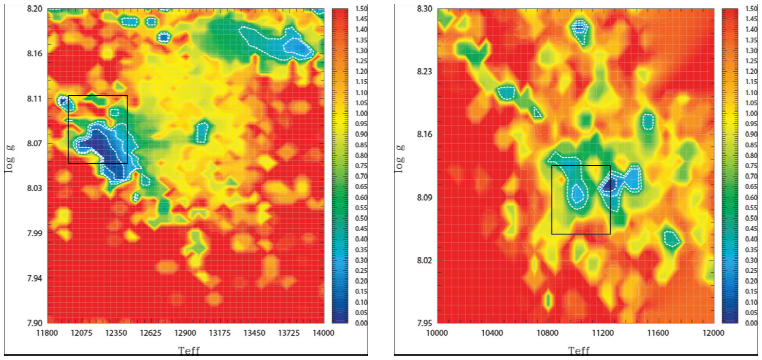

Figure 2. Projection on the $T_{\rm eff}$-log g plane of the merit function S^2 for KIC 119 (*left*) and GD 1212 (*right*). The spectroscopic solution given within 1σ is illustrated with a black box.

Figure 2 shows the projection on the $T_{\rm eff}$-log g plane of the merit function for KIC 119 and GD 1212. The logarithmic scale emphasizes the great contrast in S^2 between the minimum solution (blue) and maxima located elsewhere in parameter space (red). In both cases, we converge toward a particular solution that fits nicely within the spectroscopic solution bounding box. Resulting parameters for both stars are presented in Table 1.

	$T_{\rm eff}$	Spect. $T_{\rm eff}$	log g	Spect. log g	D(H)	D(He)
KIC 119	12,161	12,115	8.07	8.08	-7.52	-2.37
GD 1212	11,244	11,035	8.10	8.08	-6.04	-2.82

The case of the use of non-parameterized C/O core descriptions coming from evolutionary sequences, has to be dealt with great precaution. White dwarf models derived from main sequence evolution suffer from many uncertainties and are numerically too noisy to use for quantitative adiabatic asteroseismology. We can see an example of such an experiment in the case of GD1212 in Figure 3. Not only the best S^2 is noticeably degraded from 28 to 252, the mapping of the solution on the $T_{\rm eff}$-log g plane is scattered with local minima due to the numerical noise from the evolutionary profile. The best fit does not even lie within the spectroscopic limits anymore. Similar experiment with KIC 119 yelds similar results. Parameterized models are much better suited for this purpose.

Now we focus entirely on GD 1212 as this star presents rather unusual results. If we look at Figure 4a, we can see the weight functions of the different modes present in the pulsation spectrum. Evolution has pushed the g-modes to the outside because of the increase of degeneracy along the cooling track. This implies as we see in Figure 4a that weight functions have large amplitude in the outermost layers. But we can also notice

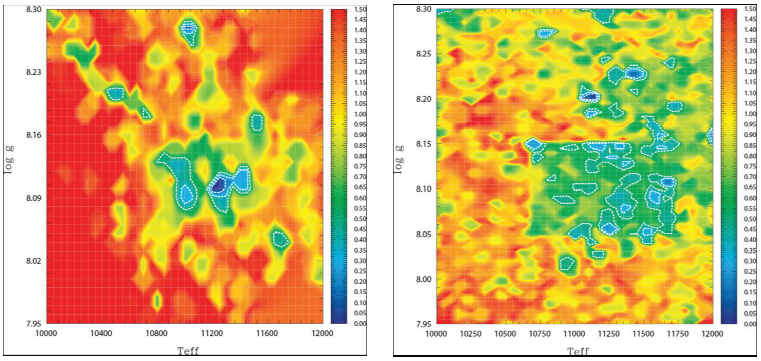

Figure 3. Projection on the $T_{\rm eff}$-log g plane of the merit function S^2 for GD 1212. *Left:* Homogeneous C/O core. *Right:* Non-homogeneous core with chemical profiles coming from evolutionary models.

that the core is almost entirely sampled by low-amplitude weight functions. Taking advantage of this behavior, we can properly assess the bulk C/O core composition to be 47-53 %. Since the interior of the star is not entirely sampled, it is important in order to infer the proper bulk composition of the star to have some kind of normalization. If we consider a profile coming from evolutionary sequences at the same effective temperature and similar surface gravity, by normalizing with the weight functions we can compare directly the two compositions. By doing so, we find quite a nice agreement between the two C/O core compositions found, the latter coming from evolutionary model being 43-57 %. We find slightly more carbon in our homogeneous composition, but, all in all, it agrees nicely and boost our confidence in the proper sampling of the core.

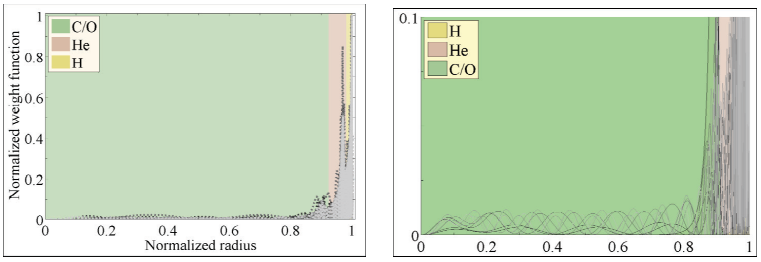

Figure 4. *Left:* Normalized weight functions of the modes present in GD 1212 as a function of the radius of the star. The area under the each curve is the same. *Right:* Zoom-in view of the normalized rotation kernels as a function of radius for each mode identified in the optimal model of GD 1212.

3. Internal Rotation Profile

Figure 4b emphasizes the low-amplitude, but still present, rotational kernels in the interior of the star. Many rotationally-split structures sound the deep interior. Based on the optimal model of GD 1212, we determined its internal rotation profile as seen in Figure 5. Probing more than 85% of the radius, and more than 90% of the total mass, we can assert that GD 1212 is rotating as a solid body. Unlike other ZZ Ceti stars analysed, it is the first time that such a depth into the interior of a star of the kind is probed. Indeed, and unfortunately, "simple" blue edge pulsators analysed so far do not exhibit rotational splitting on modes present in the core of the star. KIC 119 is one of these stars, and we can only sound a few percent of the radius into the interior.

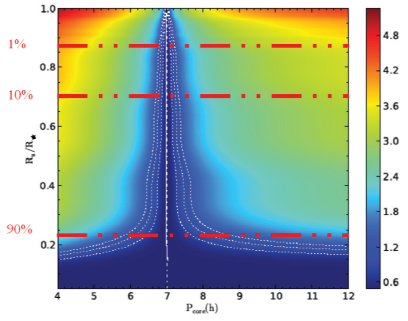

Figure 5. Contour map showing the behaviour of the normalized merit function S^2 in terms of the radius and in terms of the rotation period of the inner region for solid body rotation in a two-zone approach defined by Charpinet et al. (2009). Horizontal dot-dashed curves give an indication on the encompassed mass. The solution is illustrated by the nearly vertical white curve and the dotted white curves depict the 1, 2 and 3σ contours. In comparison, the vertical dot-dashed white curve gives the exact solution for solid-body rotation. At larger depths, the gravity modes lose their ability to measure local rotation, giving the divergence in the 1, 2 and 3σ contours.

4. Conclusion

These results boost our confidence in the reliability of the forward method with parameterized models for sounding white dwarf internal structure with asteroseismology. For the first time, we explore to great depths the internal composition and rotation profile of a ZZ Ceti star.

References

Charpinet, S., Fontaine, G., & Brassard, P. 2009, Nat, 461, 501
Fontaine, G., & Brassard, P. 2008, PASP, 120, 1043
Greiss, S., Gänsicke, B. T., Hermes, J. J., et al. 2014, MNRAS, 438, 3086
Hermes, J. J., Charpinet, S., Barclay, T., et al. 2014, ApJ, 789, 85

Annexe G

19^{th} European Workshop on White Dwarfs

19th European Workshop on White Dwarfs
ASP Conference Series, Vol. 493
Dufour, Bergeron, and Fontaine, eds.

Determination of the Core Composition of ZZ Ceti Stars through Seismic Means

N. Giammichele,[1] G. Fontaine,[1] S. Charpinet,[2] and P. Brassard[1]

[1]*Université de Montréal, Montréal, Québec, Canada;*
[redacted]

[2]*Institut de Recherche en Astrophysique et Planétologie (IRAP), Observatoire Midi-Pyrénées, Université Paul Sabatier / CNRS, Toulouse, France*

Abstract. As we know, the exact chemical profile in the core of a white dwarf is still very much uncertain, and comparing results from different investigators yields significant differences with the addition of the numerical noise coming from the accumulated uncertainties through all the various stages of pre-white dwarf evolution. We believe that until significant progress is made on that front, we can only probe the bulk core composition as a whole. In effect, the low sensitivity of the pulsation periods on the core composition can be exploited as long as we rely on the detection of confined modes that have relatively large amplitudes in the core. We show that the bulk composition of Ross 548 can be effectively determined, while that of GD 165 is not easily pinned down due to the lack of detected confined modes in that latter case.

1. Astrophysical Context

The pulsation periods detected in ZZ Ceti pulsators are mostly sensitive to the surface gravity (total mass), effective temperature, and envelope layering, particularly the thickness of the outermost hydrogen envelope. There is also some sensitivity of the pulsation periods to the core composition, but this is more difficult to exploit and must usually rely on the detection of modes that have relatively large amplitudes in the core, i.e., modes that are confined below the envelope (as opposed to modes that may be trapped above in the outermost layers). Unfortunately, the exact details of the C/O composition profile in the core are still very much uncertain as demonstrated by comparing the results obtained by various investigators: Falk Herwig, Maurizio Salaris, the La Plata Group, and results obtained with the recently-available MESA code. In brief, for comparable masses, significant differences exist in the final post-AGB core chemical profile. As an example, we can see in Figure 1 these significant discrepancies between two different oxygen profiles derived by Maurizio Salaris and the La Plata Group.

Until significant progress is made on that front, we believe that only the bulk composition of the core, as opposed to its detailed chemical profile, can be inferred with some confidence for ZZ Ceti stars and, furthermore, only if the circumstances are favorable. In addition, the core chemical profiles derived from post-AGB evolution suffer from numerical noise which is the consequence of the accumulated uncertainties associated with the way the various codes handle the technical difficulties of pre-white dwarf evolution. This numerical noise is a real "killer" in asteroseismological exercises

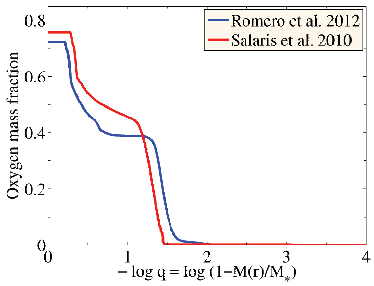

Figure 1. Differences in post-AGB core profiles: Internal oxygen profile predicted by two different codes for very similar masses. MESA would yet give another result. For asteroseismological purposes, it is then unwise to adopt one particular recipe. Parameterized models are better suited.

as clearly revealed by the failure of the so-called "fully evolutionary model" approach to provide seismic models able to account reasonably well (say within 1%) for the observed periods in ZZ Ceti pulsators, even in the cases where there are very few modes detected. A contrario, some very remarkable global period fits have been obtained using parameterized models (see, e.g., Giammichele et al. 2013). An eloquent example is presented in Figure 2 where we can see results of such fits with parameterized homogeneous core as opposed to fits with non-homogeneous core.

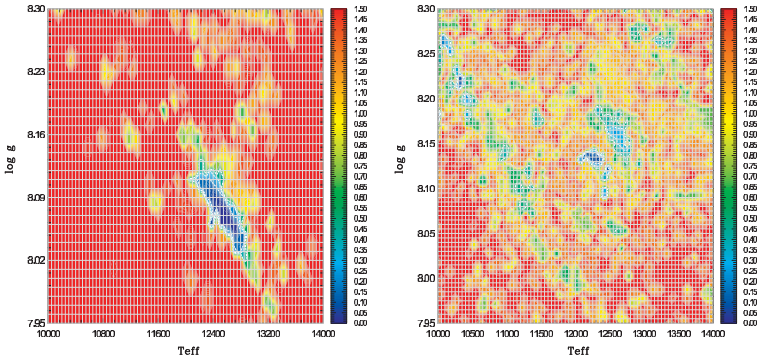

Figure 2. Homogeneous vs non-homogeneous cores: Comparison of the results of two asteroseismological exercises, one carried out with uniform-core models (*left panel*), and the other carried out with models incorporating Salaris-type C/O profiles (*right panel*), the latter having been smoothed but are suffering still from little unphysical bumps which produce noise in the calculated period spectrum. A clear definite "valley" in the merit function S^2 is seen in the left panel, and the best (minimum) value is $S^2 = 6.7$. In contrast, non-uniform core models lead to the rather patchy results shown on the right, and the best fit is then given by $S^2 = 40.7$. These are attempts to model the period spectrum observed in the Kepler DAV star KIC07594781 (Greiss et al. 2013).

We believe that the parametric approach, free of numerical noise and artefacts of pre-white dwarf evolution, remains the only practical way to carry out quantitative seismology for pulsating white dwarfs. In this context, it is always possible to parameterize the chemical profile in the core of a ZZ Ceti star model (this was attempted years ago by Bradley 1998), but it comes a point where the number of free parameters may become excessive in view of the limited number of detected periods which often characterizes the ZZ Ceti's, particularly those close to the empirical blue edge of the instability strip. In those cases, we prefer to use models with uniform core compositions, with no depth-dependent chemical composition as must be the case in reality, and exploit instead the dependence of the core composition on the integrated value of the Brunt-Väisälä frequency (as opposed to its detailed profile). Of course, only the bulk composition can be potentially inferred that way. Direct application of our procedure shows that the bulk core composition of Ross 548 (ZZ Ceti itself) can be effectively determined that way, while that of its near spectroscopic twin GD 165 (both are close to the blue edge) is not easily pinned down. The key difference is that, by chance, two out of the five detected modes in Ross 548 happen to be partially confined below the envelope and thus have non-negligible amplitudes in the core, while none of the six independent modes detected in GD 165 probe as deep.

2. Probing the Bulk Core Chemical Composition

Performing our asteroseismic exercise, we can use the homogeneous core composition as a variable. By doing so, we can independently and directly probe the bulk core composition without any further assumption. Results for two comparison stars, Ross 548 and GD 165, are given in Table 1. We can see that the two optimum C/O profile compositions (first column) differ significantly. We can also notice in Figure 3 that the optimum solution of Ross 548 is far more sensitive to the core composition than GD 165. The answer to this behavior lies in the distribution of the different weight functions. By looking at Figure 4, we can notice that confined modes allow us to probe from the surface down to 20% of the radius for the case of Ross 548, which is rather remarkable in a ZZ Ceti. In the case of GD 165, the lack of confined modes does not allow us to probe deep enough to correctly size the bulk core composition.

	Optimum bulk C/O	C/O obtained from normalized Salaris profile
Ross 548	63-37%	62-38%
GD 165	94-6%	88-12%

But how does that compare to evolutionary-based models? The second column of Table 1 shows the bulk core composition that we would obtain by normalizing a Salaris chemical profile with the weight function of the different modes for both stars. We can notice here the very nice agreement between these values and the optimum value found in our calculation for Ross 548. The agreement is still roughly similar for its spectroscopic twin GD 165, indicating that we should maybe have a slight change in the distribution of carbon and oxygen, or in the slope of their profile, towards the transition between the core and the enveloppe for this particular star.

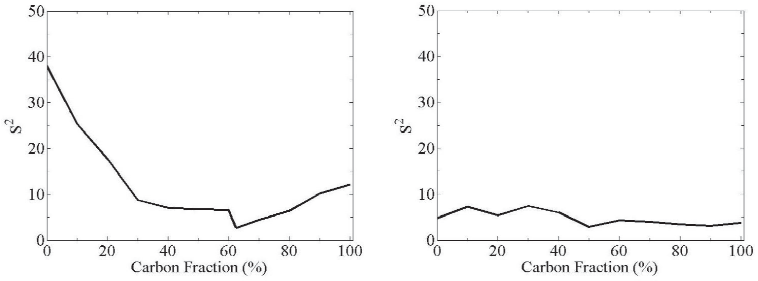

Figure 3. Determination of the optimal bulk composition of the optimal model. The lack of deep confined modes in GD 165 prevents us from having a better sensitivity for the bulk core composition. *Left:* Ross 548. *Right:* GD 165.

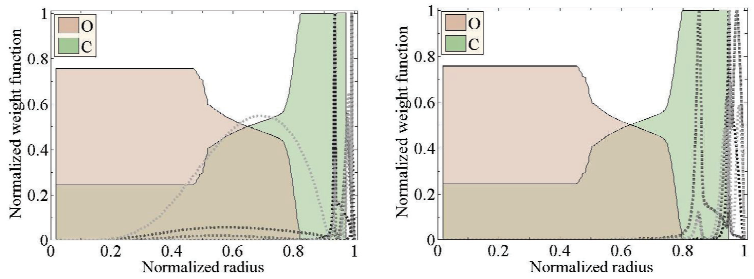

Figure 4. Weight functions of the optimal model. The confined modes of Ross 548 allow us to probe from the surface down to 20% of the radius, which is not the case of GD 165 as we can only probe down to 80% of the radius. *Left:* Ross 548. *Right:* GD 165.

3. Conclusion

White dwarf models derived from main sequence evolution suffer from many uncertainties and are numerically too noisy to use for quantitative adiabatic asteroseismology. Parameterized models are much better suited for the purpose. We can infer the bulk core composition of ZZ Ceti stars provided we detect deep confined modes. The C/O ratio in Ross 548 and GD 165 is consistent with the expectations of standard evolution theory.

References

Bradley, P. A. 1998, ApJS, 116, 307
Giammichele, N., Fontaine, G., & Brassard, P. 2013, in 18th European White Dwarf Workshop, ASP Conf. Series, 469, 49
Greiss, S., Gänsicke, B., Hermes, J. J., et al. 2013, in 18th European White Dwarf Workshop, ASP Conf. Series, 469, 223

Annexe **H**

IAU General Assembly

Astronomy in Focus, Volume 1
XXIXth IAU General Assembly, August 2015
Piero Benvenuti, ed.

DOI: 00.0000/X000000000000000X

Ultra-High Precision White Dwarf Asteroseismology

Noemi Giammichele[1], Stéphane Charpinet[2], Gilles Fontaine[1], Pierre Brassard[1], and Weikai Zong[2]

[1]Département de Physique, Université de Montréal, Montréal, QC H3C 3J7, Canada
[2]CNRS, UPS-OMP, Université de Toulouse, Toulouse, France

Abstract. We present a brief progress report in our quest for deriving seismic models of pulsating white dwarfs that can account simultaneously for all the observed periods at the precision of the observations. We point out that this is possible from a pratical point of view only if parametrized models are used to complement evolutionary models. We adopt a double optimization procedure that insures that the best possible model in parameter space is found objectively and automatically. Our ultimate goal is to be able to account for the exquisite period data gathered with *Kepler* and *Kepler-2* on key pulsating white dwarfs of both the DA (ZZ Ceti) and DB (V777 Her) type.

Keywords. stars — oscillations, white dwarfs

1. Astrophysical Context

The quest for credible and realistic seismic models for pulsating white dwarfs has been on for more than two decades now. Despite some remarkable early successes (e.g., Winget et al. 1991), progress has been slow, and conflicting results have sometimes been obtained (see, e.g., Section 8.2 of Fontaine & Brassard 2008 for a historical survey of the field through 2008). In particular, reliable and convincing seismic models of the pulsating white dwarfs have remained far and few despite the efforts of several groups. The observed periods still cannot be reproduced at a satisfactory level of accuracy, and, consequently, the inferences on the internal structure of these pulsators have remained weak, at best.

We have recently decided to revisit the problem of the seismic modeling of white dwarf stars using current and proven techniques, typical of those used highly successfully for the class of pulsating hot subdwarf B stars as reviewed and used recently in Charpinet et al. (2013) and Van Grootel et al. (2013). Our approach rests on a new detailed parametrization of white dwarf models coupled to a double optimization procedure that insures an objective search in parameter space for the best fitting model.

2. The Need for Parametrized Models

When some of us started investigating the application of the forward asteroseismological method to pulsating hot subdwarf and white dwarf stars more than a decade ago (see, e.g., Brassard et al. 2001 or Fontaine & Brassard 2002), we realized at the outset that the only practical way to do that would be through the use of parametrized models. It has been our assertion since that parametrized models, as compared to full evolutionary models, provide the best, if not the only way, to thoroughly search in parameter space for an optimal seismic model. In principle, state-of-the-art evolutionary models provide the best physical descriptions of stars. However, they suffer from two important drawbacks in the context of searching for the best seismic model.

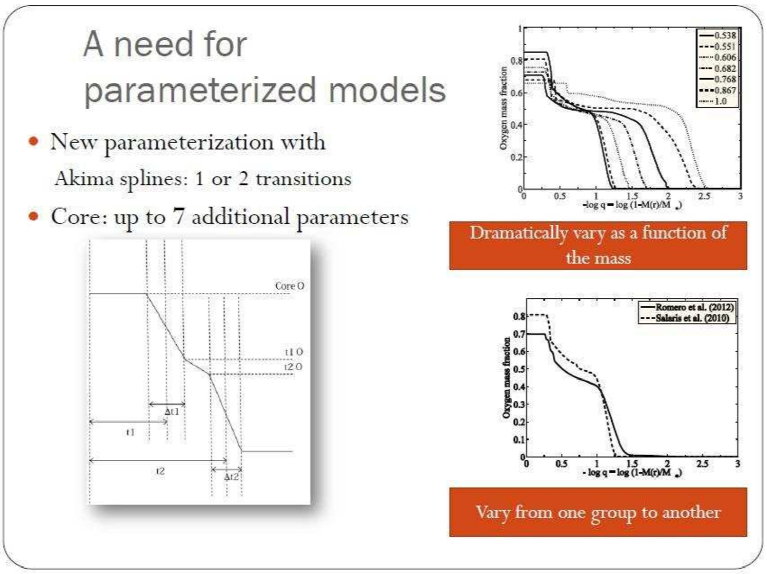

Figure 1. Our proposed scheme for parametrizing the composition profile in the C/O core of static white dwarf models and comparison with some results coming from evolutionary calculations. We note the significant differences between the results of two different studies, which should be seen as a warning against fixing the core chemical profile in a seismic search. The so-called "fully evolutionary models" of white dwarfs carry with them numerical defects that add up and may prevent, through noise, the success of an asteroseismic exercise.

The first of these shortcomings is their lack of flexibility. It is indeed nearly impossible, even with large computer clusters, to cover finely all of the relevant domains of parameter space with evolutionary sequences; it would take too much computing time. The practical consequence is that evolutionary sequences, necessarily limited in number, may actually miss the "correct" region of parameter space where resides the best seismic model.

The second drawback is that, by construction, it is implicitly assumed that the constitutive physics used in the construction of state-of-the-art evolutionary models is "perfect". Of course, this cannot be the case, especially in domains of the phase diagram corresponding to extreme physical conditions, such as those, for example, encountered in white dwarf stars. It may very well be the case in these circumstances that the input constitutive physics is not realistic enough and, consequently, that the observed pulsation periods cannot be accounted for at an acceptable level of accuracy on the basis of such evolutionary models.

In contrast, parametrized models offer maximum flexibility and speed for searching in parameter space. They can also compensate partly for uncertain input physics, and are most useful at that level for identifying the part of the input physics that needs improvement. They thus are most useful for providing feedback on the constitutive physics itself. Ultimately, they must of course be validated by improved evolutionary models.

Figure 1 illustrates the scheme that we adopted to parametrize the variable chemical composition in the C/O core of a white dwarf model. We point out in this context

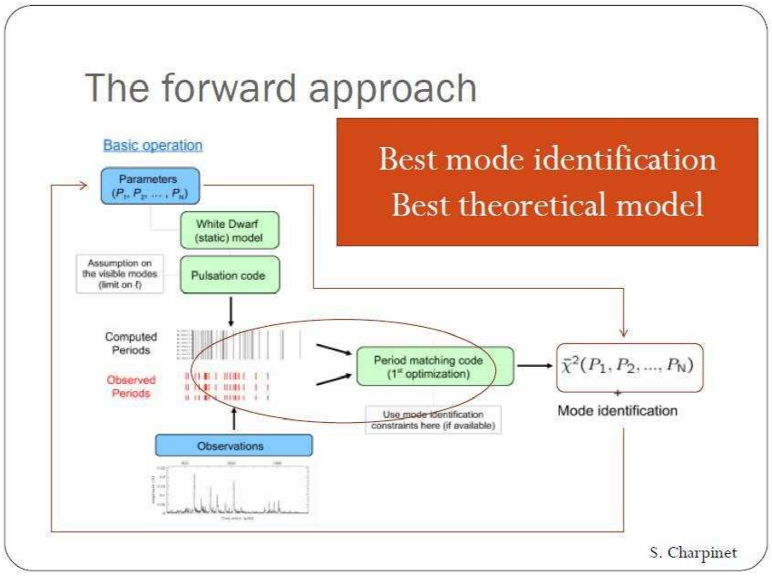

Figure 2. Schematic view of the basic operation in the double optimization procedure. The observed pulsation periods are optimally matched (first optimization) with periods computed for a model of given parameters. The fit is quantified using a χ^2-type merit function. This quantity is then further minimized as a function of the model parameters through the second optimization.

that evolutionary models are subject to major uncertainties, especially in late stages of stellar evolution, that usually pile up by the time the modeled star becomes a white dwarf. Relying on such models for accurate seismic analyses of individual white dwarfs is therefore dangerous. Instead, we prefer more flexible parametrized static models that can provide seismic measurements that do not depend on these uncertainties.

3. Objective Search in Parameter Space

Our strategy is based on the forward modeling approach that consists of finding the best possible match between a set of oscillation periods detected in a given star and the periods computed from stellar models. However, in order to provide trustable results, this global search has to be *objective* in the following sense: 1) A thorough exploration of the usually vast model parameter space has to be carried out, 2) the optimal solution best matching the pulsation properties has to be robustly found, 3) the uniqueness of the solution must be evaluated and other eventual secondary solutions must also be found, and 4) consistency with available external constraints (e.g., from spectroscopy or, ultimately, with improved evolutionary models) must be achieved. These requirements are fulfilled by a double optimization scheme and the associated optimization tools that we developed for that purpose.

The basic operation in the double optimization procedure is schematically illustrated in Figure 2 (see also Van Grootel et al. 2013 and references therein). The second op-

timization then takes place in the N-dimensional parameter space where the best fit model(s) is (are) searched. This optimization can be difficult depending on the complexity of the χ^2-type merit function and is dealt with LUCY (genetic evolLUtion Code for asteroseismologY), a powerful optimizer specifically developped for that purpose. This code is a massively parallel hybrid genetic algorithm capable of multimodal optimization which provides several advantages: 1) It does not rely on model grids (the parameter space is explored continuously), leading to a much higher computational efficiency and avoiding grid resolution problems, and 2) It is very robust at finding the global optimum (best solution) as well as all potentially interesting secondary optima. More details on this technique, as adapted to white dwarfs, can be found in Charpinet et al. (2015).

At the time of the conference, we reported on some preliminary results that were extremely encouraging. That trend has been confirmed since then, although we have not yet completely finished our investigations. We will report elsewhere the final results of our ongoing effort, which is part of the Ph.D. thesis of the lead author.

References

Brassard, P., Fontaine, G., Billères, M., Charpinet, S., Liebert, J., & Saffer, R.A. 2001, ApJ, 563, 1013

Charpinet, S., Giammichele, N., Brassard, P., Van Grootel, V., & Fontaine, G. 2015, 19th European Workshop on White Dwarfs, ASP Conference Series, Vol. 493, 15

Charpinet, S., Van Grootel, V., Brassard, P., Fontaine. G., Green, E.M., & Randall, S.K. 2013, EPJ Web of Conferences, Vol. 43, 04005

Fontaine, G., & Brassard, P. 2002, ApJ, 581, L33

Fontaine, G., & Brassard, P. 2008, PASP, 120, 1043

Van Grootel, V., Charpinet, S., Brassard, P., Fontaine, G., & Green, E.M., 2013, A&A, 553, A97

Winget, D.E., Nather, R.E., Clemens, J.C., et al. 1991, ApJ, 378, 326